MULTISCALE NUMERICAL SIMULATIONS OF THE MAGNETIZED PLASMA SHEATH WITH MASSIVELY PARALLEL ELECTROSTATIC PARTICLE-IN-CELL CODE

BY

RINAT KHAZIEV

DISSERTATION

Submitted in partial fulfillment of the requirements
for the degree of Doctor of Philosophy in Nuclear, Plasma, and Radiological Engineering
in the Graduate College of the
University of Illinois at Urbana-Champaign, 2018

Urbana, Illinois

Doctoral Committee:

Assistant Professor Davide Curreli, Chair
Professor David Ruzic
Professor Rizwan Uddin
Professor Jonathan Makela

Abstract

Understanding the physics of the plasma boundary and plasma-surface interactions is one of the key scientific challenges in fusion science and engineering. Large-scale integrated simulations and high-performance computing can provide valuable insights on the dynamic phenomena involved at the interface between the plasma and the material surface. Current state-of-the-art simulations of magnetically-confined fusion devices are typically performed using gyrokinetic approximations, aimed at resolving the physics of the core plasma, scrape-of-layer, and a portion of the divertor. However, the region of plasma near to the surface, called the plasma sheath, where the plasma ions accelerate from subsonic to supersonic conditions, is typically either not handled or treated with ad-hoc approximations. The characteristic scale of the near-surface plasma (sheath and presheath) is comparable to the Debye length, which is of the order of, or smaller, than the ion gyroradius. A detailed description of the kinetic processes occurring during the supersonic acceleration across the collisional and magnetic presheaths and requires a fully-kinetic model that is not present in any current fusion code, thus limiting a detailed evaluation of the energy-angle spectrum of the ions impacting on the surface of a tokamak.

We have developed and verified a new massively-parallel Particle-in-Cell code, named hPIC, solving the multi-species Boltzmann-Poisson integro-differential set of equations. We give an overview of the model equations, of the architecture of the code, and summarize the verification tests, also presenting the scalability tests performed on the Blue Waters supercomputer at the University of Illinois. The model has been used for the numerical characterization of the plasma sheath and presheath in strong magnetic fields. Thanks to the new Particle-in-Cell, we have performed a systematic analysis of the structure of

the magnetized plasma sheath, in order to determine the trends of the Ion Energy-Angle Distributions (IEAD) of the particles impacting on the wall after crossing the presheath and sheath regions. The model provides the dependance of the IEAD on the level of magnetization and magnetic inclination with respect to the surface. We have found that in regimes of intermediate-to-strong magnetization, the ion flow has a characteristic three-dimensional structure, which appears in all evidence within the magnetic presheath after the ions transition from sonic to supersonic. The model also suggests the disappearance of the electrostatic (Debye) sheath at high magnetic angles, with an interesting reduction of the ion flow down to subsonic conditions. Furthermore, detailed Particle-in-Cell simulations have been compared to simplified representations of the magnetized plasma sheath based on a set of fluid equations coupled to a Monte-Carlo particle-tracer for the reconstruction of the Ion Energy-Angle Distributions (IEAD) of the particles impacting on the wall, finding qualitative agreement and suggesting strategies of model reduction which could be used in Whole-Device Modeling.

Finally, the model of the magnetic and collisional presheath has been validated against three-dimensional tomographic Laser-Induced Fluorescence measurements taken at the HELIX helicon facility at WVU. Our analysis highlights the role of neutral gas pressure, background neutral flow, and ambient electric field on the structure of the collisional and magnetic presheath, finding absolute quantitative agreement between our calculated data and experimental measurements. In particular, the work gives clear evidence of the three-dimensional structure of the magnetized plasma sheath, a unique feature not present in the classical thermal sheath in unmagnetized conditions.

To my grandmother Devletberdina Almabika Garifovna (01/01/1938-01/01/2013), who passed away shorty after starting my doctoral studies

Acknowledgments

First and foremost, I would like to thank my parents, Rafit, and Zabida, for instilling in me the love of learning and thirst for knowledge. I am infinitely grateful for the years of your dedicated efforts, helping me to find my passions and interests. Your support in all of my endeavors has led me to completing my studies. I want to thank my extended family for your encouragement and support.

A special thank you goes to my advisor, Davide Curreli. It has been an honor to be your first PhD student. Thank you for being my mentor. You have taught me how to be a good scientist by being a wonderful example. I appreciate the academic freedom that I have had as a member of your group: you have given me a unique chance to explore my interests and ideas that have led me to this work. I could not have asked for a more patient and supportive advisor than you.

This thesis would be impossible without our collaboration with Derek Thompson, Umair Siddiqui and Professor Earl Scime from West Virginia University. Our fruitful discussions and the plasma sheath measurement that you have made have led us to unexpected and fascinating findings. I want to also especially thank Derek Thompson for relentlessly answering my long, tedious, and endless questions about the measurements performed at HELIX facility; I appreciate your patience and insightful answers.

I would also like to thank Professors David Ruzic and James Stubbins, for expanding and reinvigorating the plasma physics program in the Nuclear, Plasma, and Radiological Engineering Department. Without your vision and actions, I would not have had a chance to work with my advisor, Davide Curreli, on many interesting problems.

I want to thank the members of the Laboratory of Computational Plasma Physics for

the engaging discussions, encouragements and friendships. Shane and Jon, it has been a pleasure working with both of you on the same topic and having discussions on the plasma sheath and the plasma-material interactions throughout my graduate studies. Alyssa and Cameron, I appreciate your help working on hPIC, and I hope that you have enjoyed your time at LCPP. Steven, it has always been delightful to have conversations with you on supercomputing and the HPC. Mikhail, Moutaz and Kurt, it has been a pleasure working with all of you, and I wish you the best in your graduate studies.

I would like to also thank my friends who I have met during my internships at University of Illinois Research Park. You have given me the support, encouragement and sanity during the most challenging period of my studies. I want to thank the staff, especially Mark Moran, of John Deere Technology and Innovation Center for supporting my studies.

To everyone, who has not been mentioned here by name, I want to thank you for your support, discussions, friendships and keeping me sane throughout my studies.

This work was supported by the NCSA Faculty Fellowship and the Blue Waters Exploratory Allocation of the National Center for Supercomputing Applications at the University of Illinois-Urbana Champaign and U. S. Department of Energy, Office of Science, Office of Fusion Energy Sciences and Office of Advanced Scientific Computing Research through the Scientific Discovery through Advanced Computing (SciDAC) project on Plasma-Surface Interactions, under Award No. DE-SC00-08875.

Table of Contents

List of Tables

List of Figures

Chapter 1

Introduction

1.1 Taming the Plasma-Material Interface

In early tokamaks, the plasma was touching the wall of the vacuum chamber causing significant erosion of the wall material. The particles released by the wall diffuse into the core of the tokamak plasma, significantly polluting the plasma and increasing radiation losses. Modern tokamak designs include divertor devices, which are specifically designed to withstand these energetic particles fluxes. Figure 1.1 shows the diagram configuration of the tokamak with a single divertor. In presence of the divertor, the magnetic fields create three regions with closed and open magnetic lines that are separated by the separatrix: the core, scrape-off layer located outside of the separatrix and the divertor region located behind the separatrix and x-point. Since the magnetic lines are open particle transport in the scrape-off layer is mostly convective, rather than diffusive like in the core of the tokamak [7].

In the divertor region of magnetically-confined plasmas the interaction between the plasma and material surfaces poses significant challenges to the survivability of plasma-facing components (divertor plates), limiting the successful development of commercially-viable nuclear fusion reactors. Taming the Plasma-Material Interface is one of the top priorities for fusion science to enable a demonstration fusion power plant [8]. When exposed to plasma irradiation, plasma-facing materials exhibit evidence of surface morphology modifications and nano-structuring [9], with detrimental consequences on the thermomechanical integrity of the wall. The challenges are multiple, ranging from understanding the spectrum of the energetic particles impacting on the surface, to predicting the effects of the particle bombardment to the surface erosion and reconstitution.

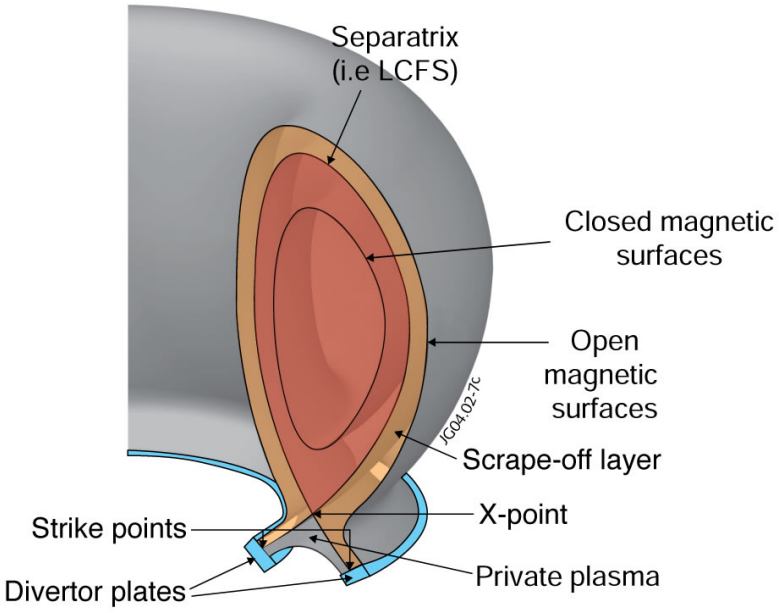

Figure 1.1: Schematic diagram of the fusion reactor with a single divertor [4]
.

1.2 Role of High-Performance Computing

When designing large fusion devices, an empirical trial-and-error approach becomes soon economically inviable. Large-scale integrated simulations and high-performance computing can greatly help on all aspects of the design of a fusion device [10], including plasma-material interactions, providing valuable insight on the dynamic phenomena involved at the interface between the plasma and the material surface. For example, coupling different physics components describing the near-surface plasma to other accounting for surface erosion would allow to describe for the strongly-dynamic phenomena occurring at the interface. In particular, the transport processes involving both the plasma species and the material impurities occur at the similar time scales in the conditions expected in a fusion reactor [11], thus requiring a self-consistent model directly coupling a fully-kinetic sheath simulation to a coarse-grained material model.

The importance of the advanced modeling of the whole device using first-principle ap-

proaches was recently highlighted in the DOE-FES Exascale Requirement Report for fusion energy [12]. Whole device modeling often relies on a set of the simplified models. Such models can be derived from both empirical information and/or first-principle modeling. Integrated models of Plasma-Material Interactions, which are currently missing in whole device codes, are critical for engineering design, where multiple configurations of the engineering solutions have to be considered before making a final decision. Additionally, first-principle models are a necessary tool for better fundamental understanding of the processes involved.

At the plasma-material interface, the collisional and magnetic presheath act as an interface layer between the Scrape-Off-Layer plasma and the material surface. Such interfaces include a multitude of processes, highly kinetic in nature, involving multiple plasma species (electrons, ions, neutrals, material impurities) in a dynamically evolving environment tightly coupled to the surface. At the nominal conditions anticipated for a reactor, the majority of sputtered material ionizes close to the surface and is redeposited nearby. The redeposition process forms a new reconstituted surface layer with different and unknown thermo-mechanical properties that differ from the original ordered lattice. This continuously eroded and re-deposited surface can significantly alter the PFC lifetime, affect the retention of hydrogenic species (deuterium, tritium), and affect the mechanisms associated with microscopic erosion of the surface (both net and gross erosion). Thus, the boundary plasma and the wall are dynamically interacting with each other, constantly changing chemical composition of plasma and the wall, forming the an non-equilibrium system that displays multiple time and spacial scales. Short times scales (μs) affect plasma composition and equilibrium; the erosion, redeposition, and plasma polution with impurities occur on the medium time scales; and the long term evolution of the material surfaces occur typically on on the scale of the hours.

1.3 Modeling the Near-Surface Plasma

A self-consistent description of the physical processes in the boundary region of the plasma has requires to consistently resolve all time scales in the numerical simulations. Each time-

scale can be characterized by its own model:

1. A Plasma sheath/presheath sovler handling kinetically the evolution of the plasma species on the short to medium time-scales: ion, electrons, neutrals and material impurities. The sheath is resolved by the Boltzmann-Poisson or Boltzmann-Maxwell systems.

2. A material model, characterizing the plasma-material interaction itself. Material solver has to handle material erosion processes, such as sputtering, backscattering, etc. The model has to resolve long-term evolution of the material morphology and compositions.

3. Collisional physics module, that can robustly resolve most relevant plasma compositions. The collisional modules are relevant to producing predictive simulations for the transport of the heavy and light plasma particles across the plasma sheath and presheath.

The goal of this thesis is addressing the first of these three points, by developing an accurate and validated set of models at the fluid and kinetic level necessary for the description of the near-surface plasma, namely the plasma presheath (both collisional and magnetic), and the Debye sheath. Three key steps have been undertaken:

1. The development of a large-scale, HPC-oriented kinetic model (named hPIC) of the near-surface plasma, for the description of the sheath/presheath region;

2. A systematic and detailed investigation of the structure of the plasma sheath and presheath in magnetized conditions using both the kinetic model and simplified reduced-parameters fluid models, in both collisionless and collisional conditions;

3. A validation of the magnetic presheath models, both kinetic and fluid, against the most accurate three-dimensional tomographic Laser-Induced Fluorescence measurements available to date.

These three key steps have been successfully accomplished during the development of this Thesis, and they will be described in Chapters 3, 4, and 5 respectively of the present

work. The following sections provide some additional background information necessary to the chapters.

1.4 Need of a new HPC code for Near-Surface Plasmas

According to the reports from the Plasma-Material Interaction [9] and Integrated Simulations for Magnetic Fusion Energy Science [10] workshops, understanding the physics of the plasma boundary and evolving material is one of the key scientific problems in the fusion engineering. The current state-of-the-art simulations of fusion devices are performed with gyrokinetic particle in cell codes and are able to resolve the physics of the core plasma [13, 14, 15] and scrape-of-layer [16, 17] of the tokamak. In gyrokinetic PIC methods, the particle motion is split into motion of the guiding center and gyrational motion around the guiding center; the state vector of a single particle is then described by the coordinate of the guiding center $\mathbf{x}$, particle velocity parallel to the magnetic field line $V_{\parallel}$ and gyro-velocity $V_{\perp}$. Gyrokinetic PIC codes are able to resolve spatial scales comparable to the gyroradius $r = mV_{\perp}/|q|B$ (m particle mass, q charge and B magnetic field), which make then applicable and beneficial in the plasma core and the scrape-off layer of a fusion device. However, the characteristic scale of the magnetized plasma sheath is comparable to the Debye length, which is of the order of, or smaller, than the ion gyroradius. Therefore, the gyrokinetic approximation does not hold in the plasma sheath. Boundary conditions in gyrokinetic PIC codes typically avoid explicitly resolving the plasma sheath through use of the simplified models (the so called "logical sheath") [18].

A detailed description of the kinetic processes occurring in the plasma sheath is not resolved by any current state-of-the-art fusion code, which limits the possibility of thorough numerical studies of plasma-material interactions in tokamaks. A comprehensive simulation of the whole device requires a kinetic simulation of the magnetized plasma sheath in two or three spatial dimensions and three velocity dimensions, over large domains [17]. The kinetic simulations could be performed using Vlasov [19, 20, 21] or PIC methods [22]. According to the Vlasov method, the plasma is described using a continuum approximation and the dis-

tribution function is evolved in 6-dimensional phase space. Such calculations are memory- and computationally expensive, and they are challenging even for the next generation exascale computers. On the other side, PIC methods are more suitable to parallelization and high-performance computing. The goal of this work is developing a robust electrostatic PIC (ES-PIC) method and a code capable of performing large scale simulations of the plasma sheath in strongly magnetized conditions, accounting for the dynamics of both electrons and more massive ion species.

1.5 Plasma Sheath in Strong Magnetic Fields

The boundary layer between the bulk plasma and a material wall is called a plasma sheath. The usual quasi-neutrality condition of plasmas is broken in the plasma sheath, and large electrostatic forces are present which accelerate the plasma ions toward the wall up to supersonic conditions. In presence of a magnetic field, the plasma sheath can be divided into three major areas (Fig. 1.2), as classified by Chodura [23]: the collisional presheath, magnetic presheath, and Debye sheath. Despite the plasma density gradually decreasing in the plasma presheath, the quasineutrality condition still holds in that region. When the drift velocity of the ions in the direction *parallel* to the magnetic lines, $V_{\|}$, reaches the ion acoustic speed, the ions enter the magnetic presheath. The location at which the ion drift velocity in the direction *perpendicular* to the wall V_y equals the ion acoustic speed characterizes the entrance to the Debye sheath.

The influx of the charged ions on the material surface can induce morphological transformations of the surface and modification of the chemical and structural composition of the near-surface layers. In addition, the material wall can release charged and neutral particles which cause degradation of the plasma facing components (PFC). One of the key drivers of the material response to the incident particle fluxes is the physical sputtering of surface material. The sputtering yield $Y = N_{sputtered}/N_{incident}$ is determined by the ratio of the number of sputter particle $N_{sputtered}$ to the number of the incident particle $N_{incident}$.

The sputtering yield Y demonstrates strong nonlinear dependence to the ion impact

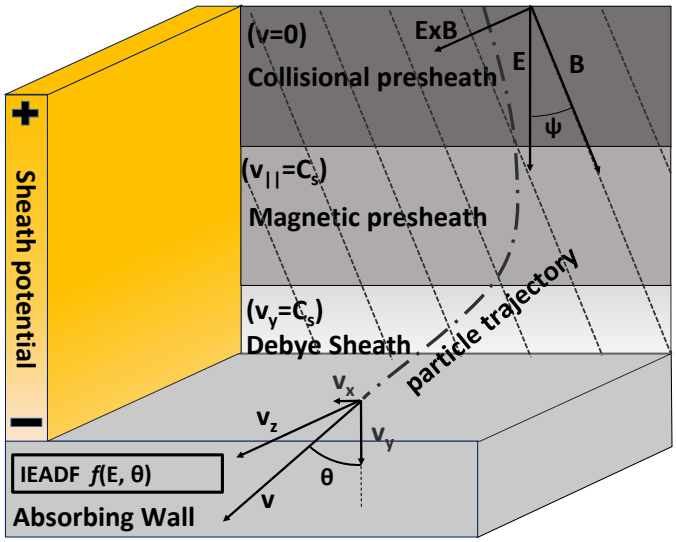

Figure 1.2: Structure of the magnetized plasma sheath in front of a material wall

angle and the energy of the impacting particles [24] [25] [26]. Thus the material response to the incident ions is determined by the distribution function of those particles at the material surface $f(\theta, E)$; here $\theta = \tan^{-1}(V_{xz}/V_y)$ is the impact angle of the ions on the wall, V_{xz} is magnitude of the ion velocity on the plane parallel to the wall, and E is the kinetic energy of the ions at the time of impact. Some industrial applications benefit from high sputtering rates from the surface. However, the plasma facing components of a fusion device are expected to have a lifespan over thousands of discharges [11], and the degradation rate of the plasma facing components is desired to be small ($Y \sim 10^{-6}$). Hence, understanding and controlling the fluxes and the distribution functions of the ions incident to the material wall is critical for engineering of the plasma facing component for the next generation of fusion devices.

Besides understanding the fluxes of plasma ions impacting on the material wall, it is also relevant to estimate the transport of the impurities released by the wall and entering the scrape-off layer and the core of fusion devices. When impurity particles diffuse through the scrape-off-layer to the core of a fusion device, they can contaminate the plasma resulting in increased radiation losses, reduced fusion performance, and under some conditions thermal

quenching and termination of the discharge. Therefore, minimizing the fluxes of the wall impurities is a necessary requirement for the successful deployment of nuclear fusion reactors.

1.6 Understanding the Ion Energy-Angle Distributions

The distribution function of the ions impacting the wall might have significant deviations from thermal distribution, which makes fluid models inapplicable for the calculation of the Ion Energy-Angle Distributions (IEADs) at the material surface.

Fluid models have been developed by previous authors [27, 28, 29, 30, 31]. Such models provide an accurate description of the particle fluxes in the quasi-neutral region of the plasma (presheath), where particles are distributed according to drifting Maxwellian distributions. In order to account for kinetic effects, the dynamics of charged particles in the magnetized plasma sheath can be resolved using kinetic approaches. A Vlasov-Poisson kinetic model was developed by Manfredi and Devaux [19, 20, 21] in one spatial dimension and three velocity dimensions (1D3V). A semi-analytical form of the IEAD was obtained using a 1D2V gyro-kinetic model [32, 33] and previously developed 1D3V PIC simulations [34]. The Vlasov model was able to produce IEADs of ions at the wall, but the shape and the scale of the resulting IEADs were not dependent on the ion mass contradicting previous studies [35]. The giro-kinetic theory has limitations in the plasma sheath, and previous PIC simulations did resolved plasma only in a single spatial dimension.

Despite IEADs being obtained in the previous works, the underlying restrictions imposed by the chosen dimensionality of the simulation setup prevents the applications of these methods and codes to realistic engineering problems, which involve complex plasma profiles, arbitrary distribution function, gradients of the magnetic field, and arbitrary surface morphologies [36, 24]. In order to fully capture the complexity of this problem, kine tic models with two or three spatial dimensions and three velocity dimensions are required.

1.7 Thesis Overview

The goal of this thesis is developing and validating a multi-species kinetic model of the plasma sheath and presheath in strong magnetic fields, capable to handle the evolution of the distribution function of electrons, ions, neutrals, and material impurities from the quasi-neutral region to the first surface layers.

The target mathematical problem that we solved is the multi-species Boltzmann-Poisson set of equations, which has been discretized using Particle-in-Cell techniques. Chapter 2 gives a review of the fundamental theory of Particle-in-Cells. At the same time, we are interested in developing reduced models based on the moments of the Boltzmann equation (fluid equations), in order to understand the limitations of such models with respect to fully-kinetic approaches. In Chapter 2 we will highlight the fundamental differences between kinetic and fluid approaches. In addition to that, in Chapter 2 we will discuss the fundamental assumptions behind the Particle-in-Cell discretization technique, and the implications on the behavior of the simulated plasma.

Chapter 3 describes the development and the architecture of a new massively-parallel Particle-in-Cell code developed as part of this Thesis, named hPIC, solving the multi-species Boltzmann-Poisson set of equations. In the same chapter we also summarize the results of the verification tests done on the code, and the scalability tests performed on the Blue Waters supercomputer at the University of Illinois. The code is currently stored on a private repository of the LCPP group (Laboratory of Computational Plasma Physics) and available at the following url: `https://github.com/lcpp-org/hPIC`. An overview of the code has also been published in Computer Physics Communications [37].

Chapter 4 presents a systematic study of the magnetized plasma sheath, performed with both Particle-in-Cell simulations *and* fluid models. First, we have developed a simplified representation of the magnetized plasma sheath based on a set of fluid equations coupled to a Monte-Carlo particle-tracer for the reconstruction of the Ion Energy-Angle Distributions (IEAD) of the particles impacting on the wall of a strongly magnetized plasma. In the same chapter we have also explored coupling techniques between the fluid and the kinetic model,

proposing a simple technique to account for kinetic corrections in a reduced fluid model. Some of the results presented in Chapter 4 have been published in Physics of Plasmas [35]

Finally, Chapter 5 is focused on the experimental validation of both Particle-in-Cell and fluid models of the magnetized plasma sheath. After highlighting the importance of the collisional processes in the plasma sheath, we present a systematic comparison of our simulation results with three-dimensional tomographic Laser-Induced Fluorescence measurements taken at the HELIX helicon facility at West Virginia University. The validation activity has been performed as part of a fruitful collaboration between West Virginia University (D. Thompson and Prof. E. Scime) and our group at the University of Illinois at Urbana Champaign. In the chapter we analyze the role of neutral gas pressure, background neutral flow, and an ambient electric field on the structure of the collisional and magnetic presheath, finding absolute quantitative agreement between the calculated data and the experimental measurements. In particular, the work gives clear evidence of the three-dimensional structure of a magnetized plasma sheath, a unique feature not present in the classical thermal sheath in unmagnetized conditions.

Chapter 2

Electrostatic Particle-in-Cell Method

This chapter is focused on the kinetic theory of plasma and the theory of the kinetic plasma simulations. Section 2.1 summarizes kinetic plasma theory highlighting the assumptions of kinetic and fluid plasma models. An overview of the Particle-in-Cell method [22] is presented in the section 2.2. The consequences of the Particle-in-Cell approximations on the behavior of the simulated system are discussed in section 2.3. Sections 2.4 and 2.5 are focused on Particle-in-Cell simulations with realistic collisional processes and simplified electron models.

2.1 Dynamics of the Many Particle Systems

Since the quantum effects in plasmas are negligible, the state of a single particle can be represented by its location in the physical space $\mathbf{x} = [x, y, z]^T$ and its velocity $\mathbf{V} = [V_x, V_y, V_z]^T$. The particle coordinate $\mathbf{x}$ and velocity $\mathbf{V}$ vectors form the phase space: a combination of all possible states that a particle can take in the system. In Klimontovich's formalism, a single particle is considered to be infinitely small, and its location in phase space is described by a product of the two delta functions

$$\delta\left(\mathbf{x} - \mathbf{x}_p\left(t\right)\right)\delta\left(\mathbf{V} - \mathbf{V}_p\left(t\right)\right), \tag{2.1}$$

where $\mathbf{x}_p(t)$ and $\mathbf{V}_p(t)$ are the coordinates and velocity of the particle p at time t.

In a system with N_p particles of the same kind (species), where N_p is relative large, the

total population of the particles can be described by the distribution function $f^*(\mathbf{x}, \mathbf{V}, t)$

$$f^*(\mathbf{x}, \mathbf{v}, t) = \sum_{p=1}^{N_p} \delta(\mathbf{x} - \mathbf{x}_p)\delta(\mathbf{V} - \mathbf{V}_p). \tag{2.2}$$

On a small length scale Λ (microscopic length scale), when Λ is smaller than the average distance between particles d_p

$$d_p = LN_P^{-1/D} \tag{2.3}$$

where L is a typical length scale and D is the dimensionality of a system, the distribution function $f^*(\mathbf{x}, \mathbf{v}, t)$ has non-zero values only in the vicinity of the particle coordinates in phase space $[\mathbf{x}_p, \mathbf{V}_p]$.

However, the microscopic distribution function can be averaged over macroscopic length scales $\lambda_D > \Lambda > d_p$

$$f\left(\mathbf{x}, \mathbf{V}, t\right) = \left\langle f^*\left(\mathbf{x}, \mathbf{V}, t\right)\right\rangle = \frac{\int d^3\mathbf{x} \int d^3\mathbf{V} f^*\left(\mathbf{x}, \mathbf{V}, t\right)}{\int d^3\mathbf{x} \int d^3\mathbf{V}}, \tag{2.4}$$

where the distribution function $f\left(\mathbf{x}, \mathbf{V}, t\right)$ is continuous and "smooth" in phase space, and quantifies the expected number of particles in the infinitely small volume of the phase space $d^3\mathbf{V}d^3\mathbf{x}$ around $\mathbf{x}$ and $\mathbf{V}$

$$f(\mathbf{x}, \mathbf{V}, t)d^3\mathbf{V}d^3\mathbf{x}. \tag{2.5}$$

The integral of the distribution function over the velocity space yields the particle density $n\left(\mathbf{x}, t\right)$

$$n\left(\mathbf{x}, t\right) = \int d^3\mathbf{V} f(\mathbf{x}, \mathbf{V}, t), \tag{2.6}$$

and integrating over both velocity and coordinate space yields the total number of particles in the system N_p at time t

$$N_p(t) = \int \mathbf{d}^3\mathbf{V} \int \mathbf{d}^3\mathbf{x} f(\mathbf{x}, \mathbf{V}, t). \tag{2.7}$$

On the microscopic scale, the particle densities can be defined using Klimontovich's formal-

ism

$$n^*(\mathbf{x},t) = \sum_p^{N_p} \delta(\mathbf{x} - \mathbf{x}_p(t)). \tag{2.8}$$

In the presence of electric and magnetic fields, the trajectories of a single particle p will follow Newton's equation of motion

$$\begin{aligned} m\frac{d\mathbf{V}_p}{dt} &= q\left(\mathbf{E} + \mathbf{V}_p \times \mathbf{B}\right) && (2.9)\\ \mathbf{V}_p &= \frac{d\mathbf{x_p}}{dt}, && (2.10) \end{aligned}$$

where $\mathbf{E}$ and $\mathbf{B}$ are the electric and magnetic fields acting on the particle p at time t, respectively. By chain rule, the time evolution of the microscopic distribution function (2.2) becomes

$$\begin{aligned} \frac{\partial f^*(\mathbf{x},\mathbf{V},t)}{\partial t} &= \frac{\partial}{\partial t}\sum_{p=1}^{N_p}\delta(\mathbf{x}-\mathbf{x}_p(t))\delta(\mathbf{V}-\mathbf{V}_p(t)) \\ &= \sum_{p=1}^{N_p}\Big[\frac{\partial\delta(\mathbf{x}-\mathbf{x}_p(t))}{\partial t}\delta(\mathbf{V}-\mathbf{V}_p(t)) \\ &+ \delta(\mathbf{x}-\mathbf{x}_p(t))\frac{\partial\delta(\mathbf{V}-\mathbf{V}_p(t))}{\partial t}\Big] \end{aligned} \tag{2.11}$$

Using the equation of motion (2.9) and (2.10), the first term of equation (2.11) becomes

$$\begin{aligned} \delta(\mathbf{V}-\mathbf{V}_p(t))\frac{\partial\delta\left(\mathbf{x}-\mathbf{x}_p\left(t\right)\right)}{\partial t} &= -\delta(\mathbf{V}-\mathbf{V}_p(t))\frac{d\mathbf{x}_p}{dt}\cdot\nabla_x\delta(\mathbf{x}-\mathbf{x}_p(t)) \\ &= -\mathbf{V}_p(t)\cdot\nabla_x\left[\delta\left(\mathbf{x}-\mathbf{x}_p\left(t\right)\right)\delta\left(\mathbf{V}-\mathbf{V}_p\left(t\right)\right)\right], \end{aligned} \tag{2.12}$$

and the second term becomes

$$\begin{aligned} &\delta(\mathbf{x}-\mathbf{x}_p(t))\frac{\partial\delta(\mathbf{V}-\mathbf{V}_p(t))}{\partial t} = -\delta(\mathbf{x}-\mathbf{x}_p(t))\frac{d\mathbf{V}_p}{dt}\nabla_V\delta(\mathbf{V}-\mathbf{V}_p(t)) \\ = \; &-\frac{q}{m}\left[\mathbf{E}+\mathbf{V}_p(t)\times\mathbf{B}\right]\nabla_V\left[\delta(\mathbf{x}-\mathbf{x}_p(t))\delta(\mathbf{V}-\mathbf{V}_p(t))\right]. \end{aligned} \tag{2.13}$$

Substituting equations (2.12) and (2.13) into the time derivative of the distribution function

(2.11) gives the Klimontovich equation

$$\begin{aligned}\frac{\partial f^{*}\left(\mathbf{x},\mathbf{V},t\right)}{\partial t} &= -\sum_{p=1}^{N_p}\left[\mathbf{V}_p(t)\cdot\nabla_x\left[\delta\left(\mathbf{x}-\mathbf{x}_p\left(t\right)\right)\delta\left(\mathbf{V}-\mathbf{V}_p\left(t\right)\right)\right]\right. \\ &+ \left.\frac{q}{m}\left[\mathbf{E}+\mathbf{V}_p(t)\times\mathbf{B}\right]\nabla_V\left[\delta(\mathbf{x}-\mathbf{x}_p(t))\delta(\mathbf{V}-\mathbf{V}_p(t))\right]\right] \\ &= -\mathbf{V}\cdot\nabla_x f^{*}\left(\mathbf{x},\mathbf{V},t\right)-\frac{q}{m}\left[\mathbf{E}+\mathbf{V}\times\mathbf{B}\right]\nabla_V f^{*}\left(\mathbf{x},\mathbf{V},t\right), \qquad (2.14)\end{aligned}$$

which describes the time evolution of the microscopic distribution function of a population of charged particles in the presence of electro-magnetic forces. In plasma physics, the macroscopic distribution provides more significance as it describes the average (or observed) behavior of the system. Applying the averaging procedure (2.4) to the Klimnotovich equation (2.14) yields the Vlasov equation:

$$\begin{aligned}\frac{\partial f(\mathbf{x},\mathbf{v},t)}{\partial t} &+ \mathbf{v}\cdot\nabla f(\mathbf{x},\mathbf{v},t)+\frac{q}{m}\left(\mathbf{E}+\mathbf{v}\times\mathbf{B}\right)\cdot\nabla_v f(\mathbf{x},\mathbf{v},t) \\ &= -\frac{q}{m}\left\langle\left(\mathbf{E}+\mathbf{V}\times\mathbf{B}\right)-\langle\mathbf{E}+\mathbf{V}\times\mathbf{B}\rangle\cdot\frac{\partial(f^{*}-f)}{\partial\mathbf{V}}\right\rangle \\ &= C(f), \qquad (2.15)\end{aligned}$$

which describes the time evolution of the observed distribution function f in the presence of electric and magnetic fields. The right-hand side of the Vlasov equation (2.15) is known as the collision integral, which accounts for changes to the distribution function due to particle interactions (collisions). In the collisionless system, the right-hand side of the Vlasov equation is zero $C(f)=0$.

In plasmas, it is common to observe several particle populations of different species: ions, electrons neutrals, charged dust particles, etc. In a system of S charged plasma species each having N_s particles, an electric field is created by a combination of point charges:

$$\mathbf{E}\left(\mathbf{x}\right)=\frac{1}{4\pi\varepsilon_0}\sum_{s=1}^{S}\sum_{j=1}^{N_s}\frac{q_s}{\left(\mathbf{x}-\mathbf{x}_j\right)^2}\mathbf{r}_j, \qquad (2.16)$$

where $\mathbf{r}_j$ is the unit vector from the location of particle j to the location $\mathbf{x}$ and q_s is the unit charge of species s. Direct calculation of the electric field using equation (2.16) is

computationally inefficient, as it requires summations over all particles to be performed at every location of interest ($\mathbf{x}$), and has a computational complexity of $O(SN_s)$ for each location. In a many particle system, the variation of the electric field is observed on a scale much larger than the average distance between particles d_p, and the electric field can be evaluated using Poisson's equation

$$\mathbf{E} = -\nabla\phi \tag{2.17}$$

$$\varepsilon_0\nabla^2\phi = -\sum_s q_s n_s \tag{2.18}$$

where ϕ is the electrostatic potential, and n_s is the density (equation (2.8)) of species s. Equations (2.15), (2.17) and (2.18) form the Vlasov-Poisson system of integro-differential equations. The Vlasov-Poisson approximation is valid when magnetic fields are created externally (for example by a magnet or electromagnet), and variations in the magnetic field created by the plasma are negligible.

The Vlasov-Poisson system describes the evolution of plasmas in six-dimensional phase space, however in some cases this description is unnecessarily extensive. For example, at thermal equilibrium the particle velocities follow a Maxwellian distribution:

$$f(\mathbf{V}) = \left(\frac{m}{2\pi kT}\right)^{3/2} \exp\left[-\frac{m\mathbf{V}^2}{2k_B T}\right], \tag{2.19}$$

where T is the temperature of the plasma species. A simplified description of plasma can be found by integrating the distribution function over the velocity space, which will remove the velocity distribution information, but preserve variations in the plasma properties over space $\mathbf{x}$ and time t. Thus, integrating the distribution function over velocity space (zero-th moment) yields the particle density (2.6), and the particle flux is found as a first moment of the distribution function

$$n\mathbf{u} = \int d^3\mathbf{V} V f(\mathbf{x}, \mathbf{V}, t), \tag{2.20}$$

where $\mathbf{u}$ is the ensemble averaged velocity, or fluid drift velocity. The second moment of the

distribution function yields the stress tensor

$$\mathbf{P}\left(\mathbf{x},t\right)=\int d^{3}\mathbf{V}m\mathbf{V}\mathbf{V}f\left(\mathbf{x},\mathbf{V},t\right), \tag{2.21}$$

which can be split into the sum of the pressure tensor $\mathbf{p}$

$$\mathbf{p}\left(\mathbf{x},t\right)=\int d^{3}\mathbf{V}m(\mathbf{V}-\mathbf{u})(\mathbf{V}-\mathbf{u})f\left(\mathbf{x},\mathbf{V},t\right) \tag{2.22}$$

and the kinetic pressure

$$\mathbf{p}_{k}=mn\mathbf{u}\mathbf{u}. \tag{2.23}$$

The scalar "ideal gas" pressure is defined as

$$p=\frac{1}{3}\mathrm{Tr}(\mathbf{p}). \tag{2.24}$$

Finally, the energy flux is given by the third moment of the distribution function

$$\mathbf{Q}\left(\mathbf{x},t\right)=\frac{1}{2}\int d^{3}\mathbf{V}m|\mathbf{V}|^{2}\mathbf{V}f\left(\mathbf{x},\mathbf{V},t\right). \tag{2.25}$$

The energy flux can be related to the heat flux $\mathbf{q}$

$$\mathbf{q}\left(\mathbf{x},t\right)=\frac{1}{2}\int d^{3}\mathbf{V}m|\mathbf{V}-\mathbf{u}|^{2}(\mathbf{V}-\mathbf{u})f\left(\mathbf{x},\mathbf{V},t\right). \tag{2.26}$$

as

$$\mathbf{Q}=\mathbf{q}+\mathbf{p}\cdot\mathbf{u}+\frac{3}{2}p\mathbf{u}+\frac{1}{2}mn|\mathbf{u}^{2}|\mathbf{u}. \tag{2.27}$$

The conservation laws for the particle density, momentum and energy are obtained as the moments of the Vlasov equation (2.15). Thus, the continuity equation is given by the zeroth moment of the Vlasov equation

$$\frac{\partial n}{\partial t}+\nabla\cdot n\mathbf{u}=0, \tag{2.28}$$

the first moment yields the momentum conservation equation

$$\frac{\partial mn\mathbf{u}}{\partial t} + \nabla \cdot [mn\mathbf{uu} + \mathbf{p}] - n\mathbf{F} = \int d^3\mathbf{V} m\mathbf{V} C(f), \tag{2.29}$$

and the second moment of the Vlasov equation yields the energy conservation equation

$$\frac{\partial}{\partial t}\left(\frac{3}{2}p + \frac{1}{2}mn\mathbf{u}^2\right) + \nabla \cdot \mathbf{Q} - n\mathbf{F} \cdot \mathbf{u} = \int d^3 \frac{m\mathbf{V}^2}{2} \mathbf{V} C(f) + \mathbf{u} \int d^3\mathbf{V} m\mathbf{V} C(f). \tag{2.30}$$

The right-hand sides of equations (2.29) and (2.30) characterize the rate of momentum and energy transfer due to collisional processes between plasma species.

Equations (2.29) and (2.30) can be simplified by combining terms using the convective derivative

$$\frac{d}{dt} = \frac{\partial}{\partial t} + \mathbf{u} \cdot \nabla \tag{2.31}$$

and coproduct operator

$$\mathbf{p}\, \nabla \mathbf{u} = (p)_{\alpha\beta} \frac{\partial \mathbf{u}_\alpha}{\partial \mathbf{x}_\beta}, \tag{2.32}$$

where α and β are the Cartesian components of the coordinate $\mathbf{x}$ and velocity $\mathbf{V}$ vectors, respectively. Thus, the continuity equation becomes

$$\frac{dn}{dt} + n\nabla \cdot \mathbf{u} = 0, \tag{2.33}$$

and substituting Lorenz force for $\mathbf{F}$ into equation (2.29) gives the fluid momentum conservation equation

$$mn\frac{d\mathbf{u}}{dt} + \nabla p + \nabla \cdot \Pi - nq\left(\mathbf{E} + \mathbf{u} \times \mathbf{B}\right) = \int d^3\mathbf{V} m\mathbf{V} C(f). \tag{2.34}$$

The fluid energy conservation equation becomes

$$\frac{3}{2}\frac{dp}{dt} + \frac{5}{2}p\nabla \cdot \mathbf{u} + \Pi\, \nabla \mathbf{u} + \nabla \cdot \mathbf{q} = \int d^3 \frac{m\mathbf{V}^2}{2} \mathbf{V} C(f). \tag{2.35}$$

At long time scales much larger than the time between collisions τ, the collision integral can

be approximated as

$$\int d^3\mathbf{V} m\mathbf{v} C(f) \cong \int d^3\mathbf{V} m\mathbf{v}\nu \left(f_0 - f\right) = -mn\mathbf{u}\nu, \tag{2.36}$$

where ν is the collision frequency. Neglecting the pressure tensor and assuming that pressure can be described using the ideal gas approximation, the momentum conservation equation (2.34) becomes

$$mn\frac{d\mathbf{u}}{dt} + k_B T\nabla n - nq\left(\mathbf{E} + \mathbf{u}\times\mathbf{B}\right) - mn\mathbf{u}\nu = 0. \tag{2.37}$$

Thus, a system of charged particles can be model using either the Vlasov (2.15) equation or the system of fluid equations (2.33), (2.34) (2.35). The fluid equations provide a reduced description of the plasma system as the complete velocity information is reduced to drift velocity and plasma temperature. Despite limitations, the system of fluid equation can be easily solved numerically. If the simulation domain is discretized in D_x physical dimensions and the grid has M nodes in each dimension (total of M^{D_x} nodes), the cost of solving the fluid equations is M^{D_x}. The Vlasov equation keeps full information on the ensemble of charged particles, and it can be solved directly by discretizing phase space on a finite mesh. Assuming that the phase space is resolved for D_x spacial and D_V velocity dimensions, and the phase space mesh has m nodes in each dimensions, the total mesh size is rather large with memory complexity $O\left(M^{D_v+D_x}\right)$. The computational cost of the Direct Vlasov solver depends on the cost of the numerical evaluation of the advection of the distribution function ($O\left(M^{D_v+D_x}\right)$) and the numerical solution of the Poisson equation (best case $O\left(M^{D_x}\right)$). The Particle-in-Cell (PIC) is an alternative approach of solving the Vlasov equation with computational and memory complexity $O\left(M^{D_x} + N_p\right)$. The details of the Particle-in-Cell algorithm are presented in section 2.2. Since the computational complexity of Particle-in-Cell methods is smaller than the computational complexity of the Direct Vlasov solver, the Particle-in-Cell is a preferred method for the simulation of high dimensional problems ($D_x, D_V \geq 2$) when plasma species are not thermalized and velocity information is a relevant scientific output. Table 2.1 summarizes the complexity of Direct Vlasov, Particle-in-Cell and fluid models. The complexity of algorithms presented in the table 2.1 do not consider the

parallel versions of those algorithms. The complexity of a parallel implementation of the Particle-in-Cell method is described in details in the Chapter 3.

Table 2.1: Computational and memory complexity of the direct solver of the Vlason-Poisson system and Particle-in-Cell method, here D_V and D_x are velocity and physical space dimensionalities

Parameters	Fluid	Direct	PIC
Grid size (single dimension)	M	M	M
Number of Particles	-	-	N_p
Storage	$O\left(M^{D_x}\right)$	$O\left(M^{D_v+D_x}\right)$	$O\left(\max\left(M^{D_x}, N_p\right)\right)$
Computation w/o Poisson Solve	$O\left(M^{D_x}\right)$	$O\left(M^{D_v+D_x}\right)$	$O\left(N_p\right)$
Poisson Solve	$O\left(M^{D_x}\right)$	$O\left(M^{D_x}\right)$	$O\left(M^{D_x}\right)$

2.2 Particle-in-Cell Method

The Particle-in-Cell method approaches the Vlasov-Poisson problem by sampling distributions of the plasma species. Thus, PIC simulations are executed with N_{PIC} particles, which is smaller than the real number of particles N_p

$$N_p = \texttt{p2c} \times N_{PIC}, \tag{2.38}$$

where `p2c` is the ratio of real to simulated number of particles. The contribution of each simulated particle to the global parameter estimates is defined by the shape function $w(\mathbf{x})$. A commonly used linear weighting can be found as a product of three triangular functions along each dimension x, y and z

$$w(x, y, z) = \left(1 - |x - \Delta x|\right)\left(1 - |y - \Delta y|\right)\left(1 - |z - \Delta z|\right), \tag{2.39}$$

where Δx, Δy and Δz represent the grid spacing along the x, y and z axis, respectively. For example, particle densities in PIC codes are estimated using the following equation

$$\hat{n}\left(\mathbf{x}\right) = \texttt{p2c} \times \sum_p w(\mathbf{x} - \mathbf{x}_p), \tag{2.40}$$

where the index p of the sum runs over the number of computational particles of species s. Notably, Equation (2.40) is an approximate form of the microscopic distribution function described by equation (2.8) with the function $w(\mathbf{x})$ replacing Dirac's delta functions. Thus, computational particles in the Particle-in-Cell method occupy a finite volume in the phase space, which is defined by the width Δx of the shape function.

Equation (2.40) summarizes the particle weighting step of PIC algorithms. If a particle of species s is located within a three dimensional grid cell with indices i, j and k, the particle weighting takes the following form

$$\begin{aligned}
\hat{n}^s_{i,j,k} &= \hat{n}^s_{i,j,k} + (1-w^x)(1-w^y)(1-w^z) && (2.41)\\
\hat{n}^s_{i+1,j,k} &= \hat{n}^s_{i,j,k} + w^x(1-w^y)(1-w^z) && (2.42)\\
\hat{n}^s_{i,j+1,k} &= \hat{n}^s_{i,j,k} + (1-w^x)w^y(1-w^z) && (2.43)\\
\hat{n}^s_{i+1,j+1,k} &= \hat{n}^s_{i,j,k} + w^x w^y(1-w^z) && (2.44)\\
\hat{n}^s_{i,j,k} &= \hat{n}^s_{i,j,k} + (1-w^x)(1-w^y)w^z && (2.45)\\
\hat{n}^s_{i+1,j,k} &= \hat{n}^s_{i,j,k} + w^x(1-w^y)w^z && (2.46)\\
\hat{n}^s_{i,j+1,k} &= \hat{n}^s_{i,j,k} + (1-w^x)w^y w^z && (2.47)\\
\hat{n}^s_{i+1,j+1,k} &= \hat{n}^s_{i,j,k} + w^x w^y w^z, && (2.48)
\end{aligned}$$

where weights in three dimensions are determined as follows

$$\begin{aligned}
w^x &= (x - i\Delta x) && (2.49)\\
w^y &= (y - j\Delta y) && (2.50)\\
w^z &= (z - k\Delta z). && (2.51)
\end{aligned}$$

The charge density ρ that is used in the right-hand side of the Poisson equation is evaluated as a sum of the charge densities of individual plasma species

$$\hat{\rho} = \sum_{s=1}^{S} q_s \hat{n_s}, \qquad (2.52)$$

where S is the total number of plasma species in the simulation.

The Poisson equation (2.18) is numerically solved on the structured grid in one, two or three dimensions using a second-order finite-difference approximation of the Poisson stencil. Numerical formulation of the Poisson equation in two dimensions is given by the following equation

$$\frac{\Phi_{i-1,j} - 2\Phi_{i,j} + \Phi_{i+1,j}}{\Delta x^2} + \frac{\Phi_{i,j-1} - 2\Phi_{i,j} + \Phi_{i,j+1}}{\Delta y^2} + \frac{\hat{\rho}_{i,j}}{\varepsilon_0} = 0 \tag{2.53}$$

$$\begin{aligned}(\Phi_{i-1,j} - 2\Phi_{i,j} + \Phi_{i+1,j})\frac{\Delta y}{\Delta x} &+ (\Phi_{i,j-1} - 2\Phi_{i,j} + \Phi_{i,j+1})\frac{\Delta x}{\Delta y} + \\ &+ \Delta x \Delta y \frac{\hat{\rho}_{i,j}}{\varepsilon_0} = 0,\end{aligned} \tag{2.54}$$

where $\hat{\rho}_{i,j} = \sum_s q_e \hat{n}_{s,i,j}$ is the charge density on i, j of the structured grid. A visual representation of the 5-point stencil of equation (2.54) is shown in Figure 2.1. The finite

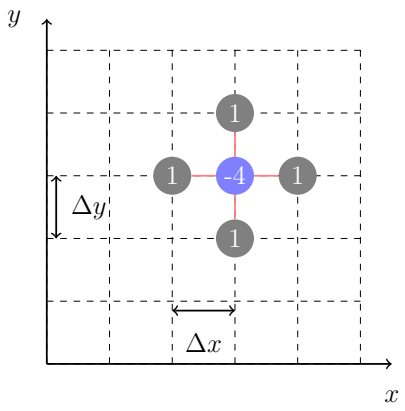

Figure 2.1: Finite-difference representation of two-dimensional Poisson stencil

difference equation (2.54) can be reformulated in the form of a linear problem

$$L\mathbf{\Phi} = \frac{\Delta x \Delta y}{\varepsilon_0}\rho, \tag{2.55}$$

where $\mathbf{\Phi}$

$$\mathbf{\Phi} = \begin{bmatrix} \Phi_{1,1} & \Phi_{1,2} & \dots & \Phi_{1,M_y} & \dots & \dots & \Phi_{M_x,1} & \Phi_{M_x,2} & \dots & \Phi_{M_x,M_y} \end{bmatrix}^T \tag{2.56}$$

and ρ

$$\rho = \begin{bmatrix} \rho_{1,1} & \rho_{1,2} & \dots & \rho_{1,M_y} & \dots & \dots & \rho_{M_x,1} & \rho_{M_x,2} & \dots & \rho_{M_x,M_y} \end{bmatrix}^T \tag{2.57}$$

are vectors of size $M_x \times M_y$ representing the two-dimensional potential and charge density on the structured grid of size M_x along the x axis and M_y along the y axis, and L is a square matrix of size $M_xM_y \times M_xM_y$ representing the finite difference operator of the Poisson equation

$$L = \begin{bmatrix} C & \frac{\Delta y}{\Delta x}I & 0 & 0 & 0 & \dots & 0 \\ \frac{\Delta y}{\Delta x}I & C & \frac{\Delta y}{\Delta x}I & 0 & 0 & \dots & 0 \\ 0 & \frac{\Delta y}{\Delta x}I & C & \frac{\Delta y}{\Delta x}I & 0 & \dots & 0 \\ \vdots & \vdots & \vdots & \vdots & \vdots & \ddots & \vdots \\ 0 & \dots & 0 & \frac{\Delta y}{\Delta x}I & C & \frac{\Delta y}{\Delta x}I & 0 \\ 0 & \dots & \dots & 0 & \frac{\Delta y}{\Delta x}I & C & \frac{\Delta y}{\Delta x}I \\ 0 & \dots & \dots & \dots & 0 & \frac{\Delta y}{\Delta x}I & C \end{bmatrix} \tag{2.58}$$

where I is the identity matrix of size $M_y \times M_y$, and the matrix C of size $M_y \times M_y$ is defined as

$$C = \begin{bmatrix} -2\left(\frac{\Delta x}{\Delta y} + \frac{\Delta y}{\Delta x}\right) & -\frac{\Delta x}{\Delta y} & 0 & 0 & \dots & 0 \\ -\frac{\Delta x}{\Delta y} & -2\left(\frac{\Delta x}{\Delta y} + \frac{\Delta y}{\Delta x}\right) & -\frac{\Delta x}{\Delta y} & 0 & \dots & 0 \\ \vdots & \vdots & \vdots & \ddots & \vdots & \vdots \\ 0 & \dots & \dots & -\frac{\Delta x}{\Delta y} & -2\left(\frac{\Delta x}{\Delta y} + \frac{\Delta y}{\Delta x}\right) & -\frac{\Delta x}{\Delta y} \\ 0 & \dots & \dots & 0 & -\frac{\Delta x}{\Delta y} & -2\left(\frac{\Delta x}{\Delta y} + \frac{\Delta y}{\Delta x}\right) \end{bmatrix}. \tag{2.59}$$

Traditionally, the numerical solution of the Poisson equation (2.55) is not considered to be

scalable due to the non-local nature of its elliptic differential operator L. However, recent (2012) advancements [38] in the implementation of multigrid methods and their combination with opportune preconditioners allow reasonable scaling to be achieved even on the largest computing machines. Such methods have been adopted in our implementation, and they have been successfully tested up to 8,192 nodes on the Blue Waters supercomputer (262,144 cores), as reported in Chapter 3.

After the electrostatic potential has been evaluated numerically as the solution of equation (2.55), the values of the electric field $\mathbf{E}$ in each dimension (x, y and z) are calculated on each grid node using numerical differentiation

$$E^x_{i,j,k} = -\frac{\Phi_{i+1,j,k} - \Phi_{i-1,j,k}}{2\Delta x} \tag{2.60}$$

$$E^y_{i,j,k} = -\frac{\Phi_{i,j+1,k} - \Phi_{i,j-1,k}}{2\Delta y} \tag{2.61}$$

$$E^z_{i,j,k} = -\frac{\Phi_{i,j,k+1} - \Phi_{i,j,k-1}}{2\Delta z}. \tag{2.62}$$

Assuming that a particle belongs to a grid cell with indices i, j, k in three dimensions, the electric field acting on an individual particle is interpolated to its location $\mathbf{x} = [x, y, z]^T$ using the shape function $w(x, y, z)$ (equation (2.39))

$$\begin{aligned} E^x(\mathbf{x}) &= E^x_{i,j,k}(1-w^x)(1-w^y)(1-w^z) + E^x_{i+1,j,k}w^x(1-w^y)(1-w^z) \\ &+ E^x_{i,j+1,k}(1-w^x)w^y(1-w^z) + E^x_{i+1,j+1,k}w^xw^y(1-w^z) \\ &+ E^x_{i,j,k+1}(1-w^x)(1-w^z)w^z + E^x_{i+1,j,k+1}w^x(1-w^y)w^z \\ &+ E^x_{i,j+1,k+1}(1-w^x)w^yw^z + E^x_{i+1,j+1,k+1}w^xw^yw^z \end{aligned} \tag{2.63}$$

$$\begin{aligned} E^y(\mathbf{x}) &= E^y_{i,j,k}(1-w^x)(1-w^y)(1-w^z) + E^y_{i+1,j,k}w^x(1-w^y)(1-w^z) \\ &+ E^y_{i,j+1,k}(1-w^x)w^y(1-w^z) + E^y_{i+1,j+1,k}w^xw^y(1-w^z) \\ &+ E^y_{i,j,k+1}(1-w^x)(1-w^z)w^z + E^y_{i+1,j,k+1}w^x(1-w^y)w^z \\ &+ E^y_{i,j+1,k+1}(1-w^x)w^yw^z + E^t_{i+1,j+1,k+1}w^xw^yw^z \end{aligned} \tag{2.64}$$

$$\begin{aligned} E^z(\mathbf{x}) &= E^z_{i,j,k}(1-w^x)(1-w^y)(1-w^z) + E^z_{i+1,j,k}w^x(1-w^y)(1-w^z) \\ &+ E^z_{i,j+1,k}(1-w^x)w^y(1-w^z) + E^z_{i+1,j+1,k}w^xw^y(1-w^z) \end{aligned}$$

$$
\begin{aligned}
&+ \quad E^z_{i,j,k+1}(1-w^x)(1-w^z)w^z + E^z_{i+1,j,k+1}w^x(1-w^y)w^z \\
&+ \quad E^z_{i,j+1,k+1}(1-w^x)w^y w^z + E^z_{i+1,j+1,k+1}w^x w^y w^z. \qquad (2.65)
\end{aligned}
$$

Using the same shape function for interpolating fields on the particles as in density estimation (2.41) guarantees charge and mass conservation [22].

Then, individual particle coordinates and velocities are updated using the following discretized equations of motion [39]

$$
\begin{aligned}
\mathbf{v}^{t+1/2} &= \mathbf{v}^{t-1/2} + \Delta t(q/m)\left(\mathbf{E}^t + \mathbf{v}\times\mathbf{B}^t\right) \\
\mathbf{x}^{t+1} &= \mathbf{x}^t + \mathbf{v}^{t+1/2}\Delta t, \qquad (2.66)
\end{aligned}
$$

A robust implementation of Eqs. (2.66) is Boris' leapfrog method [39, 40]. In Boris' scheme, the particle advance is split into two acceleration steps (due to the presence of the electric field $\mathbf{E}$) and one rotation step (due to the magnetic field $\mathbf{B}$) of the velocity vector:

$$
\begin{aligned}
\mathbf{v}^- &= \mathbf{v}^{t-1/2} + \Delta t\frac{q}{2m}\mathbf{E}^t \qquad (2.67) \\
\mathbf{b} &= \mathbf{B}/\left\|\mathbf{B}\right\|_2 \\
\mathbf{t} &= \mathbf{b}\tan\left(q\left|\mathbf{B}\right|\Delta t/2m\right) \qquad (2.68) \\
\mathbf{v}' &= \mathbf{v}^- + \mathbf{v}^-\times\mathbf{t} \qquad (2.69) \\
\mathbf{v}^+ &= \mathbf{v}^- + 2\mathbf{v}'\times\mathbf{t}/\left(1+t^2\right) \qquad (2.70) \\
\mathbf{v}^{t+1/2} &= \mathbf{v}^+ + \Delta t\frac{q}{2m}\mathbf{E}^t \qquad (2.71) \\
\mathbf{x}^{t+1} &= \mathbf{x}^t + \mathbf{v}^{t+1/2}\Delta t \qquad (2.72)
\end{aligned}
$$

Thus, each iteration of the Particle-in-Cell method has four major steps, shown in Figure 2.2(a): interpolation of the fields on particle locations, particle push, weighting (density estimation), and numerical solution of the Poisson equation. The first three steps of Particle-in-Cell methods are operating on particles and are referred to as particle advance operations in this work. The complexity of the particle advance operations depends only on the number of particles used in simulation N_p, and complexity of the Poisson solver depends on the

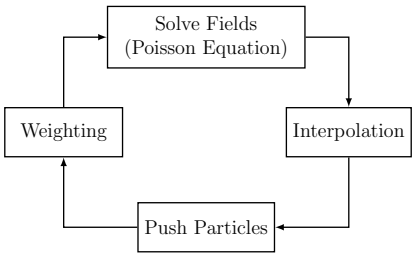

(a) Classical PIC cycle

Figure 2.2: Major steps of the classical Particle-in-Cell method

number of grid point in the simulation domain M^{D_x}. If numerical solution of the Poisson equation is much slower than the particle advance operations, the complexity of the Particle-in-Cell simulation is proportional to the size of computational grid $O(M^{D_x})$, and if more time is spent on the particle operations, then the complexity of the simulation is directly proportional to the number of particles in the simulation $O(N_p)$.

2.3 Plasma Dispersion Relation under Particle-in-Cell Assumptions

As a result of the assumptions made in the Particle-in-Cell approach, the resulting simulation differs from the physical system [22], [41]. First, the number of computational particles N_{PIC} resolved in the computer simulation is smaller than the number of physical particles in the corresponding physical system N_p. Second, the particles in the Particle-in-Cell simulation occupy a finite size in phase space $w(\mathbf{x})$, that is larger than the physical size of the particles. Finally, the particle properties are estimated on the computational grid and are evolved at discretized time steps. Improperly chosen combinations of particle size, grid size and time step can introduce unphysical behavior in conducted simulations. The effects that are introduced by finite times step, structured grid and finite particle size can be characterized by the dispersion relation corresponding to the Particle-in-Cell simulation. This section present the derivation of such a dispersion relation and follows the works of Tajima [41] and Birdsall [22].

2.3.1 Effect of the Approximate Coarse-Graining on the Dispersion Relation

The number of particles in real systems is still unattainable for direct simulation even by modern supercomputers. As discussed earlier, Particle-in-Cell codes simulate only a small sample of the real particle population using an approximate coarse-graining approach (2.40), that is characterized by the shape function w. In this section, we present a derivation of the dispersion relation for a physical system of finite-sized particles in the gridless electrostatic case at thermal equilibrium.

At thermal equilibrium, the distribution function of a charged species $f(\mathbf{x}, \mathbf{V}, t)$ can be split into the sum of a time-constant "equilibrium" distribution function $f_0(\mathbf{x}, \mathbf{V})$ and a small perturbation that is changing in time $f_1(\mathbf{x}, \mathbf{V}, t)$

$$f(\mathbf{x}, \mathbf{V}, t) = f_0(\mathbf{x}, \mathbf{V}) + f_1(\mathbf{x}, \mathbf{V}, t). \tag{2.73}$$

The force field $\mathbf{F}(\mathbf{x}, t)$ acting on the charged particles is created only by small perturbations in the particle distributions

$$\mathbf{F}(\mathbf{x}, t) = 0 + \mathbf{F}_1(\mathbf{x}, t), \tag{2.74}$$

where $\mathbf{F}_1(\mathbf{x}, t)$ is the small perturbation component of the force. Since an average force field $\mathbf{F}_0(\mathbf{x}, t) = 0$ is nonexistent at equilibrium, the values of $\mathbf{F}_1(\mathbf{x}, t)$ and $\mathbf{F}(\mathbf{x}, t)$ are equivalent and interchangeable.

Then, the Vlasov equation with the Krook's collision operator [42] for unmagnetized plasma is written as

$$\frac{\partial f(\mathbf{x}, \mathbf{V})}{\partial t} \quad + \quad \mathbf{V}\nabla \cdot f(\mathbf{x}, \mathbf{V}) + \frac{q\mathbf{F}\left(\mathbf{x}\right)}{m} \cdot \nabla_V f(\mathbf{x}, \mathbf{V}) = \nu \left(f\left(\mathbf{x}, \mathbf{V}\right) - f_0\left(\mathbf{x}, \mathbf{V}\right) \right), \tag{2.75}$$

where ν is a collision frequency and $\mathbf{F}$ is a force field acting on particles. The collisions introduced by the Krook's collision operator become large when the particle distribution

function deviates from the equilibrium distribution function f_0. Hence, the Krook's collision operator is thermalizing the particle system if it deviates from its equilibrium conditions.

Then, the Vlasov equation (2.75) can be simplified using equation (2.73) and (2.74) after dropping second order terms ($\mathbf{F}f_1$)

$$\frac{\partial f_1(\mathbf{x},\mathbf{V})}{\partial t} \quad + \quad \mathbf{V}\nabla\cdot f_1(\mathbf{x},\mathbf{V}) + \frac{\mathbf{F}}{m}\cdot\nabla_V f_0(\mathbf{x},\mathbf{V}) = \nu f_1(\mathbf{x},\mathbf{V}). \tag{2.76}$$

The force fields in the Particle-in-Cell method are projected to the particle location $\mathbf{x}_p$ using equation (2.65) (particle force). In the gridless system, this results in convolution of the force field with the shape function

$$\mathbf{F}\left(\mathbf{x}_p\right) = q\int d^3\mathbf{x} w\left(\mathbf{x}-\mathbf{x}_p\right)\mathbf{E}(\mathbf{x}), \tag{2.77}$$

where q is the charge of plasma species. The Fourier transformation of equation (2.77) gives an expression of the particle force in the frequency space

$$\hat{\mathbf{F}}\left(\mathbf{k}\right) = q\hat{w}\left(\mathbf{k}\right)\hat{\mathbf{E}}\left(\mathbf{k}\right), \tag{2.78}$$

where hatted values represent the Fourier transformed values of the corresponding functions

$$\hat{\mathbf{F}}\left(\mathbf{k}\right) = \int d^3\mathbf{x}\mathbf{F}(\mathbf{x})\exp\left(-i\mathbf{k}\mathbf{x}\right) \tag{2.79}$$

$$\hat{\mathbf{E}}\left(\mathbf{k}\right) = \int d^3\mathbf{x}\mathbf{E}(\mathbf{x})\exp\left(-i\mathbf{k}\mathbf{x}\right) \tag{2.80}$$

$$\hat{w}\left(\mathbf{k}\right) = \int d^3\mathbf{x} w(\mathbf{x})\exp\left(-i\mathbf{k}\mathbf{x}\right). \tag{2.81}$$

The Vlasov equation is Fourier transformed in coordinate $\mathbf{x}$ and time t spaces, and velocity dependence is preserved in the physical space

$$i\left(\mathbf{k}\mathbf{V}-\omega\right)\hat{f}(\mathbf{k},\mathbf{V},\omega) \quad + \quad \frac{\hat{\mathbf{F}}}{m}\frac{\partial\hat{f}_0}{\partial\mathbf{V}} = -\nu\hat{f}(\mathbf{k},\mathbf{V},\omega) \tag{2.82}$$

$$\hat{f}(\mathbf{k},\mathbf{V},\omega) = -\frac{\hat{\mathbf{F}}\frac{\partial\hat{f}_0}{\partial\mathbf{V}}}{m\left[-i\left(\omega-\mathbf{k}\mathbf{V}\right)+\nu\right]}, \tag{2.83}$$

where

$$\hat{f}(\mathbf{k}, \mathbf{V}, \omega) = \int d\omega \int d^3\mathbf{x} f(\mathbf{x}, \mathbf{V}t) \exp\left(-i\mathbf{k}\mathbf{x} + i\omega t\right) \tag{2.84}$$

is the Fourier transformation of the particle distribution function.

The approximate coarse graining results in the convolution of the shape function w and the particle density

$$n^*\left(\mathbf{x}\right) = \int \mathbf{d}\mathbf{y} n\left(\mathbf{y}\right) w(\mathbf{x} - \mathbf{y}), \tag{2.85}$$

or in the frequency space

$$\hat{n}^*\left(\mathbf{k}\right) = \hat{w}\left(\mathbf{k}\right) \hat{n}\left(\mathbf{k}\right). \tag{2.86}$$

The Fourier transformation of the triangular weight function (2.39) is given by the sinc function $\mathrm{sinc}(x) = sin(x)/x$

$$\hat{w}\left(\mathbf{k}\right) = \left(\frac{\sin(\pi \Delta x/2)}{\pi \Delta x/2}\right)^2, \tag{2.87}$$

which acts as a low-pass filter on the particle density by removing high frequency (or short distance oscillations) from the particle density.

The local value of the electric potential is found from Poisson's equation (2.18)

$$-\varepsilon_0 \nabla^2 \phi\left(\mathbf{x}, t\right) \quad = \quad q \int \mathbf{d}\mathbf{y} n\left(\mathbf{y}\right) w(\mathbf{x} - \mathbf{y}) \tag{2.88}$$

using Fourier transformation

$$\hat{\phi} = \frac{q n_0 \hat{w}\left(\mathbf{k}\right)}{\varepsilon_0 \mathbf{k}^2} \int \mathbf{d}\mathbf{V} \hat{f}(\mathbf{k}, \mathbf{V}, \omega), \tag{2.89}$$

where n_0 is the normalization constant of the particle density, and q is the particle charge of the plasma species. The electric field is then found in the frequency space as

$$\hat{\mathbf{E}}\left(\mathbf{k}, \omega\right) \quad = \quad -i\mathbf{k}\hat{\phi}\left(\omega\right) \tag{2.90}$$

$$\quad = \quad \frac{-i\mathbf{k} q n_0 \hat{w}\left(\mathbf{k}\right)}{\varepsilon_0 \mathbf{k}^2} \int \mathbf{d}\mathbf{V} \hat{f}(\mathbf{k}, \mathbf{V}, \omega). \tag{2.91}$$

Combination of equations (2.78) and (2.91) gives an expression for the Fourier transformation of the distribution function

$$\hat{f}(\mathbf{k},\mathbf{V},\omega) = -\frac{\mathbf{F}(\mathbf{k},\omega)\frac{\partial \hat{f}_0}{\partial \mathbf{V}}}{m\left[-i\left(\mathbf{kV}-\omega\right)+\nu\right]} \tag{2.92}$$

$$= -\frac{q\hat{w}(\mathbf{k})\mathbf{E}(\mathbf{k},\omega)}{m\left[i\left(\mathbf{kV}-\omega\right)+\nu\right]}\frac{\partial \hat{f}_0}{\partial \mathbf{V}} \tag{2.93}$$

$$= \frac{\mathbf{k}n_0q^2\hat{w}^2(\mathbf{k})}{m\varepsilon_0\mathbf{k}^2\left[\left(\omega-\mathbf{kV}\right)+i\nu\right]}\frac{\partial \hat{f}_0}{\partial \mathbf{V}}\int \mathbf{dV}\hat{f}(\mathbf{k},\mathbf{V},\omega). \tag{2.94}$$

Integration of equation (2.94) over the velocity space gives an expression for the dispersion function $D(\mathbf{k},\omega)$

$$\int \mathbf{dV}^*\hat{f}(\mathbf{k},\mathbf{V},\omega) = \frac{\mathbf{k}n_0q^2\hat{w}^2(\mathbf{k})}{m\varepsilon_0\mathbf{k}^2}\int \mathbf{dV}^*\frac{\frac{\partial \hat{f}_0}{\partial \mathbf{V}^*}}{\omega-\mathbf{kV}^*+i\nu}\int \mathbf{dV}\hat{f}(\mathbf{k},\mathbf{V},\omega) \tag{2.95}$$

$$1 = \frac{\mathbf{k}n_0q^2\hat{w}^2(\mathbf{k})}{m\varepsilon_0\mathbf{k}^2}\int \mathbf{dV}\frac{\frac{\partial \hat{f}_0}{\partial \mathbf{V}}}{\omega-\mathbf{kV}+i\nu} \tag{2.96}$$

$$D(\mathbf{k},\omega) = 1-\frac{\omega_p^2\hat{w}^2(\mathbf{k})}{\mathbf{k}^2}\mathbf{k}\int \mathbf{dV}\frac{\frac{\partial \hat{f}_0}{\partial \mathbf{V}}}{\omega-\mathbf{kV}+i\nu}, \tag{2.97}$$

where $\omega_p=\sqrt{n_oq^2/m\varepsilon_0}$ is a plasma frequency. At thermal equilibrium, particle velocities follow the Maxwellian distribution

$$f_0=\sqrt{\frac{m}{2\pi k_BT}}\exp\left(-\frac{mV^2}{k_BT}\right). \tag{2.98}$$

Then the dielectric function becomes

$$D(\mathbf{k},\omega)=1-\frac{1}{2}\left(\frac{\hat{w}(\mathbf{k})\omega_p}{kV_T}\right)^2Z'\left(\frac{\omega}{\sqrt{2}kV_T}\right) \tag{2.99}$$

where $V_t=\sqrt{k_BT/m}$ is thermal velocity, and Z' is

$$Z'(\omega)=\frac{1}{\sqrt{\pi}}\int \mathbf{d}x\frac{e^{-x^2}}{x-\omega-i\eta}. \tag{2.100}$$

When $kV_T/w(k)\omega_p \ll 1$, the Z' function can be expanded asymptotically, which leads to

the following dispersion relation

$$\omega^2 = \omega_p^2 \hat{w}^2 (\mathbf{k}) + 3\mathbf{k}^2 V_t^2, \tag{2.101}$$

and the damping rate of the oscillations becomes

$$\gamma = \mathrm{Im}\omega = -\sqrt{\frac{\pi}{8}} \hat{v}(\mathbf{k}) \omega_p \left(\frac{\omega_p}{k\lambda_D} \right)^3 \exp\left[-\frac{1\hat{w}^2 (\mathbf{k})}{2k^2\lambda_D^2} - \frac{3}{2} \right]. \tag{2.102}$$

Substituting equation (2.87) into (2.101) yields a dispersion relation for a triangular shape function

$$\omega^2 = \omega_p^2 \frac{\sin(k\Delta x/2)}{k\Delta x/2} + 3k^2 V_t^2. \tag{2.103}$$

For small particle sizes $k\Delta X \propto k\lambda_D \ll 1$, Fourier transformation of the shape function ($\mathrm{sinc}^2(x) = \sin^2(x)/x^2$) can be expanded using the first two terms of the Taylor series

$$\begin{aligned} \omega^2 &= \omega_p^2 \left(1 - \frac{k^2 \Delta x^2}{3 \times 2^2} \right) + 3 \left(k^2 V_t^2 - \frac{1}{3} \omega_p^2 b^2 \right) & (2.104) \\ &= \omega_p^2 + 3 \left(k^2 V_t^2 - \frac{\omega_p^2 \Delta x^2}{36} \right). & (2.105) \end{aligned}$$

In order to maintain positive group velocity, the width of the window function Δx should be less than $\sqrt{36}\lambda_D = 6\lambda_D$.

The dispersion relation for the coarse-grained system is similar to the dispersion relation of the physical system, for which $w() = \Delta((x))$

$$\omega^2 = \omega_p^2 + 3k^2 V_t^2. \tag{2.106}$$

The particle shape function w acts as a low-pass filter for the high-frequency (in time) oscillations, reducing the frequency of high short-range oscillations ω and damping rate γ. In other terms, coarse-grained systems remove short-range correlations (in distance) from the physical system.

2.3.2 Effect of Structured Grid on the Plasma Dispersion Relation

In a Particle-in-Cell simulation, the density of the particle species is defined only on the nodes of the structured grid, denoted by the superscript j, located at $\mathbf{x}^j$. Particle density is estimated from the particle locations at time t using an approximate coarse-graining process (2.40). For simplicity, it is assumed that the number of particle in the Particle-in-Cell simulation is equal to the physical number of particles `p2c` $= 1$. Then, the particle density is estimated at the grid node j as

$$n\left(\mathbf{x}^j\right) = \sum_p w(\mathbf{x}^j - \mathbf{x}_p). \tag{2.107}$$

The spectrum of charge density in this case is given by the discrete Fourier transformation

$$\hat{n}\left(\mathbf{k}\right) = \Delta x \sum_j n^j(\mathbf{x}^j) e^{-i\mathbf{k}\mathbf{x}_j}, \tag{2.108}$$

and the inverse transformation of quantity (2.108) yields the charge density on the structured grid

$$n\left(\mathbf{x}^j\right) = \frac{1}{L} \sum_{j=-\pi M/L}^{\pi M/L} n(\mathbf{k}) e^{i\mathbf{k}\mathbf{x}_j}, \tag{2.109}$$

where L is the length of the simulated domain, and M is the number of nodes on the structured grid along a single dimension.

Fourier transformation of the finite-difference form of the Poisson equation (2.54) is different from the continuous version, and it is taken as follows for a one-dimensional grid

$$\mathbf{k}^2 \frac{\sin^2\left(\frac{k\Delta x}{2}\right)}{k^2\Delta x^2/4} \hat{\phi}\left(\mathbf{k}\right) = \hat{\rho}\left(\mathbf{k}\right). \tag{2.110}$$

Denoting K as

$$K^2\left(\mathbf{k}\right) = \mathbf{k}^2 \frac{\sin^2\left(\frac{k\Delta x}{2}\right)}{k^2\Delta x^2/4} \tag{2.111}$$

equation (2.110) takes the following form

$$K^2(\mathbf{k})\,\hat{\phi}(\mathbf{k}) = \frac{q\hat{n}(\mathbf{k})}{\varepsilon_0}. \tag{2.112}$$

The electric field calculated with a central difference equation is transformed into frequency space as (2.62)

$$\hat{\mathbf{E}} = -i\hat{\phi}(\mathbf{k})\,\frac{\sin\left(\frac{k\Delta x}{2}\right)}{k\Delta x/2} \tag{2.113}$$

Denoting the spectral effect of the finite differencing as

$$\kappa(\mathbf{k}) = (\mathbf{k})\,\frac{\sin\left(\frac{k\Delta x}{2}\right)}{k\Delta x/2}, \tag{2.114}$$

the electric field (2.113)equation in frequency space becomes

$$\begin{aligned}\hat{\mathbf{E}}(\mathbf{k}) &= -i\kappa(\mathbf{k})\,\hat{\phi}(\mathbf{k}) \\ &= -\frac{iq\kappa(\mathbf{k})}{\varepsilon_0 K^2(\mathbf{k})}\hat{n}(\mathbf{k}).\end{aligned} \tag{2.115}$$

The particle force is then found using the interpolation procedure (2.65)

$$\mathbf{F}_p = q\sum_j \mathbf{E}^j w\left(\mathbf{x}^j - \mathbf{x}_p\right), \tag{2.116}$$

which represent a discrete convolution, and results in multiplication of the shape function and the electric field in frequency space (using $\hat{w}(\mathbf{k}) = \hat{w}(-\mathbf{k})$)

$$\hat{\mathbf{F}}_p(\mathbf{k}) = q\hat{\mathbf{E}}(\mathbf{k})\hat{w}(\mathbf{k}). \tag{2.117}$$

The effect of the structured grid can be represented as a sampling function ζ

$$\zeta(\mathbf{x}) = \sum_j \delta(x - \mathbf{x}^j), \tag{2.118}$$

that is applied to the continuous particle density. The "gridded" version of the particle

density $n^\dagger$ becomes (2.85)

$$n^\dagger(\mathbf{x}) = \zeta(\mathbf{x}) n^*(\mathbf{x}). \tag{2.119}$$

In the frequency space, multiplication is replaced by convolution, and the Fourier transformation of equation (2.118) yields

$$\begin{aligned} \hat{n}^\dagger(\mathbf{k})\zeta(\mathbf{x}) &= \hat{\zeta}(\mathbf{k}) * \hat{n^*}(\mathbf{k}) \\ &= \sum_j \hat{w}(\mathbf{k}_j)\hat{n}(\mathbf{k}_j), \end{aligned} \tag{2.120}$$

where $\mathbf{k}_j = \frac{2\pi}{\Delta x} \times j$. Substituting equation (2.120) into (2.115) yields

$$\hat{\mathbf{E}}(\mathbf{k}) = -\frac{iq\kappa(\mathbf{k})}{\varepsilon_0 K^2(\mathbf{k})} \sum_j \hat{w}(\mathbf{k}_j)\hat{n}(\mathbf{k}_j). \tag{2.121}$$

Neglecting collision frequency, the integral of equation (2.83) over the velocity space gives the perturbation density

$$\hat{n}(\mathbf{k},\omega) = \frac{n_0 \hat{\mathbf{F}}(\mathbf{k},\omega)}{im} \int d^3\mathbf{V} \frac{1}{\omega - \mathbf{kV}} \frac{\partial \hat{f}_0}{\partial \mathbf{V}}. \tag{2.122}$$

Using the particle force (2.117) and density perturbation (2.122) equations, the electric field equation in frequency space (2.121) becomes

$$\hat{\mathbf{E}}(\mathbf{k}) = -\frac{qn_0\kappa(\mathbf{k})}{\varepsilon_0 m K^2(\mathbf{k})} \sum_j \hat{w}(\mathbf{k}_j)\hat{\mathbf{F}}(\mathbf{k}_j,\omega) \int d^3\mathbf{V} \frac{1}{\omega - \mathbf{kV}} \frac{\partial \hat{f}_0}{\partial \mathbf{V}}. \tag{2.123}$$

The dielectric function is obtained by dividing equation (2.123) by $\hat{\mathbf{E}}(\mathbf{k},\omega)$:

$$D(\mathbf{k},\omega) = 1 + \frac{\omega_p^2 \kappa(\mathbf{k})}{K^2(\mathbf{k})} \sum_j \hat{w}^2(\mathbf{k}_j) \int d^3\mathbf{V} \frac{1}{\omega - \mathbf{k}_j\mathbf{V}} \frac{\partial \hat{f}_0}{\partial \mathbf{V}}. \tag{2.124}$$

If f_0 is Maxwellian (2.98)

$$D(\mathbf{k},\omega) = 1 - \frac{\omega_p^2 \kappa(\mathbf{k})}{2K^2(\mathbf{k})} \sum_j \hat{w}^2(\mathbf{k}_j) \frac{1}{k_j} Z'\left(\frac{\omega}{\sqrt{2}|\mathbf{k}_j|V_T}\right). \tag{2.125}$$

The zeroth term $p = 0$ of equation (2.125) is equivalent to the gridless dispersion function (2.99). The non-zero terms $p \neq 0$ introduce mode coupling with periodicity $2\pi/\Delta x$. The simulated system can become unstable if the grid spacing is too large as the particle density becomes undersampled to resolve even long range interactions accurately.

2.3.3 Effect of the Finite Time Step Δt

Assuming that particle forces (or acceleration) are not changing significantly between t and $t + \Delta t$, the particle location and velocity at $t + \Delta t$ can be found as

$$\mathbf{x}(t + \Delta t) = \mathbf{x}(t) + \mathbf{V}(t)\Delta t + \frac{\mathbf{a}(t)\Delta t^2}{2} \tag{2.126}$$

$$\mathbf{V}(t + \Delta t) = \mathbf{V}(t) + \frac{\mathbf{a}(t)\Delta t}{2}. \tag{2.127}$$

In the collisionless system, particle are not correlated and a single particle distribution function f_1 can be found deterministically from its previous state

$$f(\mathbf{x}^{k+1}, \bar{\mathbf{V}}^{k+1}, t^{k+1}) = f(\mathbf{x}^k, \bar{\mathbf{V}}\mathbf{x}^k, t\mathbf{x}^k), \tag{2.128}$$

where $\bar{\mathbf{V}}^k = (\mathbf{V}^{k-1/2} + \mathbf{V}^{k+1/2})/2$. Using leapfrog estimates of the particle coordinate (2.126) and velocity (2.127) on the next time step, conservation of the single particle distribution function (2.128) is obtained

$$f(\mathbf{x}^k, \bar{\mathbf{V}}^k, t) = f \left[\mathbf{x}^k + \bar{\mathbf{V}}^k \Delta t + \frac{\mathbf{a}^k \Delta t^2}{2}, \bar{\mathbf{V}}^k + \frac{\left(\mathbf{a}^k + \mathbf{a}^{k+1}\right)\Delta t}{2}, t + \Delta t \right]. \tag{2.129}$$

The Taylor series expansion of equation (2.129) yields

$$f(\mathbf{x}^k, \bar{\mathbf{V}}^k, t) = f(\mathbf{x}^k + \bar{\mathbf{V}}^k \Delta t, \bar{\mathbf{V}}^k, t + \Delta t) + \frac{\mathbf{a}^k \Delta t^2}{2} \cdot \nabla_{\mathbf{x}} f + \frac{\left(\mathbf{a}^k + \mathbf{a}^{k+1}\right)\Delta t}{2} \nabla_{\mathbf{V}} f. \tag{2.130}$$

At equilibrium, the average acceleration in the system is zero, and total acceleration is

created by the oscillations in the system $\mathbf{a}_1$

$$\mathbf{a}\left(\mathbf{x},t\right)=0+\mathbf{a}_1\left(\mathbf{x},t\right). \tag{2.131}$$

Using the linearized distribution function (2.73) and the acceleration (2.131), equation (2.130) becomes

$$\begin{aligned} f_1(\mathbf{x}^k,\bar{\mathbf{V}}^k,t) &= f_1(\mathbf{x}^k+\bar{\mathbf{V}}^k\Delta t,\bar{\mathbf{V}}^k,t+\Delta t) \\ &+ \frac{\mathbf{a}\left(\mathbf{x}^{\mathbf{k}},t\right)+\mathbf{a}\left(\mathbf{x}^{\mathbf{k}}+\Delta t\bar{\mathbf{V}}^k,t+\Delta t\right)}{2}\Delta t\frac{\partial f_0}{\partial\mathbf{V}}, \end{aligned} \tag{2.132}$$

which yields expression of the distribution function in the frequency space

$$\hat{f}_1\left(\mathbf{k},\mathbf{V},\omega\right)=-\frac{i\Delta t\hat{F}}{2m}\cot\left[\left(\omega-\mathbf{kV}\right)\frac{\Delta t}{2}\right]\frac{\partial\hat{f}_0}{\partial\mathbf{V}}. \tag{2.133}$$

The integral of equation (2.133) over velocity space yields the particle density equation for the finite time-step system

$$\begin{aligned} \hat{n}(\mathbf{k},\omega) &= -\frac{n_0 i\Delta t\hat{\mathbf{F}}(\mathbf{k},\omega)}{2m}\int d^3\mathbf{V}\cot\left[\left(\omega-\mathbf{kV}\right)\frac{\Delta t}{2}\right]\frac{\partial\hat{f}_0}{\partial\mathbf{V}} \\ &= -\frac{n_0 i\hat{\mathbf{F}}(\mathbf{k},\omega)}{m}\sum_{l=-\infty}^{\infty}\int d^3\mathbf{V}\frac{1}{\omega-\mathbf{kV}-2\pi l/\Delta}\frac{\partial\hat{f}_0}{\partial\mathbf{V}}. \end{aligned} \tag{2.134}$$

Substituting (2.134) into (2.121) and repeating the process that was applied for analysis of a time-continuous system with a grid (equation (2.123)) yields a dispersion relation for a plasma sytem with a grid and a finite time step

$$D(\mathbf{k},\omega) = 1+\frac{\omega_p^2\kappa\left(\mathbf{k}\right)}{K^2\left(\mathbf{k}\right)}\sum_j\hat{w}^2(\mathbf{k}_j)\sum_{l=-\infty}^{\infty}\int d^3\mathbf{V}\frac{1}{\omega-\mathbf{kV}-2\pi l/\Delta}\frac{\partial\hat{f}_0}{\partial\mathbf{V}}. \tag{2.135}$$

In addition to low-pass filtering of the short-range interactions introduced by coarse-graining and the spacial mode coupling introduced by the structured grid, the time step introduces additional modes with the period $2\pi/\Delta T$. Thus, choosing a small grid step $\Delta x<\lambda_D$ and a small time step $\Delta T<2/\omega_p$ is sufficient to control unphysical mode coupling in the

simulation.

2.4 Simluation of the Collisional Processes in Particle-in-Cell Codes

The classical Particle-in-Cell scheme, described earlier in this chapter, does not include any explicit collisional interaction between charged plasma species, except those that are generated from random particle noise. In real-world plasmas, species interact with each other and the background gas species through collisions that may include but are not limited to elastic scattering, excitations, ionization and charge exchange. The exact set of collisional processes depends on the chemical composition of the simulated plasma and, usually, only reactions with a high probability of occurrence are selected as candidates for the simulation.

2.4.1 Collisionality in Particle-in-Cell Codes due to Numerical Noise

Computational experiments performed by Hockney [43] have demonstrated empirically that numerical collisions are generated in collisionless Particle-in-Cell simulation due to random noise. In Hockney's experiment, the particles were initialized randomly in two-dimensional simulation domain $D_x = 2$. Particle velocities were sampled in a two dimensions as well $D_V = 2$ (2D2V). The stochastic fluctuations of the electric field deflected the particles from their original trajectories, and the collision time was measured as the decay rate of average particle velocity along their original direction measured at the initial time step

$$\frac{d\left\langle V_{\parallel}(t)\right\rangle}{dt} = \frac{\left\langle V_{\parallel}(t)\right\rangle}{\tau_s}, \text{at } t = 0 \tag{2.136}$$

where $V_{\parallel}(t)$ is the component of particle velocity along its original trajectory, and τ_s is the collision time, which is referred to as slowing-down time in the original paper. It was determined empirically that the slowing-down times are proportional to the period of the electron plasma oscillations τ_{pe} and depend on the number of computational particles in the

Coulomb sphere N_c

$$\tau_s = \tau_{pe} = N_c/K_1, \tag{2.137}$$

where K_1 was estimated to be 0.98 with a standard deviation of 0.2. The number of particles in the Debye sphere is determined as

$$N_c = n\left(\lambda_D^2 + (R\Delta x)^2\right), \tag{2.138}$$

where n is the density of computational particles and R is the scaling factor specific to the particular shape function: for the triangular shape function (2.39) the scaling parameter R equals to 1. Notably, values of the K_1 coefficient do not always equal to 0.98, and strongly depend on sampling of the Debye sphere in the Particle-in-Cell simulations and the type of shape function used for particles. For example, Hockney reports that, depending on the sampling of the Debye sphere, K_1 can range from 0.004 to 3.6.

Using the slow-down time (2.137), the collisional frequency in a two-dimensional simulation is determined as

$$\nu_c \approxeq \frac{\omega_{pe}}{2\pi N_c} = \frac{\omega_{pe}}{2\pi K_1 n\left(\lambda_D^2 + (R\Delta x)^2\right)}. \tag{2.139}$$

Equation (2.139) demonstrates that the collision frequency due to random noise is smaller than the physical collision frequency by a factor of N_c, and depends on the width of the shape function Δx (grid spacing). Tajima [41] asserts that the collision frequency also depends on the dimensionality of the simulation D_x. Thus, in a one dimensional case, the collision frequency is

$$\nu_c \approxeq \frac{\omega_{pe}}{2\pi n\lambda_D} F, \tag{2.140}$$

in a two-dimensional case is

$$\nu_c \approxeq \frac{\omega_{pe}}{16\pi n\lambda_D^2} F, \tag{2.141}$$

and in a three-dimensional case is

$$\nu_c \cong \frac{\omega_{pe}}{27\pi n\lambda_D^3} F \log\left(9n\lambda_D^3\right). \tag{2.142}$$

In Tajima's notation, F is a parameter that is estimated empirically from the simulation, and is directly related to the scaling factor K_1 reported in Hockney's work. As with the coefficient K_1, the value of the scaling coefficient F depends on the dimensionality of the simulated problem and the number of computational particles in the Debye sphere $N_d = n\lambda_D^{D_x}$, where D_x is the dimensionality of the simulation. Even though both authors provide general insight on the nature and behavior of the random-noise collisionality, there is no reliable way of estimating the coefficients F or K_1 theoretically.

2.4.2 Simulation of the Physical Collisions in Particle-in-Cell codes with Monte-Carlo Collision Approach

Each of the plasma species can participate in a collisional process with any of the plasma species present in the system. In a Particle-in-Cell code, collisional processes are treated independently. Thus, in the context of this chapter, collisions are discussed for a pair of active a and background b plasma species (for example ions and neutrals). The collisional process is applied to the active species without affecting the background species: this is the ab process. The background species can be changed by collisions in the reverse ba-process, that can be simulated sequentially after the ab-process.

Thus, collisional physics for the ab-process are commonly included into Particle-in-Cell simulations via Monte-Carlo Collisions methods (MCC) [44]. The Monte-Carlo Collisions step is usually applied after the solution of the field equations, and consists of the following conceptual steps at every PIC iteration: calculation of the expected number of collided particles for each plasma species, random selection (sampling) of particles that will participate in collisions for each species, and applying randomized collision processes for each particle that was selected at the previous step.

For a particle p of a species a with kinetic energy E_p and velocity V_p:

$$E_p = \frac{m}{2}\left(V_{px}^2 + V_{py}^2 + V_{pz}^2\right), \tag{2.143}$$

the probability of collision with particles of species b can be modeled using a Poisson process. The rate of collision processes, or collision frequency ν_{ab}, for an individual particle p of species a with velocity V_p depends on the collisional cross-section of the process and velocity distribution $f_b\left(\mathbf{V}_b\right)$ of the colliding particles of species b

$$\nu_{ab}(\mathbf{x}_p, \mathbf{V}_p) = n_b(\mathbf{x}_p) \int d^3\mathbf{V}_b f_b(\mathbf{V}_b) \left|\mathbf{V}_p - \mathbf{V}_b\right| \sigma_{ab}\left(\frac{m_a\left(\mathbf{V}_p - \mathbf{V}_b\right)^2}{2}\right), \tag{2.144}$$

where $\mathbf{x}_p$ is the particle location at the time t, and n_b is the density of particles of species b, and σ_{ab} is the total collisional cross-section for the ab-process

$$\sigma_{ab}(E) = \sum_{i=1}^{J} \sigma_{ab}^j(E), \tag{2.145}$$

where J is the total number of collisional processes between particle species a and b, and σ_{ab}^j is the collisional cross-section of process j. Then, the times between collisions are exponentially distributed, and the probability of undergoing a collision for particle p in a period of time Δt is defined as

$$P_{ab}\left(\mathbf{V_p}\right) = 1 - \exp\left[\nu_{ab}\left(\mathbf{V}_p\right)\Delta t\right]. \tag{2.146}$$

Each particle in the Particle-in-Cell simulation can be randomly selected to undergo a collision process using equation (2.146) based on the particle velocity, however such a calculation is costly as it requires to execute a random number generator for every particle of species a, and would have a computational complexity $O(N_a)$. Hence, it is more efficient to calculate the collision probability for the whole ensemble of particles in a Particle-in-Cell simulation

using a distribution function f_a of the species a

$$\nu_{ab} = n_b \int d^3\mathbf{x} \int d^3\mathbf{V_a} \int d^3\mathbf{V}_b f_a(\mathbf{x}, \mathbf{V}_a) f_b(\mathbf{x}, \mathbf{V}_b) \left|\mathbf{V}_a - \mathbf{V}_b\right| \sigma_{ab} \left[\frac{m_a \left(\mathbf{V}_a - \mathbf{V}_b\right)^2}{2}\right]. \tag{2.147}$$

Notably, the ensemble collision frequency ν_{ab} is calculated in the whole simulation domain. Then, ensemble collision probability during a single time step Δt is found as

$$P_{ap} = 1 - \exp\left[-\Delta t \nu_{ab}\right], \tag{2.148}$$

and the total number of collided particles is

$$N^a_{collided} = N_a P_{ap}, \tag{2.149}$$

where N_a is the number of particles of species a in the simulation. Calculation of the exact number of collided particles using equations (2.147-2.149) is challenging as it involves functional forms of the distribution function, which are not readily available in the Particle-in-Cell codes. Vahedi [44] developed a method based on rejection sampling that does not require exact evaluation of quantity (2.149).

In Vahedi's approach, the ensemble collision frequency is overestimated as

$$\begin{aligned}
\nu_t &= \max_{\mathbf{x}, |\mathbf{V}_a - \mathbf{V}_b|} \left[n_b\left(\mathbf{x}\right) \left|\mathbf{V}_a - \mathbf{V}_b\right| \sigma_{ab} \left(\frac{m_a \left(\mathbf{V}_a - \mathbf{V}_b\right)^2}{2} \right) \right] \\
&= \max_{\mathbf{x}} \left[n_b\left(\mathbf{x}\right) \right] \max_{|\mathbf{V}_a - \mathbf{V}_b|} \left[\left|\mathbf{V}_a - \mathbf{V}_b\right| \sigma_{ab} \left(\frac{m_a \left(\mathbf{V}_a - \mathbf{V}_b\right)^2}{2} \right) \right] \\
&= \max_{\mathbf{x}} \left[n_b\left(\mathbf{x}\right) \right] \max_{\mathbf{V}_r} \left[\left|\mathbf{V}_r\right| \sigma_{ab} \left(\frac{m_a \mathbf{V}_r^2}{2} \right) \right].
\end{aligned} \tag{2.150}$$

The collision frequency (2.150) depends only on the maximum density of the background species b in the simulation domain and the maximum value of the product of the cross-section σ_{ab} and the relative velocity $\mathbf{V}_r$ of species a and b. Using ν_t, the ensemble collision

probability P_t during the time-step Δt is calculated as

$$P_t = 1 - \exp\left(\nu_t \Delta t\right), \tag{2.151}$$

and the expected number of particles that should be selected as candidates for collision processes is found as

$$N_t = P_t N_a \left[1 - \exp\left(\nu_t \Delta t\right)\right], \tag{2.152}$$

where N_a is the number of computational particle of species a, are overestimated. Both P_t and N_t are larger than P_{ab} and $N^a_{collided}$ respectively, therefore P_t is used to select a candidate set of particles randomly from the particle population of species a. Then, the individual particle collision probability $P_{ab}\left(V_p\right)$ and collision frequency $\nu_{ab}\left(V_p\right)$ are used to select particles from the candidates using rejection sampling. The rejection sampling for Monte-Carlo Collision method is summarized in the algorithm 1, where I_J is an indicator

Algorithm 1 Monte-Carlo Collision (MCC) Algorithm

$P_t = 1 - \exp\left(\nu_t \Delta t\right)$
$N_t = P_t N_a \left[1 - \exp\left(\nu_t \Delta t\right)\right]$
$ps =$ Sample of the size N_t from Discrete Uniform Distribution between 0 and N_a
for i in $1 \ldots N_t$ **do**
    $p = ps[i]$
    Generate a uniform random variable $u \sim \texttt{Uniform}(0, \nu^t)$
    if $u < \sum_{j=1}^{J} \nu_j(\mathbf{V}_p)$ **then**
        no_collision
    else
        $j = \arg\max_J I_J \left\{ \sum_{j=1}^{J-1} \nu_j(\mathbf{V}_p) < u <= \sum_{j=1}^{J} \nu_j(\mathbf{V}_p) \right\}$
        Modify $\mathbf{V}_p$ according to process j
    end if
end for

function that is used to select the collision process j. If $u < \sum_{j=1}^{J} \nu_j(E_p)$, the candidate particle does not undergo any collision process, and such an event is called *null collision*.

2.4.3 Details of Monte-Carlo Collision Involving Ion-Neutral Processes

Since the Particle-in-Cell method is designed for simulations of the charged particle species only, the neutral species are usually not simulated directly in PIC codes. Thus, the parameters of the neutral species (density, temperature, etc.) are assumed to be fixed in the simulation. In addition to that, it is commonly assumed that neutrals follow a Maxwellian distribution

$$f_n(\mathbf{V}) = n_n \left(\frac{m_n}{2\pi k_B T_n} \right)^{3/2} \exp\left[-\frac{m\left(\mathbf{V}-\mathbf{V}_n\right)^2}{2k_B T_n} \right], \tag{2.153}$$

where T_n, $\mathbf{V}_n$ and n_n are the temperature, drift velocity and density of the neutral background. Then, for each ion that undergoes a collision with a particle of a neutral species, the neutral is randomly sampled from the Maxwellian distribution (2.153).

The interactions between ion and neutral particles can be approximated by elastic scattering. Assuming that the ion energy before and after scattering is E_i and E_s respectively, the ion energy after scattering can found as

$$E_s = (1-\alpha)E_i, \tag{2.154}$$

where α is the energy loss factor

$$\alpha = \frac{2m_i m_n}{\left(m_i+m_n\right)^2}\left(1-\cos\theta\right), \tag{2.155}$$

where m_i and m_n are the atomic masses of the colliding ion and neutral respectively, and θ is the scattering angle in the center-of-mass frame.

The direction of the velocity of a scattered ion is then found as

$$\mathbf{v}_s = \mathbf{v}_i \cos\chi + \mathbf{v}_i \times \mathbf{i}\frac{\sin\chi\sin\phi}{\sin\theta} + \mathbf{v}_i \times (\mathbf{i}\times\mathbf{v})\frac{\sin\chi\cos\phi}{\sin\theta}, \tag{2.156}$$

where $\mathbf{v}_s$ and $\mathbf{v}_i$ are the unit vectors along the velocity of the incident and scattered ion,

and angle ϕ is determined as

$$\phi = \arccos\left(\mathbf{v}_i \cdot \mathbf{i}\right). \tag{2.157}$$

The elastic scattering process is significantly simplified if the masses of the interacting ion and neutral are equal $m_i = m_n$. Then, the scattering angle in the laboratory frame is found as

$$\chi = \theta/2, \tag{2.158}$$

and the energy of the scattered ion is defined as

$$\begin{aligned} E_s &= E_i \frac{2m_i m_n}{\left(m_i + m_n\right)^2}\left(1 - \cos\phi\right) && (2.159)\\ &= E_i \frac{1}{2}\left(1 - \cos\theta\right) = E_i \cos^2\chi. && (2.160) \end{aligned}$$

Assuming that scattering angle in the center-of-mass frame is distributed uniformly and isotropically, then

$$\cos\chi = \sqrt{1-u}, \tag{2.161}$$

and the azimuthal scattering angle ϕ is determined as

$$\phi = 2\pi u, \tag{2.162}$$

where $u \sim \mathrm{Unif}(0,1)$ is drawn from a standard uniform distribution.

2.5 Electrostatic Particle-in-Cell with Adiabatic Electrons

In order to resolve the electron plasma oscillations, the time step of the PIC code has to be smaller than the plasma period, $T_p = 2\pi\sqrt{m\varepsilon_0/n_e e^2}$, which is of the order of picoseconds, $O\left(10^{-12}\right)$ s. However, the relaxation time of the simulation $t_{relax} = L/V_{th}$ depends on the characteristic size L of the simulation domain and the thermal velocity of the slowest species

V_{th}. Typical relaxation times range from half a microsecond (for 10 eV deuterons at 1 cm from the surface) to tens of microseconds (for 1 eV tungsten under the same conditions). Thus, a fully kinetic simulation must resolve multiple time scales ranging from picoseconds to multiple microseconds, 10^{-12} – 10^{-6} before a steady-state condition is reached.

A possible solution of the multi-scale problem is resolving the evolution of heavy plasma species with the complete kinetic model, and approximating the physics of the light plasma species (electrons) with a simplified model. Typically, the electron dynamics are assumed to be regulated only by electric and pressure forces:

$$\mathbf{0} \approx qn\mathbf{E} - \nabla p \tag{2.163}$$

so that the electron density follows the Boltzmann distribution:

$$n_e = n_0 \exp\left[\frac{\Phi}{T_e}\right] \tag{2.164}$$

where n_0 is the normalization constant that has units of density, Φ is the electrostatic potential in volts, and T_e is the electron temperature in eV. The value of n_0 is given by the conservation of the total charge inside the plasma domain:

$$n_0 = \frac{Q_{domain}}{e}\left[\int_V \mathrm{d}V \exp\left(\frac{\Phi}{T_e}\right)\right]^{-1}, \tag{2.165}$$

where Q_{domain} is the total electric charge in the simulation domain. Using equation (2.164), the charge density on the right hand side of the Poisson equation (2.18) becomes

$$\rho = e\left[n_i - n_o \exp\left(\frac{\Phi}{T_e}\right)\right], \tag{2.166}$$

and the Poisson equation (2.18) takes on its non-linear form

$$\begin{aligned} \nabla^2\Phi &= -\frac{e}{\epsilon_o}\left[n_i - n_o \exp\left(\frac{\Phi}{T_e}\right)\right] \\ \nabla^2\Phi &+ \frac{en_i}{\varepsilon_0} - \frac{en_0}{\varepsilon_0}\exp\left(\frac{\Phi}{T_e}\right) = 0. \end{aligned} \tag{2.167}$$

This equation could be solved using Newton's methods

$$f\left(\mathbf{x}_{i+1}\right) = f\left(\mathbf{x}_i\right) - \mathbf{J}_k^{-1}(\mathbf{x}_i) f(\mathbf{x}_i), \tag{2.168}$$

where $\mathbf{x}_i$ is a vector of unknown variable x and $\mathbf{J}$ is a Jacobian of the function $f = \nabla^2\Phi + en_i/\varepsilon_0 - en_0 \exp\left(\frac{\Phi}{T_e}\right)/\varepsilon_0$. Using a test function γ, the Jacobian of the function f can be found via finite differentiation:

$$\begin{aligned} \mathbf{J}\left(\Phi_{i,j}\right) &= \left(\gamma_{i-1,j} - 2\gamma_{i,j} + \gamma_{i-1,j}\right)\frac{\Delta y}{\Delta x} + \left(\gamma_{i,j-1} - 2\gamma_{i,j} + \gamma_{i-1,j+1}\right)\frac{\Delta x}{\Delta y} - \\ &\quad \Delta x \Delta y \frac{en_0}{\varepsilon_0 T_e} \exp\left(\frac{\gamma_{i,j}}{T_e}\right) = 0, \end{aligned} \tag{2.169}$$

and its inverse $\mathbf{J}_k^{-1}$ could be evaluated using the methods developed in chapter 3

In the plasma sheath simulation with an absorbing boundary, a fraction of the PIC particles are leaving the simulation domain at every time step. In stationary conditions, for every particle lost at the boundary there must be one particle replenished back into the domain. If the electrons are simulated using a Boltzmann distribution [45], the loss of electrons must be compensated by an update of the value of the reference density:

$$\frac{\partial n_0 p}{\partial t} + \frac{1}{4} v_e n_0 q = r, \tag{2.170}$$

where $p = \int_V \mathrm{d}V \exp\left(\Phi/T_e\right)$ and $q = \int_A \mathrm{d}A \exp\left(\Phi/T_e\right)$ are the volumetric and surface integrals of the exponential Boltzmann factor. The first term in equation (2.170) is the rate of change of the total number of electrons in the simulation domain, the second term shows the electron loss at the walls due to thermal fluxes, and the last term r is the rate of electron generation in the simulation domain. Using a finite difference scheme for the time derivative of the total electron charge in the simulation domain we get

$$\frac{n_0^{t+\Delta t} p^{t+\Delta t} - n_0^t p^t}{\Delta t} + \frac{1}{4} v_e n_0 q^t = r^t, \tag{2.171}$$

where t is the current time and Δt is the time step. The value of the electric potential $\Phi^{t+\Delta t}$

and the values of the integrals of the Boltzmann factor p and q are also undetermined at the future time step $t + \Delta t$ and could be estimated using damped values of the integrals of the Boltzmann factor p and q from the previous time steps:

$$n_0^{t+\Delta t} = n_0 \left[(1 - f) \frac{p^{t-\Delta t}}{p^t} + f - \frac{f^2}{4} \right] + \frac{r^t \Delta t}{p^t}. \tag{2.172}$$

Once the simulation with the reduced electron model achieves a steady-state condition, the reduced electron model can be converted to a kinetic population of electrons, up to convergence on the electronic phase space. The density of the kinetic electron species will be found initially using values of the electric potential ϕ, the normalization constant n_0, and the assumed plasma temperature T. Now, a spatially varying value of the electron temperature can be estimated locally from the kinetic population of electrons as $T(y) = 2m_e \mathrm{Var}(V_{xz})/k_B$, where V_{xz} is the ion velocity in the plane parallel to the wall. The value of the density normalization constant n_0 can be also estimated from the kinetic description of the particles as

$$\hat{n}_0 = \frac{\int_V \mathbf{d}V n_e}{\int_V \mathbf{d}V e^{\phi/T_e(x)}}. \tag{2.173}$$

From the iteration among the reduced electron model and the fully kinetic model, both the ion and electron phase space will be obtained.

Chapter 3

hPIC: A Massively-Parallel ES-PIC Code for Near-Surface Plasmas

In this chapter we present the hPIC code, a full-f (full distribution), full-orbit, electrostatic (ES) Particle-in-Cell (PIC) specifically developed for near-surface Plasma-Material Interaction (PMI) problems. The code handles bounded plasma domains in both magnetized and unmagnetized conditions, where user-specified boundaries are connected to material codes handling the surface erosion and implantation physics, such as TRIDYN [46], Fractal-TRIDYN [24], and other routines dedicated to surface physics and ion-matter interaction.

The hPIC code is particularly suitable for simulation of the plasma sheath and pre-sheath in strongly magnetized conditions, as those normally encountered at the wall of magnetic fusion reactors. The plasma sheath acts as a boundary layer between the bulk plasma and the material wall. Inside the plasma sheath, the ions accelerate to supersonic conditions up to the point where quasi-neutrality is broken and large electrostatic fields appear. In presence of a magnetic field inclined at grazing angle with respect to the wall, the structure of the plasma sheath is dominated by finite-Larmor radius effects, exhibiting the formation of a magnetic presheath in addition to the classical collisional presheath and Debye sheath. The magnetized plasma sheath can thus be divided into three major areas based on the local Mach number of the ionic species, as classified by Chodura [23]: collisional presheath, magnetic presheath, and Debye sheath. Three-dimensional finite-Larmor-radius effects due to particle drifts strongly affect the ion energy-angle distributions at the surface and must be taken into account.

The hPIC code has been used to perform analyses of the plasma sheath in strongly-magnetized conditions. The results of the physics analyses [35] have been reported in the following Chapter 4. In this chapter we give an overview of the physical model implemented

in hPIC, of the code architecture, and of the scalability tests performed on the Blue Waters supercomputer at Illinois. All scaling plots have been reported as a function of the number of Blue Waters nodes; one Blue Waters node corresponds to 32 cores. The code architecture is described in Section 3.2, presenting the code structure and parallelization scheme and concluding with functions and data structures specific to the code. In sections 3.3.2 and 3.3.3 we describe the dimensionless framework used for testing the weak scaling of the code, which is applicable to any other ES particle-in-cell code. Finally, in section 3.3.6 we report the scaling of hPIC and of each individual component as measured on the Blue Waters supercomputer. The chapter concludes with an overview of the verification tests performed on hPIC.

The results reported in this chapter are reproduced in parts from "hPIC: A scalable electrostatic Particle-in-Cell for Plasma-Material Interactions" which was accepted for publication in Computer Physics Communications [37].

3.1 Motivation of a new code for near-surface plasmas

The development of a massively-parallel 2D3V/3D3V full-orbit PIC code like hPIC is motivated by the harsh requirements of simulating divertor plasmas on spatial and temporal scales relevant to near-surface impurity transport with consideration of surface erosion and prompt redeposition. For example, a fully-kinetic 2D3V hPIC simulation of 2×2 cm^2 of detached divertor plasma at temperature $T_e = T_i = 5$ eV and density $n_e = 2 \times 10^{19}$ m^{-3} requires a grid of the order of $27,000 \times 27,000$ cells and 434×10^9 computational particles (at 600 particles per cell) on 71,456 cores. Previous ES PIC codes tackling the PMI problem [47, 48] have been developed in 1D3V with scaling reported [47] up to 1,000 processors on 20,000×1 cells and 40×10^6 particles. Other recent full-orbit ES-PIC codes have been developed for magnetospheric [49] [50], arc discharges [51], and fusion [52] applications. Such codes have not reported or demonstrated scaling at more than 1,000 cores as required to enable large-scale plasma-surface interaction simulations.

The best scalability to date has been obtained with gyrokinetic PIC approaches, either

electrostatic [53, 54, 55, 56, 17, 57] or electromagnetic [58, 59]. Gyrokinetic codes have proven to be very effective for the simulation of the plasma core and the scrape-off-layer (SOL), allowing studies of the pedestal and SOL plasmas on spatial scales as large as the full ITER device and temporal scales up to transport time scales (tens of milliseconds). Such codes typically do not handle the plasma-material boundary explicitly. Boundary conditions in gyrokinetic PIC codes typically resolve the plasma sheath through the use of simplified models, like the "logical" sheath [18]. The development of a sheath/surface code like hPIC has the potential to extend the boundary treatments of large-scale gyrokinetic codes with an explicit plasma-material boundary and a proper representation of the ion energy-angle distributions impacting on the material surface. Direct coupling of gyrokinetic codes to a surface/sheath code like hPIC would enable studies of the simultaneous, long-time evolution of the plasma and the surface.

3.2 Code Architecture

3.2.1 Code Structure

The hPIC code is a fully-kinetic, full-orbit, electrostatic Particle-in-Cell designed to operate on High-Performance Computing (HPC) systems, specifically developed for the treatment of near-surface plasmas and coupling to material surface codes. In this section we describe the characteristic features of the code, namely: the domain decomposition adopted, the particle functions, and relevant data structures. No discussion is reported on the field solver, since it is based on the existing PETSc numerical library [60, 61] and Hypre's multigrids [62].

The hPIC code is written in C and has been designed with a high level of abstraction, on both the *data structures* storing the physical quantities used by the algorithm, and the *methods* operating on the data structures. Such abstraction allows a greater flexibility, like the possibility to add additional features without breaking the workflow of the program. Using software abstraction is quite natural for the implementation of all the major components of a PIC algorithm, which can be divided in particle functions and field functions, as described hereafter.

The particle functions in hPIC are merged into a single, optimized algorithm named "Particle Advance" (described in Sec. 3.2.2) performing all three particle steps of a classical PIC cycle (moving, weighting, and interpolation). Figures 2.2(a) and 3.2.1 compares the architecture of a classical PIC cycle (Fig. 2.2(a)) and hPIC's one (Fig. 3.2.1). The classical particle functions of a PIC algorithm, namely (1) interpolation of fields at particle's location, (2) particle moving, and (3) weighting of particle properties on the mesh nodes, are merged into a single step of "Particle Advance". An additional step named "Post-process Special Particles" performs any additional and/or optional operation to the particles.

The field functions are managed by PETSc numerical library. An abstract interface is established between hPIC's domain and the Poisson solver to manage the data passage between hPIC's and PETSc' data structures. The interface between hPIC and PETSc handles the inputs required by the Poisson solver (charge density), and receives back the outputs provided by PETSc (electric field, electric potential). Keeping the field solver as a separate module increases the flexibility and allows to substitute the numerical library upon needs.

Finally, hPIC offers a set of general objects to perform operations among its components, like for example handling the communication between MPI processes, defining simulation domains, and an abstract definition of data structures which facilitate the development of advanced diagnostics and advanced methods without worrying about the performance and the implementation of the algorithms.

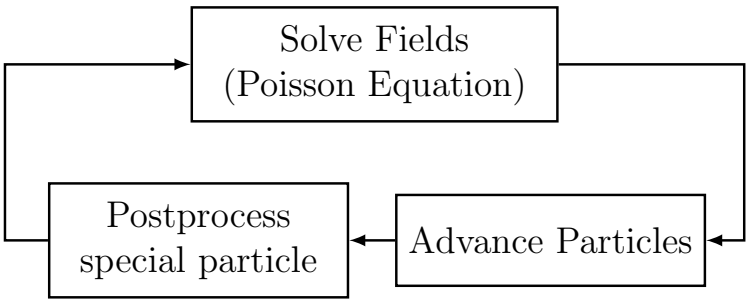

Figure 3.1: Major steps of the hPIC cycle

3.2.2 Cache-Optimized Particle Advance Scheme

The original set of Boris' equations was designed for moving particles in the physical space. A more efficient numerical treatment can be obtained by rescaling the particle coordinates as a sum of the index $\mathbf{i} = [i_x, i_y, i_z]^T$ of the cell the particle belongs to, and the offset $\mathbf{w} = [w_x, w_y, w_z]^T$ within the cell (directly related to the shape function w)

$$\mathbf{x} = \mathbf{S}\left(\mathbf{i} + \mathbf{w}\right), \tag{3.1}$$

and renormalizing the particle velocity $\mathbf{v}$ to obtain the velocity $\mathbf{U}$ scaled with the grid spacing,

$$\mathbf{v} = \mathbf{S}\mathbf{U}, \tag{3.2}$$

where $\mathbf{S}$ is the grid scale matrix (related to the Jacobian of the grid in case of non-uniform grids),

$$\mathbf{S} = \begin{bmatrix} \Delta x & 0 & 0 \\ 0 & \Delta y & 0 \\ 0 & 0 & \Delta z \end{bmatrix} \tag{3.3}$$

Then, instead of updating the positions and velocities of the particles in the physical space, we update the index of grid cell i the particle belongs to, the local coordinates of the particle inside the grid cell $\mathbf{w}$, and the grid velocity $\mathbf{U}$. The original Boris update equations can be recast in a convenient way by switching from physical coordinates to a discrete set of coordinates measured in grid units ("grid space") in the following form:

$$\mathbf{U}^- = \mathbf{U}^{t-1/2} + \mathbf{S}^{-1}\frac{q\Delta t}{2m}\mathbf{E}^t \tag{3.4}$$

$$\mathbf{b} = \mathbf{B}/\left\|\mathbf{B}\right\|_2$$

$$\mathbf{t} = \mathbf{b}\tan\left(q\left|\mathbf{B}\right|\Delta t/2m\right) \tag{3.5}$$

$$\mathbf{U}' = \mathbf{U}^- + \mathbf{U}^- \times \mathbf{t} \tag{3.6}$$

$$\mathbf{U}^+ = \mathbf{U}^- + 2\mathbf{U}' \times \mathbf{t}/\left(1 + t^2\right) \tag{3.7}$$

$$\mathbf{U}^{t+1/2} = \mathbf{U}^+ + \mathbf{S}^{-1}\frac{q\Delta t}{2m}\mathbf{E}^t \tag{3.8}$$

$$\mathbf{s}^{t+1} = \mathbf{w}^t + \mathbf{U}^{\mathbf{t+1/2}}\Delta t \tag{3.9}$$

$$\mathbf{w}^{t+1} = \mathbf{s}^{t+1} \quad \text{rem } 1 \tag{3.10}$$

$$\mathbf{i}^{t+1} = i^t + \text{floor}(\mathbf{s}^{t+1}) \tag{3.11}$$

With this scheme, most of the operations routinely necessary in a PIC scheme (particle weighting, particle interpolation, particle localization inside the mesh) are directly done inside the particle advance algorithm. Notably, the local coordinate of the particle is related to the shape function Eq. (2.39) and allows to perform the calculation of the density Eq. (2.40) on the fly, dramatically improving the cache hit/miss performance of the code. Finally, we note that the physical values of the particle location and velocity can be easily reconstructed at every iteration for diagnostic purposes using equation (3.1) and (3.2).

Furthermore, the algorithm does not require double precision, since the particle position is described only by the cell index (an integer number) and by the local coordinate within a cell (either a double or a single-precision float number). When single-precision is used for the local coordinates, it allows to store twice the number of particles with respect to equivalent algorithms working in double precision. Similar approaches exploiting single-precision arithmetics have been used in the works of Bowers et al. [63], Fonseca et al. [64] and Germaschewski et al. [65].

3.2.3 Parallelization Strategy and Domain Decomposition

The parallelization strategy of the code is handled by a structure named `hpic_domain`, which stores the information about the physical boundaries of the regions, the grid data, and the information required for communication. The structure `hpic_domain` is used to handle the portions of the physical domain stored on a single process. However, the structure allows more freedom in the definition of the parallelization strategy, enabling, for example, the arrangement of nested `hpic_domain` structures in a hierarchical fashion. An `hpic_domain` structure can contain another `hpic_domain` structure, and define a hierarchy of domain levels. A single `hpic_domain` can refer to a larger region, identified simply as "super-domain", and a set of smaller regions as "sub-domains". For example, in the simplest parallel simulation the global simulation domain is a super-domain connected

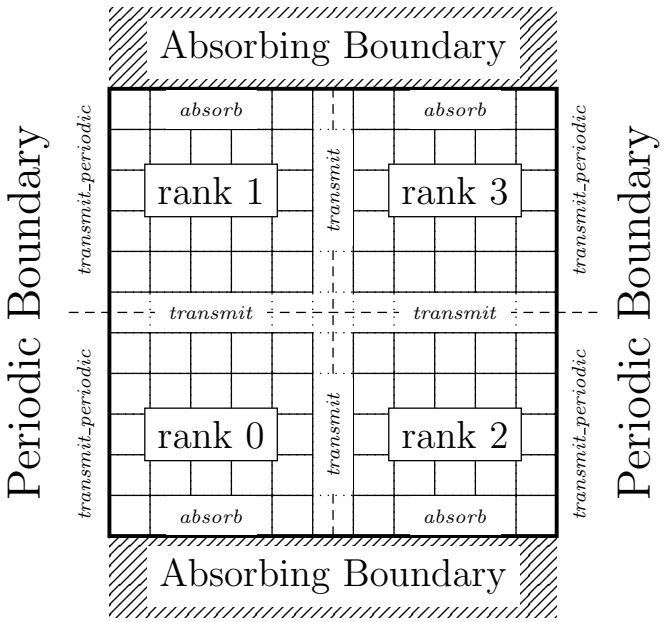

Figure 3.2: Example of a 12×12 grid partitioning on 4 MPI processes of a simulation domain with periodic boundary conditions in x direction and absorbing boundaries along y. Dashed lines represent the logical boundaries between partitioned domain blocks, and the type of the particle boundary is labeled on top of the boundary

to a number of local sub-domains. As a consequence, all the particle and field objects are generated on each process simply using information stored in the local `hpic_domain`, thus improving the "locality" of the code and its parallel performance.

The connection between adjacent `hpic_domains` is handled by a data structure named `grid_graph`, containing: the handles (rank of the processes) to the adjacent sub-domains, the type of relation with the neighboring sub-domains, and additional information required for particle tracking. The type of sub-domain relationships specifies the type of boundary between domains (reflective, transmissive, periodic, etc), as described in more detail in Section 3.2.4.1. Figure 3.3 shows an example of neighbor graph for a domain of rank 4 with a 3×3 partitioning of the global grid. The arrows represent the ranks of the processes that process 4 is connected to.

The particle transport between different hPIC sub-domains is governed by the `grid_graph`

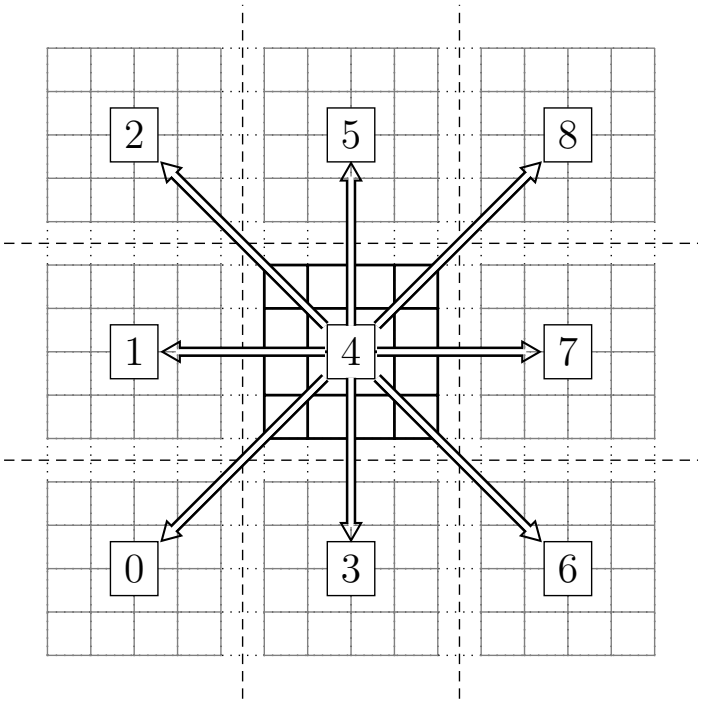

Figure 3.3: An example of a neighbor graph for a process 4 for a global simulation domain partitioned into 3×3 sub-domains. The neighbor graph points to the ranks of neighboring sub-domains

data structure. The number of neighboring sub-domains is stored together with the array of the sub-domain's ranks (`ranks`) and the corresponding grid information (`grid_info`). The `grid_info` array is configured to store `hpic_domain` structures for the corresponding `rank`.

3.2.4 Particle Functions

Classical PIC algorithms (Algorithm 2) include four major steps: solution of field equations, interpolation of fields at particles' location, moving particles along the characteristics, and weighting of particle properties on the grid nodes. In hPIC (Algorithm 3), all particle functions are combined into a single optimized algorithm performing the interpolation, moving, and weighting steps within a single operation named "particle advance". Particles requiring special handling (deletion, communication, etc.) are recorded to a post-processing queue, that is handled outside the particle loop in a Particle Post-Processing module. The particle post-processing operations include: (1) material boundary treatments: particle that cross the boundaries of the simulation domain are either deleted, or reflected, or added to the PMI buffer; (2) particle communication: the particles that require to be moved from one MPI process to another are packed to appropriate communication buffers. The final step of the particle post-processing function is the message passaging of the particle buffers, and of their corresponding fluid moments on the ghost nodes around the edge of the simulation domain.

Algorithm 2 Conventional PIC algorithm with weighting and cell memorization

```
1: for particle in particles do
2:     Interpolate fields on particle
3: end for
4: for particle in particles do
5:     Moving particle (e.g. Boris push)
6: end for
7: for particle in particles do
8:     Weighting particle
9: end for
```

Algorithm 3 hPIC particle loop

```
1: Initialize Queue
2: for particle in particles do
3:     Interpolate fields on particle
4:     Boris push in logical space for particle
5:     Deposit particle
6:     if particle leaves hpic_domain then
7:         append particle to Queue
8:     end if
9: end for
10: Process Queue
```

3.2.4.1 Particle Events

Table 3.1: Comparison (FLOPS) of the classical 3D Boris Leapfrog with hPIC's 3D Leapfrog in Logical Space

	Classical PIC Method (3D)	hPIC Particle Algorithm (3D)
Interpolation		
Obtain Cell Index	6	0
Linear Weights	6	3
Linear Interpolation	45	45
Particle Moving (Boris)		
Half Acceleration	9	9 (with scaled **E** fields)
Rotate	47	47
Half Acceleration	9	9
Push Position	6	15
Weighting		
Obtain Cell Index	6	0
Linear Weights	6	3
Linear Deposition	32	32
Total (FLOPS/particle)	163	154

An innovative particle advance function is implemented in hPIC, combining the three steps of particle interpolation, moving, and weighting of a classical PIC method. The algorithm, whose mathematical details are presented in Sec. 3.2.2, is analyzed here on its computational performance. Table 3.1 reports a comparison of the floating point operations (FLOPS) of a classical PIC method and hPIC's algorithm, showing the advantage of hPIC's method. Despite the larger FLOPS number during particle moving, both interpolation and weighting are less expensive, giving an overall advantage on the number of floating point

operations required to process each particle.

3.2.4.2 Particle Post-processing

In order to ensure good cache performance, hPIC iterates only once over the particle array. During the particle loop, the state vector of the particle is updated. All the indices of the particles requiring additional operations are pushed to the two queues for particle tracking, and packing of communication buffers. After the particle loop is over, hPIC processes the particles listed in the queue, performing the particle tracking, and packing the particles into communication buffers. During the post-processing operation, no additional data is

Table 3.2: Cache performance of hPIC on BlueWaters supercomputer

	hits	misses
L1 cache	96.0%	4%
L2 cache	94.8%	5.2%

moved from RAM to caches, which ensures high cache hit ratios. In the current version of the code, hPIC achieves $\sim 95 - 96\%$ of hits for both L1 and L2 caches, as reported in Table 3.2 from measurements on Blue Waters. As usual on modern CPUs, for commonly used data-types having size 4 bytes (float, int) or 8 bytes (double, long int), the data are moved in blocks of 64 bytes (depending on the processor) from the relatively-slow random access memory (RAM) to the faster memory located on CPU ships (caches). Maintaining a high cache hit ratio in hPIC allows the accessibility of particle data during post-processing operations, with consequent efficient utilization of the memory bandwidth and improvement of the code performance during RAM intensive processes. Particles requiring special post-processing procedures are also placed in a queue during the main particle loop and then handled with dedicated functions. Examples currently implemented include: (1) crossing of periodic boundaries, (2) particle impacting on a material surface, and (3) particle reflection.

Algorithm 4 Boundary crossing algorithm of hPIC

```
1: function PARTICLE_TRACKER(particle, domain)
2:     if boundary_crossed = reflect then
3:         reflect particle
4:         if particle in domain then
5:             return no_action
6:         else
7:             return repeat
8:         end if
9:     else if boundary_crossed = absorb then
10:        return free_particle
11:    else if boundary_crossed = transmit then
12:        domain_next ← domain_next.neighbors[boundary]
13:        write particle to buffer
14:        if particle in domain_next then
15:            return free_particle
16:        else
17:            domain ← domain_next
18:            return repeat_action
19:        end if
20:    else if boundary_crossed = transmit_periodic then
21:        particle ← periodic_bc(particle, domain_global)
22:        domain_next ← domain_next.neighbors[boundary]
23:        write particle to buffer
24:        if particle in domain_next then
25:            return free_particle
26:        else
27:            domain ← domain_next
28:            return repeat_action
29:        end if
30:    end if
31:    return action
32: end function
```

3.2.4.3 Particle Tracking

A particle crossing the local domain boundaries is handled by the `particle_tracker` function. Depending on the path traversed by the particle, the function returns a set of actions that may ask to call `particle_tracker` function again, stop/delete the particle from the particle array, record an event, or not perform any action on the particle. The pseudocode of the particle post-processing functions is shown in Algorithm 4, summarizing the possible types of boundary events generated by hPIC, namely `reflect`, `absorb`, `transmit`, `transmit_periodic`. While processing the transmitting boundaries (`transmit` in the algorithm 4), particles are packed into communication buffers. Each MPI process stores a single pair of receiving and sending communication buffers per each process requiring communication. The particle buffers are sent using non-blocking message passaging, and processed as soon as they are received. The absorbing boundaries (`absorb`) are treated similarly to the `transmit` communication boundaries, with the difference that the absorbed particles are not communicated at the end of the cycle, and processed to generate information required for interfacing with PMI modules. The `absorb` buffer is flushed after a large number of particles are gathered. The example in Fig. 3.2 shows different types of boundaries, labeled "*absorb*" for absorbing boundary, "*transmit*" for communication boundary, "*transmit_periodic*" for periodic communication boundary. Each particle crossing one of those boundaries is processed by the function `particle_boundary_event` as described earlier.

3.2.5 Particle Initialization from Arbitrary Distribution Functions

In some cases, Particle-in-Cell simulations have to be initialized with arbitrary distribution function. For example, in a plasma sheath simulation the initial density can be initialized with a profile obtained from another simulation, or even from an experiment. Initializing particle distributions on a parallel computer with distributed memory is a non trivial task. hPIC achieves this task using a statistical technique called rejection sampling, which can be used to create samples from high-dimensional multi-variate distributions. In the rejec-

tion sampling method, the sample from a desired distribution (target distribution) is not sampled directly. Instead, a candidate sample is first randomly drawn from an "instrument" distribution, which can be easily sampled using standard statistical techniques (for example a uniform or normal distribution). Observations from a candidate sample are then either randomly rejected or accepted according to Algorithm 5 to satisfy target distribution function.

Algorithm 5 Rejection sampling algorithm implemented in hPIC

1: Generate $\mathbf{x}$ from `Instrument`
2: Generate u from Uniform[0, `scale` $\times$ `Instrument`($\mathbf{x}$)]
3: **while** $u >$ `Density`($\mathbf{x}$) **do**
4: Generate $\mathbf{x}$ from `Instrument`
5: Generate u from Uniform[0, `scale` $\times$ `Instrument`($\mathbf{x}$)]
6: **end while**.

In Algorithm 5, `Uniform` refers to a uniform distribution function, u is a random variable sampled from a uniform distribution. The `scale` variable is used to modify the algorithm for sampling from an arbitrary densities, that do not have to normalize to 1. The value of the `scale` can be effectively chosen as $\max\left[\texttt{Instrument}(\mathbf{x})/\texttt{Density}(\mathbf{x})\right]$ for all possible values of $\mathbf{x}$ on the simulation domain.

The efficiency of the rejection sampling is measured as a ratio of the number of accepted particles N_a and the number of candidate particles generated from an instrument distribution $\eta = N_{gen}\ \eta_{sampling} = N_a/N_{gen}$. The choice of an efficient instrument distribution is crucial to keeping the number of the rejected particles small. An example of rejection sampling for a one-dimensional case is reported in Figure 3.4. In this case, the sample was generated from a normal distribution by using the uniform distribution as an instrument. The green and red dots represent a set of accepted and rejected points respectively. The efficiency of a uniform instrument in this case is $\eta \approxeq 31\%$. The efficiency of rejection sampling can be improved by using an instrument distribution function that closely follows the target distribution. For example a step-wise uniform instrument distribution

$$f_p\left(\mathbf{x}\right) = c_R I\left(\mathbf{x} \in S_R\right), \tag{3.12}$$

where $I(\mathbf{x} \in S_R)$ is an indicator function, and c_R is the value of the distribution function f_p in the region of space S_R, achieves efficiency of 56%. Since the density functions are usually slowly varying quantities within a few grid cells, the step-wise uniform distribution is well suited for parallel execution as the simulation domain is partitioned in smaller sub-domains, and target distribution can be set a constant within a rank-local sub-domain.

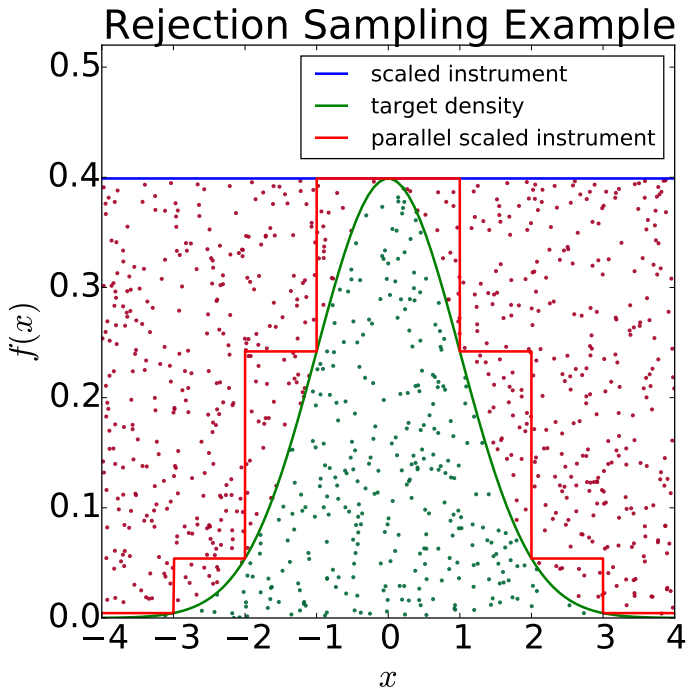

Figure 3.4: Example of the one-dimensional rejection sampling from the standard normal distribution (green lines) using uniform instrument distribution function (blue line). The dots represent samples generated from the instrument distribution. Red dots represent rejected samples, and the green dots represent accepted samples. The red line represents an example of locally-uniform instrument distribution function that is used in parallel simulation

.

Figure 3.5 reports an example of the parallel rejection sampling algorithm implemented in hPIC for two-dimensional density functions. The test was performed with 10 cores on a computational grid of 100x250 nodes. The particles were sampled from a multivariate normal distribution (Figure 3.5 right) with mean $\mu = 10^{-5} \times [7.4, 7.4]^T$ and covariance

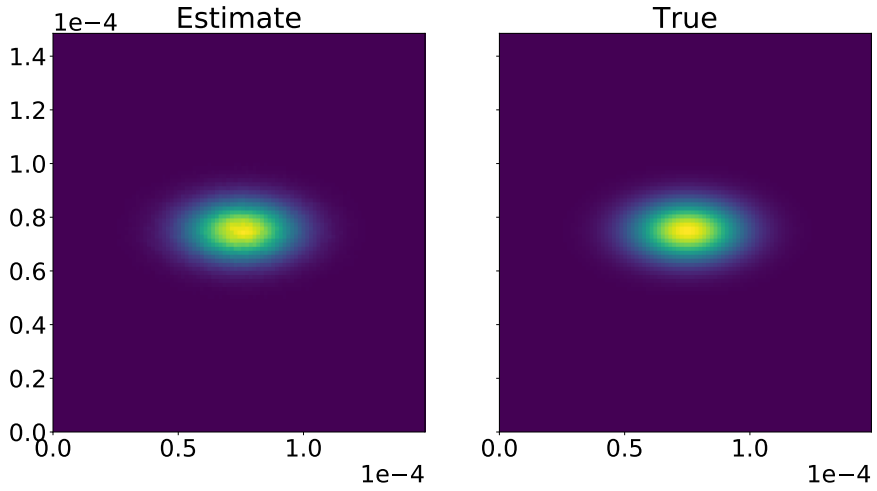

Figure 3.5: Estimated density of the particles sampled using rejection sampling method from a multivariate normal distribution $N(\mu, \Sigma)$, $\mu = 10^{-5} \times [7.4, 7.4]^T$, $\Sigma = 10^{-5} \times \text{diag}(1.6, 0.75)$. Particle density was estimated using hPIC internal particle deposition routines and reported here for comparison

matrix $\Sigma = 10^{-5} \times \text{diag}(1.6, 0.75)$ using multi-dimensional rejection sampling. An estimate of the particle density was provided by standard hPIC particle deposition function. As seen from the figure, the estimated particle density closely resembles the target distribution function. In addition, Table 3.3 shows that the difference between the sample mean and the standard deviation and their respective expected values does not exceed 1%.

Table 3.3: Comparison of the expected value of the sample mean, μ, and standard deviation, σ, in x and y dimensions

	μ_x	μ_y	σ_x	σ_y
observed	7.425e-05	7.425e-05	1.485e-05	7.425e-06
expected	7.426e-05	7.425e-05	1.489e-05	7.499e-06

3.3 Scaling Tests on the Blue Waters Supercomputer

Scaling tests of the hPIC code were performed on the Blue Waters (BW) supercomputer to characterize the weak-scaling of the code, i.e. comparing the time required to solve a given

problem on one process to the time that is required to solve a computational problem X times larger on X processes. In this section, we summarize the main measurements taken on the machine.

All the timings and efficiencies are measured with respect to single-node performance, rather than a single computing process. Each BW node is equipped with dual AMD 6276 Interlagos processors chip which include 8 Bulldozer cores each, and two Integer Scheduling Units (ISU) per Buldozer cores. Thus, a total of 32 processes can be executed on a single BW node. Referencing the measurements with respect to a single computing process could be misleading, because the execution of the code on a single node does not involve any network communication, which results instead every time a node-to-node communication is invoked, and also because the inter-node bandwidth is much slower than the in-node communication. In addition to that during in-node execution the parallel processes share a significant amount of RAM and caches on ISUs. Hence, it is expected to observe some decline from perfect scaling when more than one compute node is used. A more consistent comparison would be better done with N larger than 1, even if the decision of which N should be used would be arbitrary. Since there is no consensus on the best practice to adopt, we will adopt a conservative approach and refer the measurements to single-node performance.

For weak scaling purposes hPIC has been tested for test cases of Maxwellian plasmas (Sec. 3.3.3) on square or rectangular simulation domains. Even if the tests with Maxwellian plasmas do not show the scaling of hPIC when applied to the particular physical problem of the plasma sheath, nevertheless they allow a more general evaluation of the code performance. In addition, the specific plasma problem for which hPIC will be mostly used, i.e. plasma sheath simulations, resembles to some degree a Maxwellian problem, or better a drifting Maxwellian problem [66], on a significant portion of the simulation domain (pre-sheath, some parts of the sheath and bulk plasma).

The tests were performed such as to characterize all the critical parameters affecting scaling: edge of the local sub-domain k (within in each rank), particle Courant number C_T, number of particle per cell `ppc`, and grid spacing Δx (affecting the sampling of the Debye

sphere). As an important remark, which allowed a meaningful comparison among all tests, we have kept the plasma temperature and plasma density equal for all tests (controlled through the physical-to-computational ratio of the particles, `p2c`), in order to maintain the average electrostatic force equal across all tests.

In the following sections, first we give the basic definitions adopted for quantifying the scaling of the code. Then, Section 3.3.4 reports the scaling of the particle push functions, while Sec. 3.3.6 presents the scaling of the full PIC cycle including the field solver. Data on the weak scaling specific to the Poisson solver are reported in Sec. 3.3.5.

3.3.1 Definitions of timing used for the scaling

The execution time of a parallel code is given by the sum of the time spent on computation, and the time spent for communication or synchronization between the processes. For PIC methods, the total computational time is given by the sum of the time required to perform two types of actions: particle actions (particle moving, interpolation of fields at the particle location, weighting of particle properties on mesh nodes), and field actions (either solving the Maxwell equations or a subset of them, like the Poisson equation in the case of an electrostatic PIC). Similarly, for hPIC the total computational time is given by the number of seconds required for particle-related operations and field-related operations,

$$t_{\mathrm{PIC}} = T_{\mathrm{ptcl}} + t_{\mathrm{Poisson}}. \tag{3.13}$$

Deposition and interpolation are related to the discrete representation of the distribution function, and hence fall under the first category of particle actions. In hPIC all particle operations (interpolation, moving, weighting) are aggregated in a single optimized algorithm, so that the access to the particle array is performed only once. Such implementation benefits the simulation on supercomputers, when several billions of particles are used, and it also reduces the data passage between CPU caches and random-access memory (RAM) to a single one.

When used in sequential mode (single process), the computational time taken by particle

advance function $T_{\text{ptcl},1}$ to advance N particles on 1 process is given by the product of the total number of computational particles N and the cost associated with moving a single particle t_{ptcl},

$$T_{\text{ptcl},1} = N \cdot t_{\text{ptcl}} \tag{3.14}$$

In parallel (MPI) simulations, the execution time is also affected by the time spent on communications between the processes and increased usage of the memory bandwidth of the of machine. The latter can increase the value of t_{ptcl}, but in first approximation the memory bandwidth can be neglected. Thus, for a simulation with k MPI processes and even distribution of the particles between processes, the ideal computational time of the particle advance is given by (where P is the total number of computing nodes):

$$T_{\text{ptcl,P}} = \frac{N}{P} t_{\text{ptcl}} + t_{\text{comm}}. \tag{3.15}$$

The time spent on communication of particle data t_{comm} strongly depends on the parallelization scheme and algorithms used. We describe the parallelization scheme in Sec. 3.3.2. Here we remark that the simplification adopted in Eq. 3.13 of separating the computational time spent for the particle actions and the time spent for the field solve still holds in our case; in fact, even though the particle pusher does not have MPI blocks, all of the processes are synchronized at the step of the Poisson solver, where the PETSc implementation of the CG and Multigrid includes MPI blocks.

Finally, we define computational efficiency on P compute nodes as:

$$\text{efficiency}_P = T_1/T_P, \tag{3.16}$$

where T_1 is the wall-clock time that is required to execute hPIC on a single compute node, and T_P is the wall-clock time required to solve a problem P times larger on P compute nodes.

3.3.2 Memory size of the passed messages and communication time

A general approach followed during the development of hPIC was the reduction of the amount of FLOPS that each rank has to perform along with the communication time. According to Hockney's model [67] [68], the communication time between MPI processes could be modeled as $t_{\text{comm}} = t_l + M \times R_{bw}$, where t_l is the latency of the communication network (time required to establish a connection between MPI ranks), M is the size of a passed message (bytes), and R_{bw} is the reciprocal of the bandwidth of the network (sec/bytes). Despite its simplicity, Hockey's model of communication still provides a reasonable estimate of the communication time [69], and can be used for performance analyses of the code. Since latency and bandwidth of an interconnect depend solely on the topology of the computational machine and its hardware, the only available way to decrease communication time (for a given computing machine) is to reduce the message size M.

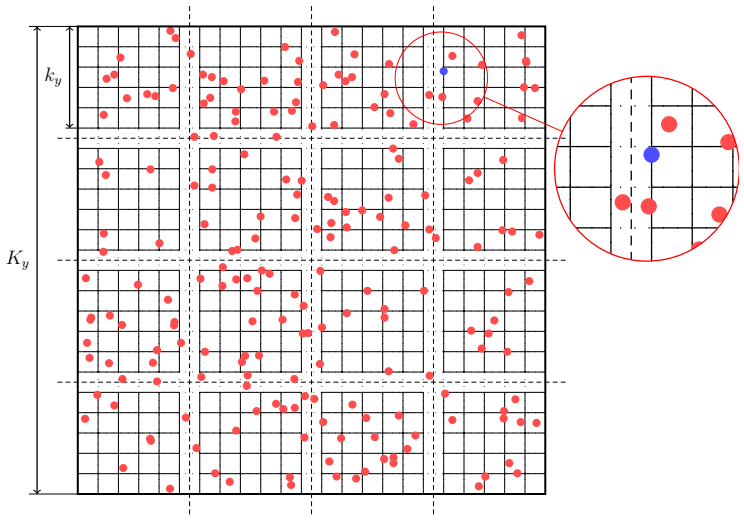

Figure 3.6: Uniform partitioning of the global grid with $K_x \times K_y$ grid cells on 16 MPI processes. The red dots represent particles distributed with uniform random distribution on the domain

In a particle-in-cell simulation with uniform domain partition, the average size M of the passed message depends on the physics of the simulation, which dictates how many

particles are crossing a given domain partition, and on the amount of information required to describe each particle. Figure 3.6 shows one example, with a square domain partitioned into squares of equal size. In the figure, the particles are represented by dots randomly distributed inside the domain. The edge between partitions is defined at the cell centers. Once a particle crosses the edge, it has to be passed to the adjacent rank, contributing to the amount of memory M that need to be passed. For the case represented in the figure, the average size M of the message results equal to:

$$M = k \left[\frac{\sqrt{8}\,\texttt{ppc} \cdot V_T \cdot \Delta t}{\sqrt{\pi}\Delta x} \cdot \texttt{ptcl\_size} + 4 \cdot N_f \cdot \texttt{float} \right] \tag{3.17}$$

$$t_{\text{comm}} = t_l + R_{bw} \times M \tag{3.18}$$

where $k = k_x = k_y$ is the number of grid cells along one side of the local portion of the domain, k^2 is the number of grid cells stored on each of the P processes, `ppc` is the average number of particles per cell, $V_T = \sqrt{k_B T/m_s}$ is the thermal velocity of the particles of species s, Δt is the time step, `ptcl_size` is the memory required to store a single PIC particle, L_x and $\Delta x = L_x/K_x$ are physical size of the domain and cell size respectively, N_f is the number of scalar fields communicated, and `float` is the size required to store a floating point number.

In a more general situation, for n-D PIC simulations the message size M scales as $O\left(1/P^d\right)$, where d is the number of the physical dimensions of the grid. Then the communication required at each iteration of the code is defined by the number of particles leaving their local domain and moving towards adjacent domains, plus the communication of the grid ghost nodes for scalar or tensor fields (for example, scalar potential, moments of the particle distribution, etc).

3.3.3 Test Setup with Maxwellian plasmas

For a Maxwellian plasma with electron temperature T_e [eV], electron density n_e, and a given number of particles per cell `ppc`, each Particle-in-Cell simulation is set up using the

following parameters. The grid spacing is defined as a fraction α of the Debye length λ_D,

$$\Delta x = \alpha \lambda_D = \alpha \sqrt{\frac{T_e \varepsilon_0}{e n_e}} \tag{3.19}$$

with typical values ranging from $\alpha = 1/20$ to $\alpha = 1/10$. This ensures a proper sampling of the Debye length also at locations near to the wall and inside the Debye sheath and the magnetic presheath, where the electric field gradients are large. Then computational-to-physical ratio `p2c` is determined based on the desired density (an input parameter) and the number of physical particles per cell:

$$\texttt{p2c} = \frac{n_i \times \Delta x^2}{\texttt{ppc}} = \frac{n_i T_e \varepsilon_0}{e n_e} \cdot \frac{\alpha^2}{\texttt{ppc}} \propto \frac{\alpha^2 T_e}{\texttt{ppc}}, \tag{3.20}$$

where T_e is expressed in eV. Finally, the time step is chosen to keep the relative particle velocity U small compared to local grid size $U\Delta t \lesssim 1$:

$$U = V_T/\Delta x = \sqrt{\frac{eT_e}{m_e} \frac{en_e}{\alpha^2 T_e \varepsilon_0}} = \sqrt{\frac{n_e e^2}{m_e \varepsilon_0 \alpha^2}} \propto \sqrt{n_e/\alpha^2} \tag{3.21}$$

or

$$\Delta t \quad \lesssim \quad \sqrt{\frac{m_e \varepsilon_0 \alpha^2}{n_e e^2}} = \frac{\alpha T_p}{2\pi} \tag{3.22}$$

so that on average a thermal particle does not cross more than one cell within one time step. Since the factor $\alpha/2\pi \ll 1$, the condition (3.22) also ensures that time step resolves the period of plasma oscillations T_p.

3.3.4 Scaling of the Particle Push Functions

The tests on weak scaling of the particle pusher were parametrized using the Courant number C_T of a thermal particle, $C_T = \Delta t V_T/\Delta x$ (thermal Courant number), where $V_T = \sqrt{k_B T/m}$. In one dimension a particle from a thermal distribution crosses on average $\sqrt{2/\pi}\, C_T$ cells per time step. And for a particle population with a uniform density

n in a local grid of size m^2 and length l^2, the fraction particles communicated per single dimension results equal to:

$$\begin{aligned} f &= \int_0^l \mathbf{d}x \frac{1}{L} \int_x^\infty \mathbf{d}x_t \sqrt{\frac{2}{\pi X_t^2}} \exp\left(-\frac{x_t^2}{2X_t^2}\right) \\ &= \int_0^{L_g^l} \mathbf{d}x \frac{1}{2L} \left[1 - \mathrm{erf}\left(\frac{x}{\sqrt{2}X_t}\right)\right] \\ &= \frac{1}{2} - \frac{1}{2L}\left[\sqrt{\frac{2}{\pi}} X_t \left(e^{-L_g^{l\,2}/X_t^2} - 1\right) + L_g^l \,\mathrm{erf}\left(\frac{L_g^l}{\sqrt{2}X_t}\right)\right], \end{aligned} \tag{3.23}$$

where $X_t = V_T \Delta t$ is the displacement of a thermal particle per time step. In most of the practical cases the number of cells in each local grid is significantly larger than the number of cells crossed by a particle with thermal velocity during one time step, and therefore the argument of the error function $L_g^l/\sqrt{2}X_t = m\Delta x/\sqrt{2}X_t$ is much larger than 1, so that the error function factor in Eq. 3.23 tends to one. Thus the flux of the particles communicated through a single sub-domain boundary equals

$$\begin{aligned} f &\approx \sqrt{\frac{1}{2\pi}} \frac{X_t}{L_g^l} \left(1 - e^{-L_g^{l\,2}/X_t^2}\right) \\ &\approx \sqrt{\frac{1}{2\pi}} \frac{X_t}{L_g^l} = \sqrt{\frac{k_B T}{2m\pi}} \frac{\Delta t}{m\Delta x}. \end{aligned} \tag{3.24}$$

As a consequence, for a fixed value of m, the value of the thermal Courant number C_T is directly proportional to the number of communicated particles by every MPI process, and to the size of the communicated message.

The weak scaling tests of the particle advance function were performed at four different values of the thermal Courant number, $C_T = \Delta t V_T/\Delta x = 0$, 0.05, 0.5 and 5. For a typical fully-kinetic simulation of an electron-ion plasma, $C_T = \Delta t V_T/\Delta x = 0.05 \ldots 0.5$ would represent the ion species and $C_T = \Delta t V_T/\Delta x = 5$ would represent electron species. The results are reported in Figs. 3.7(a) and 3.7(b) for up to 2,048 Blue Waters nodes (each node has 32 cores), showing respectively the efficiency with respect to single-node, and the wall-clock time in seconds. Here we recall that according to our new particle-push algorithm, the particle advance function includes not only the particle push, but also the weighting and

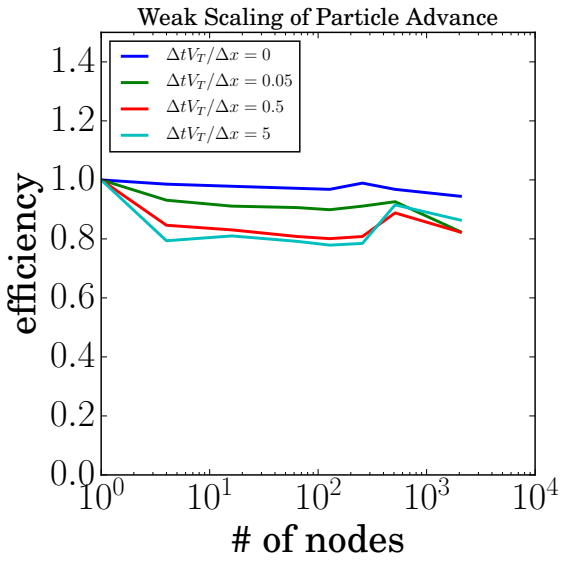

(a) Weak scaling of particle advance function

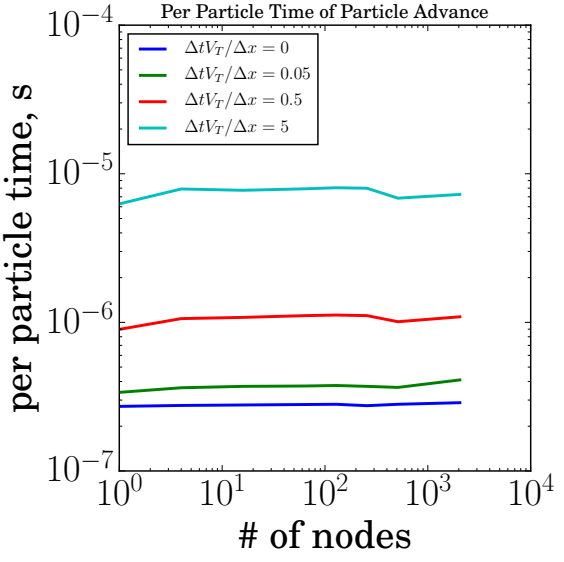

(b) Per particle time

Figure 3.7: Scaling and timing of the particle push for hPIC, $k = 100$

the interpolation steps, plus the deposition of the fluid moments and the communication of the particle and ghost node values. The efficiency of the particle advance function drops off only 5% for $C_T = \Delta t X_t/\Delta x = 0.05$, and 20% for $C_T = \Delta t X_t/\Delta x = 5$ when more than one computational node is used, however no further reduction of efficiency is observed when the number of computational nodes used is increased. The decrease in efficiency related to the extreme case $C_T = 5$, and the consequent timing increase reported in Fig. 3.7(b), is mainly due to the increased cost of particle communication rather than actual floating point operations. In fact, when the thermal Courant number is as high as $C_T = 5$, most of the particles transverse multiple cells in a single time step, hence increasing the particle communication cost. The efficiency plot demonstrates an anomaly at 512 nodes, which is considered to be related either to an inhomogeneity of the allocated nodes used for the test, or to a local peak in performance due to the (toroidal) topological connectivity of Blue Waters.

3.3.5 Scaling of the Poisson solver

Given the elliptic nature of the Poisson problem, a scalable implementation of the electrostatic solver is an issue by itself. The hPIC code uses a finite-difference discretization of the Poisson problem (Sec. 3.3.5), whose parallel implementation is based on the PETSc parallel library. The results of our weak scaling tests of the Poisson solver of hPIC on Blue Waters have been reported in Table 3.4 and Figs. 3.8(a)-3.8(b). The best performance was obtained by combining PETSc' Conjugate Gradient solver with Hypre BoomerAMG Algebraic Multi-Grid preconditioner [60, 61, 62]. The table reports the wall clock timing between 2 and 2,048 Blue Waters nodes, and for edges of the local grid between $k^2 = 50^2$ and 500^2 cells per core (cells/core). The largest problem solved during the weak-scaling tests corresponds to the solution of a Poisson problem on a two-dimensional grid with a total number of cells $500^2 \times 2048 \times 32 = 16,384,000,000$.

Two strategies could be devised to achieve good scaling of the code: either (1) simulate a very large domain (for example 500×500) on each MPI process with a low particle count per cell (50 `ppc`), or (2) keep small domains on each MPI process and use large number of

particles per cell. The second approach is of course preferred because it allows to increase the statistical accuracy of the results, but it is limited by the amount of particles each computing node has to store in memory. All tests here reported have been done using double precision for the local coordinates $\mathbf{w}$ of a particle within a cell; when used on the XE6 nodes of Blue Waters (64 GB of RAM per node), it allows to store up to $\sim$ 250M particles per computing node. With a small local grid of 50×50 on each MPI process hPIC is capable of achieving up to 3000 particles per cell, that is enough for achieving a satisfactory level of statistical noise. When used as in the first approach with a larger grid (e.g. 400×400 cells/core) the code can use only up to 50 particles per cell, with a consequent deterioration of particle noise. As a rule of thumb, the desired number of particles per cell should be at least 100 or preferably higher (500-600 particles per cell).

Figure 3.9 and Table 3.5 report the results of our strong scaling tests (problem of fixed size solved on an increasing number of processes) of hPIC's Poisson solver on Blue Waters. The problem was a 2D Poisson equation with a global domain sampled with $K \times K$ points, and corresponding Laplacian matrix of size $(K \times K)^2 = K^4$. Since most of the values of the Laplacian matrix are zeros it is stored in a sparse format and occupies the amount of memory on the scale of $O(K^2)$ bytes. The tests were performed from 4 to 8,192 nodes ($8,192 \times 32 = 262,144$ cores). The values reported in the figure and the table are the average time in seconds required for the solution of the Poisson problem by means of PETSc conjugate gradient solver with BoomerAMG preconditioner. The characteristic trend of strong-scaling can be recognized from the plots. At the largest scale of 8,192 nodes, the time to solution for the two allocatable cases of K=16k, 32k was around $\sim$1.6 seconds. A particular mention goes to the largest problem solved of K = 100k, solved respectively on 256, 512, and 2,048 Blue Water nodes. The solution of such a large problem required to switch PETSc indexing from the usual signed 32-bit integers to 64-bit, and more specifically to 8-bytes signed Long Integers having an integer limit of `_I64_MAX`$= 9,223,372,036,854,775,807 \approx 9.22 \times 10^{18}$. For the corresponding problem with $K = 10^5$, the grid size and Laplacian matrix have $K^2 = 10^{10}$ grid cell and $K^4 = 10^{20}$ elements correspondingly. The indices of the Laplacian matrix are running from 0 to $10^{10} - 1$, which can be allocated only using 64-bit unsigned

long integers. Such a problem was solved in 13.4, 6.8, and 2.1 seconds respectively on 256, 512, and 2,048 Blue Water nodes.

Table 3.4: Timing (in seconds) of Conjugate Gradient Poisson solver with BoomerAMG preconditioner as measured on Blue Waters (BW)

BW nodes	BW cores	Local grid size, k^2 (grid cells/core)					
		50^2	100^2	200^2	300^2	400^2	500^2
2	64	0.028	0.051	0.240	0.606	1.130	1.810
8	256	0.029	0.063	0.305	0.740	1.370	2.180
32	1024	0.038	0.074	0.309	0.761	1.400	2.230
128	4096	0.057	0.091	0.336	0.779	1.660	2.620
512	16384	0.105	0.145	0.450	0.959	1.730	2.680
2048	65536	0.268	0.313	0.613	1.180	2.150	2.860
$t_{2048} - t_2$		0.240	0.261	0.373	0.578	1.020	1.047
t_2/t_{512}		0.266	0.354	0.534	0.632	0.653	0.676
t_2/t_{2048}		0.104	0.164	0.392	0.512	0.525	0.634

Table 3.5: Strong scaling test of PETSc conjugate gradient solver for a 2D Poisson problem of size K^4 and grid size K^2. The values reported in the table are the average time (in seconds) required for the solution of the Poisson problem.

nodes	$K = 4096$	$K = 8192$	$K = 16000$	$K = 32000$	$K = 64000$	$K = 100000$
4	0.76	3.12	-	-	-	-
8	0.50	1.99	7.66	-	-	-
16	0.26	1.19	4.57	-	-	-
32	0.17	0.69	2.52	9.97	-	-
64	0.10	0.37	1.34	5.28	-	-
100	0.09	0.25	0.90	3.49	13.70	-
128	0.07	0.19	0.74	2.75	10.70	-
256	0.14	0.14	0.47	1.58	5.53	13.40
512	0.09	0.14	0.26	0.87	2.95	6.80
2048	-	-	0.60	0.71	1.27	2.11
8192	-	-	1.64	1.69	-	-

3.3.6 Scaling of the full PIC cycle

The weak-scaling of the full PIC cycle of hPIC was tested for the following simulation parameters: $m_i = 1$ amu (Hydrogen), number of particles per cell 300, 400, 500, and 600, plasma density $n_e = 10^{17}$ m^3, $T_e = T_i = 1.0$ eV, grid size $4.71 \ldots 5.88$ μm (3-5 grid point per Debye length), `p2c`=5524, size of the local domain $m = 100$, time step $\Delta t = 7 \times 10^{-12}$ s.

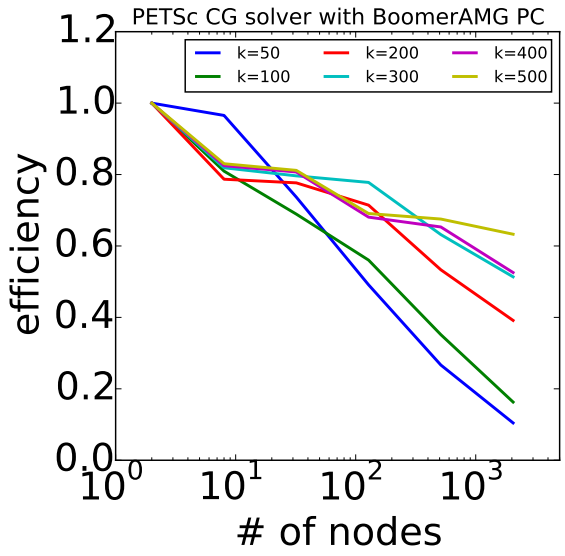

(a) Efficiency

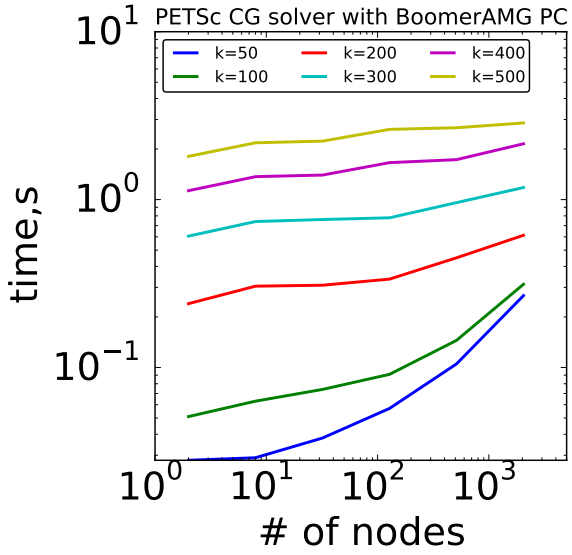

(b) Timing

Figure 3.8: Efficiency with respect to one node and timing of the PETSc conjugate gradient solver with BoomerAMG preconditioner on BlueWaters supercomputer

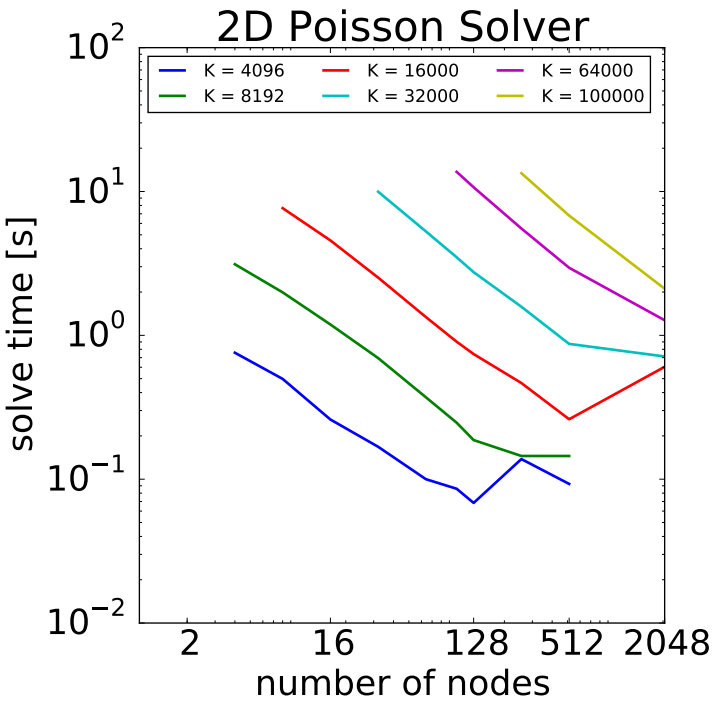

Figure 3.9: Strong scaling of the conjugate gradient solver with BoomerAMG preconditioner on the BlueWaters supercomputer, for simulation domains of size $K \times K$ and the problem size K^4.

Under these conditions each MPI process is simulating a 2D plasma of 0.47 mm $\times$ 0.47 mm. The largest case of 2,048 Blue Waters nodes simulates a plasma domain of size 12 cm $\times$ 12 cm.

The results are reported in Fig. 3.10, showing the efficiency with respect to single-node performance and the wall-clock time per PIC cycle. Values are averaged over 20 PIC time steps. The weak-scaling efficiency is slowly decreasing with the node count, but still remains always in the range $\sim 78-88\%$ even for the largest simulations (2,048 nodes, or 65,536 cores). Higher values of efficiency are obtained when a larger number of the particle per grid cell are used; observed values at 2,048 nodes are: $78\%, 85\%, 87\%, 88\%$ for $\texttt{ppc} = 300, 400, 500, 600$. The trend of the efficiency curves does not exhibit the anomaly at 512 nodes observed in the particle advance tests. The execution time was for all tests dominated by the particle pusher, thus guaranteeing good scaling and good efficiency despite the intrinsic limitations of the Poisson solver.

Table 3.6: Weak scaling test of hPIC for plasma density $n_e = 10^{17}$ m^{-3}, and temperature $T_e = T_i = 1$eV, where ppc: number of particles per cell, p2c: physical/computational particle ratio.

dt, s	ppc	Δx, m	p2c	$m = m_x = m_y$	Particle per BW node
7.04e-12	300	5.88e-06	11508	100	9.60×10^7
7.04e-12	400	4.71e-06	5524	100	1.28×10^8
7.04e-12	500	4.71e-06	4419	100	1.60×10^8
7.04e-12	600	4.71e-06	3682	100	1.92×10^8

3.4 Verification

When performing the verification of a Particle-in-Cell code, it is of great importance to test each individual component of the code against analytical results, like known solutions of the field equations in simplified cases, or particle trajectories for assigned fields. Such simple tests verifying a single portion of the code are called *unit tests*. During the development of the code, it is also of great importance performing the so called *integration tests*, in which two or more components of the code interact together (e.g. particles and fields) and concur to the result of the simulation. In an integration test, a known physical phenomenon involving

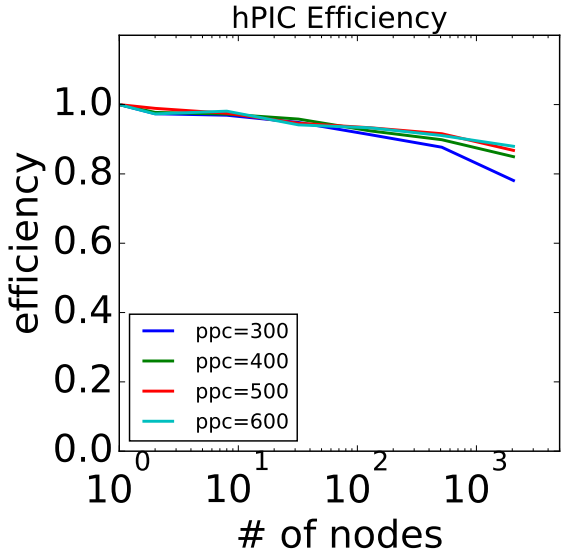

(a) Weak scaling of hPIC main cycle

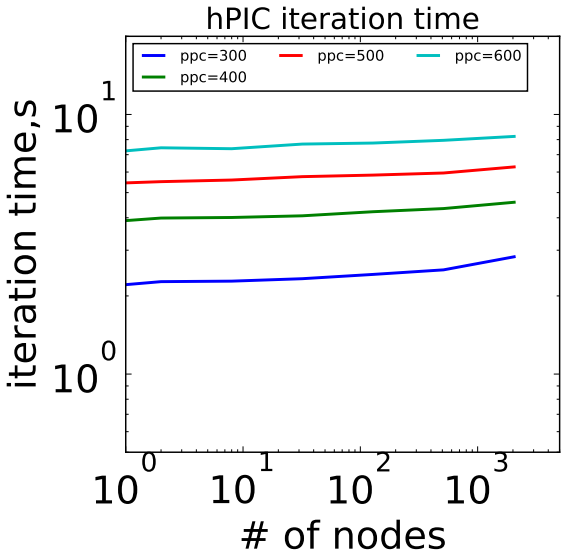

(b) Per particle time

Figure 3.10: Efficiency and iteration time of electroscatic version of the full PIC cycle of hPIC, for Hydrogen plasma with $T_i = T_e = 1$ eV, $n_e = 1e17$. In this test each rank stores 100x100 grid points, and each grid cell contains ppc number of particles per cell

the interaction among particles and fields is simulated, and the results are compared to the expected theoretical values.

In this section we report the verification tests performed during the development of the hPIC code. Sections 3.4.1, 3.4.2 and 3.4.3 describe the unit tests performed to verify single particle motion and both linear and nonlinear Poisson solvers respectively. Integration tests were performed on two classical tests for kinetic plasma codes: (1) Landau damping and (2) two-stream instability. The results of Landau damping and two-stream instability tests are reported in sections 3.4.4 and 3.4.5.

3.4.1 Verification tests of Particle Motion in hPIC

The trajectories of charged particles in magnetized plasma are governed by the Newton-Lorentz equation

$$m\frac{d\mathbf{v}}{dt} = q\left(\mathbf{E} + \mathbf{v} \times \mathbf{B}\right), \tag{3.25}$$

which can be solved analytically when the fields have a simple analytical representation and for given initial condition. Assuming that the magnetic field is zero and the electric field varies proportionally to a function $f(t)$

$$\mathbf{E(t)} = [E_x^*, E_y^*, E_z^*]^T f(t), \tag{3.26}$$

where E_x^*, E_y^*, E_z^* are the scaling constants for x, y and z components of the electric field, the coordinate of a single particle at time t can be found by integrating Eq. (3.25) over time twice (represented by variables u and s)

$$\begin{aligned} \mathbf{x}(t) &= \mathbf{x_0} + \mathbf{v_0}t + \int_0^t \mathbf{d}s \int_0^s \mathbf{d}u \frac{d\mathbf{v}}{dt} \\ &= \mathbf{x_0} + \mathbf{v_0}t + [E_x^*, E_y^*, E_z^*]^T \frac{q}{m} \int_0^t \mathbf{d}s \int_0^s \mathbf{d}u f(u), \end{aligned} \tag{3.27}$$

where $\mathbf{x_0}$ and $\mathbf{v_0}$ are the particle location and velocity at initial time step $t = 0$. The values of the integral

$$I_s = \int_0^t \mathbf{d}s \int_0^s \mathbf{d}u f(u) \tag{3.28}$$

can be found analytically when the function f has a quadrature that can be expressed analytically. Table 3.7 summarizes the value of this integral for a few simple cases when f is constant, linearly increasing, linearly decreasing, and quadratically decreasing in time.

Table 3.7: Analytical solution of the integral for selected $f(t)$ (3.28)

$f(t)$	$\int_0^t \mathbf{d}s \int_0^s \mathbf{d}u f(u)$
$1/(1+t)^2$	$\log(1+t)$
$1/(1+t)$	$(1+x)\log(1+t) - x$
t	$t^3/6$
1	$t^2/2$

Using Eq. (3.27), analytical values of particle coordinates are compared to the respective values calculated numerically according to Boris push equations (3.2-3.3). Table 3.8 summarizes the comparison results of the numerical solution and analytical solution for the four cases of 3.7. The unit test is executed for a particle of mass $m = 2$, electric charge $q = 1$, time step $dt = 10^{-1}$, virtual grid with $dx = 3$, integrated for 100 iterations. With constant electric field $f(t) = 1$ the numerical values of the final particle location are matching exactly with the analytical solution. With increasing electric field $f(t) = t$, the final location of the particle is underestimated by 0.01%, and with decreasing electric field the location of the particle is overestimated by 0.06% and 0.23% for $f(t) = 1/(1+t)$ and $f(t) = 1/(1+t)^2$ respectively. The difference between numerical and analytical solution is caused by assumption made in Boris push algorithm: leapfrog equations (3.3- 3.2) assume that electric field is constant during particle update. However, the electric field is continuously changing, and electric field is always smaller during a single time-step in the time-increasing and larger in the time-decreasing electric fields. Boris leap-frog is a well established integration scheme, and particle push tests were performed in order to verify the validity of our implementation.

As a second unit test, the code checks for the consistency of the Larmor gyration in a uniform magnetic field constant in time in absence of electric fields. The radius of gyration

Table 3.8: Example of comparison of numerical and analytical solution of the particle Newton-Lorentz equation (3.25) using Boris leapfrog (3.3- 3.2) and analytical solution (3.7). In the test case $\mathbf{x}_0 = \mathbf{v}_0 = [0,0,0]^T$ and $\alpha = [10,5,3]^T$

$f(t)$	α			αt		
value	x	y	z	x	y	z
numerical	250.0	125.0	75.00	833.2	416.6	250.0
analytical	250.0	125.0	75.00	833.3	416.7	250.0
difference, %	0.00	0.00	0.00	0.01	0.01	0.01
$f(t)$	$\alpha/(1+t)$			$\alpha/(1+t)^2$		
value	x	y	z	x	y	z
numerical	81.93	40.96	24.58	38.10	19.05	11.43
analytical	81.88	40.94	24.57	38.01	19.01	11.40
difference, %	-0.06	-0.06	-0.06	-0.23	-0.23	-0.23

(Larmor radius) of a particle of mass m and charge q is as usual $r_L = \frac{mv_\perp}{|q|B}$ where B is the strength of the magnetic field, and $v_\perp$ is the particle velocity perpendicular to the magnetic field. The magnetic field is set to a constant value along the y axis, $B = (0, B, 0)$ and the particle is initialized at the coordinate $r = (r_L, 0, 0)$. The test is repeated with the magnetic field aligned along other directions to check for the consistency of the rotation step of the Lorentz integrator. hPIC is routinely tested against three directions of the magnetic field and initial particle velocity. The parameters of those tests are reported in the Table 3.9. In each of the three test cases the simulation is initialized for a single particle with mass $m = 2$, electric charge $q = 1$, the time step was chosen as a fixed fraction of gyro-period $dt = 0.01 \times 2\pi qB/m$, and the simulation is executed for 100,000 iterations (1000 gyro-periods). Numerical estimates of the Larmor radius at the end of the integration match the theoretical value of the Larmor radius up to 4 significant digits (see table 3.9). Figures

Table 3.9: Comparison of the numerically estimates and theorical values of the Larmour radius for three test case initialized with particles with mass $m = 2$ and charge $q = 1$ for various magnetic fields $\mathbf{B_0}$ and initial velocities $\mathbf{V_0}$

	Test 1	Test 2	Test 3
Magnetic field $\mathbf{B}$, T	$[100,0,0]^T$	$[0,100,0]^T$	$[0,0,10^{-1}]^T$
Initial velocity $\mathbf{V_0}$, m/s	$[0,10^{-2},0]^T$	$[0,0,100]^T$	$[100,0,0]^T$
Numerical estimate fo Larmor radius r_L, m	2.000×10^{-4}	2.000	2.000×10^{3}
Theoretical value of Larmor radius r_L, m	2.000×10^{-4}	2.000	2.000×10^{3}

3.11(a), 3.11(b), 3.11(c) report few examples of trajectories produced during the three test

cases. As expected, the particle trajectories are circles. Since the Boris algorithm is energy conserving at the second order, it is expected for particles to preserve their kinetic energy in the gyration test cases. Figure 3.11(d) reports the evolution of the particle kinetic energy for all three cases. The resulting standard deviation of the kinetic energy fluctuations is equal to $4.287 \times 10^{-3}\%$, as expected from the second order accuracy of the scheme.

3.4.2 Verification of the Linear Poisson Solver

3.4.2.1 Verification with Analytical Solution

The hPIC code solves the full Poisson equation (2.18) by means of finite-difference methods (2.54). Unit tests are run for simple assigned charge density distributions having analytical solutions, in order to verify the accuracy of the numerical solver and the consistency of the implementation. For a one-dimensional Poisson problem,

$$\frac{\partial^2 \phi}{\partial x^2} = \rho_0 \tag{3.29}$$

the solution has a simple polynomial form

$$\phi = \frac{\rho_0 x^2}{2} + c_1 x + c2, \tag{3.30}$$

where the constants $c_1 = -\rho_0 L/2$ and $c_2 = 0$ are determined by the boundary conditions (3.31). With Dirichlet boundary conditions on both ends of the simulation domain of length L

$$\phi(0) = \phi(L) = 0, \tag{3.31}$$

the solution becomes

$$\phi = \frac{\rho_0 x}{2} (x - L). \tag{3.32}$$

The one dimensional solution of Eq. (3.32) is still applicable in 2D domains when the charge is assumed uniform along one of the two dimensions and periodic boundary conditions are applied. Then each one-dimensional of the two-dimensional slice is identical to each and is

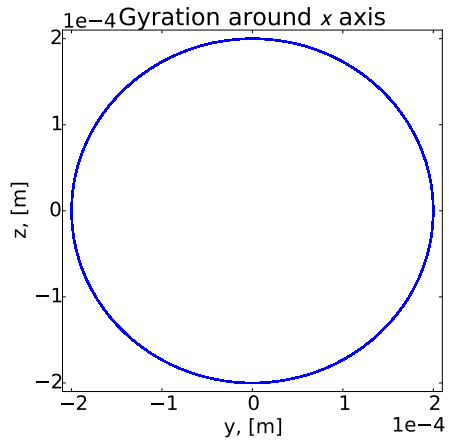

(a) Test case 1 (gyration around x-axis)

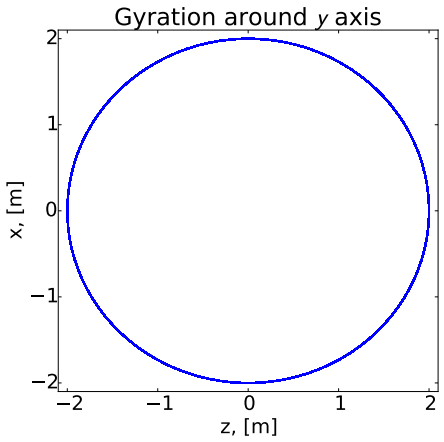

(b) Test case 2 (gyration around y-axis)

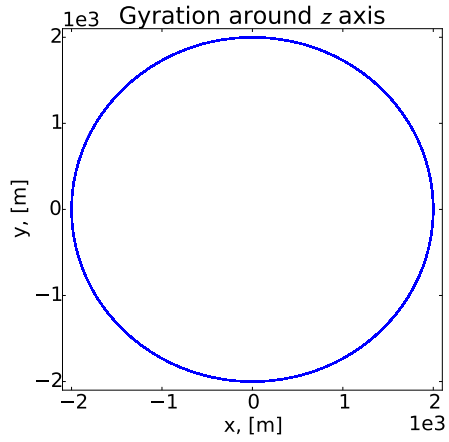

(c) Test case 3 (gyration around z-axis)

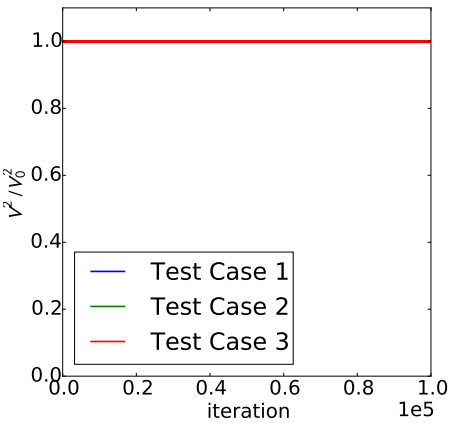

(d) Energy Conservation

Figure 3.11: Trajectoies and energy conservation of a charged particle with $q = 2$ in the constant magnetic field B with initial velocity v_0. Particle state vector is updated with the Boris index-based based leapfrog (equations (3.3- 3.2)). All curves overlap on figure (d), which implies exact energy conservation.

governed by equation (3.32).

Such comparison is routinely performed in hPIC, and Figure 3.12 demonstrates two cases of comparison between the numerical two-dimensional solution of the Poisson equation with the analytical solution given by equation 3.32. In the first case the simulation domain has periodic boundary conditions along the x direction. The second test case is a reversal of the first one: Dirichlet boundary conditions are set at $x = 0$ and $x = L_x$, and y direction has periodic boundary conditions. In both test cases the charge density was set to $\rho_0 = 10^{-5}$, and numerical solution was obtained on the rectangular domain of the size 400 m $\times$ 300 m with grid spacing $dx = 1$ m (see Figures 3.12(a) and 3.12(c)). One dimensional slices the two dimensional solutions for first test case (see Figures 3.12(a) and second test case 3.12(c)) are plotted against the corresponding analytical solutions (Figures 3.12(b) and 3.12(d))). In both test cases the maximum value of the residual (difference between analytical and numerical solutions) for the electric potential did not exceed 6×10^{-7} V or $5 \times 10^{4}\%$.

3.4.2.2 Benchmark with Fourier Solver for Periodic Boundary Conditions

The analytical solution described in Section 3.4.2.1 provides a convenient and computationally inexpensive way to verify the Poisson solver in simplified cases. However, realistic charge densities are usually not smooth and in general they can be arbitrary. In this cases, two different Poisson solvers implementing different numerical methods can be used to verify the solution (*benchmark*). For simulation domains with periodic boundary conditions, the Poisson problem can be conveniently solved using Fourier transform method. Defining Fourier transformations of the left-hand-side ϕ and right-hand-side ρ of the equation (3.29) as

$$\hat{\phi}(k,j) = \frac{1}{2\pi}\int \mathbf{d}x \int \mathbf{d}y \phi(x,y) \exp\left[-ikx - ijy\right] \tag{3.33}$$

$$\hat{\rho}(k,j) = \frac{1}{2\pi}\int \mathbf{d}x \int \mathbf{d}y \rho(x,y) \exp\left[-ikx - ijy\right], \tag{3.34}$$

where k and j are the wavenumber along the x and y directions respectively, and hatted values denote Fourier transformed quantities. Then, Fourier transformation of the Poisson

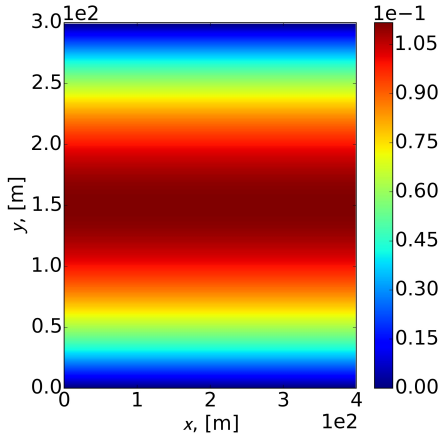

(a) Two-dimensional (2D) numerical solution with periodic boundary conditions in x direction

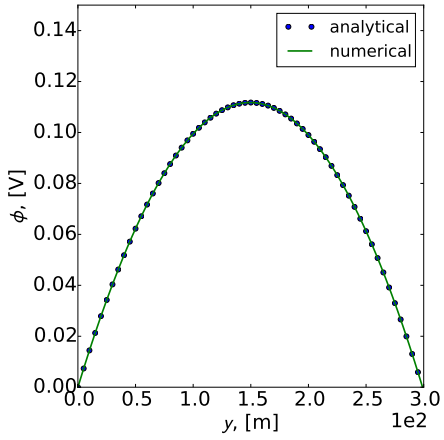

(b) One-dimensional slice of the 2D numerical solution with periodic boundary conditions alogn x axis

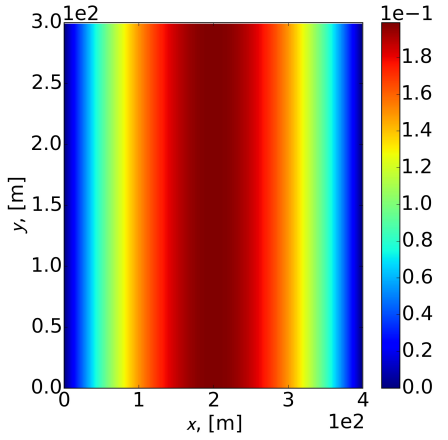

(c) Two-dimensional (2D) numerical solution with periodic boundary conditions in y direction

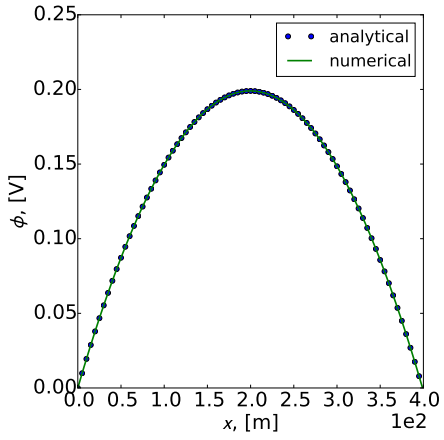

(d) One-dimensional slice of the 2D numerical solution with periodic boundary along in y axis

Figure 3.12: Comparison of quasi two-dimensional numerical solution of the Poisson equation on rectangular domain of the size 400×300 m^2 with periodic boundary conditions in x or y directinos with corresponding analytical solution. Charge density $\rho_0 = 10^{-5}$ in all of the test cases

equation (3.29) becomes

$$-\left(k^2+j^2\right)\hat{\phi}\left(k,j\right)=\hat{\rho}\left(k,j\right) \tag{3.35}$$

which gives

$$\hat{\phi}\left(k,j\right)=-\frac{\hat{\rho}\left(k,j\right)}{k^2+j^2}. \tag{3.36}$$

Performing the inverse Fourier transform of the equation (3.36) gives the solution of Poisson equation in the real (physical) space,

$$\phi\left(x,y\right)=-\frac{1}{2\pi}\int\mathbf{d}k\int\mathbf{d}j\frac{\hat{\rho}\left(k,j\right)}{k^2+j^2}\exp\left[ikx+ijy\right]. \tag{3.37}$$

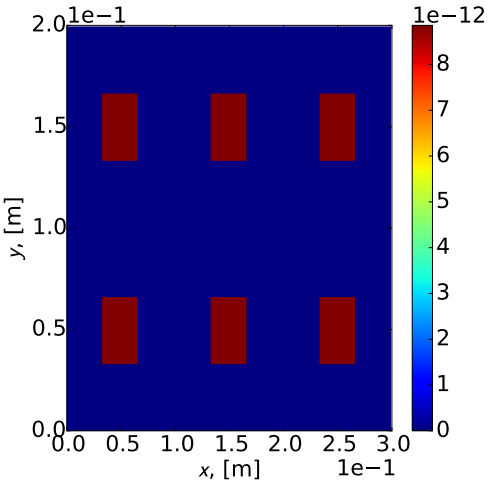

Figure 3.13: Peicewise uniform charge density, Eq. 3.38, used for periodic boundary verification test of the numerical Poisson Solver

Numerical solution with the periodic boundary conditions is tested in hPIC with piecewise uniform charge density function defined as

$$\rho_s(x,y) \quad = \quad \rho_0 I\left(x,y\in S_d\right) \tag{3.38}$$

$$S_d \quad = \quad \left\{x, y \in \mathbb{R} : l_x/3 \leq x - x_s^d < 2l_x/3, l_y/3 \leq y - y_s^d < 2l_y/3\right\}, \qquad (3.39)$$

where S_d is the square region in the center of each process-local sub-domain d, x_s and y_s are the left value of the x and y store on process-local sub-domain, l_x and l_y are the lengths of local sub-domain in x and y directions, and ρ_0 is the value of charge density withing S_d.

An example of piecewise uniform charge density for a test executed on 6 MPI processes is reported in Figs. 3.13–3.14. In this test, each process handled a local numerical grid of size 100×100 points, resulting in a global grid of size 300×200 grid cells. The charge density within each region S_d was set to a value equal to the dielectric constant $\rho_0 = \varepsilon_0$. The results of the benchmark between the two methods (Fourier Transform and Finite Differences) are shown in Figs. 3.14(a) and 3.14(b) for the Fourier Transform, Eq. (3.37), and the Finite Difference, Eq. (3.32), solutions respectively. Selected slices of two-dimensional solutions at $x = 0.05, 0.10$ m and $y = 0.07, 0.15$ m are reported on the figures (Figs. 3.14(c) and 3.14(d)), showing an absolute difference between the two methods not larger than 10^{-7} V or 0.1% .

3.4.3 Verification of Nonlinear Poisson Solver

The solution of the screened Poisson problem associated to adiabatic electrons (Sec. 2.5) requires the solution of the nonlinear Poisson equation Eq. 2.167; in one spatial dimension the problem can be cast in the form

$$\frac{\partial^2 \phi}{\partial x^2} = a + b \exp\left[c\phi\left(x\right)\right]. \qquad (3.40)$$

An analytical solution to this problem, even in the most simple case of uniform charge densities, cannot be expressed using analytical functions. However, a one-dimensional analytic solution can be found for the simplified nonlinear Poisson problem

$$\frac{\partial^2 \phi}{\partial x^2} = b \exp\left[c\phi\left(x\right)\right], \qquad (3.41)$$

where b and c are arbitrary constants. Equation (3.41) represents a Poisson equation for plasma with no ion population, and electron population distributed according to a Botlz-

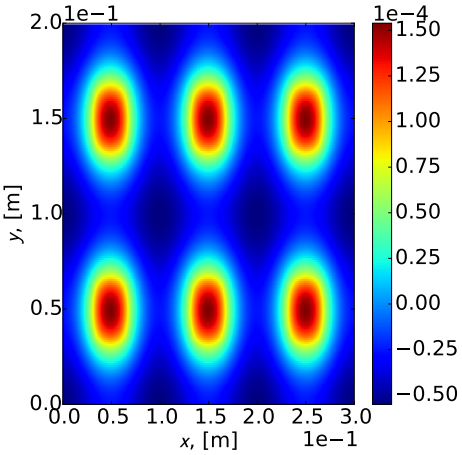

(a) Fourier Transform based solution

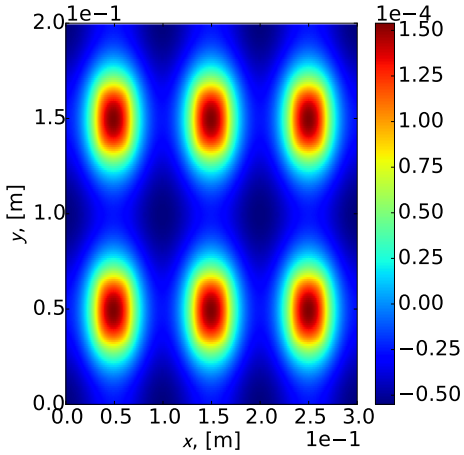

(b) Finite Difference based solution

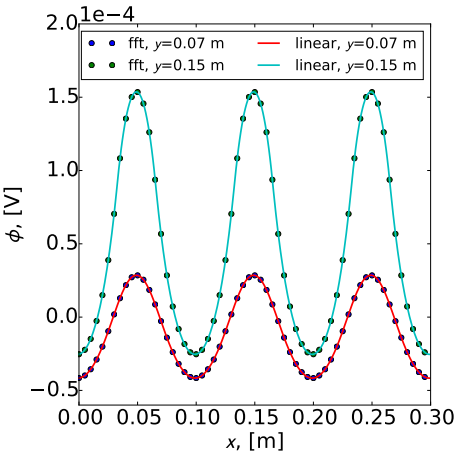

(c) Slices along x axis

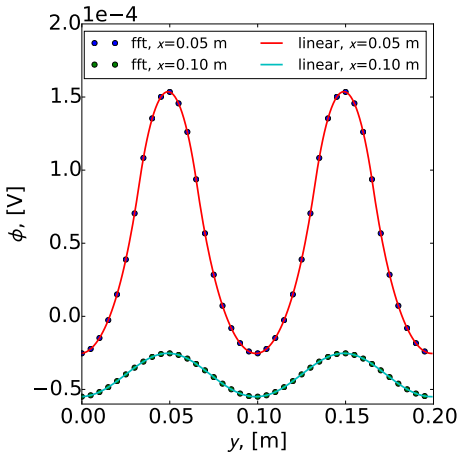

(d) Slices along y axis

Figure 3.14: Comparison of the Finite Difference and Fourier Transform based solvers of the Poisson equation for piecewise unifrom charge density and periodic boundary conditions. One-dimensional slices of the two-dimensional solution obtained with Fourier Transform (dots) and Finite Difference (solid lines) solvers of the Poisson equation.

mann distribution (free electrons in a potential field). An analytical solution for the problem of Eq. 3.41 can be found by means of variable substitution. Calling

$$v = \frac{\partial \phi}{\partial x} \tag{3.42}$$

into nonlinear Poisson equation (3.41)

$$v \frac{\partial v}{\partial \phi} = b \exp\left[c\phi\right]. \tag{3.43}$$

Integral of equation (3.43) gives an expression for v

$$\begin{aligned}
\int v \mathbf{d}v &= \int b \exp\left[c\phi\right] \mathbf{d}\phi - k_1 && (3.44)\\
\frac{v^2}{2} &= \frac{b}{c} \exp\left[c\phi\right] - k_1 && (3.45)\\
v &= \sqrt{\frac{2b}{c} \exp\left[c\phi\right] - k_1}. && (3.46)
\end{aligned}$$

Now, differential equation for electric potential ϕ can be obtained by substituting definition of v (3.41) into equation (3.46)

$$\frac{\partial \phi}{\partial x} = \sqrt{\frac{2b}{c} \exp\left[c\phi\right] - k_1}, \tag{3.47}$$

which can be easily integrated

$$\begin{aligned}
\int \mathbf{d}x + k_2 &= \int \frac{1}{\sqrt{\frac{2b}{c} \exp\left[c\phi\right] - k_1}} \mathbf{d}\phi && (3.48)\\
x + k_2 &= \frac{2}{c\sqrt{k_1}} \tan^{-1}\left[\sqrt{\frac{2b}{ck_1} \exp\left[c\phi\right] - 1}\right] && (3.49)\\
\sqrt{\frac{2b}{ck_1} \exp\left[c\phi\right] - 1} &= \tan\left[\frac{c\sqrt{k_1}}{2}\left(x + k_2\right)\right] && (3.50)\\
\phi\left(x\right) &= \frac{1}{c} \log\left[\frac{ck_1}{2b}\left(\tan^2\left[\frac{c\sqrt{k_1}}{2}\left(x + k_2\right)\right] + 1\right)\right]. && (3.51)
\end{aligned}$$

The constants k_1 and k_2 in the equation (3.51) are determined from the boundary conditions. For testing purposes, Dirichlet boundary conditions applied at both ends of the simulation domain of the size L

$$\phi(0) = \phi(L) = 0 \tag{3.52}$$

together with symmetry along the center of the domain.

$$\frac{\partial \phi}{\partial x}(L/2) = 0. \tag{3.53}$$

The value of the constant k_2 can be found from the symmetry condition (3.53). The first derivative of the electric potential (3.51) is given by

$$\begin{aligned} \frac{\partial \phi}{\partial x} &= \frac{1}{c} \frac{\frac{ck_1}{2b} 2 \tan\left[\frac{c\sqrt{k_1}}{2}(x+k_2)\right] \frac{c\sqrt{k_1}}{2}}{\frac{ck_1}{2b}\left(\tan^2\left[\frac{c\sqrt{k_1}}{2}(x+k_2)\right]+1\right)} & (3.54) \\ &= \frac{\sqrt{k_1}\tan\left[\frac{c\sqrt{k_1}}{2}(x+k_2)\right]}{\tan^2\left[\frac{c\sqrt{k_1}}{2}(x+k_2)\right]+1}. & (3.55) \end{aligned}$$

In order to satisfy symmetry condition (3.53)

$$\begin{aligned} \tan\left[\frac{c\sqrt{k_1}}{2}(x+k_2)\right] &= 0 & (3.56) \\ k_2 = -L/2 \text{ or } k_1 &= 0 & (3.57) \end{aligned}$$

Dirichlet boundary conditions (3.52) can be used to calculate value of k_1

$$\begin{aligned} \phi(0) = \frac{1}{c}\log\left[c\frac{k_1}{2b}\left(\tan^2\left[\frac{cL\sqrt{k_1}}{4}\right]+1\right)\right] &= 0 & (3.58) \\ \tan^2\left[\frac{cL\sqrt{k_1}}{4}\right] + 1 - \frac{2b}{ck_1} &= 0 & (3.59) \end{aligned}$$

When $k_1 = 0$, equation (3.59) will never be satisfied as its last term approaches infinity $\frac{2b}{ck_1} \to \infty$. Therefore $k_2 = -L/2$, and value of k_1 has to be determined as the solution of equation (3.59), which has to be solved numerical as it does not have a closed form solution.

In order to avoid complex values of k_1 and produce continuous values of the tangent function, a numerical search for k_1 that satisfies Eq. (3.59) is limited to non-negative numbers, with values of k_1 smaller than $(2\pi/cL)^2$ (tangent argument smaller than $\pi/2$, $cL\sqrt{k_1}/4 < \pi/2$). From the numerical solution of Eq. (3.59), the value of the constant k_1 is found, thus completing the analytical solution to the problem of Eq. 3.41.

Table 3.10: Verification tests of the nonlinear Poisson solver of hPIC; comparison the numerical results from hPIC with the analytical solution of Eq. 3.51.

Test	b	c	Δx, m	L_x, m	L_y, m	$\max(\lvert\phi_a - \phi_{numeric}\rvert)$, V
Periodic x	10	1	10^{-3}	0.3	0.2	2.490×10^{-8}
Periodic y	10^{-3}	1	10	3000	2000	3.046×10^{-3}

The semi-analytical solution just obtained in Eq. 3.51 is routinely used as a unit test in hPIC to verify the non-linear Poisson solver in a quasi-2D domain. The test uses Dirichlet boundary conditions along one dimension, and periodic boundary conditions along the other dimension. Table 3.10 reports the parameters of two numerical examples. In the first test, the numerical solver is initialized with periodic boundary conditions along the x direction, and the values of the constants are $b = 10$ and $c = 1$. A physical domain of size 0.3 m $\times$ 0.2 m is discretized with a grid of spacing $\Delta x 10^{-3}$ m. The maximum residual (absolute difference between analytical and numerical solutions) in the first test is 2.49×10^{-8} V or 10^{-4}%. The second test is initialized with smaller values of the constant $b = 10^{-3}$, the grid spacing Δx is set to 10, and the simulation domain is 3 km $\times$ 2 km. The maximum residual in this case is 3.046×10^{-3} V or 0.05%.

3.4.4 Linear Landau Damping

Numerical simulations of Landau damping in a one-dimensional electrostatic plasma have been used as a standard integration test for Particle-in-Cell schemes [22]. The test requires both particles and field routines, so it is among the simplest integration tests which require the proper operation of multiple pieces of the code (particle routines, field routines, non-uniform loader, etc.). The test allows to measure the rate of collisionless dissipation between a kinetic distribution of particles and the electrostatic field generated by them.

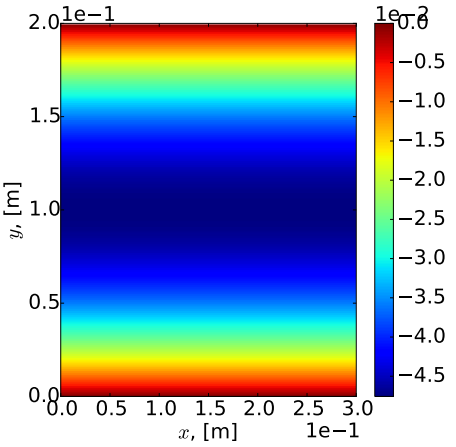

(a) Two-dimensional (2D) numerical solution with periodic boundary conditions in x direction

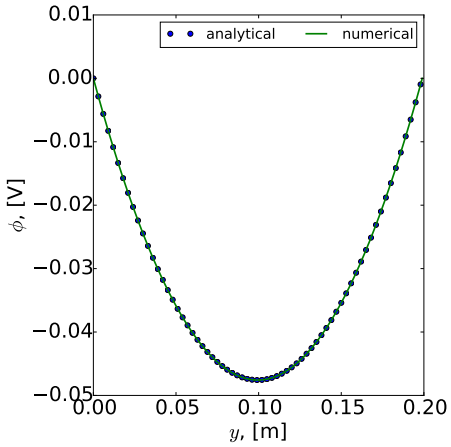

(b) One-dimensional slice of the 2D numerical solution with periodic boundary conditions alogn x axis

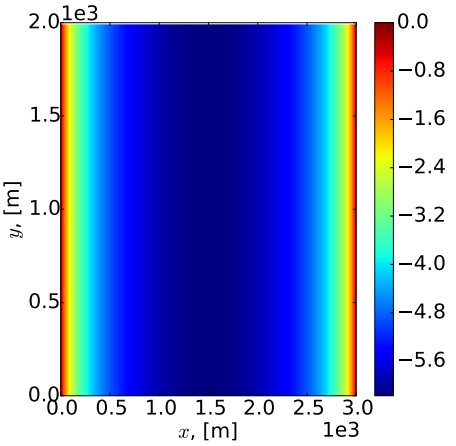

(c) Two-dimensional (2D) numerical solution with periodic boundary conditions in y direction

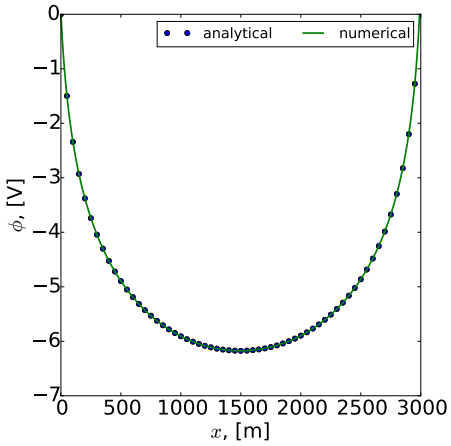

(d) One-dimensional slice of the 2D numerical solution with periodic boundary conditions alogn y axis

Figure 3.15: Verification tests of the nonlinear Poisson solver of hPIC; comparison of the quasi-2D numerical solution obtained by hPIC with the analytical solution of Eq. 3.51. The parameters of the tests are reported in Table 3.10.

In a Landau damping simulation, the domain is initialized with a population of negative charges having a small perturbation of their spatial density (typically $\delta n < 10\%$), on top of a neutralizing ion background. The density perturbation causes electrostatic oscillations which slowly decay in time via the Landau damping mechanism. The decay rate of oscillations can be obtained from the linear theory of the Vlasov-Poisson problem (Sec. 3.4.4.1). The numerical value of the decay rate obtained from the simulation can finally be compared to the theoretical value for verification purposes.

3.4.4.1 Decay rate of Landau Damping

By Fourier transforming the one-dimensional Vlasov-Poisson equation of an unmagnetized plasma

$$\frac{\partial f_e\left(x,v,t\right)}{\partial t} + \mathbf{v}\cdot\nabla f_e\left(x,v,t\right) - \frac{e}{m}E\frac{\partial f_e\left(x,v,t\right)}{\partial \mathbf{v}} = 0 \tag{3.60}$$

along the time and spatial coordinate, we get

$$-i\omega\hat{f}(k,\omega,v) + ikv_x\hat{f}(k,\omega,v) - \frac{e}{m}E\frac{\partial\hat{f}(k,\omega,v)}{\partial v} = 0. \tag{3.61}$$

Here the electron distribution f and the electric field E are assumed to be described by a linear combination of a stationary component and small perturbation,

$$\hat{f_e}(k,\omega,v) = f_0(k) + f_1(k,\omega,v) \tag{3.62}$$

$$E(k,\omega) = E_0(k) + E_1(k,\omega,v) = E_1(k,\omega,v). \tag{3.63}$$

with the stationary component of the electric field equal to zero, $E_0(k) = 0$. Expressions (3.62) and (3.63) are substituted into the Fourier transformed Vlasov equation (3.61). Since zero-order terms f_0 and E_0 describe equilibrium they will not contribute to perturbation effect and can be solved separately. Second order terms such as $E_1\frac{\partial f_1}{\partial v}$ are negligible when compared to first order terms, and can be neglected. The resulting Vlasov equation for the perturbation becomes

$$-i\omega f_1 + ikvf_1 - \frac{eE_1}{m}\frac{\partial f_0}{\partial v} = 0 \tag{3.64}$$

which immediately gives

$$f_1 = \frac{ieE_1}{m\left(\omega - kv_x\right)} \frac{\partial f_0}{\partial v} \tag{3.65}$$

Here and further on it is assumed that f_1 and E_1 are the functions of wavenumber k, wave frequency ω and particle velocity v. By using the Fourier-transformed Poisson equation for E_1

$$ikE_1 = -\frac{en_1}{\varepsilon_0} = -\frac{e}{\varepsilon_0} \int_{-\infty}^{\infty} \mathbf{d}v f_1, \tag{3.66}$$

where n_1 is perturbation of the electron density, into the equation (3.65), gives

$$ikE_x = -\frac{ie^2 E_x}{\varepsilon_0 m} \int_{-\infty}^{\infty} \mathbf{d}v \frac{1}{\omega - kv} \frac{\partial f_0}{\partial v} \tag{3.67}$$

$$1 = \frac{e^2}{\varepsilon_0 mk} \int_{-\infty}^{\infty} \mathbf{d}v \frac{1}{kv - \omega} \frac{\partial f_0}{\partial v} \tag{3.68}$$

$$= -\frac{\omega_p^2}{k^2} \int_{-\infty}^{\infty} \mathbf{d}v \frac{1}{v - \omega/k} \frac{\partial f_0/n_0}{\partial v} \tag{3.69}$$

For a Maxwellian distribution function of electrons $f_1/n_0 = \sqrt{m/2\pi kT_e} \exp\left(-mv^2/2kT_e\right)$ and under Landau's assumption [70] of having $k\lambda_D \ll 1$, the resulting damping rate is given by

$$\gamma = -\sqrt{\frac{\pi}{8}} \left(k\lambda_D\right)^{-3} \exp\left(-\frac{1}{2k^2\lambda_D^2} - \frac{3}{2}\right). \tag{3.70}$$

In our numerical test, the electron distribution function was initialized as

$$f_e(\mathbf{x}, \mathbf{V}) = n_0 \left(1 + \delta n \cos\left(\frac{2\pi x}{L_x}\right)\right) \left(\frac{m}{2\pi k_B T}\right)^{3/2} \exp\left[-\frac{m\mathbf{V}^2}{2k_B T}\right], \tag{3.71}$$

where the cosine term introduces a small spatial perturbation $\delta n \ll n_0$ in the equilibrium density profile n_0 to excite the first harmonics of the Landau instability (wavenumber $k = 1$). Figure 3.16) reports the amplitude of the first mode of the electric field oscillations E_1 obtained from hPIC by means of the numerical Fourier Transform. The following parameters were assumed: temperature $T_e = 11600K$, electron density $n_e = 10^5 \mathrm{m}^{-3}$, domain size $L_x = 20\lambda_D$, grid step $dx = \lambda_D/2$, time-step $dt = 3.5 \times 10^{-6}$ $(T_{pe}/100)$ s, number of particles per cell $ppc = 500$, initial perturbation of the electron density $\delta_n = 10\%$. For these conditions,

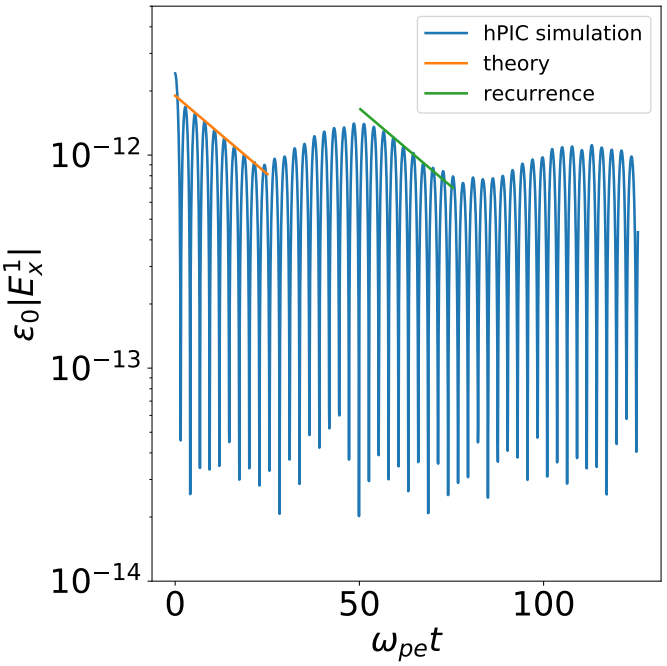

Figure 3.16: The amplitude of the first mode of the electric field oscillation vs time for Landau damping verification test of hPIC

$k\lambda_D = 0.32$, and the theoretical value of the damping rate is $\gamma = -3.386 \times 10^{-2}$. The first $\omega_{pe}t =\sim 25$ electrostatic oscillations are captured by the simulation before saturation. The numerical estimate of the rate from hPIC is $\hat{\gamma} = -3.396 \times 10^{-2}$, which corresponds to a percent relative error of 0.2%. The recurrence of the Landau Damping oscillation is observed at $\omega_{pe}\tau \approx 50$.

3.4.5 Two-Stream Instability Simulations

As a second integration test, we have implemented in hPIC a two-stream instability case. The two-stream instability is observed when one or more plasma species have different drift velocities. In the code, two counter-streaming electron populations are initialized on top of a charge-neutralizing ion background. The instability grows as the simulation advances, and the plasma forms characteristic vortices in the phase space. The growth rate of the instability can be derived by a linearized Vlasov-Poisson theory, as described in the following section. The growth rate of the instability is numerically obtained from the Particle-in-Cell code and compared to the theoretical value.

3.4.5.1 Growth rate of the two-stream instability

We consider an unmagnetized electrostatic plasma containing S electron beams, where each beam s is characterized by its density n_s, particle charge q_s, and drift velocity V_{ds}. Each additional plasma beam adds one continuity equation and one momentum balance to the problem,

$$m\frac{\mathrm{d}v_s}{\mathrm{d}t} = q_s E \tag{3.72}$$

$$\frac{\partial n_s}{\partial t} + \nabla \cdot n_e \mathbf{V_s} = 0 \tag{3.73}$$

$$\nabla \cdot E = -\frac{1}{\varepsilon_0}\sum_s n_s q_s \tag{3.74}$$

The drift velocity of the particle species can be represented as a sum of the drift velocity and a small perturbation, $v_s(x,t) = V_{ds} + v_{s1}(x,y)$. A similar approximation can be applied to the electric field $E(x,t) = E_1(x,t)$ and to the density $n_s(x,t) = n_s + n_{s1}(x,t)$ as

well. Note, that full derivative in equation (3.73) is a sum of the convective derivative and Eulerian acceleration: $\frac{\mathrm{d}}{\mathrm{d}t} = \frac{\partial}{\partial t} + v\frac{\partial}{\partial x}$. After Fourier and Laplace transforming, the system of Eqs. (3.72) takes the form

$$\begin{aligned} -mi\left(\omega - \mathbf{k}V_{ds}\right)v_{s1} &= q_s E_1 && (3.75)\\ i\mathbf{k}\left(n_s v_{s1} + n_{s1}V_{ds}\right) - i\omega n_{s1} &= 0 && (3.76)\\ -\frac{e}{\varepsilon_0}\sum_s q_s n_s &= i\mathbf{k}E_1 && (3.77) \end{aligned}$$

Eqs. (3.75)–(3.77) immediately return the drift velocity,

$$v_{s1} = \frac{q_s i E_1}{m\left(\omega - \mathbf{k}V_{ds}\right)}. \quad (3.78)$$

Substituting the velocity perturbation in equation (3.76) with (3.78), the density perturbation is found as

$$n_{s1} = \frac{\mathbf{k}n_s v_{s1}}{\omega - \mathbf{k}V_{ds}} = \frac{\mathbf{k}n_s q_s E_1 i}{m_s\left(\omega - \mathbf{k}V_{ds}\right)^2}. \quad (3.79)$$

The dispersion relation of the instability is then found by using the expressions above into the Poisson equation (3.77)

$$\begin{aligned} -\frac{1}{\varepsilon_0}\sum_s q_s n_s &= i\mathbf{k}E_1 && (3.80)\\ \frac{i\mathbf{k}E_1}{\varepsilon_0}\sum_s q_s^2 \frac{n_s q_s}{m_s\left(\omega - \mathbf{k}V_{ds}\right)^2} &= i\mathbf{k}E_1 && (3.81)\\ \sum_s \frac{n_s q_s^2}{\varepsilon_0 m_s\left(\omega - \mathbf{k}V_{ds}\right)^2} &= 1 && (3.82) \end{aligned}$$

In the classical treatment of the two-stream instability, the plasma is composed of: (1) a neutralizing background made of static singly-charged ions of mass $2M$, drift velocity $v_{di} = 0$, and density $2n_0$, (2) two electron populations of mass m_e, density $n_s = n_0$, and drift velocities directed in opposite directions $V_{ds} = \pm V_0$. The dispersion relation for this

system is then given by

$$\omega_p^2 \left[\frac{m}{M\omega^2} + \frac{1}{(\omega - \mathbf{k}V_0)^2} + \frac{1}{(\omega + \mathbf{k}V_0)^2} \right] = 1 \tag{3.83}$$

$$. \tag{3.84}$$

In the heavy ion limit $m/M \to 0$, and the dispersion relation becomes

$$1 - \frac{\omega_p^2}{(\omega - \mathbf{k}V_0)^2} - \frac{\omega_p^2}{(\omega + \mathbf{k}V_0)^2} = 0. \tag{3.85}$$

Solving (3.85) for ω gives

$$\omega = \pm\sqrt{\mathbf{k}^2V_0^2 + \omega_p^2 \pm \omega_p\sqrt{\omega_p^2 + 4k^2V_0^2}} \tag{3.86}$$

The equation has imaginary roots and the resulting system is unstable when $kV_0 < \sqrt{2}\omega_p$. Then the maximum growth rate of two-stream instability is found through maximization of the imaginary solution $\sqrt{\mathbf{k}^2V_0^2 + \omega_p^2 - \omega_p\sqrt{\omega_p^2 + 4k^2V_0^2}}$, which give the maximum growth rate of $\omega_{max} = \omega_p/2$ for the wavenumber $k_{max} = \sqrt{3}\omega_p/2V_0$.

3.4.5.2 Simulation Results

In our simulations, the initial distribution function of the two electron populations is initialized via rejection-sampling as

$$f_e(\mathbf{x}, \mathbf{V}) = \frac{n_0}{2}\left(1 + \delta n \cos\left(\frac{2\pi x}{L_x}\right)\right)\left[\delta\left(\mathbf{V} + \mathbf{V_d}\right) + \delta\left(\mathbf{V} - \mathbf{V_d}\right)\right]. \tag{3.87}$$

The cosine term introduces a small perturbation $\delta n \ll n_0$ in the equilibrium density profile n_0 to excite the first harmonics of the instability ($k = 1$). The parameters used for testing are reported in Table 3.11.

A two-dimensional electron distribution function $f(x, V_x)$ was collected on-the-fly by hPIC with resolution of 50×50 bins in the phase space. The evolution of the electron distribution function is reported in figure 3.17 at twelve different time-steps of the simulation,

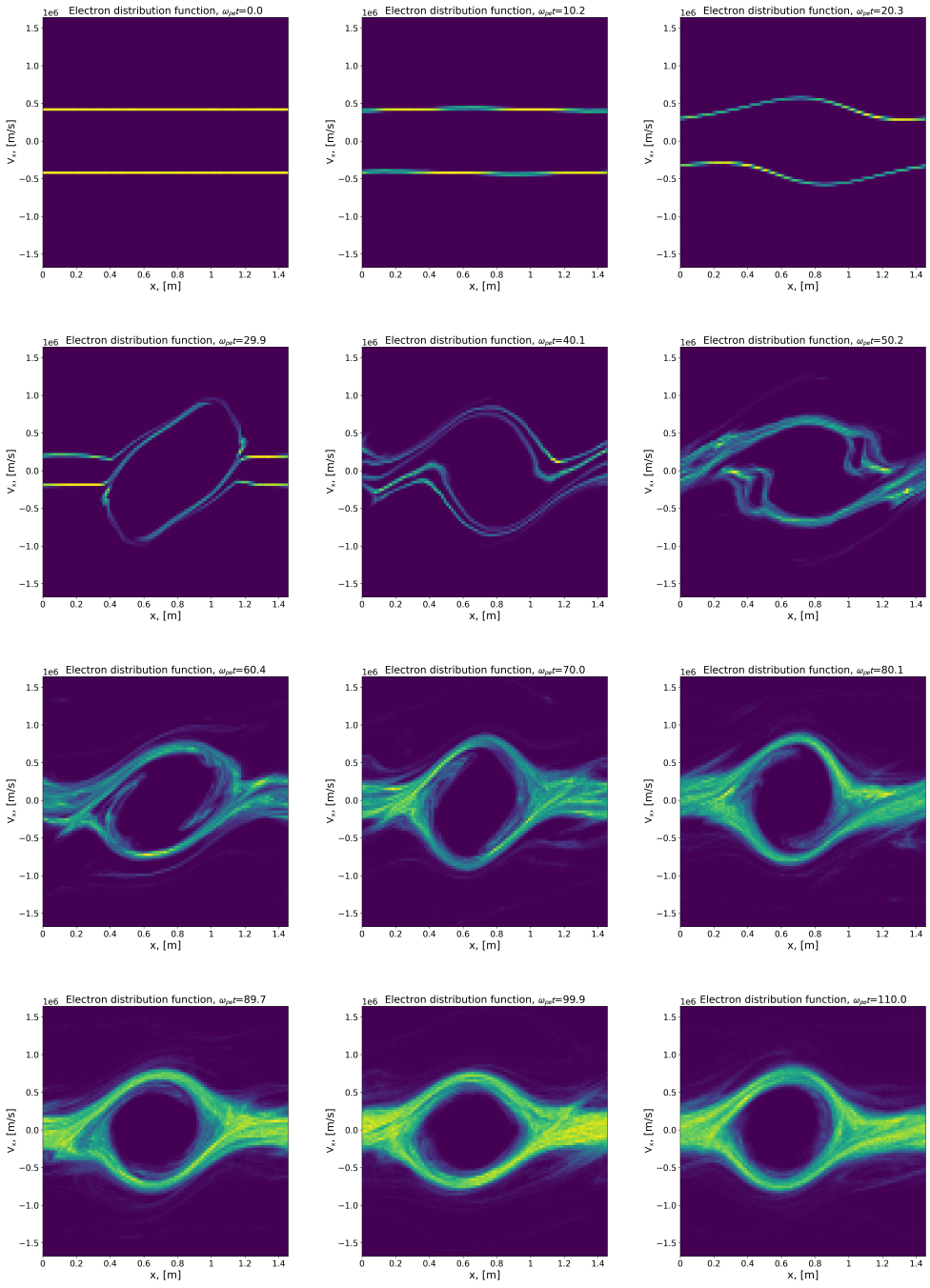

Figure 3.17: Evolution of the electron phase space in time for the two-stream instability setup

Table 3.11: Simulation parameters for verification tests

Parameter	Value
B	0 T
n_0	$\sim 100\lambda_D$
δn	$\sim 100\lambda_D$
V_0	$\sim 100\lambda_D$
T_e	1 K
L_y	$\sim 100\lambda_D$

with approximate intervals between the snapshots of $10\omega_p$. The time reported in the figure of the different snapshots is approximate, due to the finite time step chosen for the simulation, that does not produce exact multiples of the period ω_p^{-1}. During the linear onset of the instability ($\omega_p t = 0 \ldots 20$) the streams begin to interact electrostatically; at approximately $10\omega_p t$ the drift velocity of the two streams remains approximatively constant but density perturbations begin to occur. The stream velocities begin to deviate significantly at $20\omega_p t$, which precedes the onset of formation of the phase-space vortex at $\omega_p t = 30$. Between $\omega_p t = 30$ and $\omega_p t = 80$ the phase-space vortex forms and the instability fully develops, transitioning from its linear phase to the fully-saturated non-linear phase. After $\omega t = 90$ the electron phase space has reached saturation regime, and does not deviate anymore from this new condition of dynamic equilibrium.

Figure 3.18 shows the evolution of the total electrostatic energy during the simulation, highlighting the same features described so far. During the initial stages of the simulation the system undergoes two Landau damping oscillations, as also previously observed by Dawson, and at approximately $10\omega_p t$ the total electrostatic energy starts to grow until it reaches its maximum values at $30\omega_p t$. After a few additional oscillations, the values of electrostatic energy remains approximately constant and the phase space stabilizes. The growth rate of the electrostatic energy measured from the simulation matches to its expected value of $\omega_p/2$ (orange line on figure 3.18).

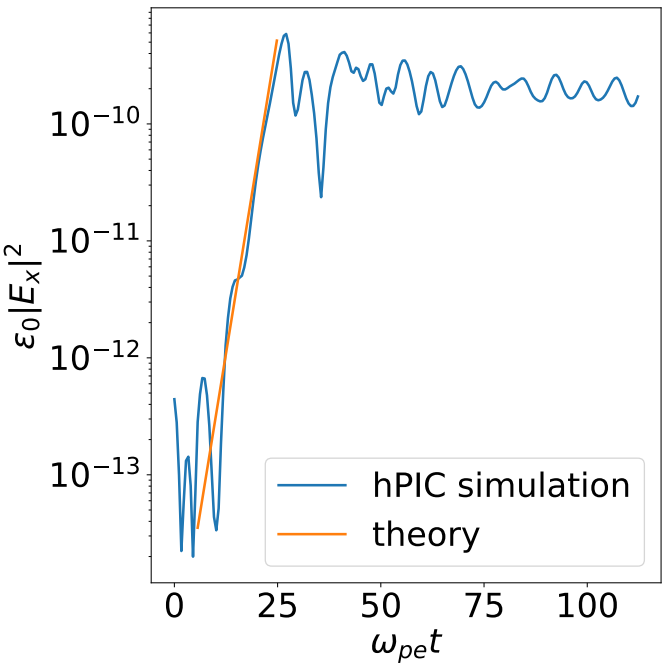

Figure 3.18: Evolutions of the electrostatic energy in time for the two-stream instability simulation. The growth rate of the two-stream instability predicted by the linear theory matches the numberical result.

3.5 Conclusions

In this work we have presented the hPIC code, a full-f, full-orbit, massively-parallel electrostatic Particle-in-Cell code specifically targeting plasma-surface interaction problems. The code has been tested for weak scaling on up to 65,536 cores on the Blue Waters supercomputer, with a demonstrated weak-scaling efficiency greater than 78% in all cases, and in the $85 \div 88\%$ range in conditions relevant for practical applications. Both the particle pusher of the code and the field solver have been verified against analytical solutions. In addition, two integration tests on Landau damping and Two-stream Instability were implemented, showing excellent agreement of the code predictions with theoretical results.

Chapter 4

Physical Characterization of Strongly Magnetized Plasma Sheaths

At the boundary of a weakly-collisional magnetized plasma, the collisional presheath, the magnetic presheath, and the electrostatic Debye sheath act as an interface between the bulk plasma and the material wall (Figure 4.1). The classical analysis done by Chodura [23] evidenced the structure of this transition layer, finding that within this region the ions are accelerated toward the material wall by a total potential drop that remains relatively insensitive to the magnetic field. The analysis was restricted to a perfectly absorbing wall. However, a material wall releases impurities into the plasma, affecting the structure of the plasma sheath and modifying the particle, current, energy and momentum balances in the quasineutral region. The physical response of the material wall is fairly sensitive to the ion energy-angle distribution function (IEAD) at the time of impact. Material properties like particle reflecton coefficients, energy reflection coefficients, sputtering yields, etc. can be conveniently parametrized in the energy-angle phase space [26]. Understanding the behavior of the ion energy-angle distribution at the wall of a magnetized plasma sheath is thus of fundamental importance for the proper determination of the material response to plasma exposure.

Fluid models of the magnetized sheath, both in collisionless and collisional regimes [27], [28], [31], [71], evidence the general features of the plasma-wall interface, but do not allow a detailed calculation of the ion energy-angle distribution at the wall. Kinetic approaches are thus preferable, at the expenses of greater computational complexity. The ion kinetics at the wall of a magnetized plasma sheath has been investigated via Particle-in-Cell simulations [34], single-particle motion analysis [72], Vlasov codes [19], [73], [21], and gyrokinetic approaches [32], [33]. Despite the vast amount of literature on this topic, a detailed charac-

terization of the ion energy-angle distributions at the wall is not readily available in literature. The IEADs at the wall are necessary whenever a calculation of the material response is needed as a function of the incoming plasma flux. This is typically the case in fusion codes involving plasma material interactions (Solps, EMC3-Eirene, Ero), in material processing codes where material release is of relevance, and in space plasmas, where a detailed understanding of the plasma-wall interaction between a spacecraft and the magnetosphere can be a matter of importance.

In the present work, we characterize the ion energy-angle distribution function at the wall of a weakly-collisional magnetized plasma using two approaches: (1) a simplified fluid-Monte Carlo model, and (2) weakly-collisional kinetic-electrons kinetic-ions particle-in-cell simulations. Our analysis has been done for magnetic angles ψ ranging from normal incidence ($\psi = 0$ degrees) to grazing incidence ($\psi = 85$ degrees). The sheath and presheath structure is resolved on the time scale of the electron gyro-frequency and provides total simulation times on the order of several ion fluid transit times across the collisional and magnetic presheaths. This allows precise calculations of the IEADs at the wall, plus the two derived "marginal" distributions IEDF (Ion Energy Distribution Function) and IADF (Ion Angular Distribution Function), to provide an accurate representation of the incident particle threat spectrum across the material interface. The ions accelerate, gyrate, and ExB-drift while falling into the sheath. In particular, our analysis evidences the three-dimensional structure of the transition layer, and the role of the ExB drift in deviating the ion flow across the magnetized sheath.

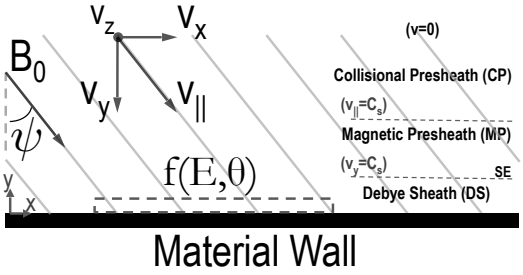

Figure 4.1: Structure of the magnetized plasma sheath

The results reported in this chapter are reproduced in parts from "Ion energy-angle distribution functions at the plasma-material interface in oblique magnetic fields" published in Physics of Plasmas [35], with the permission of AIP Publishing.

4.1 Ion Energy-Angle Distributions (IEAD)

4.1.1 Fluid-MC Model

The ion energy-angle distribution functions at the wall of a magnetized sheath can be estimated using a simple fluid-Monte Carlo model. The plasma flow in the quasi-neutral region ($n_i = n_e$), comprising the collisional presheath (CP) and the magnetic presheath (MP), is solved using a collisional version of Riemann's hydrodynamic model [28],[71]. The continuity equation of ions including volumetric ionization,

$$\nabla \cdot (n_i \mathbf{u}) = n_e \nu_{iz} \tag{4.1}$$

is solved together with the momentum balance of viscous magnetized ions,

$$n_i M_i (\mathbf{u} \cdot \nabla)\mathbf{u} = n_i q_e (\mathbf{E} + \mathbf{u} \times \mathbf{B}) - \nabla p_i - M_i n_i \nu_t \mathbf{u} \tag{4.2}$$

and the isothermal equation of state:

$$p_i = k_B T_i n_i \tag{4.3}$$

Electrons are assumed to follow a Boltzmann distribution, independently than the magnetic field:

$$n_e = n_0 \exp\left(-\frac{e\phi}{k_B T_e}\right) \tag{4.4}$$

Equations 4.1–4.4 are combined together, non-dimensionalized with the following positions:

$$X = y/\lambda_{mfp}, \quad \mathbf{V} = \mathbf{u}/C_s, \quad \Phi = -e\phi/k_B T_e, \tag{4.5}$$

$$\Delta = \nu_{iz}/\nu_t, \quad \lambda_{mfp} = C_s/\nu_t, \quad \omega\tau = eB/M_i\nu_t, \tag{4.6}$$

where $C_s = ((k_B T_e + k_B T_i)/M_i)^{1/2}$ is the Bohm acoustic velocity, and finally projected along the one-dimensional coordinate perpendicular to the wall, to find the following system of four ordinary differential equations:

$$V_y V_x' = \omega\tau \sin\alpha V_z - V_x \tag{4.7}$$

$$V_y V_z' = \omega\tau \cos\alpha V_y - \omega\tau \sin\alpha V_x - V_z \tag{4.8}$$

$$(V_y - V_y^{-1})V_y' = -\omega\tau \cos\alpha V_z - \Delta/V_y - V_y \tag{4.9}$$

$$V_y \Phi' = V_y' - \Delta \tag{4.10}$$

where the prime denotes the derivative with respect to the coordinate perpendicular to the wall, d/dy (see Figure 4.1 for the reference frame), and $\alpha = \pi/2 - \psi$ is the complementary angle of the magnetic angle ψ. The system of Eqs. 4.7– 4.10 has been numerically integrated starting from the boundary conditions

$$(V_x, V_y, V_z, \Phi)|_{y=0} = (0, \epsilon, 0, 0), \tag{4.11}$$

where ϵ is a small (e.g. $\epsilon \sim 10^{-4}$) initial velocity in the subsonic region of the plasma bulk,

$$0 < \epsilon \ll 1. \tag{4.12}$$

An example of calculation is reported in Fig. 4.2, for a strongly magnetized ($\omega_{ci}\tau_i = 100$, where ω_{ci} ion cyclotron pulsation, τ_i ion collision time; magnetic angle $\psi = 60$ deg) collisional plasma ($\Delta = 1.0$ ratio of the ionization and total collision frequency). The Y coordinate is along the direction normal to the wall, and it is measured in units of mean-free-paths. The integration ends at the Debye sheath entrance (SE) where the velocity along the normal to the wall reaches the Bohm velocity, $V_y = 1.0$. In this work, the coordinate Y at which the integration is stopped is defined as the presheath (both collisional and magnetic) size Y_{pre}. The interface between the collisional presheath and the magnetic presheath is marked with

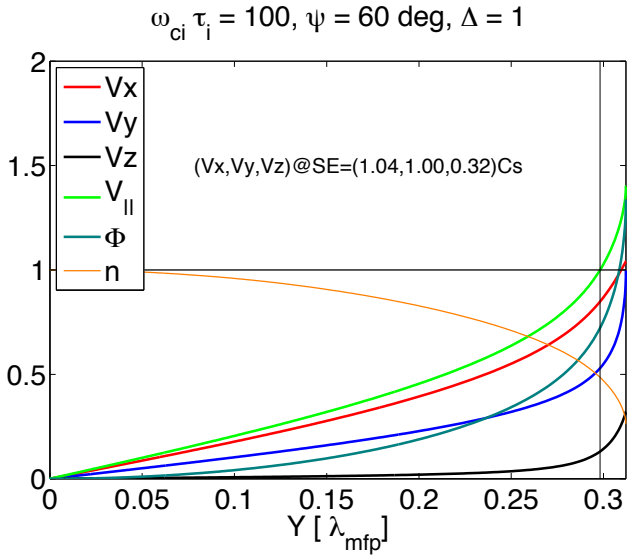

Figure 4.2: Fluid moments from the simplified 1D model, from integration of Eqs. 4.7–4.10: three components of the ion drift velocity, parallel velocity, electrostatic potential, and density.

a vertical line, corresponding to the location where the drift velocity in direction parallel to the magnetic field, $V_{||}$, becomes sonic,

$$V_{||} \sim 1.0, \quad V_{||} = V_x \cos\alpha + V_y \sin\alpha. \tag{4.13}$$

Based on the values of the Hall parameter $\omega\tau$ (magnetic field effect), the plasma sheath can be separated into three regimes: unmagnetized with $\omega\tau < 1$, partially magnetized $1 < \omega\tau < 100$, and fully-magnetized $\omega\tau > 100$. The separation of those regimes is clear from the sheath size dependence on the magnetic angle and Hall parameter (see Figure 4.3(a)). The size of the unmagnetized plasma sheath the does not depend on magnetic angle ψ, and the size of the fully-magnetized plasma sheath has cosine dependence on magnetic angle ψ (see Figure 4.3(b)). The size of the partially-magnetized plasma sheath decreases with the values of magnetic angle ψ and Hall parameter $\omega\tau$.

The approximate form of the fluid equation (4.7 - 4.10) at low magnetization $\omega\tau \ll 1$

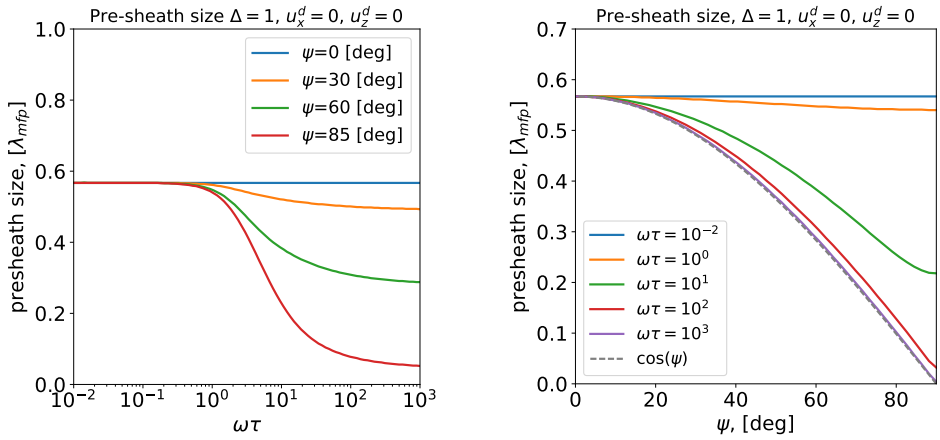

(a) Presheath size vs Hall parameters $\omega\tau$ for different magnetic angles ψ

(b) Sheath size as a function of an angle for various magnetization

Figure 4.3: Dependence of the Hall paramater $\omega\tau$ and magnetic angle ψ on the presheath size for $\Delta = 1$

can be defined as

$$V_y V_x' = -V_x \tag{4.14}$$

$$V_y V_z' = -V_z \tag{4.15}$$

$$(V_y - V_y^{-1})V_y' = -\Delta/V_y - V_y \tag{4.16}$$

$$V_y \Phi' = V_y' - \Delta. \tag{4.17}$$

Thus, the drift velocities in unmagnetized case depend only on the initial conditions of the numerical integration and the dimensionless collision parameter Δ. In this case, larger values of Δ (more ionization than collisions) will increase the gradient of the ion drift velocity V_y', therefore the sonic termination condition $V_y(Y_{pre}) = C_s$ is reached earlier reducing the presheath size Y_{pre}.

When gyrations are more frequent than collisions, and magnetization is fairly large $\omega\tau \gg 1$ (see Figure 4.3(a)), the plasma sheath is dominated by the magnetic effects. The dimensionless collision parameter Δ mainly affects the plasma potential, without making significant contributions to the velocity gradients. At $\psi = 0$ or $\alpha = 90$ degrees the $\omega\tau$ term

in equation (4.9) is canceled out, and magnetic fields do not affect the size of the magnetized plasma presheath.

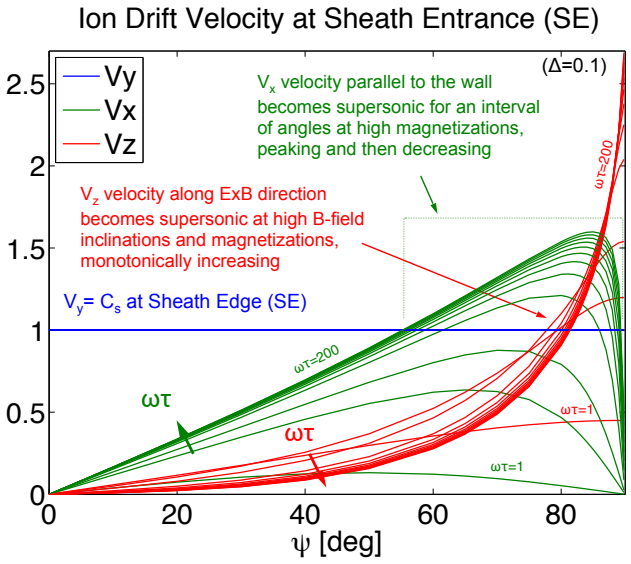

Figure 4.4: Ion drift velocity at the sheath entrance (SE, Fig. 4.1) vs. magnetic angle ψ, as calculated from the fluid model, Eqs. 4.7–4.10.

Figure 4.4 shows the three components of the velocity vector (V_x, V_y, V_z) at the sheath entrance (SE) as a function of the magnetic angle ψ, obtained from the solution of Eqs. 4.7–4.10. The velocity V_y perpendicular to the wall is equal to the Bohm velocity by definition of the SE. The velocity V_x parallel to the wall (green curves) becomes supersonic for an interval of ψ angles at high magnetizations. The velocity V_z along the E×B direction (red curves) becomes supersonic at high magnetic angles and strong magnetizations, monotonically increasing with ψ. The plots are reported for magnetizations ranging from weak, $\omega\tau \sim 1$, to strong, $\omega\tau \sim 200$. The strongly magnetized regime ($\omega\tau \to \infty$) has a well-defined asymptotic behavior. In this regime, the velocity V_z along the E×B direction (the red curves at high $\omega\tau$) increases monotonically with the field inclination ψ; at critical angles higher than approximately $\psi \sim 80$ degrees, the E×B flow becomes supersonic. The velocity parallel to the wall V_x (green curves at high $\omega\tau$) exhibits a peak, whose asymptotic value occurs at $\psi \sim$88 degrees. Magnetization (or equivalently, collisionality) drastically affects the behavior: both the velocity components V_x and V_z decrease in magnitude, and below a critical Hall factor

$\omega\tau$ they do not even become supersonic. When the Hall factor $\omega\tau \to 1$ tends toward one, collisions break the ion gyromotion around the magnetic field lines, and the ion flow along X and Z remains subsonic for all magnetic angles ψ.

From the three components of the velocity vector, the energy E_i and the inclination θ_i of the ion drift flow at the sheath entrance SE can be easily derived:

$$E_i = \frac{1}{2} M_i n_i (u_x^2 + u_y^2 + u_z^2) \tag{4.18}$$

$$\tan\theta_i = \frac{V_{xz}}{V_y} \tag{4.19}$$

Figures 4.5 and 4.6 show the plot of Eq. 4.18 and 4.19 respectively, as function of the magnetic angle ψ. In Figure 4.5 the kinetic energy of the ion flow has been normalized with respect to the energy at normal incidence ($\psi = 0$ deg). The magnetic presheath, absent at normal incidence, plays an increasing role in accelerating the ion flow up to the sonic condition $V_y = C_s$, especially at large magnetic angles. The energy gained in the presheath by the ions (Figure 4.5) has to increase at larger ψ's in order to compensate for the increasing inclination of the magnetic field. Furthermore, the effect of collisionality is also evident: higher collisionality (i.e., lower $\omega\tau$) decreases the gain of ion kinetic energy at large inclinations. Collisions provide a mechanism to dissipate the kinetic energy of the ions across the presheaths (CP and MP), with a damping mechanism that becomes more effective at high magnetic angles.

The flow inclination at SE, in Figure 4.6, is roughly equal to the magnetic field inclination at low ψ's, but depart considerably from the direction of the magnetic field at large ψ's. A detailed analysis of the components of the fluid velocity reveals that the plasma flow remains parallel to the magnetic field along most of the *collisional* presheath, and that it is mostly bent in the *magnetic* presheath, with deviations up to ~ 20 degrees at large ψ's.

The fluid model neglects the actual particle orbits, dealing only with drift velocities and fluid moments. The plot in Fig. 4.6 of the inclination of the drift flow necessarily neglects the actual kinetic distributions of particles. As the fully-kinetic particle-in-cell analysis will

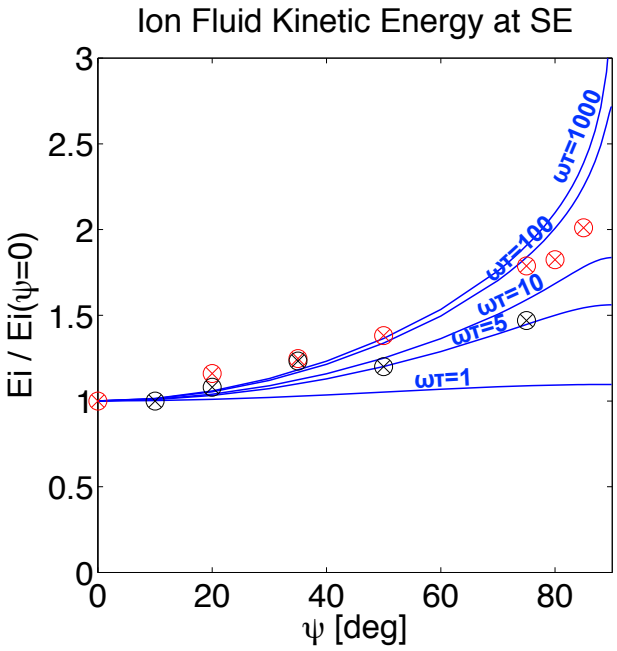

Figure 4.5: Ion fluid kinetic energy (Eq. 4.18) at the sheath entrance (SE) vs. magnetic angle ψ, calculated with the fluid model at five different magnetizations ranging from weakly magnetized ($\omega\tau = 1$) to strongly magnetized ($\omega\tau = 10^3$). The energy has been normalized with respect to the energy at normal incidence ($\psi = 0$ deg). Black and red dots are from Particle-in-Cell simulations (Sec. 4.1.2) at $\omega\tau = 5$ (black) and $\omega\tau = 25$ (red) respectively.

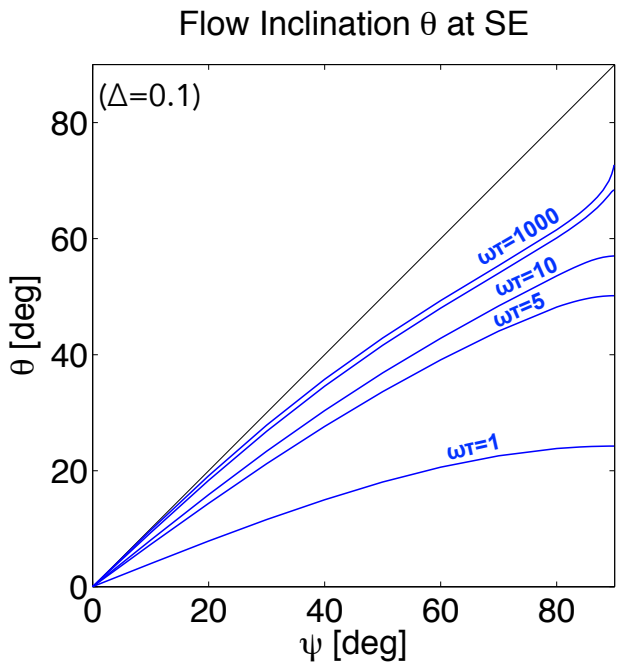

Figure 4.6: Ion flow inclination at the sheath entrance SE vs. magnetic angle ψ, as predicted by the fluid model, at five different magnetizations ranging from weakly magnetized ($\omega\tau = 1$) to strongly magnetized ($\omega\tau = 10^3$).

reveal in the next section, there are deviations of this simplified analysis from the results of the fully-kinetic calculation. A kinetic treatment is necessary to correctly evaluate the energy-angle distributions of the ions at the wall.

The validity of the fluid model breaks at the Debye sheath entrance, where quasi-neutrality is broken. The strong electric field in the Debye sheath accelerates and re-orients the plasma flow even further. In the limit of weak collisionality, the trajectories of a drifting Maxwellian population of ions can be treated as a distribution of single non-interacting particles, whose trajectories can be easily propagated across the E×B field of the magnetized free-charged layer up to the point where the ions hit the material wall. The ion velocity distributions calculated with the fluid model at the Debye sheath entrance have been discretized in a finite number of computational particles, and tracked up to the wall across the electrostatic layer of the Debye sheath. At the typical plasma density and temperature encountered in proximity of the wall (10^{17}–10^{19} m^{-3} and 1.0–10 eV's), the ion-ion collision time is several orders of magnitude larger than the characteristic time required for an ion to cross the free-charge layer. As a consequence, and only in first approximation, a single particle treatment within the Debye sheath is justified. This assumption offers an interesting and simple analytical solution allowing fast calculations of the ion energy-angle distributions at the wall.

The trajectory of the ions in the magnetized Debye sheath can be found by analytically solving the Newton-Lorentz equation of motion,

$$M_i \frac{d\mathbf{v}}{dt} = q_e(\mathbf{E} + \mathbf{v} \times \mathbf{B}) \tag{4.20}$$

where M_i and $q_e = Ze$ are, as usual, the ion mass and charge respectively, $\mathbf{v}$ is the kinetic velocity vector of the particle, and $\mathbf{E}, \mathbf{B}$ are the sheath electric field and the external magnetic field. Without loss of generality, we solve Eq. 4.20 in the Cartesian reference frame showed in Fig. 4.1, where the (x, y) is the plane containing the magnetic field vector, the Y-axis is oriented along the normal to the surface (pointing outward), and the origin of the frame is a point on the material surface corresponding to the projection of the particle

position at the sheath entrance. Thanks to this choice of the reference frame, the sheath electric field E_s is mainly directed along the normal to the surface (for planar surfaces),

$$\mathbf{E} = (0, E_s, 0) \tag{4.21}$$

and the magnetic field has only two components B_x and B_y in directions parallel and perpendicular to the surface,

$$\mathbf{B} = (B_x, B_y, 0) = (B_0 \sin\psi, -B_0 \cos\psi, 0) \tag{4.22}$$

where B_0 is the magnitude of the magnetic field and ψ is the inclination of the magnetic field with respect to the surface normal. The analytical solution of Eqs. 4.20 with the positions of Eqs. 4.21, 4.22 for a generic initial velocity vector $\mathbf{v}_0 = (v_{x0}, v_{y0}, v_{z0})$ is the following:

$$\mathbf{v}(t) = \mathbf{B}\mathbf{v}_0 + E_s\mathbf{b} + E_s\mathbf{c} \cdot t \tag{4.23}$$

where

$$\mathbf{B} = \frac{1}{B_0^2}\begin{bmatrix} B_x^2 + B_y^2\cos\omega t & B_xB_y(1-\cos\omega t) & -B_yB_0\sin\omega t \\ B_xB_y(1-\cos\omega t) & B_y^2 + B_x^2\cos\omega t & B_xB_0\sin\omega t \\ B_yB_0\sin\omega t & -B_xB_0\sin\omega t & \cos\omega t \end{bmatrix} \tag{4.24}$$

$$\mathbf{b} = \frac{1}{B_0^2}\begin{bmatrix} -(B_xB_y/B_0)\sin\omega t \\ (B_x^2/B_0)\sin\omega t \\ B_x(\cos\omega t - 1) \end{bmatrix} \tag{4.25}$$

$$\mathbf{c} = \frac{q_e}{M_i}\frac{1}{B_0^2}\begin{bmatrix} B_xB_y \\ B_y^2 \\ 0 \end{bmatrix} \tag{4.26}$$

and ω is the ion cyclotron frequency:

$$\omega = q_e B_0 / M_i \tag{4.27}$$

$$B_0^2 = B_x^2 + B_y^2 \tag{4.28}$$

The first term of Eq. 4.23 is proportional to the matrix $\mathbf{B}$, accounting for the spiraling motion of the particle in the magnetic field of components B_x, B_y. The last two terms appearing in Eq. 4.23 are proportional to the sheath electric field. The first is an harmonic motion with pulsation equal to the cyclotron frequency ω, the second retains the uniform acceleration due to the sheath voltage, corrected with the constraints due to the presence of the B-field lines. The trajectory of the particle $\mathbf{x}(t) = (x(t), y(t), z(t))$ can be easily obtained from Eq. 4.23, by analytically integrating $\mathbf{v}(t)$ over time from an arbitrary initial location $\mathbf{x}_0 = (x_0, y_0, z_0)$. The expressions are trivial but cumbersome, and thus only the $y(t)$ expression will be reported, this expression being needed for the calculation of the intersection between the particle trajectory and the wall.

The particle impacts on the material wall at time $t = t_w$, when

$$t_w = \{t : y(t) = 0\} \quad \text{Wall Impact} \tag{4.29}$$

The expression of $y(t)$ can be derived from Eq. 4.23, solving the integral of the velocity $v_y(t)$ in direction perpendicular to the wall. The explicit expression is the following:

$$y(t) = \int_0^t v_y(t)dt = y_1 t^2 + y_2 t + y_3 + y_4 \sin \omega t + y_5 \cos \omega t \tag{4.30}$$

$$y_1 = \frac{q_e E_s}{M_i} \frac{B_y^2}{B_0^2} \tag{4.31}$$

$$y_2 = \frac{B_x B_y}{B_0^2} v_{x0} + \frac{B_y^2}{B_0^2} v_{y0} \tag{4.32}$$

$$y_3 = y_0 + \frac{B_x}{B_0} \frac{1}{\omega} v_{z0} + \frac{E_s B_x^2}{B_0^3} \frac{1}{\omega} \tag{4.33}$$

$$y_4 = -\frac{B_x B_y}{B_0^2}\frac{1}{\omega}v_{x0} + \frac{B_x^2}{B_0^2}\frac{1}{\omega}v_{y0} \tag{4.34}$$

$$y_5 = -\frac{B_x}{B_0}\frac{1}{\omega}v_{z0} - \frac{E_s B_x^2}{B_0^3}\frac{1}{\omega} \tag{4.35}$$

The problem of Eqs. 4.29 and 4.30 is transcendental, and must be solved numerically.

The angle of the particle trajectory at the wall θ, measured with respect to the surface normal (pointing inward), and the kinetic energy at the wall E at the time of impact, are obtained from the three components of the velocity vector at time $t = t_w$,

$$\tan\theta = \frac{\sqrt{v_x^2(t_w) + v_z^2(t_w)}}{v_y(t_w)} \tag{4.36}$$

$$E = \frac{1}{2}M_i\left(v_x^2(t_w) + v_y(t_w)^2 + v_z^2(t_w)\right) \tag{4.37}$$

The trajectory of each particle is numerically calculated from the sheath entrance (SE) to the intersection with the material wall. The impact location and the impact time t_w are calculated solving the problem defined in Eqs. 4.29 and 4.30 with a two-step approach. First, we evaluate the closest zero to $t = t_0$ of the function $y(t)$ using a line-search method. This gives a rough estimate of the impact time t_w. Then we use a Newton-Raphson scheme to locally refine the calculation. The tolerance of the Newton- Raphson method is set to the order of the interatomic distance of the solid wall, O (10^{-10}) m. Convergence is typically found in four or five iterations. From the calculation we obtain both *when* the particle impacts on the material wall (impact time t_w), and *where* the particle hits the wall.

Figure 4.7 shows the Ion Energy-Angle Distributions (IEAD) calculated using the simplified 1D fluid-Monte Carlo model described in this section. The calculation has been done for 7.2×10^6 deuterium ions in a magnetic field of $B = 1.0$ Tesla, for a plasma of $n_e = 2\times10^{18}$ m^{-3} and $T_i = T_e = 3$ eV (isotropic). The distributions are reported at four magnetic angles, $\psi = 0, 30, 60, 85$ degrees. The computational time is of the order of 40 seconds (with single thread) on a MacBook laptop equipped with a 2.6 GHz Intel Core i5.

The marginal distributions in energy and angle of the ions at the wall, namely the Ion Energy Distribution Function (IEDF) and the Ion Angular Distribution Function (IADF),

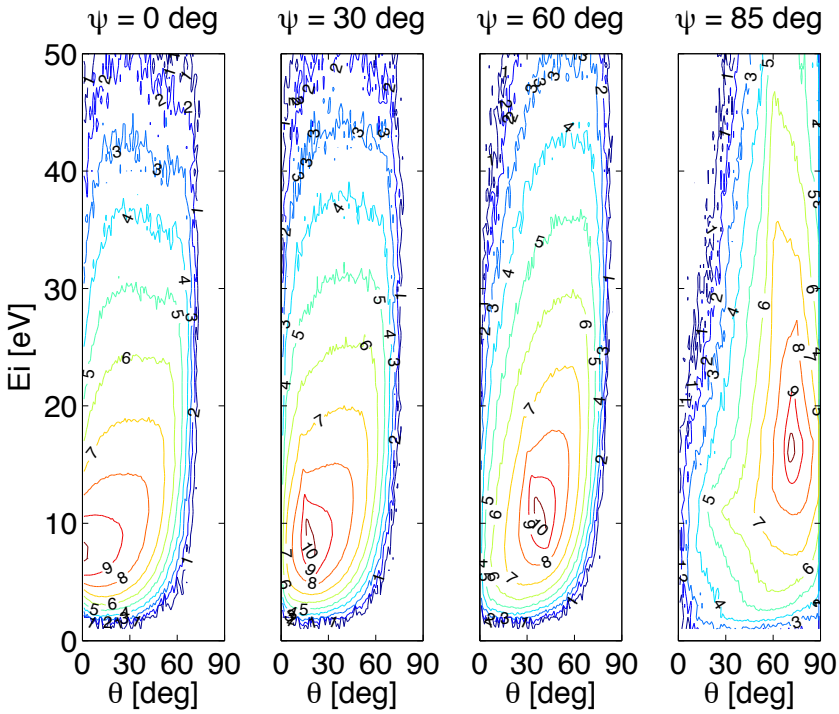

Figure 4.7: Ion Energy-Angle Distribution (IEAD) functions at the wall from the fluid-MC model. The distributions are plotted in logarithmic scale, contour numbers are $10 \log_{10}$ of the number of computational particles counted in the $dEd\theta$ volume.

are immediately obtained from the IEAD by simple integration along the angular and energy coordinate respectively:

$$f(E) = \int_0^{\pi/2} f(E,\theta)d\theta \quad \text{IEDF} \tag{4.38}$$

and

$$f(\theta) = \int_0^{\infty} f(E,\theta)dE \quad \text{IADF} \tag{4.39}$$

Figures 4.8 and 4.9 show the two marginal distributions resulting from the integration of the IEADs in Fig. 4.7.

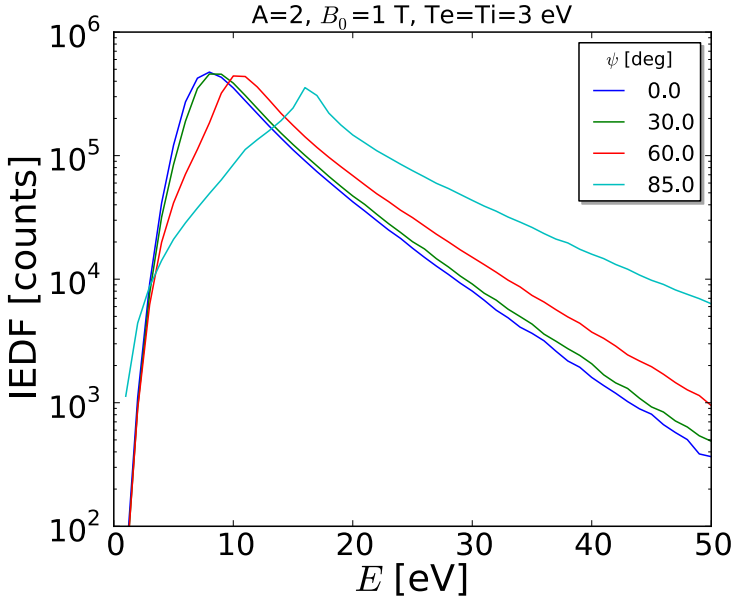

Figure 4.8: Ion Energy Distribution Functions from the simplified 1D fluid-MC model, obtained from integration of the IEAD of Fig. 4.7.

4.1.2 Weakly-collisional Particle-in-Cell Model

The ion energy-angle distributions (IEAD) at the wall have been calculated using a second method, using a Particle-in-Cell (PIC) technique. Even if the fluid-Monte Carlo model presented in the previous section contains all the fundamental elements for the calculation of the IEADs and allows extremely fast calculations, it is not self-consistent and its results

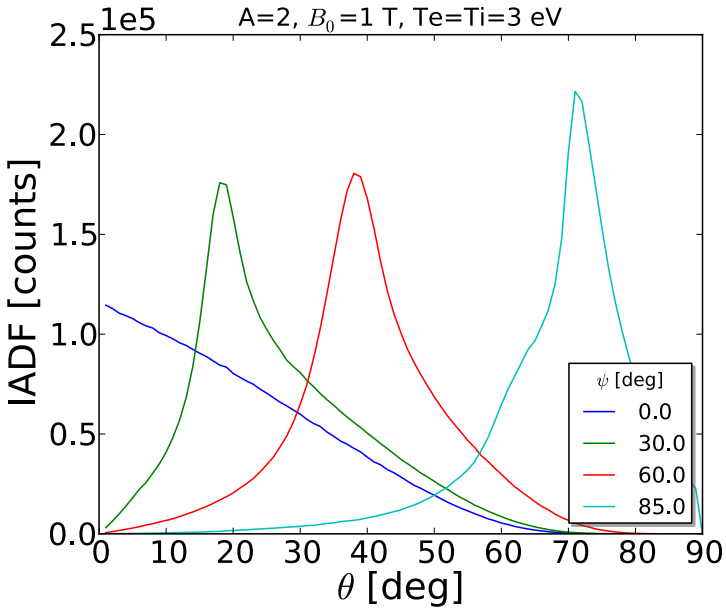

Figure 4.9: Ion Angular Distribution Functions from the simplified 1D fluid-MC model

have to be verified. Furthermore, the simplifying assumption of isothermal plasma and Boltzmann electrons (Eq. 4.4) are not justified, and have to be removed.

In the PIC model, the motion of $O(10^7)$ ions and $O(10^7)$ electrons is numerically solved in the three-dimensional space integrating the Newton-Lorentz equation with a Leapfrog scheme. The self-consistent electric field acting on the charged particles is calculated at every time step by solving the Poisson equation (using PETSc [60]) on a structured grid of square cells on the (x, y) plane containing the magnetic field vector (Figure 4.1). The wall is electrically grounded. The charge density of the Poisson equation is calculated using a linear weighting/interpolation scheme. The time step is chosen such as to sample the shortest oscillatory event with twenty points, $dt = (1/20)\min(\omega_{ce}, \omega_{pe}, \omega_{UH})$, where ω_{ce} is the electron cyclotron frequency, ω_{pe} is the electron plasma frequency, and ω_{UH} is the upper hybrid frequency. Similarly, the grid size is chosen such as to sample the smallest between the Debye length and the Larmor radius on twenty points, $dx = (1/20)\min(\lambda_D, r_L)$. The computational domain extends for approximately 400 Debye lengths in direction perpendicular to the wall. The numerical tests have been done at four magnetic angles, $\psi = 0, 30, 60, 85$

degrees. Simulations have been run using two different ion-to-electron mass ratios equal to $\mu = 100$ and 500. The computational volume is replenished with particles via a volumetric ionization source, which keeps the fluxes at the wall constant and maintain a desired density inside the domain.

After an initial transient, the plasma reaches a steady state characterized by small oscillations of the fluid moments (plasma density, temperature, drift velocities). Figure 4.10 shows the fluid moments in the region immediately facing the wall. In agreement with the fluid-MC model, the plasma density (Fig 4.10.a) at the wall decreases from a factor of 0.4 at normal incidence (case $\psi = 0$ degrees) down to 0.1 at grazing incidence (case $\psi = 85$ degrees). The ion temperature (Fig 4.10.b) decreases in the presheath and the sheath, as expected from a supersonically accelerating flow. The ion drift velocity along the Y coordinate (Fig 4.10.c) reveals a Debye sheath shrinking at larger magnetic angles ψ, accompanied by a decrease of the ion Mach number at the wall. At grazing incidence, $\psi = 85$ degrees, the ion Mach number at the wall is $M_y \sim 1.0$, suggesting that the Debye sheath is so small that is effectively disappearing. As already noted by Stangeby [74], the electrostatic layer is indeed expected to disappear at the critical angle ψ^* given by:

$$0 \approx \frac{e\phi}{k_B T_e} = -\ln(\cos\psi^*) + \frac{1}{2}\ln\left[2\pi\frac{m_e}{M_i}\left(1+\frac{T_i}{T_e}\right)\right] \tag{4.40}$$

For our case of Fig. 4.10, Eq. 4.40 would predict a theoretical critical inclination of $\psi^* = 69.2^\circ$ when $\mu = 100$, that is smaller than the observed critical angle of $\psi^* \sim 85^\circ$.

The IEADs at the wall have been reconstructed by collecting the state vector of all the computational particles crossing the wall boundary. The three-dimensional position and velocity of the particles have been converted to energy-angle coordinates, and statistically analyzed. Two-dimensional energy-angle distributions have been calculated either by binning the coordinates into classes, or by using a statistical method based on Gaussian kernel density estimators. The latter technique is preferable, because it allows a better reconstruction of the distributions than histogram-based techniques for the same amount of particle information. The amplitude of all the IEADs has been normalized to have unitary double

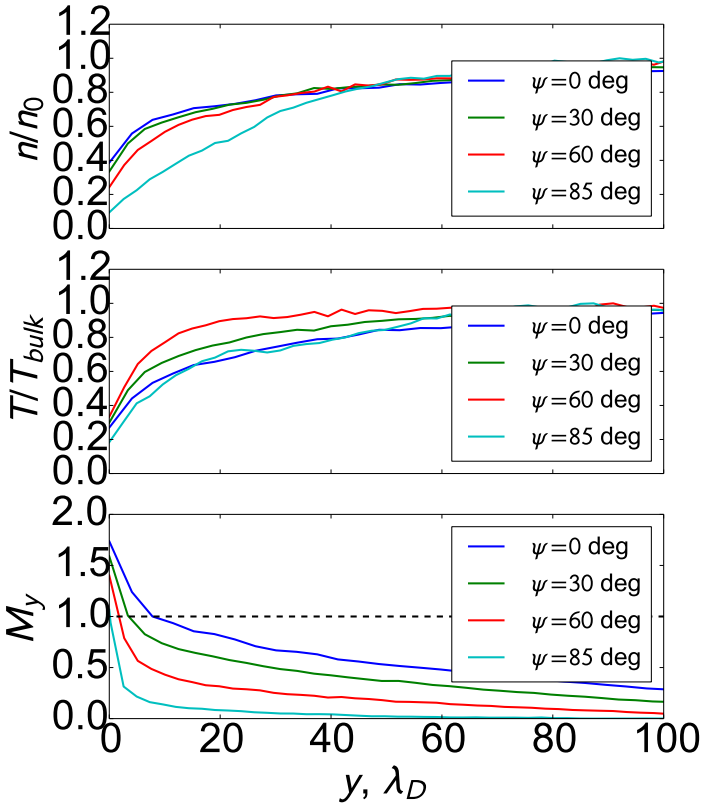

Figure 4.10: Fluid moments from the Particle-in-Cell: (a) ion density, (b) ion temperature, (c) ion drift velocity along the Y coordinate normalized to the Bohm acoustic velocity (ion Mach number). The plots are at four magnetic inclinations, $\psi = 0, 30, 60, 85$ deg.

integral in the energy-angle space, and plotted over three decades of amplitude.

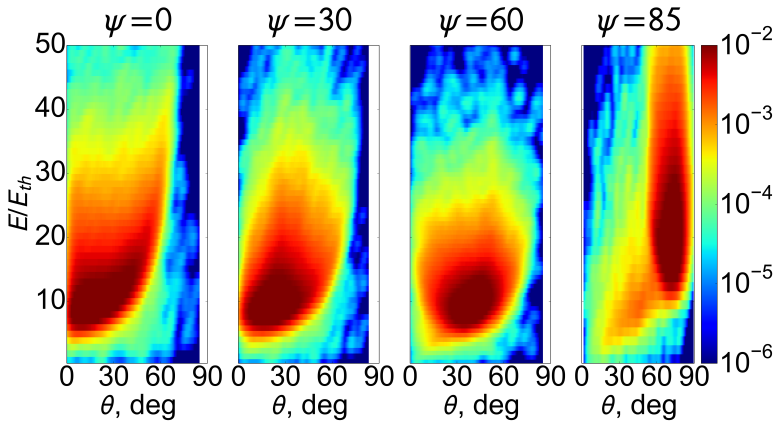

Figure 4.11: Ion Energy-Angle Distributions (IEAD) at the wall, calculated using Particle-in-Cells, of a strongly-magnetized weakly-collisional plasma sheath. The energy axis has been normalized to the ion thermal energy of the bulk (Eq. 4.41).

Figure 4.11 shows the calculated IEADs at the wall at four different magnetic angles $\psi = 0, 30, 60, 85$. The distributions are reported for impact angles θ ranging from normal incidence ($\theta = 0$ deg) to grazing incidence ($\theta = 90$ deg), where θ is the pitch angle of the particle trajectory at the wall (Eq. 4.36). The kinetic energy E of the particles at the wall is scaled with the thermal energy E_{th} of the ions in the plasma bulk,

$$E_{th} = \frac{1}{2} M_i v_{th,i}^2 = \frac{1}{2} M_i \left\langle \left(v_{y,i} - \langle v_{y,i} \rangle \right)^2 \right\rangle \tag{4.41}$$

When the magnetic field is normal to the wall, case $\psi = 0$ deg in Fig. 4.11, the IEAD peaks at an energy of $8.6 E/E_{th}$ and angle $\theta = 15$ deg. A magnetic presheath structure is absent in this case, and thus ions gain all additional momentum in the quasi-neutral region while crossing the collisional presheath. Differently than what is predicted with the fluid-MC model, the average impact angle at the wall is not equal to zero, but is of the order of $\max \theta =\sim 20$ deg, even if the field is perpendicular to the wall. When the inclination of the magnetic field increases, cases $\psi = 30$ deg and $\psi = 60$ deg in Fig. 4.11, the peak of the IEAD gradually shifts to higher energies and higher angles. The distributions become narrower along the angular coordinate and broader along the energy coordinate. The thickness of the

magnetic presheath increases at higher inclinations, being equal to $1.5\lambda_D$ at $\psi = 30$, and $2.5\lambda_D$ at $\psi = 60$. At grazing incidence, case $\psi = 85$ deg in Fig. 4.11, the IEAD peaks at an energy of $\sim 18 E/E_{th}$ and angle $\theta = 73$ deg. In this case the magnetic presheath structure extends for several Debye lengths, $\sim 5\lambda_D$.

Figures 4.12 and 4.15 show the marginal distributions IEDF and IADF at the wall, calculated from the IEAD of Fig. 4.12 using Eqs. 4.38 and 4.39 respectively. The IEDFs (Fig. 4.12) have the form of drifted Maxwellian distributions at small B-field inclinations ($\psi \leq 30$ deg), with an energy peak occurring at 8–9 E/E_{th}. Three decades of distribution amplitude are contained within an energy range between zero and $\sim 40 E/E_{th}$, forty times the energy of the plasma bulk.

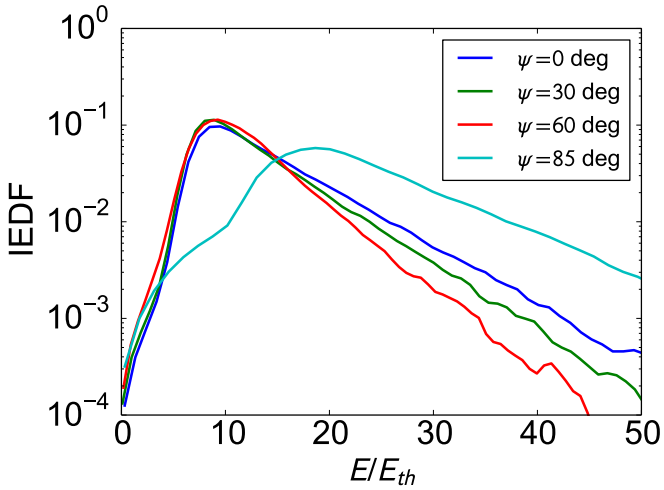

Figure 4.12: Ion Energy Distribution Function at the wall (IEDF), from Particle-in-Cell.

Figure 4.13 shows the energy scaling factor versus the magnetic angle ψ. The figure reports both the peak of the IEDF (the distribution's arg max) and the average of the angular distribution. The peak energy remains independent of the magnetic angle ψ and constant at around $\sim 8 E/E_{th}$ (at $\mu = 100$) and $\sim 10 E/E_{th}$ (at $\mu = 500$) up to a critical magnetic angle $\psi^\star \sim 75$ degrees. Above this angle, the energy peak increases with ψ. A similar energy increase has been observed also from the fluid-Monte Carlo model (Fig. 4.5)

described in the previous section. According to that model, in the weakly collisional limit both the components v_x (parallel to the wall) and v_z (along the ExB direction) largely contribute to the total kinetic energy of the plasma flow gained in the quasi-neutral region. A comparison of the fluid predictions with the PIC calculations has been also reported in Fig. 4.5 (blue lines are for the fluid model and crossed circles are for the PIC), showing agreement between the two models.

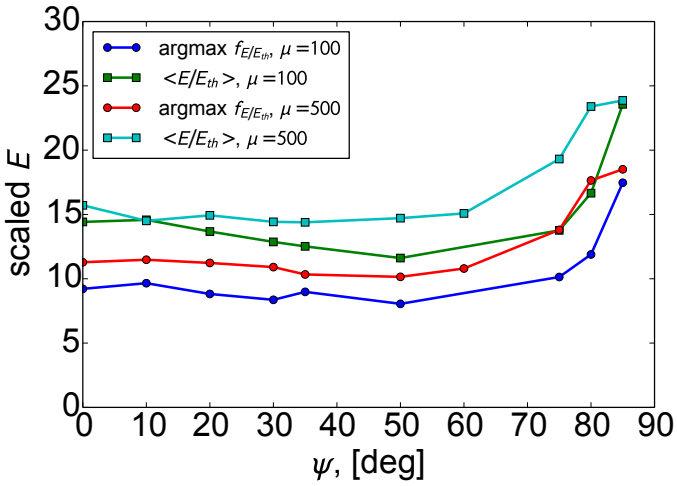

Figure 4.13: Trends of the most probable ion energy at the wall vs. magnetic angle ψ. The energy is scaled with the ion thermal energy, Eq. 4.41.

A different, useful scaling of the ion energy at the wall has been reported in Fig. 4.14, where the energy has been scaled with the one-dimensional acoustic energy E_s,

$$E_s = \frac{1}{2} M_i C_s^2 = \frac{1}{2} k_B \left(T_e + T_i \right) \tag{4.42}$$

instead of the ion thermal energy E_{th}. The temperatures Te, i are the temperatures in direction perpendicular to the wall. The acoustic energy E_s accounts for the contribution of both ions and electrons. In this scale, the energy scaling factor is a weak function of the magnetic angle ψ, being an almost constant value in the range $\sim$ 2–3E/E_s at $\mu = 100$, and $\sim$ 3–4E/E_s at $\mu = 500$.

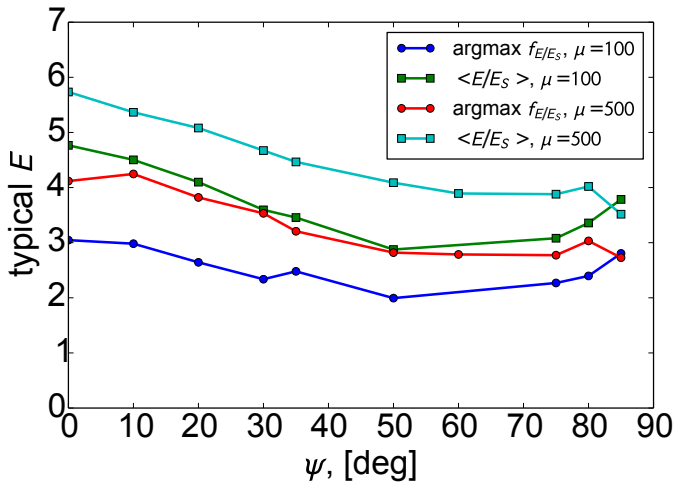

Figure 4.14: Trends of the most probable ion energy at the wall vs. magnetic angle ψ. The energy is scaled with the plasma acoustic energy, Eq. 4.42.

The IADFs are reported in Fig. 4.15 for the four ψ cases under analysis, and in Fig. 4.16 for a larger set of simulations. The angular distributions exhibit peaks (i.e. most probable angles of impact at the wall) increasing with the magnetic inclination ψ, shifting from $\theta^{max} \sim 8°$–$12°$ ($\mu = 500$–100) at normal incidence, to $\theta^{max} \sim 67°$–$68°$ at grazing incidence, where $\theta^{max} = \arg\max f(\theta)$. The average values of the angular distributions are larger at normal incidence, in the range $\theta \sim 22°$–$25°$ ($\mu = 500$–100). The dashed line in Fig. 4.16 corresponds to $\theta^{max} = \psi$. The angle θ monotonically increases with ψ. The trends show that the most probable angle θ^{max} is always different than the magnetic angle ψ, except for one case when $\theta^{max} = \psi$.

A measure of how much the E×B drift affects the ion motion in the magnetized sheath is given by the "E×B phase angle" ζ, defined as:

$$\tan\zeta = \frac{v_z}{v_x} \tag{4.43}$$

The angle ζ measures how much the ion trajectory is bent toward the Z direction by the E×B drift, and it is thus an indication of how much the magnetic field is adding three-

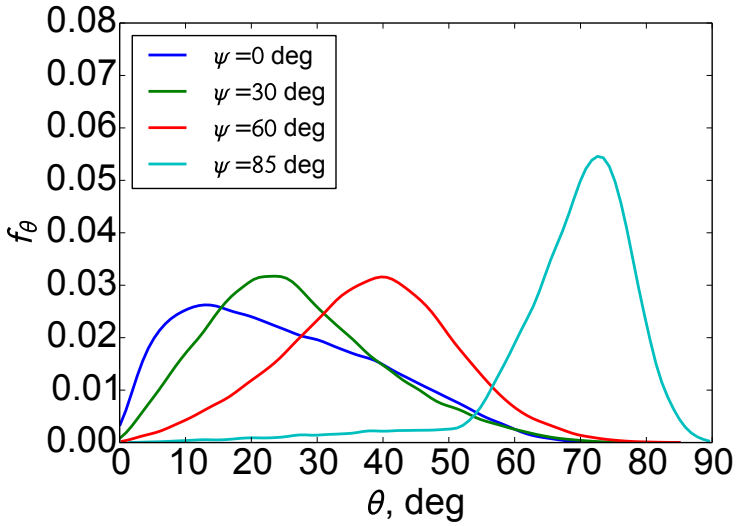

Figure 4.15: Ion Angular Distribution Function (IADF) at the wall, from Particle-in-Cell.

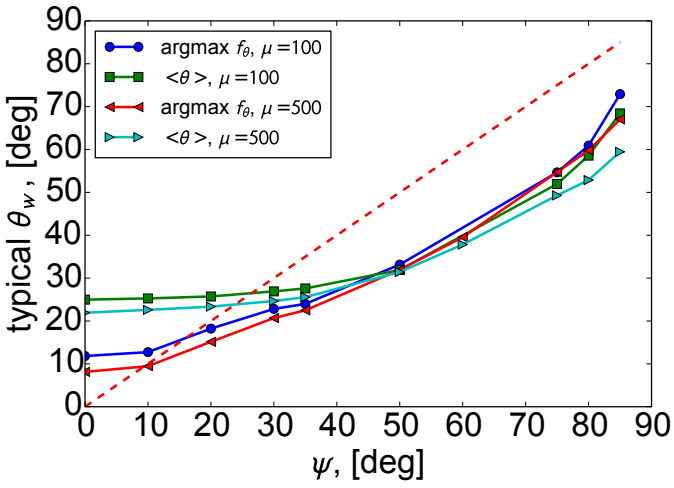

Figure 4.16: Most probable angle θ^{max} of ion impact at the wall vs. the magnetic angle ψ.

dimensional effects to the ion motion. The angle ζ has been mapped in the phase space (ζ, θ) and reported in Fig. 4.17 at four magnetic angles of $\psi = 0, 30, 60, 85$ degrees. At small magnetic angles ($\psi = 0$ deg, Fig. 4.17), the angle ζ is, as expected, independent than the pitch angle θ of the ions: when the B-field is perpendicular to the wall the particles impact with an arbitrary phase ζ. At larger ψ inclinations, the possible ζ phases are only those angles at which the ions intersect the material wall during their spiraling motion toward the wall. The larger the ψ inclination, the smaller the interval of possible ζ phase angles at the wall ($\psi = 85$ deg of Fig. 4.17).

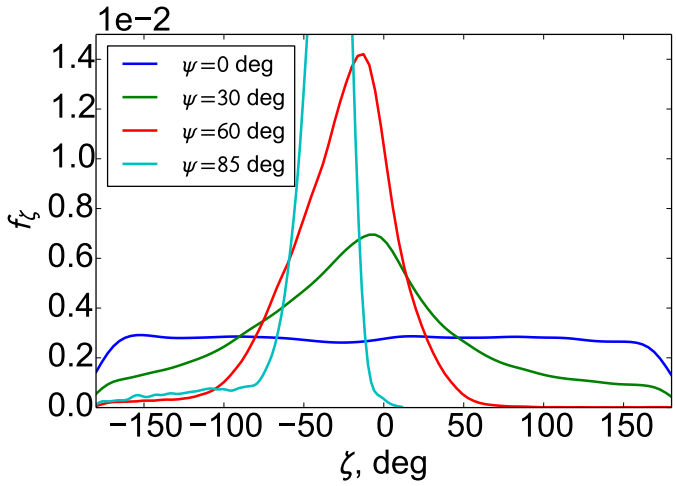

Figure 4.17: "E×B phase angle" ζ vs. ion impact angle θ at the wall, at four magnetic angles $\psi = 0, 30, 60, 85$ degrees. The angle ζ measures how much the ion trajectory is bent toward the Z direction by the E×B drift. The larger the ψ inclination, the smaller the interval of possible ζ phase angles at the wall.

4.1.3 Discussion

The ion energy-angle distributions calculated with the two previous methods (Figs. 4.7 and 4.11) show qualitative agreement and consistent trends. With a magnetic field normal to the wall, $\psi = 0°$, most of the particles impact at angles between normal and $\sim 45°$, as expected. Interestingly, the fluid-MC simulations show that the energy tail of the distribution moves

toward higher angles (see Fig. 4.7, case $\psi = 0°$). The same trend has also been observed in the corresponding Particle-in-Cell calculations (Fig. 4.11, case $\psi = 0$ deg). With magnetic fields inclined at higher angles, $\psi = 30°, 45°, 85°$, the IEAD shrinks in the angular coordinate and stretches along the energy coordinate. The PIC model reveals the most interesting features at the highest inclinations, $\psi = 85°$, where two ion populations can distinctly be observed (Fig. 4.11, case $\psi = 85°$), the first impacting on the wall at high inclinations and high energies, the second at lower inclinations and lower energies. The same behavior has been observed also in the Fluid-MC model, and further characterizations (not reported here) have shown a temperature- and density- dependance of the relative amplitude of the two populations.

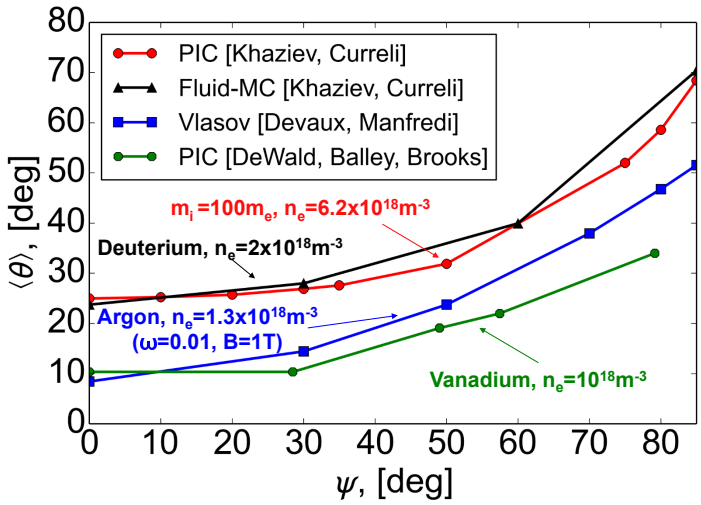

Figure 4.18: Comparison of the trends of $\langle\theta\rangle$ vs. ψ calculated in this work with other results available from literature.

Agreement has been found on the trends of the average impact angle $\langle\theta\rangle$ versus the magnetic angle ψ as calculated from the two models. Figure 4.18 shows a comparison of the trends obtained in this work with other results available from literature. The four cases reported in the figure are calculated using, respectively: the fluid-Monte Carlo method of Section 4.1.1, the kinetic-kinetic Particle-in-Cell of Section 4.1.2, a Vlasov method[21],

and a 1D Particle-in-Cell with Boltzmann-electrons[34]. The four works differ in methods, simulation strategies, and setup, but they all exhibit a common trend of the average angle $\langle\theta\rangle$ vs. ψ. The analysis from Dewald, Balley and Brooks[34] used a 1D3V PIC method with Boltzmann electrons, and ions injected from the boundary of the simulation domain, similarly to Chodura[23]. Our PIC simulations follow a different approach, since both ions *and* electrons are kinetic; furthermore, in our simulations particles were generated with a volumetric source in the plasma bulk (in analogy to the fluid-MC theory), in order to guarantee a self-consistent formation of the plasma sheath without any assumption on the particle distribution at the sheath entrance. The trend of $\langle\theta\rangle$ vs. ψ generated by Dewald *et al.*[34] showed a dependence on the plasma density and ion mass. Larger ion masses decrease the intercept of $\langle\theta\rangle$ at $\psi = 0°$. The calculated values were $\langle\theta\rangle \sim 20°$ for deuterium and $\sim 10°$ for vanadium. Despite the differences in the electron models, we have found absolute agreement between the approaches. In our simulations, the volumetric ionization source allows a consistent treatment of the two temperatures (T_e and T_i), since the system naturally evolves to the equilibrium temperatures allowed by the balance between ionizations and losses. Thus, with an increase in the magnetic angle ψ, fewer particles enter the sheath per unit area, which in turn increases the particle confinement time in the simulation domain and the plasma temperature. The range of values of the electron to ion temperature ratio observed in the simulations was within the range $\tau = T_e/T_i \sim 2.2$–5.2 for mass ratio $\mu = 100$, and $\tau = T_e/T_i \sim 1.7$–5.8 for $\mu = 500$. A different approach was used by Devaux and Manfredi[73], [21] who used a Vlasov code comprising a collisional term. Similarly to PIC models, the Vlasov simulations show the dependence of the IADF on the plasma density and ion mass. In Fig. 4.18 the quantity ω refers to the dimensionless quantity $\omega = \omega_{ci}/\omega_{pi}$. The value of the thermal energy at the material wall calculated from the PIC models agrees well with the corresponding trend presented in their Vlasov approach; more specifically, the value of the ion energy (in units of ion thermal energy) at the wall lays in a range of 12–24 when $\tau = T_e/T_i \sim 2.2$–5.2, in agreement with our observations. Finally, our fluid Monte-Carlo model provides a computationally-inexpensive way to calculate the IEAD, that is an attractive alternative than the more lengthy Particle-in-Cell or Vlasov simulations.

There are advantages to having a light, inexpensive model for the calculation of the IEADs without solving for the full computationally-intensive kinetic problem. In addition, thanks to the way our Fluid-Monte Carlo algorithm is constructed (Sec. 4.1.1), it allows trivial parallelization with shared-memory computing paradigms. Despite the simplifications of the Fluid-MC model, the model was able to reproduce quantitatively the same trends of the IEADs calculated with Particle-in-Cells.

As a final note, Figure 4.18 shows that light ions (eg. hydrogen, deuterium) have average impact angle of $\langle\theta\rangle \sim 20^\circ$ at $\psi = 0^\circ$, monotonically increasing with the inclination of the magnetic field; heavier ions have lower average impact angle $\langle\theta\rangle$ at $\psi = 0^\circ$. This mass-dependent behavior of $\langle\theta\rangle$ at $\psi = 0^\circ$ can be easily understood from a simple analytical argument. Assuming an ion population drifting with velocity v_d in direction perpendicular to the wall, Maxwellian with thermal velocity v_T along the two other directions (tangential to the wall), the resulting angular distribution can be obtained in closed form as:

$$f(\theta) = \frac{v_d^2}{v_T^2} \frac{\tan\theta}{\cos^2\theta} \exp\left[-\frac{v_d^2}{2v_T^2}\tan^2\theta\right], \quad (\psi = 0) \tag{4.44}$$

where θ is the impact angle of the ions as defined in Eq. (4.36). The distribution (4.44) si characterized by an average value

$$\langle\theta\rangle = \frac{\pi}{2}\mathrm{Erfc}\left(\frac{v_d}{\sqrt{2}v_T}\right)\exp\frac{v_d^2}{2v_T^2}, \quad (\psi = 0) \tag{4.45}$$

where the drift velocity in direction perpendicular to the wall is $v_d^2 = -2e\phi/M_i$, with a total sheath potential drop ϕ given by the right hand side of Eq.(4.40). The function (4.45) is decreasing with the ion mass, and weakly increasing with the temperature ratio $\tau = T_e/T_i$ appearing in Eq.(4.40). The dependence of $\langle\theta\rangle$ on the temperature becomes negligible for $\tau \geq 10$.

4.2 Fluid-kinetic coupling of magnetic presheath models with adiabatic electrons

Here we discuss a method for coupling fluid models of the magnetic presheath to Particle-in-Cell (PIC) kinetic models. We consider the general case of a magnetic field inclined at an angle with respect to the wall, where a magnetic presheath is formed in addition to the standard Debye sheath and collisional presheath. As previously highlighted by Chodura [23] and numerically observed in recent large-scale PIC simulations [35], the three-layer structure of the plasma-wall transition exhibits finite-Larmor radius effects and particle drifts due to non-uniform electric fields, breaking the validity of common approximations based on scale-separation such as gyrokinetic approximations. Indeed, the large electric field gradient arising in the layer closest to the surface (including the magnetic presheath and Debye sheath) is responsible of large finite-orbit perturbations to the particle trajectory, suggesting the need of fully-kinetic rather than gyro-kinetic treatments at those locations. Accounting for finite-orbit effects is particularly relevant for interfacing plasma codes to material erosion codes, where the exact energy-angle distribution of the particles impacting on the surface is required. However, fully-kinetic models are typically too computationally demanding to be included in full-device models, or in transport codes covering large spatial domains such as the divertor or the full Scrape-Off Layer.

4.2.1 Methodology

The treatment here proposed aims at bridging the gap between fluid and kinetic modeling by attempting to include kinetic effects into a simplified fluid model. Electrons are treated adiabatically both at the fluid and kinetic level, in agreement with previous models of the magnetic presheath. Our approach can be summarized as follows.

1. The plasma ions falling into the sheath are modeled as a one-dimensional fluid by means of a two-moment model;

2. An effective collision frequency $\nu_{0,1}$ is added to each moment equation in order to

account for kinetic corrections;

3. The value of the effective frequencies $\nu_{0,1}$ is calibrated using Particle-in-Cell simulations via a least-square minimization technique.

The method allows the retention of the kinetic behavior of the ions inside a simpler fluid model which can be easily solved at a smaller computational cost. All fluid moments up to order two can be obtained from such an approach, which include densities, ion drift velocity, particle fluxes, and electrostatic potential. In principle, the model can be naturally extended up to higher-order fluid moments (third, fourth, etc.), but such an extension will not be considered here. From our tests we have empirically found that accounting for the first two moments already gives excellent agreement with PIC results. The approach is quite powerful in constructing a reduced-parameter model of the magnetized plasma sheath. Furthermore, the resulting set of one-dimensional fluid equations corrected with kinetic effects can be numerically integrated quickly and efficiently using standard finite-difference methods, producing a reduced model of the magnetic presheath which retains finite-orbit effects of the ions crossing the sheath. The model is suitable for inclusion into full-device models where the behavior of the near-surface plasma and of the magnetic presheath is of interest.

4.2.2 Two-moment 1D fluid model with correction terms

Following an approach similar to Riemann [28] and Zimmermann [71], we consider the continuity and the momentum balance of strongly magnetized isothermal ions,

$$\nabla \cdot (n_i \mathbf{u}) = n_e(\nu_{iz} + \nu_0) \tag{4.46}$$

$$n_i M_i (\mathbf{u} \cdot \nabla)\mathbf{u} = n_i q_e(\mathbf{E} + \mathbf{u} \times \mathbf{B}) - KT_i \nabla n_i - M_i n_i(\nu + \nu_1)\mathbf{u} \tag{4.47}$$

and couple this model to adiabatic (Boltzmann) electrons. In order to account for kinetic effects, the ionization frequency in the continuity equation Eq. 4.46 is corrected by an effective ionization frequency ν_0. Similarly, in the momentum balance Eq. 4.47, the viscous

term is corrected by an effective collision frequency ν_1. The values of ν_0 and ν_1 are then obtained from a least-square minimization procedure to best fit the fluid model to PIC simulations under the same conditions.

4.2.3 Wall boundary conditions

The boundary conditions of the problem of Eqs. 4.46–4.47 are obtained from considerations on the particle fluxes (or equivalently, on the current densities) at the boundary. In strongly magnetized conditions, the ion and electron current densities $J_{i,e}$ on a perfectly absorbing boundary are given respectively by

$$J_i = e\Gamma_i = en_s\sqrt{\frac{k_B\left(T_i + T_e\right)}{m_i}}\cos\psi \tag{4.48}$$

$$J_e = -e\Gamma_e = -e\frac{1}{4}n_s\sqrt{\frac{8k_BT_E}{\pi m_e}}\exp\left(\frac{\phi_p e}{k_BT_e}\right)\cos\psi \tag{4.49}$$

where the cosine dependence on the magnetic angle ψ accounts for the inclination of the field with respect to the normal to the surface. The value of the plasma potential can be derived from the balance of the ion and electron currents at the wall,

$$J_i + J_e = 0 \tag{4.50}$$

which immediately returns the same floating potential of an unmagnetized wall,

$$\phi_p = \frac{k_BT_e}{2e}\log\left[\frac{2\pi m_e}{m_i}\left(1 + \frac{T_i}{T_e}\right)\right]. \tag{4.51}$$

In some treatments [cite], the cosine dependence on the electron flux Eq. 4.49 is dropped; in this cases the $\cos\psi$ factor does not cancel out from the current balance,

$$en_s\sqrt{\frac{k_B\left(T_i + T_e\right)}{m_i}}\cos\psi - \frac{1}{4}en_s\sqrt{\frac{8k_BT_E}{\pi m_e}}\exp\left(\frac{\phi_p e}{k_BT_e}\right) = 0 \tag{4.52}$$

$$\exp\left(\frac{\phi_p e}{k_B T_e}\right) = \sqrt{\frac{2\pi m_e}{m_i}\left(1+\frac{T_i}{T_e}\right)}\cos^{-1}\psi \tag{4.53}$$

and the value of the floating potential results in being a function of the magnetic angle ψ,

$$\phi_p = \frac{k_B T_e}{2e}\log\left[\frac{2\pi m_e}{m_i}\left(1+\frac{T_i}{T_e}\right)\right] - \frac{k_B T_e}{2e}\log\left(\cos^2\psi\right). \tag{4.54}$$

In these cases the floating potential increases as a function of ψ, as reported in Fig. 4.19(a), in contrast to experimental observations [cite]. Our treatment of the electron flux, Eq. 4.49, returns a floating potential independent than the magnetic field, Fig. 4.19(b).

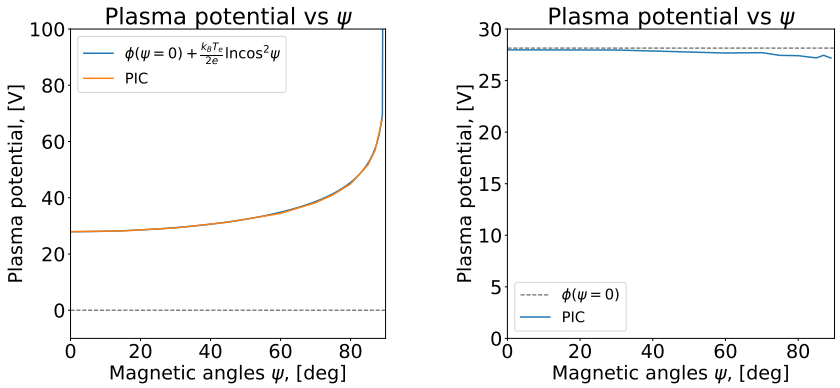

(a) Floating potential *without* magnetic corrections on the wall electron current J_e

(b) Floating potential *with* magnetic corrections on the wall electron current J_e

Figure 4.19: (a) Angular dependence of the floating potential as predicted by Eq. 4.54, which does not include magnetic corrections on the electron flux; (b) same angular dependence of the floating potential, including magnetic corrections on the electron currents as in Eq. 4.51. The same plots also include the floating potential from PIC simulations operated with different boundary conditions on the electron flux Eq. 4.54 and Eq. 4.51.

4.2.4 Inclusion of Boltzmann electrons

In all our considerations the electron behavior is assumed to be adiabatic (Boltzmann), so that we can leverage on a simpler but approximated electron treatment to reach convergence on ion equilibrium time scales. Within the fluid model, Boltzmann electrons can be included analytically. However, in the PIC model the implementation of Boltzmann electrons requires

few caveats: (1) the Poisson equation turns from a linear problem into a nonlinear problem, requiring iterative schemes such as Newton-Raphson; (2) global charge conservation in the domain must be enforced in order to avoid undesired electrostatic oscillations; (3) when enforcing global charge conservation in an open domain of finite size (i.e., not periodic), proper boundary conditions must be taken into account, which for a magnetic field inclined of an angle ψ result in Eqs. 4.48–4.49.

In time-dependent conditions, the integral electron charge conservation within the domain can be expressed as

$$\frac{\partial(n_0 p)}{\partial t} + \frac{1}{4} v_e n_0 q \cos\psi = r, \tag{4.55}$$

where as usual [45] $p = \int_V \eta \mathrm{d}V$ and $q = \int_A \eta \mathrm{d}A$ are the volumetric and surface integrals of the Boltzmann exponential factor $\eta = \exp(e\phi/KT_e)$, and r is the rate of electron generation. Once discretized using finite differences, and after introducing a second-order under-relaxation necessary to speed up convergence to steady-state [45], Eq. 4.55 becomes

$$n_0^{t+\Delta t} = n_0 \left[(1-f) \frac{p^{t-\Delta t}}{p^t} + f - \frac{f^2}{4} \cos\psi \right] + \frac{r^t \Delta t}{p^t}. \tag{4.56}$$

Eq. 4.56 takes magnetic corrections (to the wall electron flux Γ_e) into account, extending the original unmagnetized Hagelaar scheme to the magnetized case.

4.2.5 Calibration of the correction terms using PIC

The effective collision frequencies ν_0 and ν_1 of Eqs. 4.46–4.47 have been calibrated using Particle-in-Cell simulations and a non-linear least-square minimization routine. The procedure used for calibration is made of the following steps:

- A Particle-in-Cell simulation is run using physical conditions of interest, and the profiles of the electric potential, ion density, and ion drift velocities are extracted from the simulation; from the same simulation the location of the sheath entrance is automatically recognized ($V_y = C_s$), as well as the potential drop across the collisional presheath $\Delta\phi_{presh}$, and the total length of the collisional presheath L_{presh}

- Hockney's collision frequency ν_{PIC} is calculated from PIC data as

$$\nu_{PIC} = F\frac{\omega_{pe}}{N_{ppc}}, \tag{4.57}$$

  where ω_{pe} is the local electron plasma frequency, N_{ppc} is the number of particles within a cell, and F is Hockney's correction factor; the average value ν^*_{PIC} in the collisional presheath is then obtained by averaging ν_{PIC} across the collisional presheath;

- The average collisional mean-free-path is calculated from

$$\lambda^* = \frac{C_s}{\nu^*_{PIC}\cos\psi} \tag{4.58}$$

  and used to normalize the spatial coordinate of the fluid model, $X = x/\lambda^*$. Note in Eq. 4.58 the dependence on the magnetic angle ψ;

- Finally, the ODE system of equations Eqs. [ref] deriving from the fluid model Eqs. 4.46–4.47 is integrated multiple times in order to best-fit the value of $\Delta = \hat{\nu}_{iz}/\hat{\nu}$ (non-dimensional collisional frequency) best-fitting the values of $\Delta\phi_{presh}$ and L_{presh} obtained from the PIC simulations. Here $\hat{\nu}_{iz} = \nu_{iz} + \nu_0$, and $\hat{\nu} = \nu + \nu_1$. In order to speed up the computation, the search is performed within a range $\Delta = [0, ..., 10]$, comprising most if not all cases of practical interest.

One example of calibration of the fluid model vs. PIC simulations is reported in Figures 4.20–4.21, for the simulation parameters of Table 4.1. The figures show a comparison of the profiles calculated from PIC simulations vs. the best-fit profiles obtained from the fluid model. Since most of the variability of the calibration parameters $\nu_{0,1}$ occurs as a function of the magnetic angle, the numerical tests have been performed as a function of the inclination ψ of the magnetic field with respect to the surface.

Figure 4.20 reports the plasma potential and the plasma density as a function of the spatial coordinate y perpendicular to the wall. Since the dependence on the magnetic angle affects both Γ_e and Γ_i, and since the spatial coordinate is stretched as a function of λ^* (Eq. 4.58), the profiles of electric potential and plasma density are independent than the

Table 4.1: PIC simulation parameters

		value	
L_y	cm	2	Domain size
N_y	#	1001	Number of grid nodes
n_e	m^{-3}	6×10^{16}	Plasma density
T_e	eV	10	Electron temperature
B_0	T	1.0	Magnetic field
ψ	deg	0, 25, 60, 85	Magnetic angle

magnetic angle.

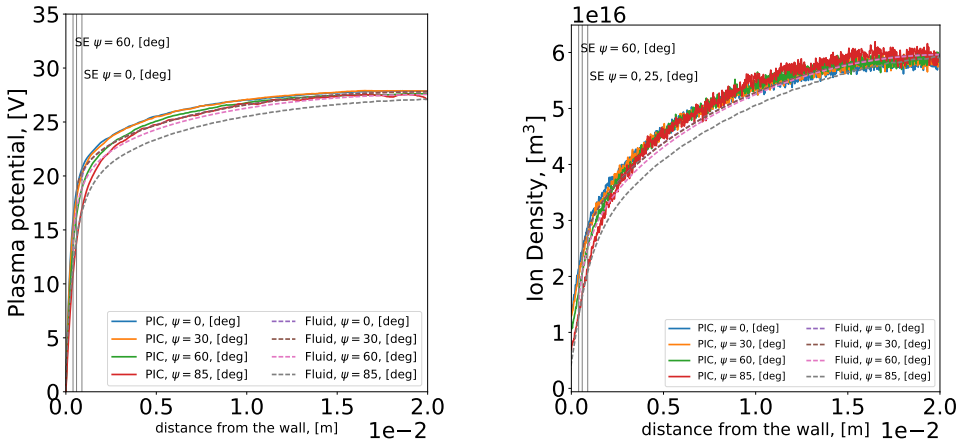

(a) Plasma potential

(b) Ion density

Figure 4.20: (a) Plasma potential and (b) plasma density as a function of distance from the wall, as obtained from the calibration procedure of the fluid model vs. PIC simulations.

Figure 4.21 reports the three components of the fluid velocity, plus one component of the particle flux Γ_x perpendicular to the wall, as obtained from the best-fit of the fluid model to the PIC simulations. Several interesting features are visible from the plots. First of all, the agreement between the calculated PIC profiles and the fluid model is remarkable, mainly thanks to the introduction of the correction factors ν_0 and ν_1 which allow to minimize the differences between models. Despite the simplistic assumptions of the correction terms $\nu_{0,1}$ introduced in Eqs. 4.46–4.47, the agreement between models suggest that the simple system of ODE equations of the fluid model is indeed able to quantitatively capture most

of the behavior of the first-moments of the plasma (drift velocity and particle fluxes) in the magnetic presheath. It is worth noting also that such a good matching can be obtained not only after the best-fit procedure, but also thanks to the rescaling procedure of the spatial coordinate y of the fluid model as a function of the mean-free-path $\lambda^*_{mfp} = C_s/\nu_t \cos\psi$, which account for the PIC collision frequency ν_t (Hockney's frequency) and compensate for the numerical effects introduced by the finite-size macroparticles of the PIC scheme. Interestingly, the component of the drift velocity perpendicular to the wall (Fig. 4.21(a)) is strongly affected by the magnetic inclination, shifting from an unmagnetized behavior at normal incidence ($\psi = 0$), down to subsonic conditions at grazing incidence ($\psi = 85°$). Similarly, the effect of the magnetic inclination is visible on the other two components of the drift velocity (Figs. 4.21(b)–4.21(b)) in direction parallel to the surface and along the E×B direction. The most outstanding feature is the fully three-dimensional nature of the plasma flow within the magnetic presheath, which stands out as a unique physical feature of the magnetized plasma sheath, and which is not present in unmagnetized conditions. Such a feature significantly affects the energy-angle distributions of the ions impacting on the wall, as analyzed also previously in this chapter.

4.3 Effect of the neutral drifts on the structure of Magnetized Plasma Sheath

Previous theoretical studies [35], [71] [74] of the magnetized plasma sheath have not considered the possibility of a flowing neutral background or the electric fields in the planes parallel to the material wall. Neutral flows in plasma devices can be created by relative position of the plasma discharge and vacuum pumps. For example, the helicon chamber (1.5m in length 15 cm in diameter) in the HELIX experiment [75] is connected to a much larger chamber on one side of the experiment (1.5m in diameter × 4.5m in length), and the gas source and smaller pump are installed on the other side of the discharge. Such configuration creates gradients of the neutral pressure, which can also create flows of neutrals. The global electric fields can be created by the configuration of the locations of the plasma sources and the

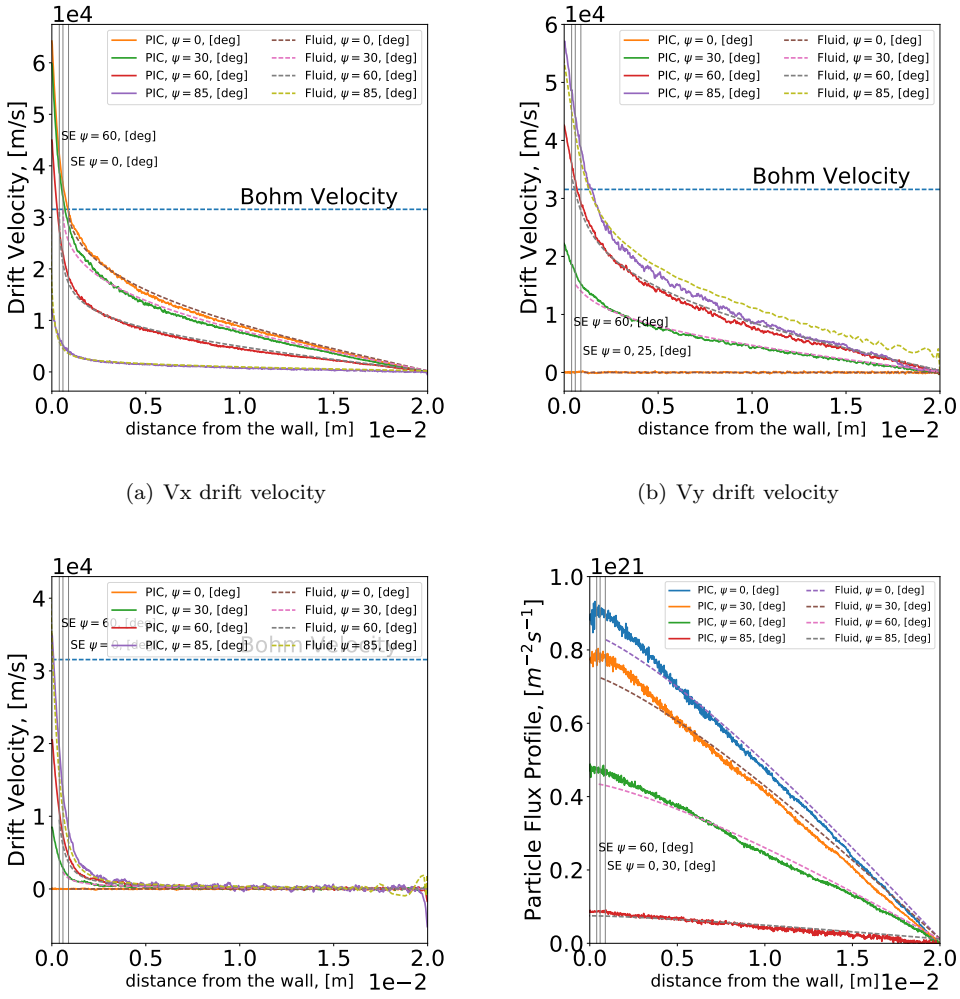

(a) Vx drift velocity

(b) Vy drift velocity

(c) Vz drift velocity

(d) Γ_x Particle Flux

Figure 4.21: (a) Plasma potential and (b) plasma density as a function of distance from the wall, as obtained from the calibration procedure of the fluid model vs. PIC simulations.

boundaries (vacuum chamber, tokamak limiters or tokamak divertors). In this section, we introduce the effect of neutral flows in our previous fluid model of the plasma sheath [35] in order to account for those effects. We perform a parametric study of the magnetized plasma sheath with the modified model. As will be shown in the following chapter, the presence of the neutral flows can affect the three-dimensional structure of the plasma sheath.

The population of neutral particles with the ensemble average velocity V^n creates a collisional friction force acting on the ions

$$\mathbf{F}_{in} = M_i \nu_{in} \mathbf{V}^n, \tag{4.59}$$

where ν_{in} is the frequency of the ion-neutral collision. The ion-neutral friction term is then added to the momentum balance equation of the fluid model 4.1

$$n_i M_i (\mathbf{V} \cdot \nabla)\mathbf{V} = n_i q_e (\mathbf{E} + \mathbf{u} \times \mathbf{B}) - \nabla p_i - M_i n_i \nu_i \mathbf{V} + M_i n_i \nu_{in} \mathbf{V}^n, \tag{4.60}$$

where frequency ν_i is the total collision frequency for ions, which can be split in a sum of the collision frequencies of ions with species j:

$$\nu_i = \sum_{j=1}^{J} \nu_{ij}. \tag{4.61}$$

In Argon plasmas, ν_i can be approximated as a sum of the ion-neutral and ion-electron collisions.

$$\nu_i = \nu_{in} + \nu_{ie}. \tag{4.62}$$

Then, the friction force in the momentum balance equation can be split into two components: the ion-electron friction force

$$- M_i \nu_{ie} \mathbf{V}, \tag{4.63}$$

and ion-neutral friction force

$$- M_i \nu_{in} (\mathbf{V} - \mathbf{V}^n), \tag{4.64}$$

The momentum balance equation becomes

$$n_i M_i (\mathbf{V} \cdot \nabla)\mathbf{V} = n_i q_e (\mathbf{E} + \mathbf{u} \times \mathbf{B}) - \nabla p_i - M_i n_i \nu_{ie} \mathbf{V} - M_i n_i \nu_{in} (\mathbf{V} - \mathbf{V}^n), \tag{4.65}$$

In this case, the continuity equation, isothermal equation of state for ions, and the Boltzmann statistic for electrons and quasi-neutrality are still valid in the plasma pre-sheath:

$$\nabla \cdot (n_i \mathbf{V}) = n_e \nu_{iz} \tag{4.66}$$

$$p_i = k_B T_i n_i, \tag{4.67}$$

$$n_i = n_e = n_0 \exp\left(-\frac{e\phi}{k_B T_e}\right). \tag{4.68}$$

Using non-dimensional variables (4.5) and (4.6), equations (4.65 - 4.68) can be rewritten as a system of non-dimensional ODEs that determine spatial derivatives of the velocity vector u

$$u_y \frac{\partial u_x}{\partial X} = \omega\tau \cos\psi - u_x + u_x^d \tag{4.69}$$

$$\left[1 - u_y^2\right] \frac{\partial u_y}{\partial X} = \Delta + \omega\tau \sin\psi u_y u_z + (u_y - u_y^d) u_y \tag{4.70}$$

$$u_y \frac{\partial u_z}{\partial X} = \omega\tau \left(u_x \sin\psi - u_y \cos\psi\right) - u_z + u_z^d. \tag{4.71}$$

The system of equations (4.69 - 4.71) is integrated until the Debye sheath entrance criterion is met, $u_y = 1$ from the initial conditions defined by the neutral drift velocity:

$$\mathbf{u}(x = 0) = \mathbf{u}_d^N. \tag{4.72}$$

In order to demonstrate the effect of the neutral drifts on the plasma sheath structure, the fluid model was executed for two test cases. In both of the test cases the values of $\Delta = 1$, u_z^n and u_x^n were fixed, and values of magnetic angle ψ and $\omega\tau$ were varied. In the first test case, the value of the neutral velocity had a non-zero value only in z-component $\mathbf{u}^d = [0, 0, u_z^d] = [0, 0, 0.6]$, and in the second test case x-component was set to a non-zero

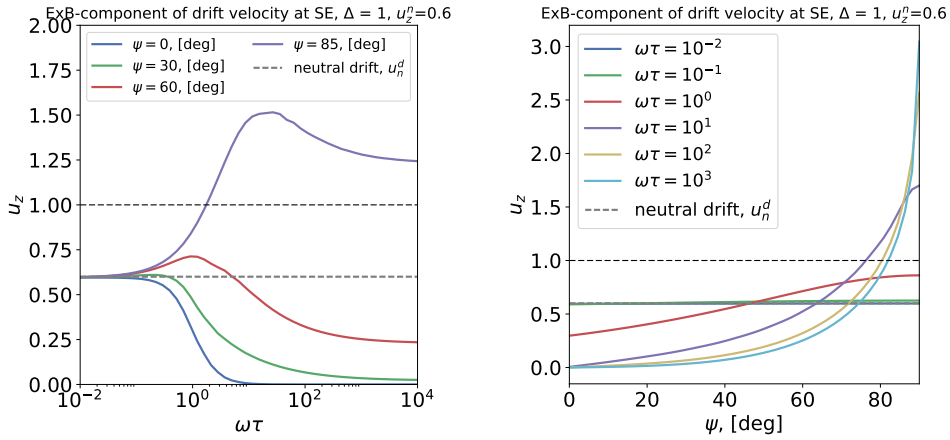

(a) ExB-component of ion drift velocity vs Hall parameter $\omega\tau$

(b) ExB-component of ion drift velocity vs magnetic angle ψ

Figure 4.22: ExB component of the drift velocity plotted against values of the Hall parameter $\omega\tau$ in the range 10^{-2} to 10^4 and values of the magnetic angle ψ from 0 to 90 degrees as predicted by fluid model; drift parameters: $u_x^d = 0$, $u_z^d = 0.6$.

value $\mathbf{u}^d = [u_x^d, 0, 0] = [0.6, 0, 0]$. Figures 4.22 and 4.23 show the results of the first and second test cases respectively.

Dependence of the x and z components of the ion drift velocity at the Debye sheath entrance as predicted by the fluid model on the Hall parameter ω and the magnetic angle is plotted on Figures 4.22 and 4.23 for the unmagnetized, partially magnetized and fully-magnetized plasma. In the unmagnetized plasma case, ion drift velocity matches the value of neutral drift velocity (see Figures 4.22(a) and 4.23(a)), and the values of the x and z z components of the ion drift velocity are independent of the magnetic angle ψ (see Figures 4.22(b) and 4.23(b)).

In the fully-magnetized case ($\omega\tau > 10^2$) the magnetized case, neutral drift flow does not affect plasma sheath structure. The value of the ExB-component(z) of the drift velocity at the normal incidence of the magnetic field $\psi = 0$ is zero $u_z = 0$. Value of the ExB component of the ion drift velocity is increasing with the magnetic angle, achieving supersonic values at the sheath entrance $M_z = 3.05$ when magnetic field is parallel to the wall $psi = 90$ deg and Hall parameter is large $\omega\tau = 10^4$ (see Figure 4.22(b)). y-component of the drift velocity

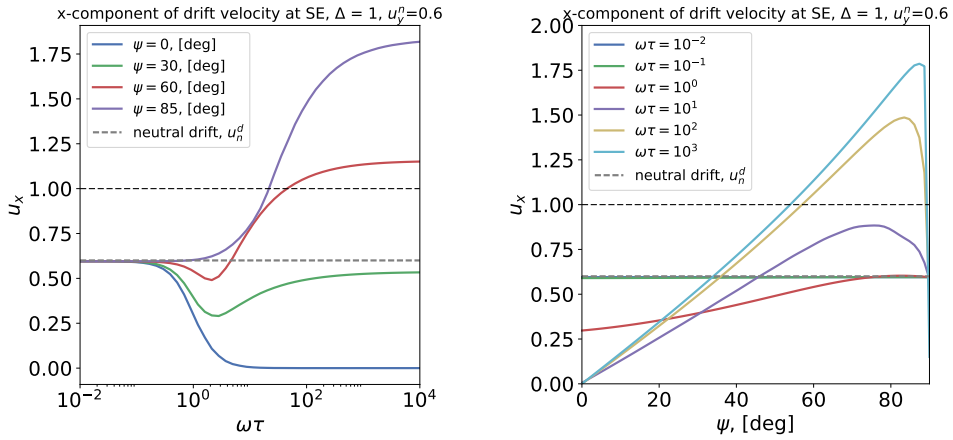

(a) x-component of ion drift velocity vs Hall parameter $\omega\tau$

(b) x-component of ion drift velocity vs magnetic angle ψ

Figure 4.23: x-component of the drift velocity plotted against values of the Hall parameter $\omega\tau$ in the range 10^{-2} to 10^4 and values of the magnetic angle ψ from 0 to 90 degrees as predicted by fluid model; drift parameters: $u_x^d = 0.6$, $u_z^d = 0$.

develops a unimodal dependence on the magnetic angle ψ (Figure 4.23(b)). The maximum of the curve is observed at some critical $\psi_c = 85 - 88$ degrees. The ion drift velocity u_x is increasing almost linearly when magnetic angle values are less than ψ_c; after the magnetic field attains ψ_c the x-component of the ion drift velocity u_x drops to 0.

The plasma sheath case is also affected by both neutral and magnetic effects in the partially-magnetized case. Both y and ExB components of the ion drift velocity undergo a nonlinear transition from the unmagnetized regime to a highly-magnetized regime. Thus, the x component of the drift velocity gradually drops to 0 from u_n^d as the Hall parameter $\omega\tau$ increases from 1 to 100 when the magnetic field is normal to the wall $\psi = 0$ deg (Figure 4.23(a)). The ExB component of the ion drift velocity increases with Hall parameter values $\omega\tau$ at grazing magnetic angle $\psi = 85$ deg, achieving maximum value of $u_z \approxeq 1.5$ at $\omega\tau$ 90 and dropping to a plateau at high magnetization. At intermediate magnetic angles the dependence of u_z on $\omega\tau$ resembles both normal and grazing magnetic field case: u_z attains maximum value at some $\omega\tau \in [1, 10^2]$, after which u_z decreases and reaches its magnetized value. Similar behavior is observed for the x component of the ion drift velocity. A similar

trend is observed for y-component of the ion drift velocity, but the y component attains a minimum instead of the maximum at intermediate values of the magnetic angle ψ, and the minimum is not observed at grazing magnetic fields (Figure 4.23(a)).

The combination of magnetic and neutral drift effects are best captured by the simulation with $\omega\tau = 1$. In the first test case, z component of the drift has value of 0.297 at $\psi = 0$ deg, which is less than neutral drift velocity $u_z^n = 0.4$. z-component of the ion drift velocity increases almost linearly to 0.861 at $\psi = 90$ degrees, surpassing neutral drift velocity at $\psi \approx 50$. In the second test case, when magnetic field is normal to the wall $\psi = 0$ the ion drift velocity $u_x = 0.297$ has value on the order of 50% of the neutral drift velocity $u_x^n = 0.6$. The component of ion velocity directed towards the wall is almost increasing with magnetic angle ψ, and reaches value of 1 at $\psi = 90$ deg (Figure 4.23(b)).

4.4 Conclusions

The Ion Energy-Angle Distributions at the boundary of a weakly-collisional magnetized plasma have been calculated for oblique magnetic fields inclined from normal ($\psi = 0$ degrees) to grazing incidence ($\psi = 85$ degrees). Two different methods have been used, namely a fluid-Monte Carlo method and an electrostatic Particle-in-Cell. The IEADs calculated with the two methods agree on their general trends, showing an energy peak scaled with the electron temperature at normal incidence, and peaks drifting along both the energy and the angular coordinate at higher magnetic angles.

According to the fluid model, the momentum gained by the ions in the presheath increases with the Hall parameter $\omega\tau$. Most of the ion acceleration occurs within the presheaths, collisional and magnetic. In the limit of high magnetizations ($\omega\tau \gg 1$) the peak ion energy increases with the magnetic angle. This increase is more evident at large inclinations.

The Particle-in-Cell calculations allow a self-consistent treatment of the problem, without the need to match a presheath model with a sheath model. According to the PIC calculations, the most probable ion kinetic energy at the wall is a weak function of the mag-

netic angle ψ. However, the size of the *magnetic* presheath increases with the inclination ψ; the magnetic presheath becomes the responsible of imparting most of the kinetic energy to the ions at large ψ angles.

The ion angular distributions exhibit surprising non-linear trends as a function of the inclination of the magnetic field. Both the fluid-MC model and the PIC show that the most probable angle of the ions at the wall are strongly dependent on the magnetic angle ψ. Contrarily to what is predicted by the simple fluid-Monte Carlo model, the PIC calculations evidence that ions never arrive at the wall at normal incidence, even when the magnetic angle is zero, $\psi = 0$ degrees. In the conditions typically encountered in tokamaks ($\psi \geq 85$ deg), the most probable angle of the ions at the wall is between 60-75 degrees, with implications for material properties. The calculated IEADs are useful in plasma-material interaction codes for the determination of the material wall response (implantation, sputtering, reflection, etc.) under plasma exposure.

Chapter 5

Validation of Magnetic Presheath Models using LIF Measurements

5.1 Introduction

The validation of the numerical simulations and plasma sheath models developed in the previous sections has been performed using three-dimensional tomographic Laser-Induced Fluorescence (LIF) data. The measurements have been performed by Siddiqui[75],[76] and Thompson [3]. The experiments of Thompson were performed as part of a scientific collaboration between the University of Illinois at Urbana Champaign and West Virginia University, in an effort to validate detailed kinetic models of the magnetic presheath against LIF measurements. A preliminary set of experimental data reported in [75] and [76] has been extended in a more extensive dataset [3] allowing direct comparison between PIC simulations and experimental measurements. The data included in this chapter were recent (2017-2018) LIF acquisitions kindly performed at the HELIX facility at West Virginia University by Derek Thompson and Professor Earl Scime. The HELIX facility features a unique capability of performing three-dimensional LIF measurements of ion velocity distribution functions on a magnetized plasma impacting on a material target with oblique magnetic field. The measurements include: the three components of the ion drift velocity, electron density, electrostatic potential, ion and electron temperatures, all measured at multiple locations in proximity of a material wall. Such an extensive quantity of data allows a detailed comparison between modeling results and experimental values, as will be shown in this chapter.

Section 5.2 describes the parameters of the experiments conducted by Thompson [3], reviewing the signal collection process and the procedure used for direct comparison of sim-

ulation results against experimental measurements. The simulation results of the validation procedure are reported in Section 5.4, with parametric analyses highlighting the role of the neutral pressure background, collisional effects, a background neutral drift, and an ambient electric field. The hypothesis of neutral flows and ambient electric fields are evaluated to describe the experimental data in highly-collisional conditions (Section (5.4)). The results of the simulation, neutral drift and ambient electric field hypothesis are discussed in Section 5.6.

5.2 Past and Current Experiments on Magnetized Plasma Sheaths

The experiments of Sidduqui [75], [76] and Thompson [3] have systematically analyzed the structure of the magnetic presheath in conditions of small Hall parameters, $\omega\tau_i \leq 1$. Those authors have reported accurate measurements of plasma temperature, plasma potential, plasma density, and drift velocity of the ions in the presheath at different values of the magnetic angle ψ.

The experiments were run at two different facilities, the MARIA facility at University of Wisconsin and the HELIX facility at West Virginia University, and presented in the works of Siddiqui [75], [76] and Thompson [1] [3]. The parameters of the typical plasma achieved at these facilities are summarized in table 5.2. The magnetic field in their experiments is still relatively small ($0.06 - 0.1$ T) and does not match the magnetic fields created in actual fusion devices. However, ion drifts along the ExB direction are expected also at such small magnetic fields, at levels sufficient to changing the structure of the plasma sheath.

The earlier LIF work of Siddiqui [75] was conducted at normal inclination of the magnetic field, $\psi = 0$ degrees, and report only one component of the ion drift velocity V_y. The later experiments of Siddiqui [76] have been conducted at multiple pressures, but ion drift velocities were reported only at a single value of the pressure $p = 1$ mTorr, and at four values of the magnetic angle $\psi = 16$, 30, 45, 60 degrees; in addition, only the component of the ion velocity parallel to the magnetic lines $V_{\parallel}$ is reported.

The recent LIF work of Thompson [3] extends the previous work of Siddiqui, providing the most complete dataset available nowadays in the plasma sheath literature. It includes all three components of the ion drift velocity in a region of several centimeters-cube in front of the target, with fine spatial resolution and acquisition points spaced only few millimeters apart. In addition, Thompson reports profiles of electron temperature and plasma potential at the same points where the LIF measurements were taken. The only drawback is that all measurements were taken at one single magnetic inclination, $\psi = 74$. Thompson's dataset represents the best data source for experimental validation to date. Thompson's dataset were used for the experimental validation of the magnetic presheath models developed as part of this work.

A linear device similar to HELIX is currently (2018) under construction at Oak Ridge National Laboratory (ORNL), to develop a next-generation helicon facility, MPEX [77], for the testing of plasma-material interaction processes in fusion-like conditions. A technological demonstrator named Proto-MPEX is currently operational at ORNL, representing the first step towards the full MPEX facility. Plans on installing additional diagnostics are also in place in order to improve the characterization of both the plasma in front of the target and the material plate facing the target.

5.3 Processing of Laser-Induced Fluorescence Data

5.3.1 Laser-Induced Fluorescence Technique

Laser-induced fluorescence (LIF) is a widely used spectroscopic technique that allows to resolve distribution functions, temperature and drift velocities of the particles in plasmas [78], [79], [80], [76], [75]. In LIF technique, the probing laser is tuned to the wavelength λ_{12} that corresponds to the energy of the selected excited the particles of a single plasma species from state S_1 with energy E_{s1} to the state s_2 with energy E_2 ($s_2 \rightarrow s_3$ process). The excited particle then emits the photons at wavelength λ_{23} as the electron moves from state E_2 to a lower energy state E_3 ($s_2 \rightarrow s_3$ process), which are registered on the detector. Appropriate selection of levels s_1, s_2 and s_3 is critical to LIF experiment: if the state s_1

Table 5.1: Parameters of the past and current magnetized plasma sheath experiments. The parameters and data for HELIX chamber is kindly provided by Derek Thompson [1], [2], [3]

Parameter	MARIA [76]	MARIA[75]	HELIX [1], [2], [3]
gas	Argon	Argon	Argon
rf power, W	500	650	650
L_x, cm	1-27	1-10	0-2.5
r_{ch}, cm	5	5	7.5
P, mTorr	3-4	1	3.6
r_p, cm	2	2	3-5
ψ, deg	0	16, 30, 45, 60	74
B	0.09 T	0.1T	0.06
T_n, eV	-	-	0.027
T_i, eV	0.1	0.1-0.6	0.4
T_e, eV	5-10, profile	2.5-5, profile	3-5 eV, profile
ϕ, V	40-50, profile	-	profile
n_e, m^{-3}	$1-3\times10^{16}$, profile	$1-3\times10^{16}$, profile	$1-5\times10^{17}$
V_y	profile	-	profile
V_x	-	-	profile
V_z	-	-	profile
$V_{\|\|}$	same as V_y	-	profile

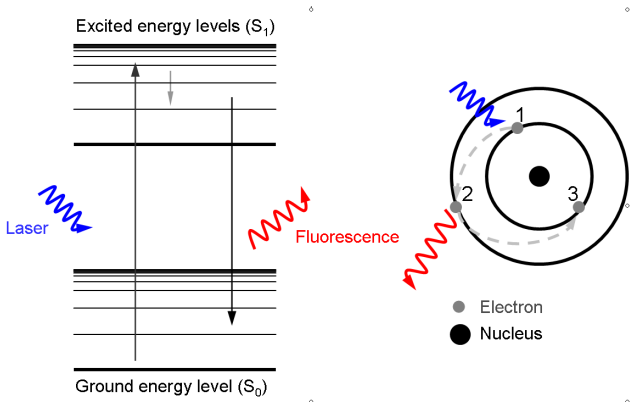

Figure 5.1: Example of the level diagram of an atom in the Laser-induced Fluorescence experiments. Blue wave denotes the incoming photon, red wave denotes photon emitted by the excited atom.

is scarce in plasmas then the production of secondary photons would not be sufficient for detection.

Due to the Doppler effect, the registered spectra of the secondary photons represent the line integral of the velocity distribution function of the plasma species: the particle moving at the speed V changes the frequency of registered photon. Thus, the particle velocity is determined as[78]

$$\Delta V = \frac{c\Delta\nu}{\nu_0 + \Delta\nu}, \tag{5.1}$$

where $\nu_0 = (E_{s2} - E_{s3})/h$ is the frequency of the photon emitted during relaxation process $s_2 \rightarrow s_3$, $\Delta\nu = \nu - \nu_0$ is the frequency shift observed due to Doppler effect, and c is the speed of light.

5.3.2 Tomographic LIF Measurements

The earliest tomographic LIF experiments have been conducted by Koslover [81] in 1986, and this technique has been applied in the the recent helicon experiments of Sidduqui [76], [75] and Thompson [1]. The velocities of the particles in LIF technique are resolved along the direction of the laser propagation. If the direction of the laser beam is given by angles $\phi = \arctan(V_y/V_x)$ and $\gamma = \arctan(V_z/\sqrt{V_x^2 + V_y^2})$ in spherical coordinates, the distribution function of the velocity $V_{\phi,\gamma}$ along the laser beam is defined as [82]

$$f\left(V_{\phi,\gamma}\right) = \int d^3\mathbf{x} \int d^3\mathbf{V} f\left(x, \mathbf{V}\right) \delta\left[\left(V_x \cos\phi + V_y \sin\phi\right)\cos\gamma + V_x \sin\gamma - V_{\phi,\gamma}\right]. \tag{5.2}$$

The velocity distribution function can be localized using tomographic techniques (see Figure 5.2): the secondary photons emitted by excited particles are collected from a small region of the plasma using angle-limited collection optics. Due to the finite focusing power, the collection optics blurs the collected signal. If the response function of the optical system is given by a function $K_o(\mathbf{x})$, the registered signal represents convolution of the distribution function $f(\mathbf{x}, \mathbf{V})$

$$f_c\left(\mathbf{x}, \mathbf{V}\right) = \int d^3\mathbf{y} f\left(\mathbf{y}, \mathbf{V}\right) K_o\left(\mathbf{x} - \mathbf{y}\right). \tag{5.3}$$

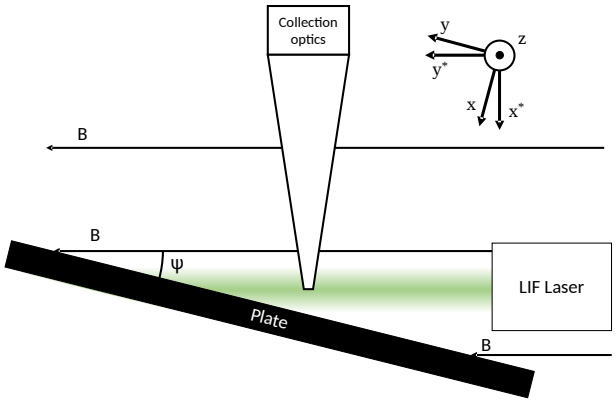

Figure 5.2: Schematic diagram of Tomographic Laser Induced Fluorescence measurements of the velocity distribution function in a typical helicon experiment. x^*, y^* denotes the experimental coordinate system, x and y denote the simulation coordinate system.

Furthermore, the collected signal is distorted by the width of the LIF laser characterized by the beam cross-section $K_l(\mathbf{x})$. Thus, the signal registered on the spectrometer f_{cl} is a result of two convolutions: first, the convolution with optics response, and second, the convolution with the laser beam shape.

$$f_{cl}\left(\mathbf{x},\mathbf{V}\right)=\int d^3\mathbf{y} f_c\left(\mathbf{y},\mathbf{V}\right)K_l\left(\mathbf{x}-\mathbf{y}\right). \tag{5.4}$$

5.3.3 Considerations on the spatial resolution of the LIF signal

Due to relatively large widths, LIF laser beams excite relatively large columns of plasma (1-2 cm), limiting the spatial resolution of the collected signal: the registered velocities are gathered from all of the locations that interacted with laser. The radial intensity $I_l(r)$ of electromagnetic fields produced by laser can be usually well approximate by Gaussian profile (see Figure 5.3(a))

$$I_l(r)=I_0\frac{1}{\sqrt{2\pi}\sigma_l}\exp\left(-\frac{r^2}{2\sigma_l^2}\right), \tag{5.5}$$

where I_0 is the normalization of the constant for the laser intensity. The radial (spatial) resolution of the LIF laser is characterized by the length-scale of the Gaussian beam σ_l, and

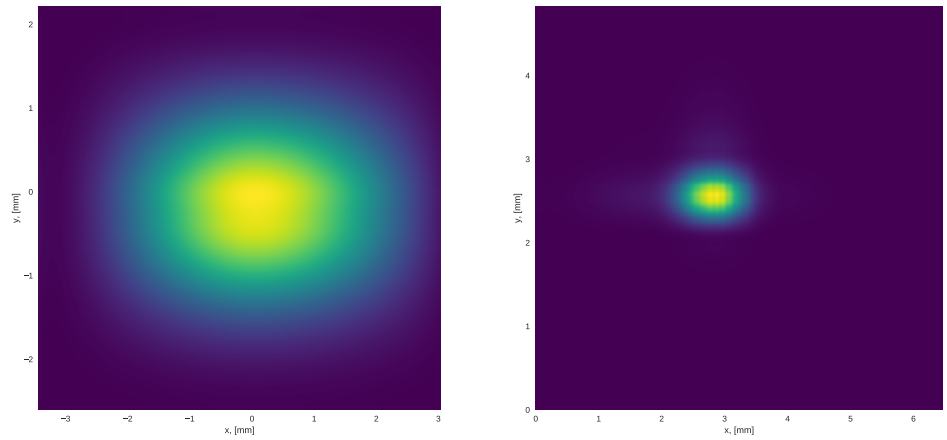

(a) The profiles of the LIF laser probing x^*z plane (b) Signal response of the telescope at the focus

Figure 5.3: Cross-section of the LIF laser beam and the profiles in the Helix experiments with confocal telescope detector. The data is courtesy of Derek Thompson [1], [2], [3]

the corresponding response function of the laser beam is Gaussian as well

$$f_l(r) = \frac{1}{\sqrt{2\pi}\sigma_l} \exp\left(-\frac{r^2}{2\sigma_l^2}\right). \tag{5.6}$$

The LIF laser is collected by the of the detector optics, which further reduces the spacial resolution of the detected signal. Thus, the view sight of the confocal telescope installed in the HELIX chamber can be approximated by the hyperboloid and collected the light emitted by excited particles at the focal point from almost circular area with diameter of 1-2 mm. The response function at focal point where confocal telescope achieves the best resolution can be effectively approximated by Gaussian function (5.6) with the length scale (standard deviation) of σ_o (see Figure 5.3).

5.3.4 Rotation of Reference Frames

In plasma sheath models, it is common to assume that the gradients of the plasma properties are not observed in the planes parallel to the wall. It is sufficient to conduct simulation with one spacial dimension $D_x = 1$ and three components of the velocity $D_V = 3$ in the

Table 5.2: Measurement configuration of the confocal optics collection axis and the laser injection axis in the HELIX experiment.

Velocity Component	V_x^*	V_y^*	V_z
Laser Injection Axis	x^*	y^*	z
Detector Collection Axis	z	x^*	x^*

simulation frame $x - y - z$. However, the three-dimensional ion velocities are measured in the laboratory frame $x^* - y^* - z$, which is dictated by the location of the windows in the HELIX experiment: the confocal telescope are installed on the side and top of the chamber with a field of view along x^* and z axis. The LIF laser directed along $x*$, y^* and z axis is probing each respective component of the ion velocity. In order to compare the modeled and experimental velocities, the ion drift velocities collected in the LIF experiments have to be converted back to simulation frame and vice-versa:

$$V_x = V_x^* \cos\psi + V_y^* \sin\psi \tag{5.7}$$

$$V_y = -V_x^* \sin\psi + V_y^* \cos\psi \tag{5.8}$$

$$V_x^* = V_x \cos\psi - V_y \sin\psi \tag{5.9}$$

$$V_y^* = V_x \sin\psi + V_y \cos\psi, \tag{5.10}$$

where V_x^* and V_y^* denote the x^* and y^* components of the ion velocity (see Table 5.3.4).

Similar treatment must be applied to ion distribution functions. Since rotation is a linear transformation, the conversion of the distribution function between the laboratory and simulation frames can be done with variable substitution using equations (5.10),

$$f\left(V_x, V_y, V_z\right) = f^*\left(V_x \cos\psi - V_y \sin\psi, V_x \sin\psi + V_y \cos\psi\right) \tag{5.11}$$

$$f^*\left(V_x^*, V_y^*, V_z^*\right) = f\left(x, V_x \cos\psi - V_y \sin\psi, V_x \sin\psi + V_y, V_z\right) \tag{5.12}$$

which returns the distribution function on the rotated frame.

5.3.5 Transfer Functions of the Collection Optics

In the simulation frame, the convolution process of the drift velocities and the distribution function with the system response function becomes much simpler, as the diagnostic optics and the laser beams blur the underlying data only along the x axis (plasma is uniform in $y-z$ planes). Figure 5.4 demonstrates an example of the measurement configuration of the y^* component of the velocity with the collection optics aligned with x^* axis. Assuming that the $K(x)$ is the arbitrary kernel, which represents either optics response function or laser beam profile, the kernel response along x for an optical system applied along axis x^*, y^* or z can be approximately projected to the simulation frame as

$$K_{x^*}(x) = \frac{K(x)}{\cos\psi} \tag{5.13}$$

$$K_{y^*}(x) = \frac{K(x)}{\sin\psi} \tag{5.14}$$

$$K_z(x) = K(x). \tag{5.15}$$

For high values of magnetic angle ψ, the largest broadening of the kernel K is observed when the optical system is applied along x^* axis, the kernel K is weakly affected by ψ, and the optic applied along z axis is not altered when transitioning from laboratory to simulation frames. Thus, the detection system in HELIX is applied along the x^* axis only to measure V_z component of the drift velocity as there is no alternative location for the detector in the vacuum chamber. The effective response of the optical system and LIF laser is given by product of the laser kernel K_l and collection optics kernel K_o in the simulation frame along axis x

$$K_{lo}(x) = K_l(u)K_o(u). \tag{5.16}$$

If the kernels of the diagnostic system and the laser beam on the x axis can be effectively approximated by one-dimensional Gaussian distributions with scale parameters σ_l and σ_o, the the effective response function of the system K_{lo} is also Gaussian with the the scale

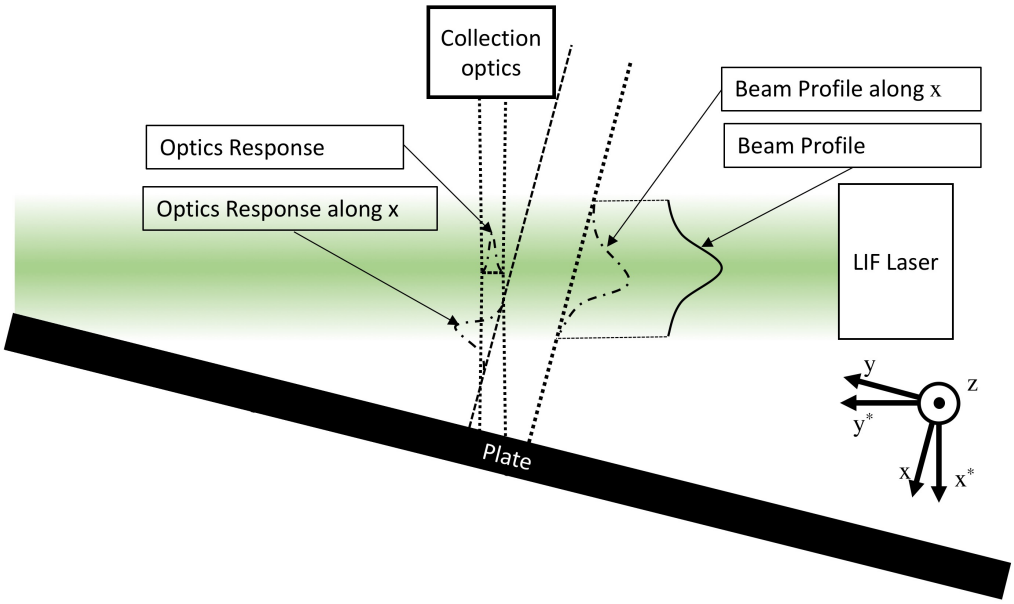

Figure 5.4: Example of the profile projection for the measurement of the y^* component of the ion drift velocity with the collection optics aligned with the x^* axis.

parameter

$$\sigma_{lo} = \sqrt{\frac{\sigma_l^2 \sigma_o^2}{\sigma_l^2 + \sigma_O^2}}. \tag{5.17}$$

The first section of Table 5.3.5 reports the scale parameters of the collection optics and laser profile collected/injected along x^*, y^* and z axis. The telescope is placed only along x^* and z axis. The lasers that are using to x^* and z components of the ion velocity are identical having broadening $\sigma_l = 0.235$ mm, and a different laser with broadening $\sigma_l = 0.191$ mm is used to excite ion along y^* axis. The second section of Table 5.3.5 reports the broadening of the aforementioned collection optics and laser profiles along x axis in the simulation coordinate system. The maximum blur is observed for x^* projection as expected. Finally, the last section of Table 5.3.5 reports the effective broadening of the $x*$, y^* and z of the ion velocity along x axis of the simulation coordinate system. The effective value is calculated using equation (5.17) considering the measurements configuration of the collection optics and laser reported in Table 5.3.4. The maximum blur of the registered particle velocity is

Table 5.3: Broadening of the laser and telescope response function injected/collected along $x*$, y^* and z axes, projections of the laser and telescope profiles along x axis of the simulation frame, and effective collection values. The laser and telescope broadening data is calcualted from the Derek Thompson [1], [2], [3]

Injection/Collection Axis	x^*	y^*	z
Injection Profile:			
Telescope σ_o, mm	0.392		0.392
LIF Lasers σ_l, mm	0.997	0.550	0.997
Projection Profile along x axis:			
Telescope σ_o along x axis, mm	1.42	-	0.392
LIF Lasers σ_l along x axis, mm	3.62	0.572	0.997
Velocity component along x axis	V_x^*	V_y^*	V_z
Effective σ_{ol}, mm	0.389	0.531	0.816

observed for x^* and z components achieving resolution of $2-3$ mm along x axis ($2-3\sigma_{ol}$).

Thus, the comparison process of the LIF experimental data and computational plasma sheath models can be separated into three steps: 1) convert simulated ion velocities from simulation to laboratory coordinate system using equation (5.10); 2) Convolve each component of the simulated ion velocities in the laboratory coordinates with the effective response function, approximated by Gaussian function with σ_{ol} reported in Table 5.3.5; 3) convert convolved simulation and experimental velocities from experimental coordinates to simulation coordinates and compare results.

5.3.6 Collisional Processes in Helicon Discharges

At the range of the plasma parameters that were used in HELIX and MARIA experiments it is important to take collisional processes into consideration in the plasma boundary region. Ion-neutral collisions, namely charge exchange and elastic scattering, are among the fastest reactions in the discharge:

$$\mathrm{Ar} + \mathrm{Ar}^+ \quad \rightarrow \quad \mathrm{Ar}^+ + \mathrm{Ar} \quad \text{(Charge Exchange)} \tag{5.18}$$

$$\mathrm{Ar} + \mathrm{Ar}^+ \quad \rightarrow \quad \mathrm{Ar} + \mathrm{Ar}^+ \quad \text{(Elastic Scattering)} \tag{5.19}$$

Even though charge exchange and elastic scattering collisions are described by similar equations, they are different in nature. In a charge exchange collision, a neutral Argon atom exchanges an electron with the ionized Argon particles. Thus, effectively the neutral particle and charge particles "swap" their plasma population. On the other hand, the ion and neutral particles exchange energy and momentum in the elastic scattering process while remaining in the same plasma population. The details of the numerical simulation of the elastic scattering process is described in details in section 2.4.3.

The cross-section of charge exchange and elastic scattering collisions are well studied and are available in literature [44]. For a colliding particle with energy E in eV, the charge-exchange cross section is parametrized in hPIC as

$$\sigma_{CX}(E) = \begin{cases} 0 & E < 0 \\ 1.065 \times 10^{-18} - 2.95 \times 10^{-19}\sqrt{E} & 0 \geq E < 4 \\ 2 \times 10^{-19} + \frac{5.5 \times 10^{-19}}{\sqrt{E}} & 4 \geq E \end{cases}, \tag{5.20}$$

and the ion-neutral elastic scattering is defined as

$$\sigma_{SC}(E) = \begin{cases} 0 & E < 0 \\ 7.8 \times 10^{-19} - 2.0 \times 10^{-19}\sqrt{E} & 0 \geq E < 4 \\ 1.8 \times 10^{-19} + \frac{4 \times 10^{-19}}{\sqrt{E}} & 4 \geq E \end{cases} \tag{5.21}$$

The cross-section of the electron-impact ionization is given as

$$\begin{aligned} \sigma_{iz}(E) &= I(E > 15.76)\frac{1.36 \times 10^{-18}}{E} \log\left(\frac{E + 120/E}{15.76}\right) \\ &\times \left[\arctan\left(\frac{E^2 - 9.76 \times E + 2.4}{20.6 \times E + 206}\right) \arctan\left(\frac{2E - 80}{10.3E + 103}\right)\right], \end{aligned} \tag{5.22}$$

where I is an indicator function. Figure 5.5 reports the plots of the relations (5.20), (5.21) and (5.23). The cross-section of the charge-exchange collisions is more than two times larger than the elastic scattering cross-section as shown on Figure 5.5(a) [44], and both of

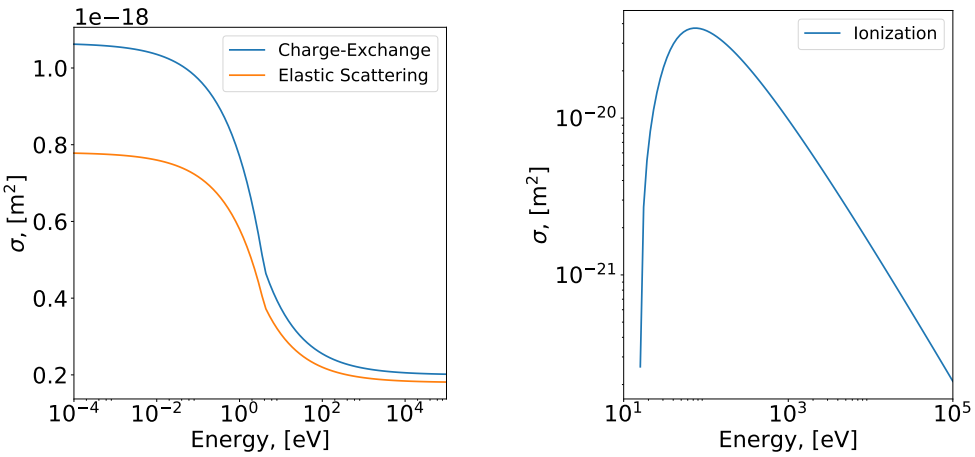

(a) Charge Exchange and Elastic Scattering cross-sections

(b) Electron impact ionization cross-section

Figure 5.5: Collision cross section of the charge exchange, scattering and electron impact ionization collisions for Argon.

the processes dominate in the low-temperature plasmas. The ionization cross-section peaks at ~ 100 eV, and its contribution to the discharge equilibrium diminishes at lower energies. Assuming that particle velocities follow a Maxwellian distribution, the collision frequencies of charge exchange, elastic scattering and electron impact ionization are evaluated using equation (2.147). The effective frequency of ion-neutral collisions is then found as a sum of the charge-exchange and elastic scattering collision frequencies:

$$\nu_{in} = \nu_{cx} + \nu_{sc}. \tag{5.23}$$

The charged particles interact with each other mostly by means of the electrostatic forces. The full derivation of the collision frequency is quite extensive, and this section summarizes the common expression used in this work. Thus, the ion-ion collision frequency ν_{ii} for thermalized population of ions (Maxwellain velocity distribution) is found as

$$\nu_{ii} = \frac{e^4 Z^4 n_i \ln \Lambda_{ii}}{12\pi^{3/2}\varepsilon_0^2 \sqrt{m_i}\,(k_B T_i)^{3/2}} \tag{5.24}$$

where Z is the ion charge number, m_i is the ion mass, T_i is the ion temperature, and $\ln \Lambda_{ii}$ is the Coloumb logarithm for the ion-ion collision, which is determined as

$$\ln \Lambda_{ii} = 17.3 - \frac{1}{2} \log \left(\frac{n_i}{10^{20}} \right) + \frac{3}{2} \log T_i[\text{keV}]. \tag{5.25}$$

Similar expression is available for the electron-ion collisions

$$\nu_{ei} = \frac{12\pi^{3/2} \varepsilon_0^2 \sqrt{m_e} T_e^{3/2}}{\sqrt{2} z^2 e^4 n_e \ln \Lambda_{ei}}. \tag{5.26}$$

The expression of the Coulomb logarithm Λ_{ee} for electron-ion collisions can be approximately evaluated as

$$\lambda_{ei} = 15.2 - \frac{1}{2} \ln \left(n_e / 10^{20} \right) + \ln T_e[\text{keV}]. \tag{5.27}$$

The ion-electron collision frequency is then obtained from electron-ion collision as

$$\nu_{ie} = \frac{n_e m_e}{n_i m_i} \nu_{ei}. \tag{5.28}$$

The recent work of Baalrud [83], [84], and Yip [80] has demonstrated that the Coulomb collision frequency described by classical expressions (5.24) and (5.26) can be enhanced when streaming instabilities develop in plasma sheath. The instabilities are damped in the plasma sheath if the damping parameter η is smaller than 1,

$$\eta = \frac{l_{mfp} \sqrt{\pi m_e / 16 m_i}}{\lambda_D}, \tag{5.29}$$

where l_{mfp} is the ion-neutral collision mean free path.

Table 5.3.6 reports the collisional frequencies in the MARIA and HELIX helicon experiments for the plasma parameters reported in Table 5.2. In HELIX experiments ion-neutral collisions have higher frequencies than other processes. However in the MARIA experiment, the ion-ion collision frequency is much higher than the ion-neutral collision frequency. In addition to that, the MARIA experiment [75] should be observing the enhanced ion-ion collisions; even so, the ion-ion collisions should not perturb the plasma sheath equilibrium.

Table 5.4: Typical ion collision cross-sections and frequencies at $n_n = n_0$.

Process	MARIA [76]	MARIA [75]	HELIX
gas	Argon	Argon	Argon
Neutral Density n_n, m^{-3}	9.3×10^{19}	3×10^{19}	1.1×10^{20}
Charge Exchange ν_{in}^{CX}, Hz	1.154×10^5	4.573×10^4	1.646×10^5
Elastic ν_{in}^{E}, Hz	8.633×10^5	3.452×10^4	1.243×10^5
Total Ion-Neutral ν_{in}, Hz	2.017×10^5	8.025×10^4	2.889×10^5
Ionization ν_{iz}, Hz	6.522×10^3	2.174×10^3	2.655×10^4
Ion-Ion ν_{ii}, Hz	1.356×10^6	2.368×10^5	1.236×10^5
Ion-Electron ν_{ie}, Hz	39.2	16.2	40.4
Dampening Parameter, η	0.606	1.364	0.466
Ion Hall Parameter, $\omega\tau_i$	0.139	0.565	0.351

5.3.7 Accounting for Neutral Depletion

As mentioned earlier, helicon discharges are capable of generating plasma of high electron density at relatively low power. The discharge is generated by means of a RF-antenna [85] that excites whistler waves bounded in a cylinder. The electrons in the plasma are heated through collisional processes via resistive heating. In order to sustain the propagation of helicon plasma waves, the discharge must be operated at low pressure (of few millitorrs), in a regime of medium-to-low collisionality. The radial equilibrium of a cylindrical helicon discharge [86] is such that the plasma density is peaked at the center while the neutral density is *depleted* at the center of the cylinder. The neutral depletion process can be understood using a diffusive model (see for example Gilland, [5]) that takes into account the competition between the outward radial diffusion from the core of the discharge, the inward flux of neutral species from outside of the discharge, and the ionization/recombination of the charged particles,

$$\frac{\partial}{\partial r}\left(D\frac{\partial n_n}{\partial r}\right) - \frac{n_n V_T^n \pi r_p}{2A_c} + \frac{n_e \pi r_p^2}{\tau A_c} = 0, \tag{5.30}$$

where r is the radius from center of the discharge, n_n is the density of the neutral population, V_T^n is thermal speed of neutrals, D is the diffusion coefficient, r_p is the radius of the plasma column, n_e is the electron density, τ is particle confinement time, and A_c is the area of the

neutral region outsize of the plasma

$$A_c = \pi(r_d^2 - r_p^2), \tag{5.31}$$

where r_d is the radius of the chamber. The diffusion coefficient is determined through the effective ion-neutral collision cross-section, which is dominant in helicon discharges:

$$D = \frac{V_T^i}{n_0 \sigma_{in}}. \tag{5.32}$$

Equation (5.30) is solved numerically for the given plasma parameters. The radial profiles of the relative neutral density $n_n(r)/n_n(r_p)$ calculated using equation (5.30) for the described plasma helicon experiments are reported in Figure 5.6. The diffusion model assumes that the neutral density recovers to the values of the ambient gas density at the boundary of the plasma r_p. Thus, the neutral density profiles have been evaluated for several possible values of the plasma column radius. The larger values of the plasma column to chamber radii ratio r_p/r_{ch} yield smaller values of the relative neutral density as the plasma occupies more volume of the vacuum chamber, and the number of neutrals outside of the chamber becomes smaller. Depending on the plasma radius, Gilland's model predicts the relative neutral densities in the range $0.44n_0$ to $0.9n_0$ at the center of the HELIX experiment, and the range of the relative neutral densities in MARIA experiment is $0.89n_0$ and $0.96n_0$. Such a difference in the relative densities between MARIA and HELIX is caused by the different plasma-to-chamber-radius ratio: the HELIX chamber has a radius of 7.5 cm with a plasma radius of 5 cm, compared to MARIA which has a chamber radius of 5 cm and a 2 cm plasma radius. Thus, the frequency of the collisional processes that involve neutral species in the helicon discharges is reduced by relative neutral density $n_n(r)/n_0$

$$\nu_{CX}(r) = \nu_{CX} n_n(r)/n_0 \tag{5.33}$$

$$\nu_{SC}(r) = \nu_{SC} n_n(r)/n_0 \tag{5.34}$$

$$\nu_{in}(r) = \nu_{in} n_n(r)/n_0 \tag{5.35}$$

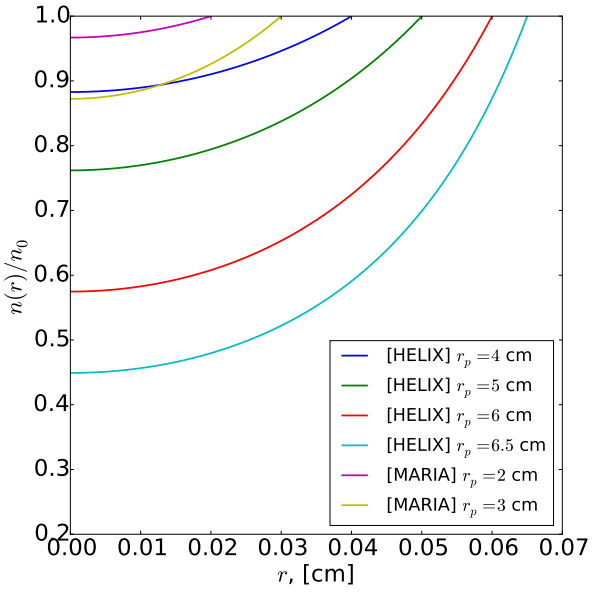

Figure 5.6: Radial dependence of the the relative neutral density $n(r)/n_0$ according to Gilland's model [5] for HELIX and MARIA experiments.

$$\nu_{iz}(r) \quad = \quad \nu_{iz} n_n(r)/n_0 \tag{5.36}$$

The appropriate values of $n_n(r)/n_0$ can be estimated by matching the numerical model to the experimental results.

5.4 Validation of Fluid and PIC simulations vs. LIF measurements

5.4.1 Role of Neutral Pressure and Collisionality

Particle-in-Cell simulations of the HELIX experiment were carried in a 1D3V setup (one spatial dimension and three velocity coordinates) resolving gradients of the plasma properties along the axis x shown in Figure 5.2. The simulation covered a plasma domain of size $L_x = 2.5$ cm discretized with a structured grid of 1000 cells. Electrons were treated adia-

batically as described in section 2.5. A total of 50000 computational particles was used in the simulations, which were conducted in both collisionless and collisional conditions. The collisional physics was resolved for ion-neutral interaction at various gas pressures $p = 0.1$, 0.36, 1.8, 3.24 and 3.6 mTorr using the Monte-Carlo Collision (MCC) approach described in section 2.4.2. The simulated profiles were treated for comparison with experimental measurement using methodology described in section 5.3.2. The particles were injected at the right boundary of the Particle-in-Cell simulation domain as Maxwellian thermal fluxes with temperature $T_i \approxeq 0.4$ eV and drift velocity $\mathbf{V} = [600, 1500, 60]^T$ m/s as measured at the boundary of the acquisition box in HELIX. The neutral species were assumed to be thermalized at temperature $T_n = 0.027$ eV with no drift.

Simulations under the same conditions were run also using the fluid model, which was solved numerically with Dirichlet boundary conditions on the right boundary for the drift velocity $\mathbf{u} = [0.2, 0.51, 0.002]^T$ (same values as before, but normalized with respect to the Bohm acoustic speed C_s) and electric potential $\phi(L_x) = 0$ V. Since collision frequencies for ion-neutral processes reported in table 5.3.6 are affected by neutral depletion, the density of neutrals in the fluid model was parametrically varied in order to match the experimental data. The calculations based on this approach yield a total ionization frequency of $\nu_i = 188$ kHz, which corresponds to reduction of the gas pressure by 40% in the discharge ($n_n = 0.6 n_0$).

Figures 5.7, 5.8 and 5.9 report the three components of the ion drift velocity (v_x, v_y, v_z respectively) as measured in the HELIX experiment and the comparison to values calculated by means of Particle-in-Cell simulations and of the fluid model. The LIF measurements are represented by blue dots, while the dashed and solid lines represent the simulated and blurred ion velocity profiles given by the plasma sheath models.

Based on results of the simulations, the V_x component of the ion velocity is in excellent agreement with the fluid model predictions: the "blurred" profile denoted by the black line follows experimental measurements almost exactly up to the Debye sheath entrance, after which fluid model is no longer valid. Ion velocities are expected to be supersonic in the Debye sheath, but the LIF signal reports values in the subsonic range. A close analysis

reveals that the measured LIF signal close is affected by spurious reflections in a region of few millimeters from the surface, mainly due to blurring of the collection optics and of the stray reflection of the LIF laser beam from the surface. As a consequence, the measured ion drift velocity at the Debye sheath entrance saturates at $\sim 0.8C_s$, while the calculated value predicted by the fluid and kinetic models is C_s, with a percent difference of 20%.

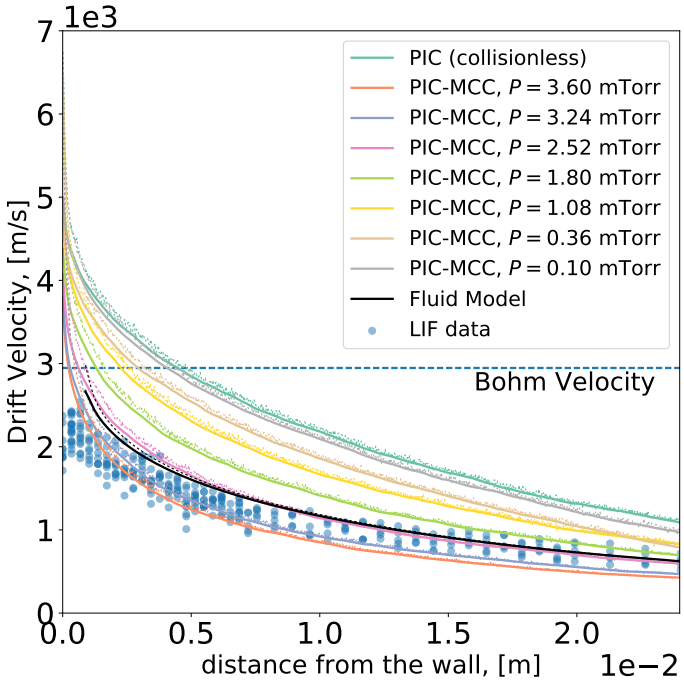

Figure 5.7: Comparison of calculated and measured ion drift velocity (V_x component, perpendicular to the wall) over a range of neutral gas pressures. Values are expressed in a reference frame with origin at the surface plate and pointing toward the plasma. Experimental values were measured using Laser-Induced Fluorescence at the HELIX facility in Argon plasma at $T_e = 4.0 \pm 1.0$ eV. Numerical simulations were performed using: a collisional fluid model, a collisionless Particle-in-Cell code, a collisional Particle-in-Cell for Ar gas pressures of p =0.1, 0.36, 1.08, 1.80, 3.24 and 3.60 mTorr. Solid lines report the convolution of the simulated profiles (dots) with the system response function reported in Table 5.3.5.

Figure 5.7 shows that an increase in ion-neutral collisionality reduces the ion drift velocity in both the presheath ($x > 0.1$) and the sheath ($x < 0.1$) regions. Furthermore, a scan over the pressure allows to indirectly measure the amount of neutral depletion in the presheath

thanks to an indirect measurement of the neutral pressure at the same location. In fact, the simulations show that values of the gas pressure higher than $p = 3.24$ mTorr correspond to ion drift velocities lower than the measured values; pressures lower than $p = 2.0$ mTorr return drift velocities higher than the measured values. A best-fit of the data returns a pressure of $p = 2.52$ mTorr in excellent agreement with the experimental measurements within the presheath region, $x > 0.5$. This indirect measurement of the neutral pressure, $p = 2.52$ mTorr, indicates values of the ion drift velocity of $1.2C_s = 3500$ m/s, which can be compared against the experimental observation of $0.85C_s = 2500$ m/s, a percent difference of 30%. Finally, our indirect measure of the neutral pressure in the presheath allows to measure the amount of neutral depletion in the presheath. The neutral pressure decreases from the pre-discharge value of 3.4 mTorr down to 2.5 mTorr, giving a 28% reduction due to neutral depletion.

Figure 5.8 reports the ion drift velocity along the direction parallel to the plate (V_y component). The data show that the ion flow remains almost constant along the y direction at a value half that of Bohm's acoustic speed $V_y(2.5 \text{ cm}) = 0.51C_s = 1500$ m/s on the right boundary and a slightly larger value at the wall $V_y(0\text{cm}) = 0.58C_s = 1700$ m/s. As mentioned earlier, the Particle-in-Cell simulations and the fluid model are each initialized with a Dirichlet boundary condition on the right boundary $V_y(2.5 \text{ cm}) = 0.51C_s$, and the ion population is let free to evolve across the presheath and sheath. Surprisingly, the collisional fluid model predicts an ion drift velocity V_y dropping to approximately $0.1C_s$ due to viscous effects in the presheath, which is in good agreement with Particle-in-Cell results at pressures of $p = 3.24$ mTorr, but in total disagreement with the LIF experimental values. A match between calculated and measured values is reconciled when an additional source of momentum is considered, acting preferentially along the y direction. As will be shown later, such a source of momentum can be interpreted in two ways, either as a viscous term, or as an electric-field term. As will be shown later, the most reasonable conclusion will be the latter; here we show that considering a viscous term would lead to the unreasonable conclusion of having a lower pressure only along the y direction (in disagreement with the other two directions x and z). In fact, as Figure 5.8 shows, the Particle-in-Cell simulations

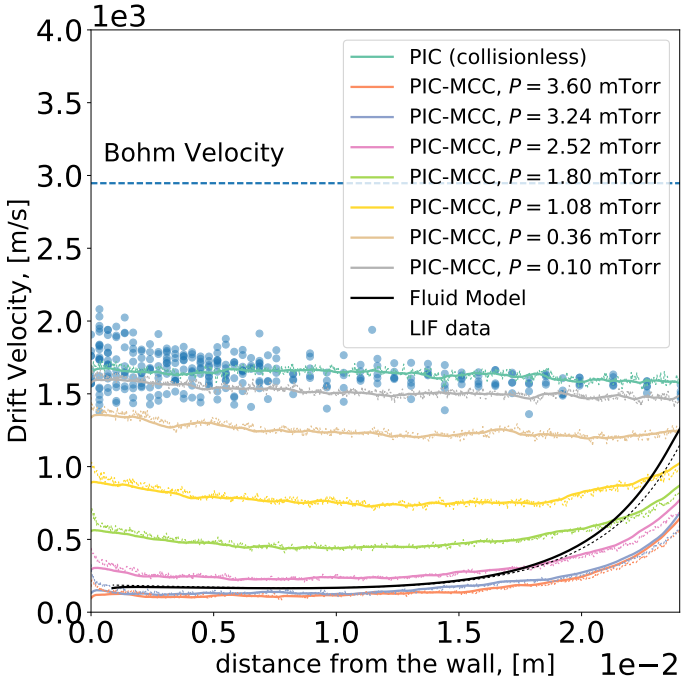

Figure 5.8: Comparison of calculated and measured ion drift velocity (V_y component, parallel to the wall) over a range of neutral gas pressures. Values are expressed in a reference frame with origin at the surface plate and pointing toward the plasma. Experimental values were measured using Laser-Induced Fluorescence at the HELIX facility in Argon plasma at $T_e = 4.0 \pm 1.0$ eV. Numerical simulations were performed using: a collisional fluid model, a collisionless Particle-in-Cell code, a collisional Particle-in-Cell for Ar gas pressures of p =0.1, 0.36, 1.08, 1.80, 3.24 and 3.60 mTorr. Solid lines report the convolution of the simulated profiles (dots) with the system response function reported in Table 5.3.5.

agree with experimental data only in collisionless or almost collisionless conditions ($p = 0.1$ mTorr). At any other gas pressure, the y component of the ion drift velocity decreases within the first 5 mm of simulation domain to a lower values that remains almost stationary in the rest of the simulation domain.

Figure 5.9 shows the ion drift velocity along the direction parallel to the plate along the E×B direction (V_z component). Similarly to the V_x component of the ion drift, the V_z component is in good agreement with PIC simulations conducted at high pressure values, $p = 3.60$ mTorr and $p = 3.24$ mTorr, with a best-fit of $p = 3.4 mTorr$ in the presheath ($< 5\%$ neutral depletion). Particle-in-Cell simulations executed at lower pressure show disagreement with the measurements, such as larger values of the V_z component of the ion drift. The increase in V_z at lower pressures is an expected feature of a plasma transitioning from collisional to collion-less conditions. Indeed the upper limit of V_z is observed in collisionless conditions or at pressure lower than $p \leq 0.4$ mTorr. In the collisionless limit, the ion drift V_z at the wall is equal to $0.5C_s$ at the wall, which is almost three times higher than the values observed in the experiments. The predictions of V_z from the fluid model have in general different trend than the PIC simulations, achieving $0.3C_s$ at the wall. From the analysis of the V_z component, we can conclude that our indirect measurement of the background neutral pressure indicates values in the range of 2-3 mTorr, in agreement with those observed along the V_x direction.

Figure 5.10 reports the Γ_x component of the particle flux, along the direction perpendicular to the wall. The experimental data are obtained from the combination of LIF measurements and Langmuir probe density acquisitions. Data are scattered mainly due to the spread of the density measurements. Despite the spread, the plot allows quite clearly to discriminate between collisional and collisionless conditions. In collisionless conditions the flux increases almost linearly toward the wall, in total disagreement with the measurements. When the neutral pressure is increased and collisional effects are properly taken into account, the particle flux gradually decreases toward the range of values experimentally observed. Both the fluid model and Particle-in-Cell simulations at pressures in the range $2.5 < p < 3.6$ mTorr) yield particles flux constant across the simulation domain, in good

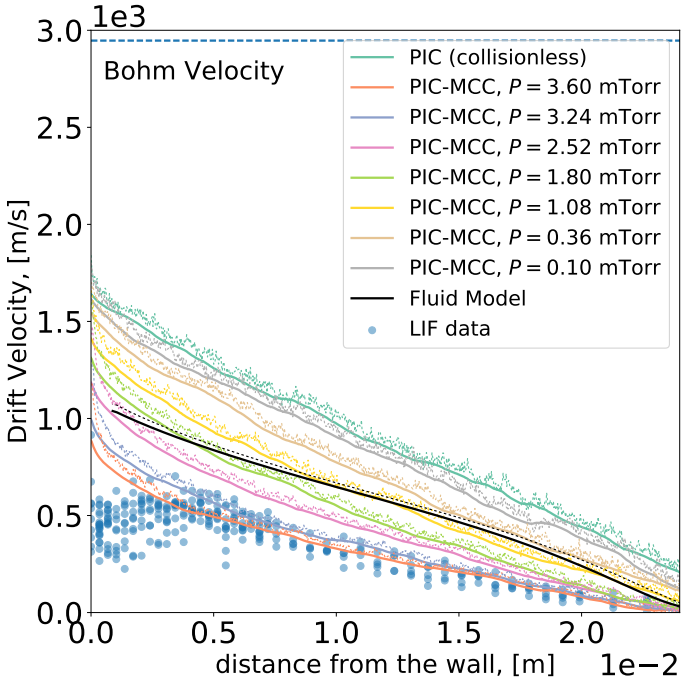

Figure 5.9: Comparison of calculated and measured ion drift velocity (V_z component, parallel to the wall along the E×B direction) over a range of neutral gas pressures. Values are expressed in a reference frame with origin at the surface plate and pointing toward the plasma. Experimental values were measured using Laser-Induced Fluorescence at the HELIX facility in Argon plasma at $T_e = 4.0 \pm 1.0$ eV. Numerical simulations were performed using: a collisional fluid model, a collisionless Particle-in-Cell code, a collisional Particle-in-Cell for Ar gas pressures of p =0.1, 0.36, 1.08, 1.80, 3.24 and 3.60 mTorr. Solid lines report the convolution of the simulated profiles (dots) with the system response function reported in Table 5.3.5.

agreement with experimental observations.

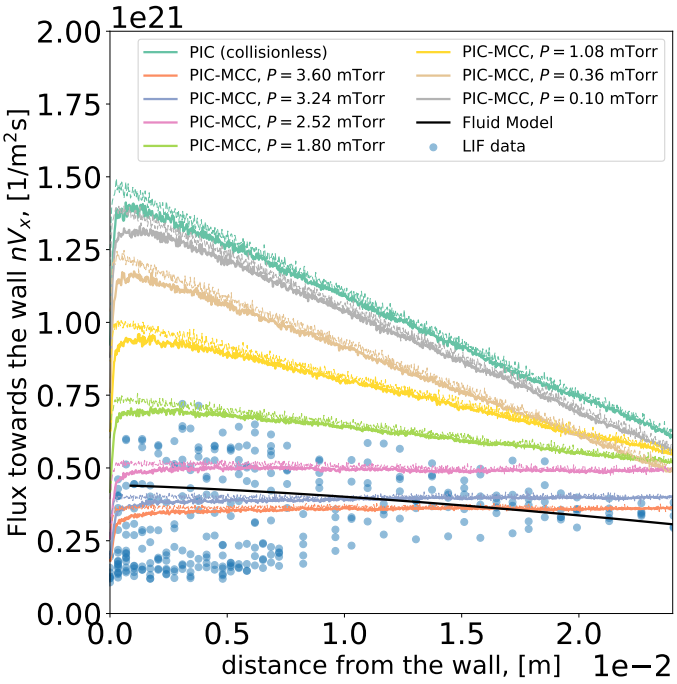

Figure 5.10: Particle flux towards the wall in the simulation frame as measured by Laser-Induced Fluorescence in HELIX experiment for Argon at $T_e = 4.0 \pm 1.0$ eV.Numerical simulations were performed using: a collisional fluid model, a collisionless Particle-in-Cell code, a collisional Particle-in-Cell for Ar gas pressures of p =0.1, 0.36, 1.08, 1.80, 3.24 and 3.60 mTorr. Solid lines report the convolution of the simulated profiles (dots) with the system response function reported in Table 5.3.5.

From the same Langmuir probe data, a validation of the calculated data against the plasma potential can be performed. Figure 5.11 shows the comparison between the measured and the calculated plasma potential. Qualitative agreement between calculated and measured values is observed across the whole simulation domain, even if distinguishing between different collisional behaviors is more challenging from the trend of the plasma potential. A general feature visible from the trend is that larger values of the electric field (steeper gradients of potential) are observed in collisional conditions, from both the PIC and the fluid models. Indeed, larger values of the electric field are required to overcome the friction forces across the presheath and the sheath. However, since the spread of experimen-

tal data spans across all the calculated curves of the electric potential, such measurement does not add more insight than what already observed from the previous LIF plots.

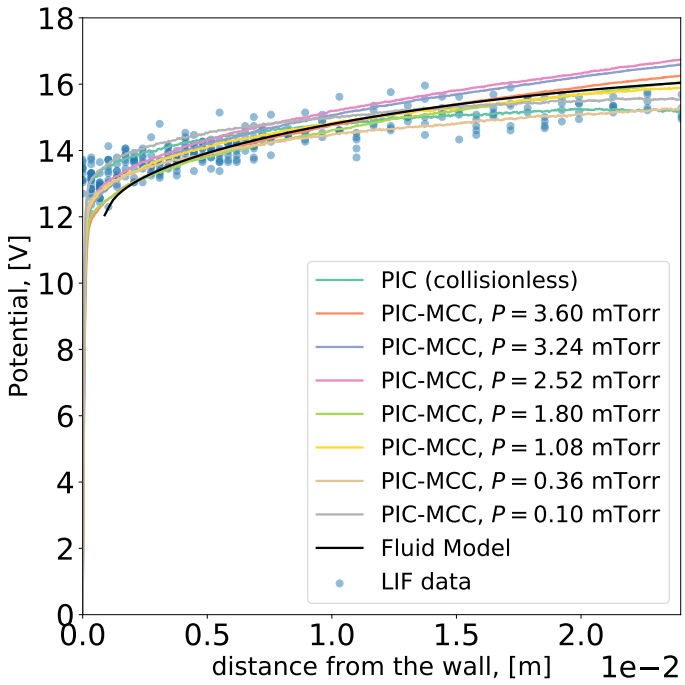

Figure 5.11: Electrostatic potential in the HELIX experiment for Argon at $T_e = 4.0 \pm 1.0$ eV. Numerical simulations were performed using: a collisional fluid model, a collisionless Particle-in-Cell code, a collisional Particle-in-Cell for Ar gas pressures of p =0.1, 0.36, 1.08, 1.80, 3.24 and 3.60 mTorr. Solid lines report the convolution of the simulated profiles (dots) with the system response function reported in Table 5.3.5. Electrostatic potential was measured with Langmuir Probes in HELIX experiment.

In conclusion, we can affirm that both the Particle-in-Cell simulations and the fluid model quantitatively agree with the experimental data. Most of the experimental insight on the behavior of the presheath is offered by Laser-Induced Fluorescence measurements, which provide detailed information about the three-dimensional structure of the ion drift flow across the magnetic presheath and the plasma sheath. As we have shown in this section, a parametric scan over the neutral pressure shows that collisional effects must be taken into account in order to properly capture the plasma sheath behavior. In particular, the V_x and V_z components of the ion drift velocity show that collisional PIC simulations accurately

reproduce the measured ion drift velocity profile. Without collisions, the drift profile are in general larger, as expected from a system that does not have any mechanism to slow the particle velocities other than a collisionless ambipolar electric field. In particular, we have found that a good agreement between the measured and calculated values of V_x and V_z can be obtained within a 20% accuracy for a neutral pressure background between $p = 2.5 - 3.4$ mTorr.

Surprisingly, the V_y component of the calculated ion drift velocity is in disagreement with the measured values. In this case an agreement is found only in *collisionless* conditions, as ion-neutral friction forces slow down particles too much. This paradox indicates that some additional contribution to the momentum balance of the plasma along the y axis must be in place, which has been neglected in the simulations run so far (both Particle-in-Cell and Fluid). In the following sections we explore the effect of the two possible candidates of such a discrepancy: (1) either a neutral flow, or (2) an ambient electric field. As we will show, the effect of a background neutral drift is one possible explanation of the observed discrepancy. However, when an ambient electric field is added along the y direction, the paradox can also be satisfactorily explained. Indeed, also in the experimental practice is common to observe small electric fields along the magnetic lines (y direction) [76], [75]. Such an electric field, due to the presheath potential drop along a magnetic flux tube along the axis of the cylinder, can fully explain the disagreement observed along the V_y direction.

5.4.2 Role of Neutral Flows

Particle-in-Cell simulations of the HELIX experiment have been performed at four different candidate values of the background neutral drift, reported in Table 5.5. In the first case the drift velocity was set to match the velocity of the ions at the right wall of the simulation domain. The second and third cases explored the possibility of reduced neutral flows towards the wall while maintaining the velocity components in the directions parallel to the plate V_y at the same level (1500 m/s). Finally, the last test case studied the possibility of the reduced flow in the direction parallel to the plate $V_y = 1500$ m/s. The fluid model was also run for all of the four test cases. The prediction of the collision frequencies and the

background gas density are listed in Table 5.5 as well.

Table 5.5: Simulation Parameters

	$\mathbf{V}_n$, [m/s]	n_n/n_0	fluid ν_i, [Hz]	fluid ν_{iz}, [Hz]	PIC $n_n/n0$
Case 1	[600, 1500, 0]	0.95	2.75×10^4	2.52×10^4	0.9-1.0
Case 2	[300, 1500, 0]	0.78	2.25×10^4	2.07×10^4	0.7-0.9
Case 3	[0, 1500, 0]	0.65	1.87×10^4	1.72×10^4	0.7-0.9
Case 4	[600, 750, 0]	0.92	2.66×10^4	2.44×10^4	-

Figure 5.12 reports the V_x component of the ion drift velocity, calculated with the PIC code and the fluid model. The effect of the neutral flow on the ion drift velocity is minimal. A difference of 300 m/s neutral drift reduces the speed of the ions by $\sim$ 50 m/s in the relevant range of pressures p = 2.5-3.6 mTorr. The general behavior of V_x-component of the ion velocity is very similar to the simulation results without neutral drift: the PIC simulations tend to agree with experimental data at high pressure and the ion velocities in collisionless case are larger than observed in experiments.

The strongest effect of the drifting neutral population is observed along the y direction (direction parallel to the wall). In this case the ions tend to be dragged by the neutral drift. A neutral drift of 1500 m/s maintains the ion drift velocity at the observed level regardless of the value of the neutral drift velocity towards the wall (x-direction). When the neutral drift velocity is reduced to 750 m/s, the ion drift V_y drops down to half the values experimentally observed. Such analysis suggests that the discrepancy of the V_y component could potentially be explained assuming a neutral drift of 1500 m/s along the y direction, and a value of $V_{x,n}$ comprised between $0 < V_{x,n} < 600$ m/s. A further constraint on this values is provided by the analysis of the V_z drift, considered hereafter.

Figure 5.14 reports the ion drift velocity V_z along the E×B direction (z axis) for the four cases of neutral drift considered above. The Particle-in-Cell simulations show that in presence of neutral flow, the ion drift velocity V_z becomes sensitive to the x and y components of the neutral drift velocity V_{nx} and V_{ny}. Larger values of V_{nx} yields larger values of the ion velocity along the E×B direction.

An agreement between experiments and simulations is found for case (a), returning an estimate of the background neutral drift $\mathbf{V}_n = [600, 1500, 0]$ m/s. In this case all three

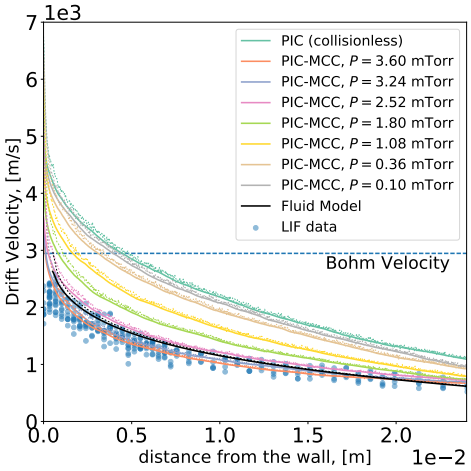

(a) Test Case 1, $\mathbf{V}_n = [600, 1500, 0]$

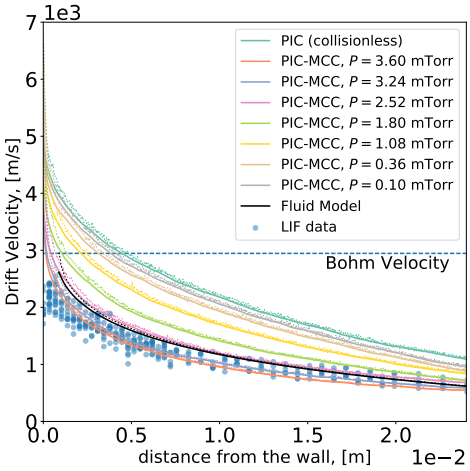

(b) Test Case 2, $\mathbf{V}_n = [300, 1500, 0]$

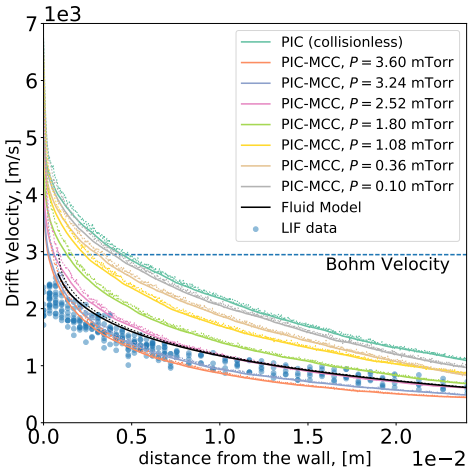

(c) Test Case 3, $\mathbf{V}_n = [0, 1500, 0]$

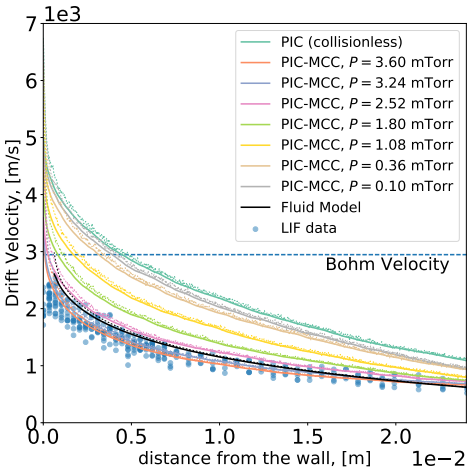

(d) Test Case 4, $\mathbf{V}_n = [600, 750, 0]$

Figure 5.12: Effect of a background neutral drift on the V_x component of the ion drift velocity. The four figures refer to four different candidate directions and magnitudes of the neutral flow. The effect of the neutral flow on this component of the ion drift velocity is minimal.

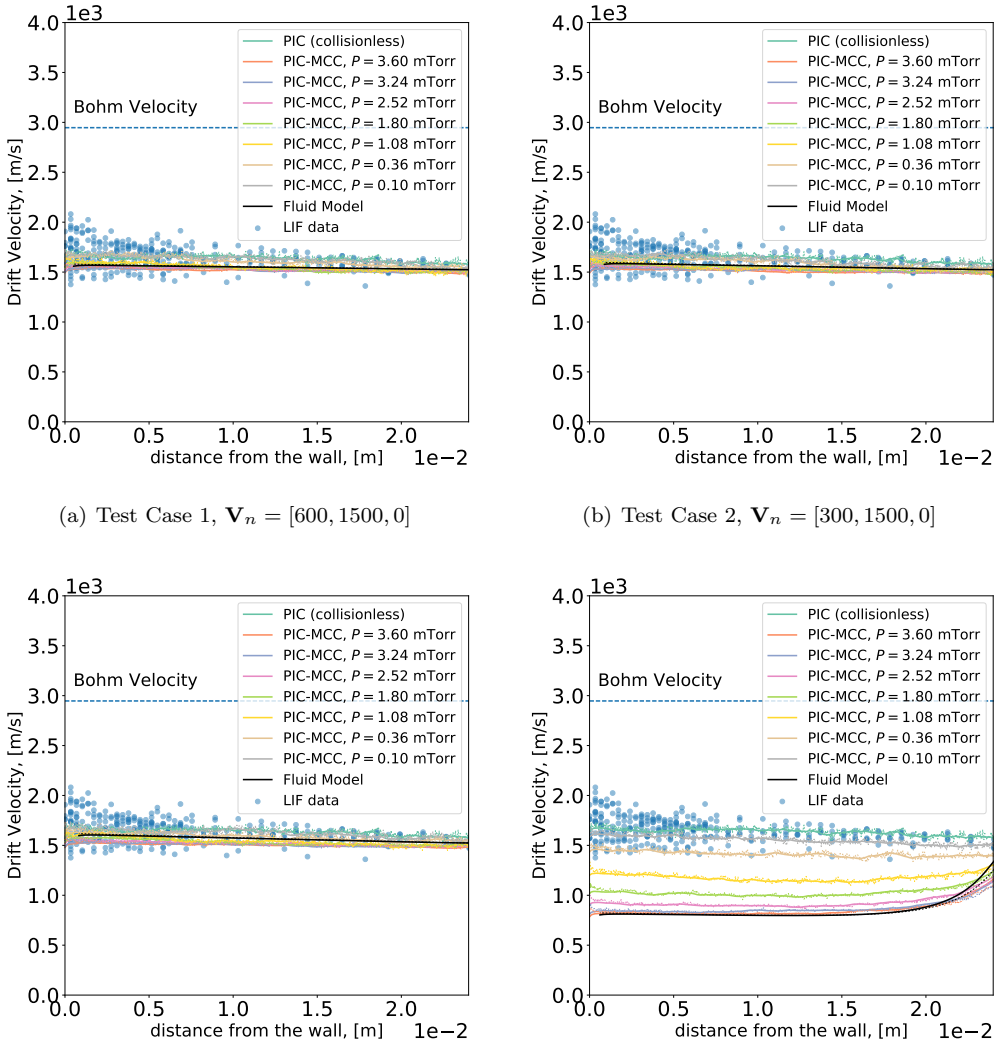

(a) Test Case 1, $\mathbf{V}_n = [600, 1500, 0]$

(b) Test Case 2, $\mathbf{V}_n = [300, 1500, 0]$

(c) Test Case 3, $\mathbf{V}_n = [0, 1500, 0]$

(d) Test Case 4, $\mathbf{V}_n = [600, 750, 0]$

Figure 5.13: Effect of a background neutral drift on the V_y component of the ion drift velocity. The four figures refer to four different candidate directions and magnitudes of the neutral flow. In this case the ions are dragged by the neutrals along the y direction.

components of the ion drift velocity (V_x, V_y, V_z) are in agreement with the experimental measurements. This analysis offers one first possible explanation of the paradox of the ion drift velocity along the y direction. The second possible explanation will be considered in the next section, where an ambient electric field along a magnetic flux tube is taken into account.

5.4.3 Role of the Presheath Electric Field

In order to evaluate the effect of an electric field along the y axis, such as those produced by the presheath potential drop along a magnetic flux tube connecting the target plate to the opposite side of the vacuum chamber, the Particle-in-Cell simulation were initialized with an electric field of magnitude E_y along the y axis; on top of this E-field, the usual E_x component of the electric field was calculated from the solution of the Poisson equation as in all previous calculations. The value of E_y was parametrically varied between $50 < E_y < 300$ V/m to analyze its effect on the profiles of the ion drift velocity.

The prediction given by the fluid model ($\nu_i = 187.8$ kHz), suggests a reduction of the gas pressure by 35% in the dicharge and electric field $E_y = 125$ V/m acting in the direction parallel to the wall in $\mathbf{E} - \mathbf{B}$ plane. Notably, the predicted density reduction in the fluid model with ambient electric field is similar to the initial simulation without ambient electric fields and neutral flows: the collisional friction forces between neutrals and ions are of the same order of magnitude in both cases, however additional electric field E_y counteracts the friction forces in y direction maintaining ion drift velocity V_y at the observed in the experiments level. The predicted fluid model profiles are in excellent agreement with the data gathered at HELIX experiment.

Figures 5.15, 5.16, and 5.17 report the results. The PIC simulations reported in figure 5.15 show that the electric field E_y has a minor influence on the ion drift along x, as expected. The V_x profile closely resembles the profiles of the simulation that did not include the ambient electric fields E_y or neutral drift. The simulation at $p = 2.52$ mTorr still best reproduces the experimental V_x profile at $x \gtrsim 0.5$ cm. V_x reaches supersonic velocities closer to the wall. The simulations at higher values of the gas pressure $p = 3.6$ and $p = 3.24$ mTorr

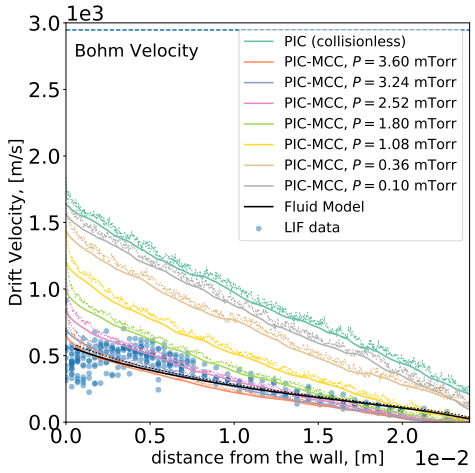

(a) Test Case 1, $\mathbf{V}_n = [600, 1500, 0]$

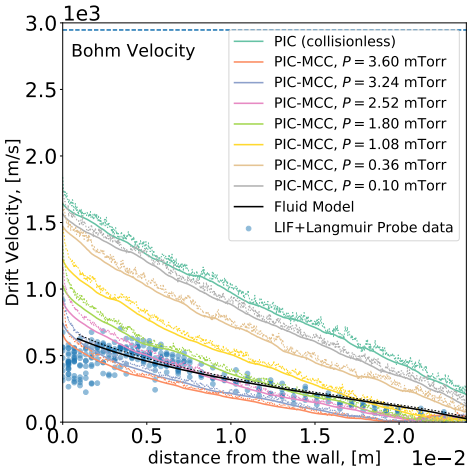

(b) Test Case 2, $\mathbf{V}_n = [300, 1500, 0]$

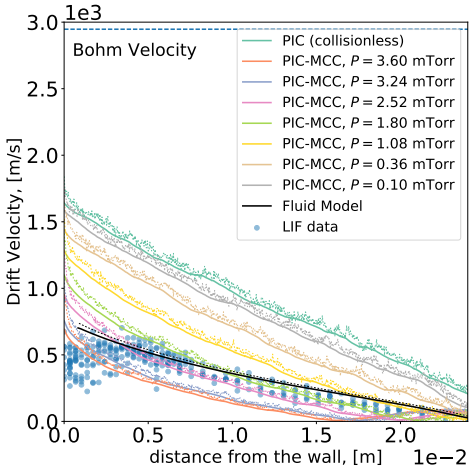

(c) Test Case 3, $\mathbf{V}_n = [0, 1500, 0]$

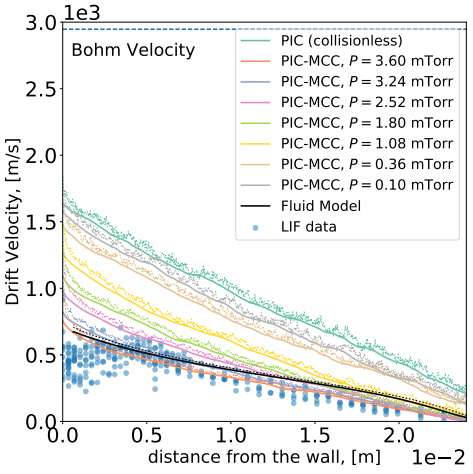

(d) Test Case 4, $\mathbf{V}_n = [600, 750, 0]$

Figure 5.14: Effect of a background neutral drift on the V_y component of the ion drift velocity. The four figures refer to four different candidate directions and magnitudes of the neutral flow. A full agreement between calculated values and measured values is found in case (a), for a background neutral drift of $\mathbf{V}_n = [600, 1500, 0]$ m/s.

Table 5.6: Initial parameters of the Particle-in-Cell simulations of the HELIX experiment with ambient electric field

Parameter	Values
Domain size L, cm	2.5
Electric field E_y, V/m	50, 100, 150, 200, 250, 300
Electron temperature T_e, eV	3-4 eV
Ion Temperature T_i, eV	0.4 eV
Gas Pressure P, mTorr	1.8, 2.52, 3.24, 3.6
Number of Grid Points	1000
Number of Particles	50000

produce smaller observed values of the ion drift velocity V_x in the presheath and larger than observed values in in front of the wall. The simulation conducted at lower pressure shows agreement with experimental data only on the right boundary, producing values of the drift velocity larger than those observed across the whole simulation domain.

Figure 5.16 clearly shows the effect of the electric field E_y on the V_y component of the ion drift. An electric field of enough intensity is able to counteracts the friction forces caused by friction of the ions with the neutral particles. In the magnetic and collisional presheaths, E_y maintains the ion velocity at an almost-constant value, and it increases V_y in front of the wall at $x < 0.5$ cm. This analysis reveal that an electric field E_y within the range $150 < E_y < 200$ V/m produces ion drift velocities V_y compatible with both the LIF experimental values and the pressure ranges previously observed. We should also note that in our parametric considerations we are assuming E_y to be constant across the simulation domain. A more realistic ambient electric field E_y would slowly decrease in the simulation domain to maintain constant V_y values. The values of the electric field E_y that sustain observed values of ion flow parallel to the plate V_y are reported in Table 5.7 as estimated from Particle-in-Cell simulations for all of the values of the gas pressure. As can be seen from the table, the ambient electric field E_y is directly proportional to the gas pressure and the ion-neutral friction force, which the electric field is attempting to cancel out.

Based on the electric field estimates which produce sufficient electrostatic force to counteract the friction forces (see Table 5.7), the simulation at $p = 2.5$ mTorr and $E_y = 150 - 200$ V/m gives the best agreement with experimental data with agreement to the previous field

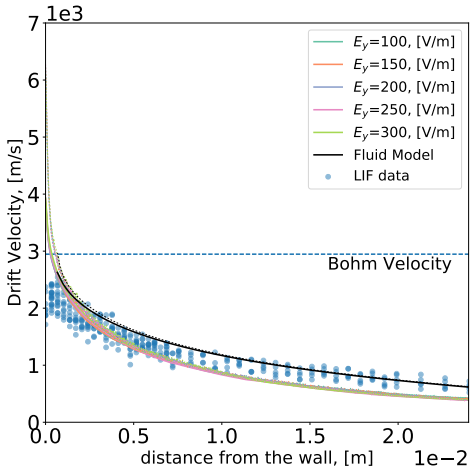

(a) Test Case 1, $P = 3.6$ mTorr

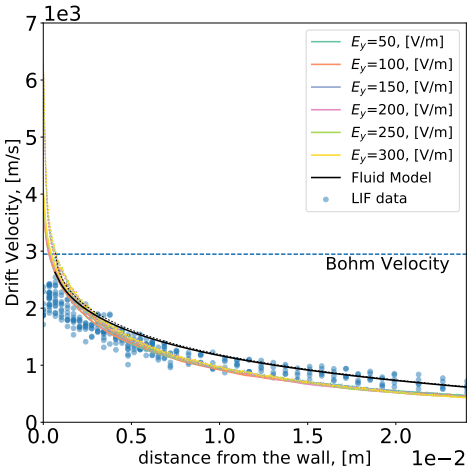

(b) Test Case 2, $P = 3.24$ mTorr

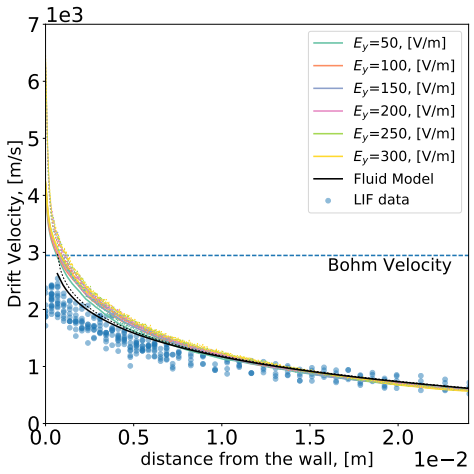

(c) Test Case 3, $P = 2.52$ mTorr

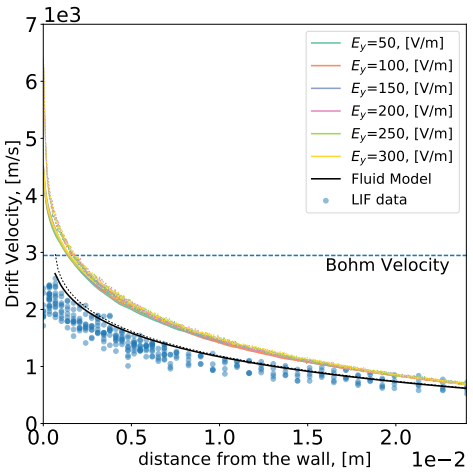

(d) Test Case 4, $P = 1.80$ mTorr

Figure 5.15: x-component of the ion drift velocity in the simulation frame as measured by Laser-Induced Fluorescence in the HELIX experiment for Argon at $T_e = 4.0 \pm 1.0$ eV, as simulated using collisionless Particle-in-Cell code, collisional Particle-in-Cell for gas pressure $p = 1.8$, 2.52, 3.24 and 3.6 mTorr and as resolved by collisional fluid model. Solid lines represent observed quantities, obtained as of convolution of the simulated profiles (dashed lines) with the system response function reported in Table 5.3.5

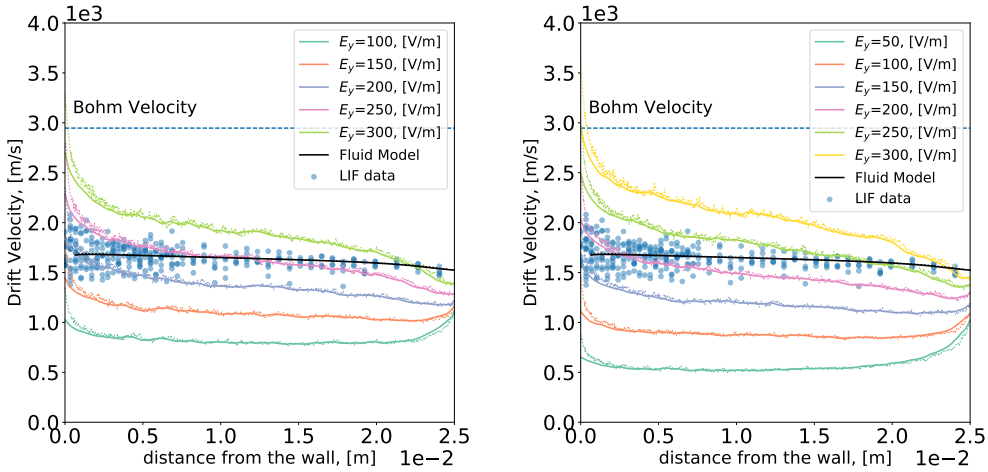

(a) Test Case 1, $P = 3.6$ mTorr

(b) Test Case 2, $P = 3.24$ mTorr

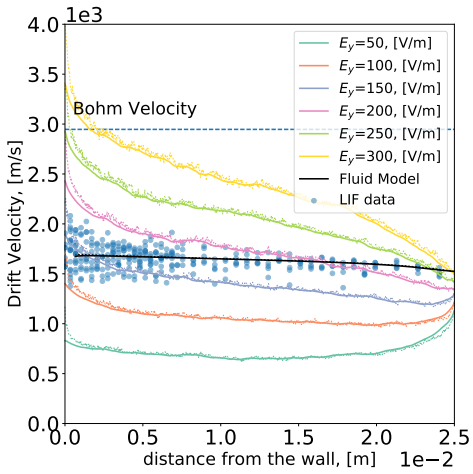

(c) Test Case 3, $P = 2.52$ mTorr

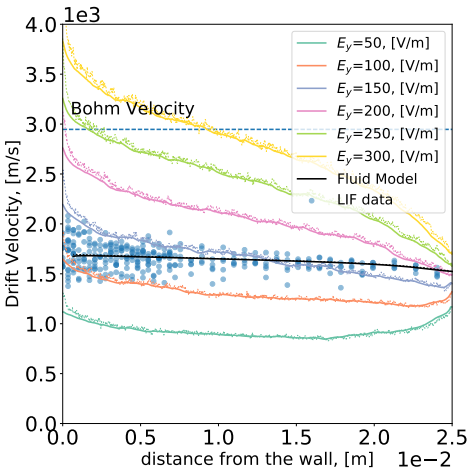

(d) Test Case 4, $P = 1.80$ mTorr

Figure 5.16: y-component of the ion drift velocity in the simulation frame as measured by Laser-Induced Fluorescence in the HELIX experiment for Argon at $T_e = 4.0 \pm 1.0$ eV, as simulated using collisionless Particle-in-Cell code, collisional Particle-in-Cell for gas pressure $P = 1.8$, 2.52, 3.24 and 3.6 mTorr and as resolved by collisional fluid model. Solid lines represent observed quantities, obtained as of convolution through simulated profiles (dashed lines) with the system response function reported in Table 5.3.5

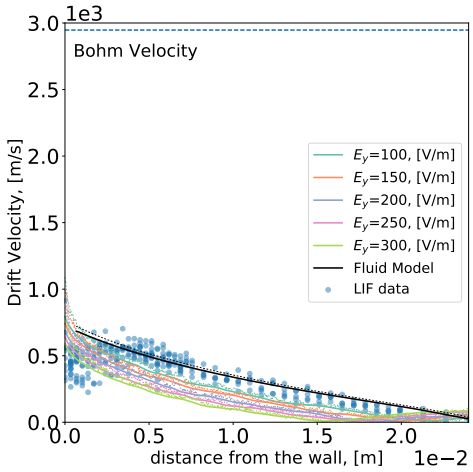

(a) Test Case 1, $P = 3.6$ mTorr

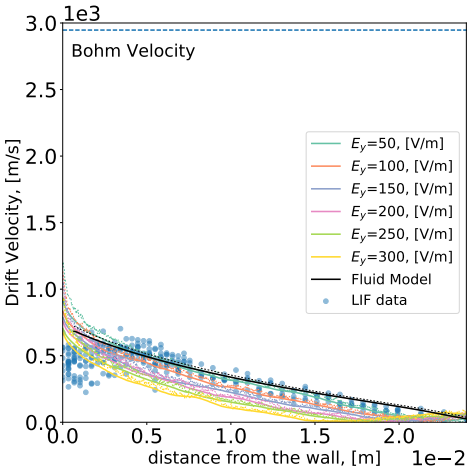

(b) Test Case 2, $P = 3.24$ mTorr

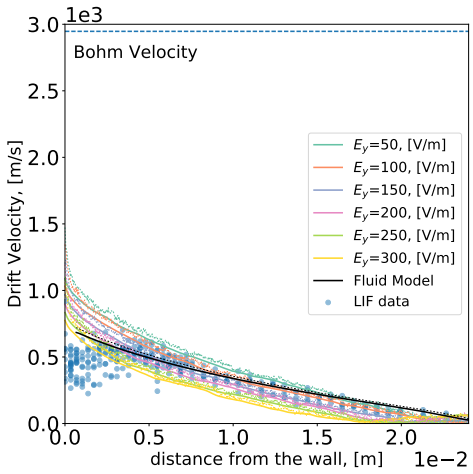

(c) Test Case 3, $P = 2.52$ mTorr

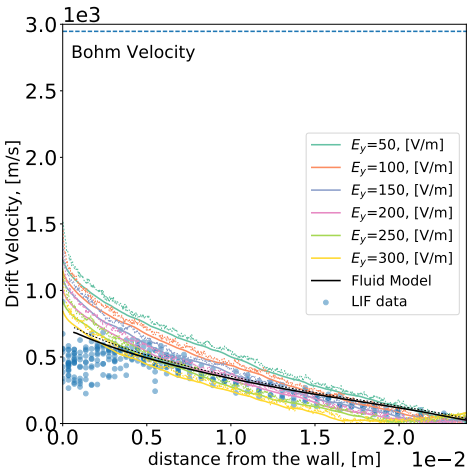

(d) Test Case 4, $P = 1.80$ mTorr

Figure 5.17: y-component of the ion drift velocity in the simulation frame as measured by Laser-Induced Fluorescence in the HELIX experiment for Argon at $T_e = 4.0 \pm 1.0$ eV, as simulated using collisionless Particle-in-Cell code, collisional Particle-in-Cell for gas pressure $P = 1.8$, 2.52, 3.24 and 3.6 mTorr and as resolved by collisional fluid model. Solid lines represent observed quantities, obtained as of convolution of the simulated profiles (dashed lines) with the system response function reported in Table 5.3.5

Table 5.7: Particle-in-Cell estimates of the ambient electric field in the HELIX chamber for different values of the gas pressure

Pressure P, mTorr	Estimated E_y, V/m
3.60	250
3.23	200-250
2.52	150-200
1.80	100-150

electric measurements in the MARIA experiment (See Figure 5.18). Simulations at high pressure return smaller-than-observed drift velocities along the E×B direction, and the simulation at lower pressure yield larger than observed velocities.

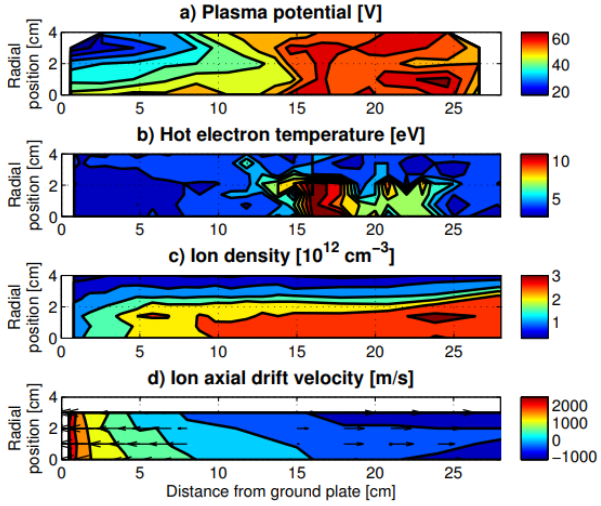

Figure 5.18: Spatial distribution of the plasma potential, electron temperature, ion density and ion drift velocity in the MARIA experiment. Reproduced from [6, p. 69] with permission of Umair Siddiqui.

5.5 Discussion

Our analysis revealed that in general, Particle-in-Cell simulations were able to reproduce experimental data better than Fluid models, as expected from the larger number of assumptions involved in the fluid approximation. First, the collision and ionization frequencies in the fluid model are assumed to be uniform in the simulation domain, which is an inaccurate

representation of the collision processes in the boundary region. The collision and ionization frequency depends strongly on the energies of the colliding particles. The ions gain significant energies in the plasma sheath due to electrostatic forces that are pulling charged particles towards the wall, which alters effective collision and ionization frequencies. Second, the fluid model has "weak" closures on the left boundary (Debye sheath entrance) by not enforcing self-consistently a total drop of the electrostatic potential across the presheath. However, besides being a simplistic model, fluid equations provide a reasonable insight on the physics of the boundary region at small computational cost, and if the collision frequencies are estimated from Particle-in-Cell simulations and stored for future references, the fluid models can serve as a reliable alternative to PIC simulation.

Interestingly, the effect of neutral depletion was observed to be remarkable. Indeed, the density of the neutrals can be significantly reduced in the helicon discharges due to the mechanism of the neutral depletion. The equilibrium model of the helicon discharge predicted a reduced neutral density at the center of the plasma column on the level $45-90\%$ of the gas density (pressure) of the gas in the chamber. In some cases neutral densities have been observed as low as 10% of the gas density [5] in similar discharges, and the neutral density was previously estimated as $0.44n_0$ in HELIX experiments [87]. Our calculation shows a depletion ratio of 28% under the conditions of interest.

Collisional processes play significant role in the equilibrium at the chamber pressure used in the HELIX experiment. The initial Particle-in-Cell simulations included realistic ion-neutral collision using the Monte-Carlo Collision method [44] for collisionless conditions and the gas pressures ranging from 0.1 mTorr to the chamber pressure 3.6 mTorr. It was demonstrated that the lowest simulated pressure 0.1 mTorr is basically equivalent to the collisionless conditions, as expected from the Knudsen numer of a simulation of length 2.5 cm. In the absence of frictional forces, the collisionless simulations yielded larger-than-observed ion velocities both in the ExB direction and perpendicular to the wall. However, the y component of the ion drift V_y was in a good agreement with the unusually large ($0.5C_s$) ion flow observed in experiments.

With the addition of ambient forces acting in the $\mathbf{E}-\mathbf{B}$ plane parallel to the wall

(y-axis), both the particle in cell simulation and fluid model achieved excellent agreement with experimental measurements at relatively high gas pressure ($0.7 \ldots 0.8 n_0$). The ambient forces counteracted the friction forces caused by ion-neutral collision. The amplitude of the ambient force was estimated at the level $1 - 2 \times 10^{-17}$ N, and can be generated by the flowing neutral background with $V_{y,n} = 0.5 C_s$ or electric field $\sim 100 - 200$ V/m acting along y axis.

The subsequent measurements at HELIX experiment have demonstrated no evidence for the flow of background gas flows. The lack of additional diagnostic windows precludes measurement of the electrostatic potential at larger distances from the plate to determine existence of an ambient electric field. However, the ion drift velocity along the magnetic lines (a proxy for V_y) was registered at 30 cm from wall on the level of 110 m/s, accelerating to 1500 m/s. Thus, the existence of the ambient forces is certain regardless their nature (electric field, gradient of the ion pressure, or neutral flows).

Overall, the assumption of adiabatic electrons is one of the weakest of both the fluid models and the Particle-in-Cell simulations. In future studies, the fluid model of the plasma sheath can be extended to add flowing fluid electron species. The Particle-in-Cell simulation can be setup with kinetic electrons. The drawback is that the kinetic electron simulations have to be executed for tens of thousands of iterations and will require the level of computational resources available only on next-generation supercomputers. A simplified representations of the electron physics can be implemented using a set of fluid equations for electrons. In this case, the Particle-in-Cell simulation will be setup with kinetic ion particles and fluid electron background.

The modeling of the boundary region in the helicon discharges with one-dimensional infinite slab models requires introduction of the ambient forces in the simulations. The quality of the models can be significantly improved by coupling the plasma sheath model to a macroscopic transport model solving the evolution of the plasma in time and space self-consistently in the whole volume of the vacuum chamber. The global models of the helicon discharge can help understanding the nature of the ambient forces that are accelerating ion from 110 m/s to 1500 m/s on the length of 30 cm. Such models can be based on the set of fluid equation extended to multiple dimensions [88], large-scale Particle-in-Cell simulations

[37] or combination of both. For example, the fluid model can be used to model the large volumes of plasma from the helicon antenna regions where plasma is generated up to the boundary region with the biased plate.

5.6 Conclusions

In this chapter we have performed an experimental validation of the magnetic presheath models developed in the previous chapter. Both fluid and kinetic (Particle-in-Cell) models were taken into account, and compared against detailed three-dimensional Laser-Induced Fluorescence (LIF) measurements taken at the HELIX helicon facility. The experiments were run for a helicon plasma impacting on a material target inclined at an oblique angle of $\psi = 74$ deg with respect to the magnetic field. Quantitative agreement has been obtained between the measured and calculated values on the following quantities: plasma potential, particle fluxes, V_x and V_z components of the ion drift velocity, where x is the direction perpendicular to the target, and z the direction parallel to the surface of the target along the E×B direction. Disagreement were initially observed for the V_y component, where y is the direction tangential to the target directly prevalently along the magnetic field. Two possible explanations were given in order to explain the discrepancy: (1) the presence of a background neutral flow dragging the ions along the y direction, and (2) the presence of a small electric field E_y along the magnetic flux tubes of HELIX. A careful analysis has revealed that the second hypothesis is the most plausible, and that an electric field within the range $150 < E_y < 200$ V/m must be present. Subsequent measurements indeed revealed the absence of significant neutral flows, and that a background electric field in the area of interest is indeed present, which can be interpreted as the electric field formed along a magnetic flux tube connecting the target plate to the opposite side of the chamber. From the parametric runs performed during the validation, we were also able to obtain an indirect measure of the background neutral pressure of $p = 2.5$ mTorr and to constrain the amount of neutral depletion within the presheath in front of the target (depletion ratio of 28%).

Chapter 6

Conclusions and Future Work

In this work, we have developed and validated a multi-species kinetic model of the plasma sheath and presheath in strong magnetic fields, capable of handling the evolution of the distribution function of electrons, ions, neutrals, and material impurities from the quasi-neutral region to the first surface layers.

A new massively-parallel electrostatic Particle-in-Cell code named hPIC has been developed as part of this work, capable to perform large-scale simulations of the magnetized presheath. The code has demonstrated good scaling on the Blue Waters supercomputer with up to 64000 cores, and the results of the verification tests demonstrate expected behavior.

A detailed analysis of the plasma sheath in strongly magnetized conditions has revealed a fully three-dimensional structure of the ion flow and non-linear trends of the distributions as a function of the magnetic angle. The inclination of the ion velocity is increasing with the inclination of the magnetic angle according to a non-linear law. At high values of the magnetic angle and large electric field the ion-energy angular distribution narrows along the angle coordinate and broadens along the energy coordinate. At magnetic field inclinations typical to tokamak divertors, the ions arrive at the wall at large angles (almost parallel to the wall)."

We have demonstrated that Particle-in-Cell simulations of the presheath can be coupled with fluid representations of plasmas using the means of the least square fitting of the first moments of the distribution functions (particle fluxes). Even though the agreement of higher moments of the distribution function (energy and particle fluxes) was not enforced, the approach have demonstrated a good agreement between the fluid moments estimated from the Particle-in-Cell simulation and the profiles calculated using reduced fluid model. The

kinetic corrections introduced to the fluid model produce an accurate first-principle-based description of the magnetized plasma sheath that can be used in engineering or parametric studies.

Validation simulations of the HELIX helicon experiment at West Virginia University [1], [2], [3] have demonstrated the importance of kinetic effects in the magnetic presheath. The inclusion of collisional processes is required for predictive Particle-in-Cell simulations for low-temperature plasmas at high neutral pressures. In the realistic plasma systems, the structure of the plasma sheath can be significantly altered by the global pressure gradients of the plasma species, the drifts of the background gas, and/or the ambient electric fields. We have demonstrated that in the helicon experiments in particular, the plasma sheath structure is strongly influenced by the configuration of the electrostatic potential, created by the relative location of the biased plates and the heating antennas. Thus, the strong electric potential gradients are observed in experiments accelerating ions towards the wall outside of the sheath region and altering the ion drift velocities in the plasma sheath.

In many tokamak, the vacuum systems are placed in the proximity of the divertor cassettes, which are used to mount the divertor plates. This configuration can create strong flows of neutral particles in front of the divertor plates. At typical neutral gas pressures [89] in tokamak divertors of 1-60 mTorr the plasma sheath is in conditions of an intermediate magnetization and collisional processes are playing a significant role in determining the sheath structure.Thus, a careful study is require to determine the magnitude of neutral flows and ambient electric fields in front of the divertor plates in the existing and future tokamak, and the effect of the global plasma equilibria on the magnetized sheath structure.

Unfortunately, even modern supercomputers are not capable of handling a fully-kinetic six-dimensional simulation of large plasma devices. Therefore the fully-kinetic simulations have to be used in the regions of most importance, where a simplified plasma description (for example, fluid) is not valid. Thus, kinetic plasma sheath simulations of tokamak divertors have to be coupled with large-length-scale plasma solvers.

Future effort can be focused on the coupling of hPIC with gyrokinetic particle-in-cell code, like XGC, that can simulate the whole scrape-off layer of the tokamak. The gyrokinetic

approximation breaks in the plasma sheath, where hPIC can serve as a boundary condition for the gyrokinetic code. On the other side of the domain, hPIC can be coupled to material codes to provide accurate particle fluxes of the charged particles coming from the scrape-off-layer of the tokamak. The statistics of the particles interacting with the wall is readily stored in hPIC, which can make coupling material wall codes like Fractal TRYDIN [24] or XOLOTL [90] straightforward. If the material and gyrokinetic couplings are accomplished, hPIC can enable the first kinetic simulation of the whole tokamak with a realistic material wall. Such a result will help to better understand the particle transport in tokamaks.

The coupling of the fully-kinetic Particle-in-Cell code with lower-dimensional representations of the plasma can be challenging as the complete simulation should preserve fluxes, energy, and the gradients of the fields at the interface of the two codes. The coupling scheme for the fluid and Particle-in-Cell model developed in this work might be insufficient for gyrokinetic and fully-kinetic Particle-in-Cell coupling, and may require additions on the proper boundary conditions for higher moments of the distribution function for both of the codes.

In order to facilitate advanced engineering of future tokamaks, Particle-in-Cell simulations can be used to build the databases of the ion distribution functions at the wall for given plasma conditions. Such databases can be integrated into the simplified whole device simulation models, like SOLPS, to provide accurate plasma sheath potential profiles, ion energy-angle distributions, and particle fluxes at the wall. The simplified Monte-Carlo model can be used as a computationally inexpensive alternative for Particle-in-Cell simulation for the same purpose to execute plasma sheath simulations on-the-fly.

Chapter 7

References

[1] D. S. Thompson, R. Agnello, I. Furno, A. Howling, R. Jacquier, G. Plyushchev, and E. E. Scime, "Ion heating and flows in a high power helicon source," *Physics of Plasmas*, vol. 24, no. 6, 2017.

[2] D. S. Thompson, M. F. Henriquez, E. E. Scime, and T. N. Good, "Confocal laser induced fluorescence with comparable spatial localization to the conventional method," *Review of Scientific Instruments*, vol. 88, no. 10, 2017.

[3] D. S. Thompson, M. F. Henriquez, E. E. Scime, R. Khaziev, S. Keniley, and D. Curreli, "Measurements and simulations of cross-field flows in a magnetically confined plasma boundary," *In Preparation for Submission to Physical Review Letters*, 2018.

[4] "EUROfusion Web Page."

[5] J. Gilland, R. Breun, and N. Hershkowitz, "Neutral pumping in a helicon discharge," *Plasma Sources Science and Technology*, vol. 7, no. 3, pp. 416–422, 1998.

[6] M. U. Siddiqui, *Presheath and Double Layer Structures in an Argon Helicon Plasma Source*. PhD thesis, 2014.

[7] D. A. D'Ippolito, J. R. Myra, S. I. Krasheninnikov, G. Q. Yu, and A. Y. Pigarov, "Blob Transport in the Tokamak Scrape-off-Layer," *Contributions to Plasma Physics*, vol. 44, pp. 205–216, apr 2004.

[8] "NAE Grand Challenges for Engineering, Provide Energy from Fusion."

[9] R. Maingi, S. Zinkle, M. Foster, H. Guo, B. LaBombard, J. Allain, R. Doerner, C. Kessel, D. Youchison, A. Hubbard, and A. Leonard, "Fusion energy sciences workshop on plasma material interactions: report on science challenges and research opportunities in plasma material interactions," tech. rep., 2015.

[10] P. Bonoli, L. C. McInnes, C. Sovinec, D. Brennan, T. Rognlien, P. Snyder, J. Candy, C. Kessel, J. Hittinger, L. Chacón, D. Estep, T. Munson, W. Bethel, M. Greenwald, D. Bernholdt, and B. Lucas, "Report of the Workshop on Integrated Simulations for Magnetic Fusion Energy Sciences," tech. rep., 2015.

[11] G. Federici, P. Andrew, P. Barabaschi, J. Brooks, R. Doerner, A. Geier, A. Herrmann, G. Janeschitz, K. Krieger, A. Kukushkin, A. Loarte, R. Neu, G. Saibene, M. Shimada, G. Strohmayer, and M. Sugihara, "Key ITER plasma edge and plasmamaterial interaction issues," *Journal of Nuclear Materials*, vol. 313-316, pp. 11–22, mar 2003.

[12] C.-S. Chang, M. Greenwald, K. Riley, K. Antypas, R. Coffey, E. Dart, S. Dosanjh, R. Gerber, J. Hack, I. Monga, M. E. Papka, L. Rotman, T. Straatsma, J. Wells, R. Andre, D. Bernholdt, A. Bhattacharjee, P. Bonoli, I. Boyd, S. Bulanov, J. R. Cary, Y. Chen, D. Curreli, D. R. Ernst, S. Ethier, D. Green, R. Hager, A. Hakim, A. Hassanein, D. Hatch, E. D. Held, N. Howard, V. A. Izzo, S. Jardin, T. G. Jenkins, F. Jenko, A. Kemp, J. King, A. Kritz, P. Krstic, S. E. Kruger, R. Kurtz, Z. Lin, B. Loring, G. Nandipati, A. Y. Pankin, S. Parker, D. Perez, A. Y. Pigarov, F. Poli, M. J. Pueschel, T. Rafiq, O. Rübel, W. Setyawan, V. A. Sizyuk, D. N. Smithe, C. R. Sovinec, M. Turner, M. Umansky, J.-L. Vay, J. Verboncoeur, H. Vincenti, A. Voter, W. Wang, B. Wirth, J. Wright, and X. Yuan, "Fusion Energy Sciences Exascale Requirements Review. An Office of Science review sponsored jointly by Advanced Scientific Computing Research and Fusion Energy Sciences, January 27-29, 2016, Gaithersburg, Maryland," tech. rep., USDOE Office of Science (SC) (United States), feb 2017.

[13] M. F. Adams, S. Ethier, and N. Wichmann, "Performance of particle in cell methods on highly concurrent computational architectures," *Journal of Physics: Conference Series*, vol. 78, p. 012001, 2007.

[14] J. Citrin, J. Garcia, T. Gorler, F. Jenko, P. Mantica, D. Told, C. Bourdelle, D. R. Hatch, G. M. D. Hogeweij, T. Johnson, M. J. Pueschel, and M. Schneider, "Electromagnetic stabilization of tokamak microturbulence in a high-beta regime," *Plasma Physics and Controlled Fusion*, vol. 57, no. 1, p. 014032, 2015.

[15] J. Chowdhury, Y. Chen, W. Wan, S. E. Parker, W. Guttenfelder, and J. M. Canik, "Particle-in-cell delta-f gyrokinetic simulations of the microtearing mode," *Physics of Plasmas*, vol. 23, p. 12513, jan 2016.

[16] D. Stotler, D. Battaglia, R. Hager, K. Kim, T. Koskela, G. Park, and M. Reinke, "Kinetic neoclassical calculations of impurity radiation profiles," *Nuclear Materials and Energy*, vol. 0, pp. 1–6, 2016.

[17] R. M. Churchill, J. M. Canik, C. S. Chang, R. Hager, A. W. Leonard, R. Maingi, R. Nazikian, and D. P. Stotler, "Kinetic simulations of scrape-off layer physics in the DIII-D tokamak," *Nuclear Materials and Energy*, vol. 0, pp. 1–6, 2016.

[18] S. Parker, R. Procassini, C. Birdsall, and B. Cohen, "A Suitable Boundary Condition for Bounded Plasma Simulation without Sheath Resolution," 1993.

[19] G. Manfredi and F. Valsaque, "Vlasov simulations of plasma-wall interactions in a weakly collisional plasma," *Computer Physics Communications*, vol. 164, pp. 262–268, dec 2004.

[20] S. Devaux and G. Manfredi, "Vlasov simulations of plasma-wall interactions in a magnetized and weakly collisional plasma," *Physics of Plasmas*, vol. 083504, no. 2006, pp. 1–12, 2006.

[21] S. Devaux and G. Manfredi, "Magnetized plasmawall transitionconsequences for wall sputtering and erosion," *Plasma Physics and Controlled Fusion*, vol. 50, p. 025009, 2008.

[22] C. K. Birdsall and A. B. Langdon, *Plasma Physics via Computer Simulation (Series in Plasma Physics)*. Taylor & Francis, 2004.

[23] R. Chodura, "Plasmawall transition in an oblique magnetic field," *Physics of Fluids*, vol. 25, no. 9, p. 1628, 1982.

[24] J. Drobny, D. Curreli, A. Hayes, and D. N. Ruzic, "F-TRIDYN: A Binary Collision Approximation Code for Simulating Ion Interactions with Rough Surfaces," mar 2017.

[25] W. Eckstein, C. Garciá-Rosales, J. Roth, and J. László, "Threshold energy for sputtering and its dependence on angle of incidence," *Nuclear Instruments and Methods in Physics Research Section B: Beam Interactions with Materials and Atoms*, vol. 83, pp. 95–109, oct 1993.

[26] Y. Yamamura and H. Tawara, "Energy dependence of ion-induced sputtering yields from monatomic solids at normal incidence," *Atomic Data and Nuclear Data Tables*, vol. 253, no. March 1996, pp. 149–253, 1996.

[27] K. U. Riemann, "The Bohm criterion and sheath formation," *Journal of Physics D: Applied Physics*, vol. 24, pp. 493–518, apr 1991.

[28] K. Riemann, "Theory of the collisional presheath in an oblique magnetic field," *Physics of Plasmas*, vol. 1, pp. 552–558, mar 1994.

[29] G. Kim, N. Hershkowitz, D. A. Diebold, and M. Cho, "Magnetic and collisional effects on presheaths," *Physics of Plasmas*, vol. 2, pp. 3222–3233, aug 1995.

[30] P. C. Stangeby, "The BohmChodura plasma sheath criterion," *Physics of Plasmas*, vol. 2, pp. 702–706, mar 1995.

[31] E. Ahedo, "Structure of the plasma-wall interaction in an oblique magnetic field," *Physics of Plasmas*, vol. 4, pp. 4419–4430, dec 1997.

[32] G. Kawamura and A. Fukuyama, "Kinetic modeling of a sheath layer in a magnetized collisionless plasma," *Physics of Plasmas*, vol. 14, p. 083502, aug 2007.

[33] G. Kawamura and A. Fukuyama, "Gyrokinetic Approach to the Analysis of Incident Angle Distribution of Ions in a Magnetized Sheath," *Contributions to Plasma Physics*, vol. 48, pp. 126–130, mar 2008.

[34] A. B. DeWald, A. W. Bailey, and J. N. Brooks, "Trajectories of Charged Particles Traversing a Plasma Sheath in an Oblique Magnetic Field," *Physics of Fluids*, vol. 30, no. 1987, pp. 267–269, 1987.

[35] R. Khaziev and D. Curreli, "Ion energy-angle distribution functions at the plasma-material interface in oblique magnetic fields," *Physics of Plasmas*, vol. 22, no. 4, 2015.

[36] J. Beal, A. Widdowson, K. Heinola, and K. J. Gibson, *Erosion and deposition in the JET divertor corners with carbon and ITER-like walls*. PhD thesis, 2015.

[37] R. Khaziev and D. Curreli, "hPIC: A scalable electrostatic Particle-in-Cell for Plasma-Material Interactions," *Computer Physics Communications*, apr 2018.

[38] A. H. Baker, R. D. Falgout, T. V. Kolev, and U. M. Yang, "Scaling Hypre's Multigrid Solvers to 100,000 Cores," in *High-Performance Scientific Computing*, vol. 9781447124, pp. 261–279, London: Springer London, 2012.

[39] J. Boris, "Relativistic plasma simulation-optimization of a hybrid code," *Proc. Fourth Conf. Num. Sim. Plasmas, Naval Res. Lab, ...*, no. NOVEMBER 1970, 1970.

[40] C. K. Birdsall and L. Fellow, "Particle-in-Cell Charged-Particle Simulations , Plus Monte Carlo Collisions With Neutral Atoms , PIC-MCC," no. April, 1991.

[41] T. Tajima, *Computational plasma physics: with applications to fusion and astrophysics*. Addison-Wesley Series in Computer Science, Addison-Wesley Publishing Company, Advanced Book Program, 1989.

[42] P. L. Bhatnagar, E. P. Gross, and M. Krook, "A model for collision processes in gases. I. Small amplitude processes in charged and neutral one-component systems," *Physical Review*, vol. 94, no. 3, pp. 511–525, 1954.

[43] R. Hockney, "Measurements of collision and heating times in a two-dimensional thermal computer plasma," *Journal of Computational Physics*, vol. 8, pp. 19–44, aug 1971.

[44] V. Vahedi and M. Surendra, "A Monte Carlo collision model for the particle-in-cell method: applications to argon and oxygen discharges," *Computer Physics Communications*, vol. 87, no. 1-2, pp. 179–198, 1995.

[45] G. J. M. Hagelaar, "How to normalize Maxwell-Boltzmann electrons in transient plasma models," *Journal of Computational Physics*, vol. 227, no. 2, pp. 871–876, 2007.

[46] W. Möller and W. Eckstein, "Tridyna TRIM simulation code including dynamic composition changes," *Nuclear Instruments and Methods in Physics ...*, vol. 2, no. 1984, pp. 814–818, 1984.

[47] D. Tskhakaya, A. Soba, R. Schneider, M. Borchardt, E. Yurtesen, and J. Westerholm, "PIC/MC Code BIT1 for Plasma Simulations on HPC," in *2010 18th Euromicro Conference on Parallel, Distributed and Network-based Processing*, no. 1, pp. 476–481, IEEE, feb 2010.

[48] D. Tskhakaya, D. Coster, and I.-T. contributors, "Implementation of PIC/MC Code BIT1 in ITM Platform," *Contributions to Plasma Physics*, vol. 54, pp. 399–403, jun 2014.

[49] G. L. Delzanno, E. Camporeale, J. David Moulton, J. E. Borovsky, E. A. MacDonald, and M. F. Thomsen, "CPIC: A curvilinear particle-in-cell code for plasma-material interaction studies," *IEEE Transactions on Plasma Science*, vol. 41, no. 12, pp. 3577–3587, 2013.

[50] B. Verleye, P. Henri, R. Wuyts, G. Lapenta, and K. Meerbergen, "Implementation of a 2D electrostatic Particle-in-cell algorithm in unified parallel C with dynamic load-balancing," *Computers and Fluids*, vol. 80, no. 1, pp. 10–16, 2013.

[51] H. Timko, P. S. Crozier, M. M. Hopkins, K. Matyash, and R. Schneider, "Why Perform Code-to-Code Comparisons : A Vacuum Arc Dis- charge Simulation Case Study," vol. 308, no. 4, pp. 295–308, 2012.

[52] R. Dejarnac, M. Komm, J. Stöckel, and R. Panek, "Measurement of plasma flows into tile gaps," *Journal of Nuclear Materials*, vol. 382, pp. 31–34, nov 2008.

[53] C. S. Chang, S. Kue, and H. Weitzner, "X-transport: A baseline nonambipolar transport in a diverted tokamak plasma edge," *Physics of Plasmas*, vol. 9, pp. 3884–3892, sep 2002.

[54] C. S. Chang and S. Ku, "Particle Simulation of Neoclassical Transport in the Plasma Edge," *Contributions to Plasma Physics*, vol. 46, pp. 496–503, sep 2006.

[55] C. S. Chang, S. Klasky, J. Cummings, R. Samtaney, A. Shoshani, L. Sugiyama, D. Keyes, S. Ku, G. Park, S. Parker, N. Podhorszki, H. Strauss, H. Abbasi, M. Adams, R. Barreto, G. Bateman, K. Bennett, Y. Chen, E. D. Azevedo, C. Docan, S. Ethier, E. Feibush, L. Greengard, T. Hahm, F. Hinton, C. Jin, A. Khan, A. Kritz, P. Krsti, T. Lao, W. Lee, Z. Lin, J. Lofstead, P. Mouallem, M. Nagappan, A. Pankin, M. Parashar, M. Pindzola, C. Reinhold, D. Schultz, K. Schwan, D. Silver, A. Sim, D. Stotler, M. Vouk, M. Wolf, H. Weitzner, P. Worley, Y. Xiao, E. Yoon, and D. Zorin, "Toward a first-principles integrated simulation of tokamak edge plasmas," *Journal of Physics: Conference Series*, vol. 125, p. 012042, jul 2008.

[56] M. F. Adams, S.-H. Ku, P. Worley, E. D'Azevedo, J. C. Cummings, and C.-S. Chang, "Scaling to 150K cores: Recent algorithm and performance engineering developments enabling XGC1 to run at scale," *Journal of Physics: Conference Series*, vol. 180, no. 1, p. 012036, 2009.

[57] E. Wang, S. Wu, Q. Zhang, J. Liu, W. Zhang, Z. Lin, Y. Lu, and Y. Du, "The Gyrokinetic Particle Simulation of Fusion Plasmas on Tianhe-2 Supercomputer," *2016 7th Workshop on Latest Advances in Scalable Algorithms for Large-Scale Systems*, pp. 25–32, 2016.

[58] M. Chen, Z.-M. Sheng, Q.-L. Dong, M.-Q. He, S.-M. Weng, Y.-T. Li, and J. Zhang, "Ion acceleration by colliding electrostatic shock waves in laser-solid interaction," *Physics of Plasmas*, vol. 14, no. 11, p. 113106, 2007.

[59] Y. Chen and S. E. Parker, "A delta-f particle method for gyrokinetic simulations with kinetic electrons and electromagnetic perturbations," *Journal of Computational Physics*, vol. 189, pp. 463–475, aug 2003.

[60] S. Balay, W. D. Gropp, L. C. McInnes, and B. F. Smith, "Efficient Management of Parallelism in Object-Oriented Numerical Software Libraries," in *Modern Software Tools for Scientific Computing* (E. Arge, A. M. Bruaset, and H. P. Langtangen, eds.), pp. 163–202, Boston, MA: Birkhäuser Boston, 1997.

[61] S. Balay, S. Abhyankar, M. F. Adams, J. Brown, P. Brune, K. Buschelman, L. Dalcin, V. Eijkhout, W. D. Gropp, D. Kaushik, M. G. Knepley, L. C. McInnes, K. Rupp, B. F. Smith, S. Zampini, H. Zhang, and H. Zhang, "PETSc Users Manual," Tech. Rep. ANL-95/11 - Revision 3.7, Argonne National Laboratory, 2016.

[62] "hipre: High Performance Preconditioners."

[63] K. J. Bowers, B. J. Albright, L. Yin, W. Daughton, V. Roytershteyn, B. Bergen, and T. J. T. Kwan, "Advances in petascale kinetic plasma simulation with VPIC and Roadrunner," *Journal of Physics: Conference Series*, vol. 180, p. 012055, jul 2009.

[64] R. A. Fonseca, L. O. Silva, F. S. Tsung, V. K. Decyk, W. Lu, C. Ren, W. B. Mori, S. Deng, S. Lee, T. Katsouleas, and J. C. Adam, "OSIRIS: A Three-Dimensional, Fully Relativistic Particle in Cell Code for Modeling Plasma Based Accelerators," in ... *ScienceICCS 2002*, vol. 2331, pp. 342–351, 2002.

[65] K. Germaschewski, W. Fox, S. Abbott, N. Ahmadi, K. Maynard, L. Wang, H. Ruhl, and A. Bhattacharjee, "The Plasma Simulation Code: A modern particle-in-cell code with patch-based load-balancing," *Journal of Computational Physics*, vol. 318, pp. 305–326, 2016.

[66] R. Chodura, "Plasma Flow in the Sheath and the Presheath of a Scrape-Off Layer," in *Physics of Plasma-Wall Interactions in Controlled Fusion*, pp. 99–134, Boston, MA: Springer US, 1986.

[67] R. W. Hockney and C. R. Jesshope, *Parallel Computers: Architecture, Programming and Algorithms*. Bristol: Institute of Physics Publishing, 1983.

[68] A. Bar-Noy and S. Kipnis, "Designing broadcasting algorithms in the postal model for message-passing systems," *Mathematical Systems Theory*, vol. 27, pp. 431–452, sep 1994.

[69] W. Gropp, L. N. Olson, and P. Samfass, "Modeling MPI Communication Performance on SMP Nodes," in *Proceedings of the 23rd European MPI Users' Group Meeting on - EuroMPI 2016*, (New York, New York, USA), pp. 41–50, ACM Press, 2016.

[70] L. Landau, "on the Vibrations of the Electronic Plasma," *Collected Papers of L.D. Landau*, vol. X, no. 1, pp. 25–34, 1946.

[71] T. M. G. Zimmermann, M. Coppins, and J. E. Allen, "Fluid model of the boundary of a one-dimensional plasma under the influence of an oblique magnetic field for a wide range of collisionality," *Physics of Plasmas*, vol. 15, p. 072301, jul 2008.

[72] R. H. Cohen and D. D. Ryutov, "Particle trajectories in a sheath in a strongly tilted magnetic field," *Physics of Plasmas*, vol. 5, no. 3, pp. 808–817, 1998.

[73] S. Devaux and G. Manfredi, "Vlasov simulations of plasma-wall interactions in a magnetized and weakly collisional plasma," *Physics of Plasmas*, vol. 13, p. 083504, aug 2006.

[74] P. Stangeby, "The Chodura sheath for angles of a few degrees between the magnetic field and the surface of divertor targets and limiters," *Nuclear Fusion*, vol. 52, no. 8, p. 083012, 2012.

[75] M. U. Siddiqui, C. D. Jackson, J. F. Kim, and N. Hershkowitz, "Direct measurements of ion dynamics in collisional magnetic presheaths," *Physics of Plasmas*, vol. 21, p. 102103, oct 2014.

[76] M. Umair Siddiqui, J. F. Kim, C. D. Jackson, and N. Hershkowitz, "Presheath and boundary effects on helicon discharge equilibria," *Plasma Sources Science and Technology*, vol. 24, p. 015022, dec 2014.

[77] J. Rapp, T. Biewer, T. Bigelow, J. Caneses, J. Caughman, S. Diem, R. Goulding, R. Isler, A. Lumsdaine, C. Beers, T. Bjorholm, C. Bradley, J. Canik, D. Donovan, R. Duckworth, R. Ellis, V. Graves, D. Giuliano, D. Green, D. Hillis, R. Howard, N. Kafle, Y. Katoh, A. Lasa, T. Lessard, E. H. Martin, S. Meitner, G.-N. Luo, W. McGinnis, L. Owen, H. Ray, G. Shaw, M. Showers, and V. Varma, "Developing the science and technology for the Material Plasma Exposure eXperiment," *Nuclear Fusion*, vol. 57, p. 116001, nov 2017.

[78] N. Hershkowitz, C. S. Yip, and G. D. Severn, "Experimental test of instability enhanced collisional friction for determining ion loss in two ion species plasmas," *Physics of Plasmas*, vol. 18, no. 5, 2011.

[79] J. Yi, Y. S. Chu, Y.-T. Chen, T.-Y. Chen, Y. Hwu, and G. Margaritondo, "High-resolution hard-x-ray microscopy using second-order zone-plate diffraction," *Journal of Physics D: Applied Physics*, vol. 44, p. 232001, jun 2011.

[80] C.-S. Yip, N. Hershkowitz, and G. Severn, "Verifying effects of instability enhanced ionion Coulomb collisions on ion velocity distribution functions near the sheath edge in low temperature plasmas," *Plasma Sources Science and Technology*, vol. 24, p. 015018, 2015.

[81] R. Koslover and R. McWilliams, "Measurement of multidimensional ion velocity distributions by optical tomography," *Review of Scientific Instruments*, vol. 57, no. 10, pp. 2441–2448, 1986.

[82] I. A. Biloiu, E. E. Scime, and C. Biloiu, "One- and two-dimensional laser induced fluorescence at oblique incidence," *Plasma Sources Science and Technology*, vol. 18, no. 2, 2009.

[83] S. D. Baalrud, J. D. Callen, and C. C. Hegna, "Instability-Enhanced Collisional Effects and Langmuir's Paradox," *Physical Review Letters*, vol. 102, p. 245005, jun 2009.

[84] S. D. Baalrud, J. D. Callen, and C. C. Hegna, "Kinetic theory of instability-enhanced collisional effects," *Physics of Plasmas*, vol. 17, no. 5, 2010.

[85] F. F. Chen, "Helicon discharges and sources: a review," *Plasma Sources Science and Technology*, vol. 24, p. 014001, jan 2015.

[86] D. Curreli and F. F. Chen, "Equilibrium theory of cylindrical discharges with special application to helicons," *Physics of Plasmas*, vol. 18, no. 11, 2011.

[87] A. M. Keesee and E. E. Scime, "Neutral density profiles in argon helicon plasmas," *Plasma Sources Science and Technology*, vol. 16, no. 4, pp. 742–749, 2007.

[88] E. Ahedo and J. Navarro-Cavallé, "Helicon thruster plasma modeling: Two-dimensional fluid-dynamics and propulsive performances," *Physics of Plasmas*, vol. 20, p. 043512, apr 2013.

[89] A. Niemczewski, I. Hutchinson, B. LaBombard, B. Lipschultz, and G. McCracken, "Neutral particle dynamics in the Alcator C-Mod tokamak," *Nuclear Fusion*, vol. 37, pp. 151–163, feb 1997.

[90] S. Blondel, D. E. Bernholdt, K. D. Hammond, and L. Hu, "Benchmarks and Tests of a Multidimensional Cluster Dynamics Model of Helium Implantation in Tungsten," *Fusion Science and Technology*, vol. 71, pp. 13–16, jan 2017.

Appendix A

Derivation of the Fluid Models

A.1 Classic Fluid Model of the Plasma Sheath

Assuming quasi-neutrality, the dynamics of the ions in the plasma pre-sheath can be described with the momentum balance equation

$$n_i M_i (\mathbf{V} \cdot \nabla)\mathbf{V} = n_i q_e (\mathbf{E} + \mathbf{V} \times \mathbf{B}) - \nabla p_i - M_i n_i \nu_t \mathbf{V} \tag{A.1}$$

$$(\mathbf{V} \cdot \nabla)\mathbf{V} = \frac{q_e}{M_i}(\mathbf{E} + \mathbf{V} \times \mathbf{B}) - \frac{\nabla p_i}{n_i M_i} - \nu_t \mathbf{V} \tag{A.2}$$

and continuity equation

$$\nabla \cdot (n_i \mathbf{V}) = n_e \nu_{iz}. \tag{A.3}$$

Then the system of equations (A.2) and (A.3) can be closed by ion isothermal equation of state

$$p_i = k_B T_i n_i, \tag{A.4}$$

and Boltzmann distribution function

$$n_i = n_e = n_0 \exp\left(-\frac{e\phi}{k_B T_e}\right). \tag{A.5}$$

The plasma parameters are assumed to vary as a function of the distance to wall y.

The expansion of continuity equation gives the relation between density gradient and

velocity gradient

$$n_i \frac{\partial V_y}{\partial y} + V_y \frac{\partial n_i}{\partial y} = n_e \nu_{iz} \tag{A.6}$$

$$\frac{\partial n_i}{\partial y} = \frac{n_i \nu_{iz}}{V_y} - \frac{n_i}{V_y} \frac{\partial V_y}{\partial y} \tag{A.7}$$

The first term of the momentum equation (A.2) becomes

$$(\mathbf{V} \cdot \nabla)\mathbf{V} = V_y \frac{\partial V_x}{\partial y}\mathbf{i} + V_y \frac{\partial V_y}{\partial y}\mathbf{j} + V_y \frac{\partial V_z}{\partial y}\mathbf{k} \tag{A.8}$$

In order to evaluate the second term, it is required to determine value of the electric field. Using equation (A.5) electric field can be obtained from the electrostatic potential

$$\phi = -\frac{k_B T_e}{e} (\log n_i - \log n_0) \tag{A.9}$$

$$E = -\frac{\partial \phi}{\partial y} = \frac{k_B T_e}{e n_i} \frac{\partial n_i}{\partial y} \tag{A.10}$$

Thus the projections of the momentum equation become

$$V_y \frac{\partial V_x}{\partial y} = \frac{q_e}{M_i} (V_y B_z - V_z B_y) - \nu_t V_x \tag{A.11}$$

$$V_y \frac{\partial V_y}{\partial y} = \frac{q_e}{M_i} \left(\frac{k_B T_e}{e n_i} \frac{\partial n_i}{\partial y} + V_z B_x - V_x B_z \right) - \frac{k_B T_i}{n_i M_i} \frac{\partial n_i}{\partial y} - \nu_t V_y \tag{A.12}$$

$$V_y \frac{\partial V_z}{\partial y} = \frac{q_e}{M_i} (V_x B_y - V_y B_x) - \nu_t V_z \tag{A.13}$$

In plasma sheath geometry $B_x = B \sin\psi$, $B_y = B \cos\psi$ and $B_z = 0$

$$V_y \frac{\partial V_x}{\partial y} = \frac{e}{M_i} V_z B \cos\psi - \nu_t V_x \tag{A.14}$$

$$V_y \frac{\partial V_y}{\partial y} = -\frac{e}{M_i} \left(\frac{k_B T_e}{e n_i} \frac{\partial n_i}{\partial y} + V_z B \sin\psi \right) - \frac{k_B T_i}{n_i M_i} \frac{\partial n_i}{\partial y} - \nu_t V_y \tag{A.15}$$

$$V_y \frac{\partial V_z}{\partial y} = -\frac{e}{M_i} (V_x B \sin\psi - V_y B \cos\psi) - \nu_t V_z \tag{A.16}$$

Substituting density gradient from equation (A.7) into equation (A.15) gives:

$$V_y \frac{\partial V_y}{\partial y} = -\left(T_i + T_e\right) \frac{k_B}{n_i M_i} \frac{\partial n_i}{\partial y} - \frac{e}{M_i} V_z B \sin\psi - \nu_t V_y \tag{A.17}$$

$$= -\frac{k_B \left(T_i + T_e\right)}{n_i M_i} \left(\frac{n_i \nu_{iz}}{V_y} - \frac{n_i}{V_y} \frac{\partial V_y}{\partial y} \right) - \frac{e}{M_i} V_z B \sin\psi - \nu_t V_y \tag{A.18}$$

$$\left[V_y - \frac{k_B \left(T_i + T_e\right)}{M_i} \frac{1}{V_y} \right] \frac{\partial V_y}{\partial y} = -\frac{k_B \left(T_i + T_e\right)}{M_i} \frac{\nu_{iz}}{V_y} - \frac{e}{M_i} V_z B \sin\psi - \nu_t V_y \tag{A.19}$$

Using following dimensionless parameters

$$X = y/\lambda_{mfp} \tag{A.20}$$

$$\mathbf{u} = \mathbf{V}/C_s \tag{A.21}$$

$$\Phi = -e\phi/k_B T_e \tag{A.22}$$

$$\Delta = \nu_{iz}/\nu_t \tag{A.23}$$

$$\lambda_{mfp} = C_s/\nu_t \tag{A.24}$$

$$\omega\tau = eB/M_i \nu_t \tag{A.25}$$

where $C_s = \left(\left(k_B T_e + k_B T_i\right)/M_i\right)^{1/2}$ is the Bohm acoustic velocity, equations (A.14), (A.19) and (A.16) become:

$$u_y \frac{\partial u_x}{\partial X} = \omega\tau \cos\psi - u_x \tag{A.26}$$

$$\left[1 - u_y^2\right] \frac{\partial u_y}{\partial X} = \Delta\omega\tau \sin\psi u_y u_z + u_y^2 \tag{A.27}$$

$$u_y \frac{\partial u_z}{\partial X} = -\omega\tau \left(u_x \sin\psi - u_y \cos\psi\right) - u_z \tag{A.28}$$